Solidification and welding metallurgy of experimental Ni-base and Fe-base superalloys containing Nb, Si and C.

INFORMATION TO USERS

This manuscript has been reproduced from the microfilm master. UMI films the text directly from the original or copy submitted. Thus, some thesis and dissertation copies are in typewriter face, while others may be from any type of computer printer.

The quality of this reproduction is dependent upon the quality of the copy submitted. Broken or indistinct print, colored or poor quality illustrations and photographs, print bleedthrough, substandard margins, and improper alignment can adversely affect reproduction.

In the unlikely event that the author did not send UMI a complete manuscript and there are missing pages, these will be noted. Also, if unauthorized copyright material had to be removed, a note will indicate the deletion.

Oversize materials (e.g., maps, drawings, charts) are reproduced by sectioning the original, beginning at the upper left-hand corner and continuing from left to right in equal sections with small overlaps. Each original is also photographed in one exposure and is included in reduced form at the back of the book.

Photographs included in the original manuscript have been reproduced xerographically in this copy. Higher quality 6" x 9" black and white photographic prints are available for any photographs or illustrations appearing in this copy for an additional charge. Contact UMI directly to order.

UMI

A Bell & Howell Information Company
300 North Zeeb Road, Ann Arbor MI 48106-1346 USA
313/761-4700 800/521-0600

SOLIDIFICATION AND WELDING METALLURGY OF EXPERIMENTAL Ni BASE AND Fe BASE SUPERALLOYS CONTAINING Nb, Si, AND C

By

John N. DuPont

Presented to the Graduate and Research Committee

of Lehigh University

in Candidacy for the Degree of

Doctor of Philosophy

in

Materials Science and Engineering

Lehigh University

January 20, 1997

Approved and recommended for acceptance as a dissertation in partial fulfillment of the requirements for the degree of Doctor of Philosophy.

2/12/97
Date

Dissertation Director

2/20/97
Accepted Date

Committee Members:

Prof. A.R. Marder, Committee Chair

Prof. M.R. Notis, Committee Member

Prof. D.B. Williams, Committee Member

Prof. A.W. Pense, Committee Member

Dr. C. V. Robino, Committee Member

ACKNOWLEDGEMENTS

During the last six years at Lehigh I have had the fortunate experience of learning, working, and spending time with many outstanding people both within and outside the University, most of which have made important contributions toward the completion of this research. I would first like to thank my advisor, colleague, and friend Prof. Arnold R. Marder who gave me the opportunity to work and develop a research program in welding in the Energy Research Center (ERC). His teaching an advising efforts have gone far beyond the laboratory and I am grateful. The ability to complete my graduate studies would not have been possible without the opportunity to work in the ERC, which was provided by Profs. E. K. Levy and A.R. Marder. The frequent help and good times shared with graduate students in the group: Brian Smith, Scott Bluni, Boris Levin, Cathy Jordan, Bruce Lindsly, Steve Banovic, Don Susan, Jesse Nawrocki, Kevin Luer, Megan Slusser, and Doug Puerta - have made the process a very enjoyable one. I would also like to thank my committee members: Profs. A.R. Marder, M.R. Notis, D.B. Williams, and A.W. Pense, and Dr. Charles Robino.

The assistance in metallographic preparation provided by Arlan Benscoter and electron microscopy provided by Kathy Repa, Jim Kerner, and Dave Ackland is greatly appreciated. The metallographic and EPMA work were important parts of this experimental research, and Kathy Repa and Arlan Benscoter are the best around in this area. Andrea Pressler provided much help in photographic preparation and Pat Newhart kept my spelling straight and always made sure my graduate requirements were in order.

Significant help was also received from Sandia National Laboratory: Drs. Brian Damkroger and Mike Macquire provided the experimental alloys, Dr. Joe Michael conducted the BEKP work, and the varestraint tester was provided by Dr. Mike Cieslak. Dr. Charles Robino devoted a great deal of time to put me in touch with all these people and make everything happen. He has also provided useful insight into the experimental results, not to mention the fact that he actually carried all the experimental alloys (~100 pounds worth) on the plane and hand delivered them (I have a feeling I owe him for that one). His efforts are greatly appreciated.

Financial support for this research was provided by the American Welding Society, Sandia National Laboratory, Oak Ridge National Laboratory, Pennsylvania Power & Light Co., Delmarva Power Co., Allegheny Power Co., Virginia Power Co., Centerior, and Ohio Edison Power Co. I would particularly like to thank the American Welding Society for their support through the National Fellowship Award.

The support of many family members was invaluable during this entire education process. My brothers and sisters: Dan, Colleen, Eileen, Susan, Lisa, Mark, Terry, and Jeff have always been there to help in one form or another. I extend a special thanks to Mr. and Mrs. William Conville who provided so much help in those early years. The start of my education would have never been possible without all the support and encouragement received from my parents, Alden and Pauline DuPont, who were always there to help. I apologize for anyone I may have missed.

Finally, I reserve the most sincere appreciation for my loving wife, Kathy, and two wonderful children, Ryan and Caitlin. Ryan and Caitlin have always been there to remind

me of the important things in life. The endless amount of love, support, patience, and encouragement displayed by Kathy can not be described in words. She has somehow managed to tolerate my schedule, most often with a smile, and simultaneously volunteer for PTO secretarial duties, Sunday School teaching, Wrestling Board activities, Parent Teacher help, and probably many other activities I have since forgotten, not to mention serve as my assistant baseball and soccer coach through the last four seasons. She has worked just as hard as I have to make this all happen and shares equally in my success. I am especially grateful for all the love and support provided by these three very special people and dedicate this dissertation to them.

Dedicated to Kathy, Ryan, and Caitlin

TABLE OF CONTENTS

LIST OF TABLES

CHAPTER 4:

LIST OF FIGURES

CHAPTER 2:

CHAPTER 4:

LIST OF SYMBOLS

a	Dimensionless parameter in Bower-Brody-Flemings model
b	Dimensionless parameter in Solari-Biloni model
ΔC	Increase in dendrite core solute concentration due to undercooling
C_e	Eutectic composition
C_l	Liquid composition
C_o	Nominal composition
$C_{s,a}$	Average solute composition in solid
C_s	Solid composition
C_s^*	Solid composition at solid/liquid interface
C_{sm}	Maximum solid solubility
C_t	Dendrite tip composition
D_l	Diffusivity of solute in liquid
D_s	Diffusivity of solute in solid
f_e	Fraction of eutectic
f_l	Fraction of liquid
f_s	Fraction of solid
G	Temperature gradient
$I(P_c)$	Ivanstov function
k	Equilibrium distribution coefficient
k_t	Effective equilibrium distribution coefficient
L	One-half dendrite spacing

m_l	Liquidus slope
m_s	Solidus slope
P_c	Peclet number
R	Growth rate
r	Dendrite tip radius
T	Temperature
ΔT	Solidification temperature range or undercooling
ΔT_c	Constitutional component of dendrite tip undercooling
T_e	Eutectic temperature
ΔT_k	Kinetic component of dendrite tip undercooling
T_l	Liquidus temperature
T_m	Melting temperature of pure solvent
ΔT_r	Radius of curvature component of dendrite tip undercooling
T_s	Solidus temperature
T_t	Dendrite tip temperature
ΔT_{th}	Thermal component of dendrite tip undercooling
t	Time
t_f	Local solidification time
x	Distance
α	Dimensionless parameter in Brody-Flemings model
Γ	Gibbs-Thomson parameter
ρ	Density

ABSTRACT

The solidification and weldability of experimental Ni base and Fe base superalloys containing Nb, Si, and C was studied using a combination of differential thermal analysis, quenching experiments, varestraint testing, and microstructural characterization techniques. The solidification reaction sequences responsible for microstructural development were found to be similar to those expected in the Ni-Nb-C ternary system. The solute rich interdendritic liquid exhibited two eutectic-type reactions at the terminal stages of solidification: $L \rightarrow (\gamma + NbC)$ and $L \rightarrow (\gamma + Laves)$. A pseudo ternary γ-Nb-C approach, modelled after the simple Ni-Nb-C system, was developed to provide a quantitative description of solidification behavior for these experimental alloys. Solute redistribution calculations in the model are based on a previous approach developed by Mehrabian and Flemings, with modifications made to account for the high diffusion rate of C in the solid. Solidification parameters for Nb and C were determined through DTA and electron probe microanalysis techniques and used as inputs to the model. Reasonable agreement is found between calculated volume fractions of the γ/NbC and γ/Laves constituents and those measured experimentally. The modelling results permit detailed descriptions of the relation between alloy composition and microstructural evolution during solidification. The results are also joined with experimental observations of fusion zone microstructures to determine the relation between alloy composition and solidification cracking susceptibility. A method is proposed for calculating the distribution of liquid in the solid+liquid zone as an aid to determining the individual effects of alloy composition on solidification cracking susceptibility.

1. INTRODUCTION

Ni base and Fe base superalloys are commonly used in critical applications which require a combination of elevated temperature strength and oxidation resistance. The Nb-strengthened alloys represent a significant portion of superalloys currently in use. Commercial examples include alloys IN519, IN625, IN706, IN718, IN903, IN909, and Thermo-span, to name a few. These alloys are used extensively on components which are often fabricated by fusion welding to both matching alloys and dissimilar materials. In these applications, extensive fusion zone solidification cracking has been observed by several investigators. The presence of this defect is often unacceptable from a mechanical property and corrosion standpoint.

Weldability (i.e., resistance to solidification cracking) depends mainly on alloy composition. Studies conducted on several nickel-base superalloys have shown that minor additions of Nb, Si, and C strongly affect the solidification behavior and associated cracking susceptibility of these alloys. The results of several limited studies have suggested that these elements also have a strong effect on the cracking tendency in dissimilar metal weld applications, where the iron content of the fusion zone is substantially increased. Although several detailed investigations have been conducted on specific commercial alloy systems, no systematic study has been conducted on experimental alloys which simulate the broad range of compositions that are possible in both autogenous and dissimilar metal weld applications. Therefore, a comprehensive solidification and weldability study was conducted on experimental superalloys in order to develop this understanding, the results of which are summarized in this dissertation.

1.1 OVERVIEW OF RESEARCH

A literature review was conducted as a first step to this research and is presented in Chapter 2. The review consists of three main sections. The first section presents a description of the phenomenological mechanism of solidification cracking, the objective being to identify the import factors which affect cracking during welding. In this section, it is shown that cracking is influenced mainly by the solidification temperature range as well as the amount and morphology of eutectic-like constituents that form during the terminal stages of solidification. Both of these factors are, in turn, controlled by solute segregation which occurs under the non-equilibrium conditions typical of welding. Thus, solute segregation plays a vital role in determining the cracking susceptibility of weld metals. Therefore, the second section of the literature review is devoted to a review of analytical solute redistribution models which have been proposed to describe microsegregation. The objective here is to identify the important alloy and solidification parameters which control microsegregation so that experimental results of this study can be properly interpreted under the solidification conditions which are unique to welding. The third section of Chapter 2 presents a review of solidification and weldability studies conducted on pertinent superalloy systems. Here, the strong effects of Nb, Si, and C on the solidification and weldability of nickel-base alloys is demonstrated through a summary of several detailed studies. The section concludes with a review of the limited work conducted on dissimilar metal welds and a statement of objectives for this research.

The experimental alloys and procedures are described in Chapter 3. The approach taken here was to design a matrix of alloy compositions which simulate the broad range

of possible fusion zone compositions that can develop in both autogenous and dissimilar metal weld applications involving Nb-strengthened superalloys. The solidification behavior of the experimental alloys was then characterized by differential thermal analysis (DTA), quenching experiments, and microstructural characterization techniques including light and scanning electron microscopy, electron probe microanalysis (EPMA), and quantitative image analysis (QIA). Varestraint solidification cracking tests were also conducted on each alloy to develop the relation between composition, solidification behavior, and fusion zone cracking susceptibility.

The general solidification behavior of the experimental alloys is presented in Chapter 4. The solidification reaction sequences responsible for microstructural development are found to generally consist of primary L $\rightarrow \gamma$ solidification followed by two eutectic type reactions in the solute rich interdendritic liquid of L $\rightarrow (\gamma + NbC)$ and L $\rightarrow (\gamma +$ Laves). These reaction sequences are qualitatively described by drawing an analogy to the Ni-Nb-C system. This analogy sets the framework for developing a quantitative analysis of solute redistribution and microstructural development by a γ-Nb-C pseudo-ternary approach. The remainder of Chapter 4 is dedicated to determining solidification parameters and selecting solute redistribution equations which are needed to apply the pseudo-ternary method. Here, the liquidus and solidus slopes and equilibrium distribution coefficients for Nb, Si, and C are determined using a combination of DTA and EPMA techniques. The solute redistribution equations which best describe mass transfer of Nb and C during solidification are considered analytically and, where possible, experimentally. From this analysis, it is demonstrated that the equilibrium lever law can

be applied to describe solute redistribution of C while the behavior of Nb can be described with the Scheil equation. A pseudo-ternary γ-Nb-C "solidification surface", analogous to the liquidus surface in the Ni-Nb-C ternary system, is then determined by combining results from QIA, EPMA, and solute redistribution calculations. The solidification surfaces are compared to similar diagrams determined from thermodynamic calculations and reasonable agreement is found. These solidification parameters and solidification surfaces provide the information needed for the quantitative analyses developed in Chapter 5. A comparison of the general solidification behavior between the experimental alloys and commercial alloys is also provided in Chapter 4.

Chapter 5 develops analytical equations which describe solute redistribution of Nb and C during both the primary and eutectic-type stages of solidification. A model previously proposed by Mehrabian and Flemings is first reviewed and then modified to account for the high diffusion rates of C in the solid. From this, two new solute redistribution equations are proposed which describe primary and eutectic-type solidification reactions in ternary systems where one solute exhibits negligible diffusion in the solid phase and the second solute diffuses infinitely fast. The solidification parameters and solidification surfaces determined in Chapter 4 are then used as inputs to the model, and a finite difference technique is used to calculate the total and individual amounts of eutectic-type constituents which form during solidification. Reasonable agreement is found between these calculated values and those measured experimentally through QIA. The modelling results are then used to quantitatively explain the relations between alloy composition and microstructural evolution during solidification.

Carbon additions are found to have a pronounced effect on microstructural development by controlling the primary solidification path. As the C content in the alloy is increased, the primary L $\rightarrow \gamma$ solidification path extends far into the C rich side of the solidification surface as the interdendritic liquid becomes enriched in C. This primary path orientation favors the L $\rightarrow (\gamma + NbC)$ eutectic type reaction, and large amounts of the γ/NbC eutectic type constituent forms as a result. In contrast, low C alloys exhibit a primary solidification path which remains close to the "binary" γ - Nb edge of the solidification surface where the L $\rightarrow (\gamma +$ Laves) eutectic type reaction is favored. The segregation potential of Nb, as measured through the Nb distribution coefficient (k_{Nb}), is found to depend on the Fe content of the alloy. In the Ni base alloys containing a nominal 10 wt% Fe, $k_{Nb} = 0.46$. The value of k_{Nb} is reduced significantly to 0.25 in the Fe base alloys which contain 45 wt% Fe. Thus, the segregation of Nb to the liquid is much more pronounced in the Fe base alloys. This causes more solute rich interdendritic liquid to be present in the Fe base alloys when the eutectic type reactions are initiated which, in turn, produces more of the eutectic-type constituents in the as-solidified microstructure. The proposed pseudo-ternary solidification model accurately predicts this behavior. The results of k_{Nb} values measured here are combined with a summary of similar values measured in commercial alloys systems, and a correlation between k_{Nb} and nominal Fe content is demonstrated.

The relation between solidification behavior and fusion zone cracking susceptibility is discussed in Chapter 6. The modelling results are joined with experimental observations of fusion zone microstructures to identify four different types of microstructural

morphologies which develop in the varestraint samples. These microstructure types are then used as an aid in developing the relation between solidification temperature range and the maximum crack length. Carbon additions are found to have a strong, beneficial effect on cracking resistance. This is explained in terms of the relation between C content and the solidification temperature range. The high C alloys favor the $L \rightarrow (\gamma + NbC)$ reaction which occurs at much higher temperatures than the $L \rightarrow (\gamma + Laves)$ reaction. Thus, C additions generally decrease the solidification temperature range and lead to a concomitant improvement in fusion zone cracking susceptibility. A method is proposed for calculating the distribution of liquid in the solid+liquid ("mushy") zone as an aid to determining the individual effects of each alloy addition on solidification cracking susceptibility. Preliminary calculations are presented for several alloys, and the results are found to reveal some important relations between alloy composition, the distribution of liquid in the mushy zone, and cracking susceptibility. In particular, the results directly show that C additions shrink the size of the crack susceptible mushy zone .

2. LITERATURE REVIEW

2.1 WELD METAL SOLIDIFICATION CRACKING

The formation of cracks during solidification can occur in ingots, castings, and welds. The phenomenon has been investigated for quite some time and the general features are understood in a qualitative sense, but work is still in progress to quantitatively determine conditions which lead to solidification cracking [2.1,2.2]. In general, cracks can form in certain alloy systems during the terminal stages of solidification when a semi-continuous liquid film is distributed along grain boundaries and interdentritic regions. At this stage, shrinkage and mechanical stresses begin to transfer across the partially solidified boundaries. If the amount of grain boundary liquid is relatively high and distributed along the boundary as a thin film, the stresses cannot be supported, causing the boundary area to rupture and form a crack. Solute segregation, the solidification temperature range, and the solidification path are major factors affecting the crack susceptibility of weld metals. The interfacial liquid morphology which exists at the terminal stages of solidification and the degree of restraint during welding are other important factors. These considerations are discussed below with emphasis placed on the first three factors since they are typically the most influential and amenable to control through alloy composition.

2.1.1 EFFECT OF SOLIDIFICATION TEMPERATURE RANGE

The effect of the solidification temperature range on cracking susceptibility is described with the aid of Figure 2.1, which schematically shows the solidification morphology at various stages between the liquidus and solidus in a binary eutectic system

under equilibrium conditions [2.3]. At stage 1, primary dendrites begin to form and the liquid can flow through the interdendritic regions. At this stage, stresses are not well developed yet since solid/solid boundaries have not formed and, therefore, cracks cannot develop. Within stage 2, the dendrites begin to impinge on one another as the coherent temperature is approached, but interdendritic liquid movement is still possible. At this stage, stresses begin to develop at the boundaries and the newly formed boundaries may rupture under the imposed residual stresses to form cracks. Although crack formation is possible, the cracks can often be healed at this stage by back-filling of the free-flowing liquid. This form of healing has been observed in aluminum and stainless steel alloys [2.4,2.5,2.6].

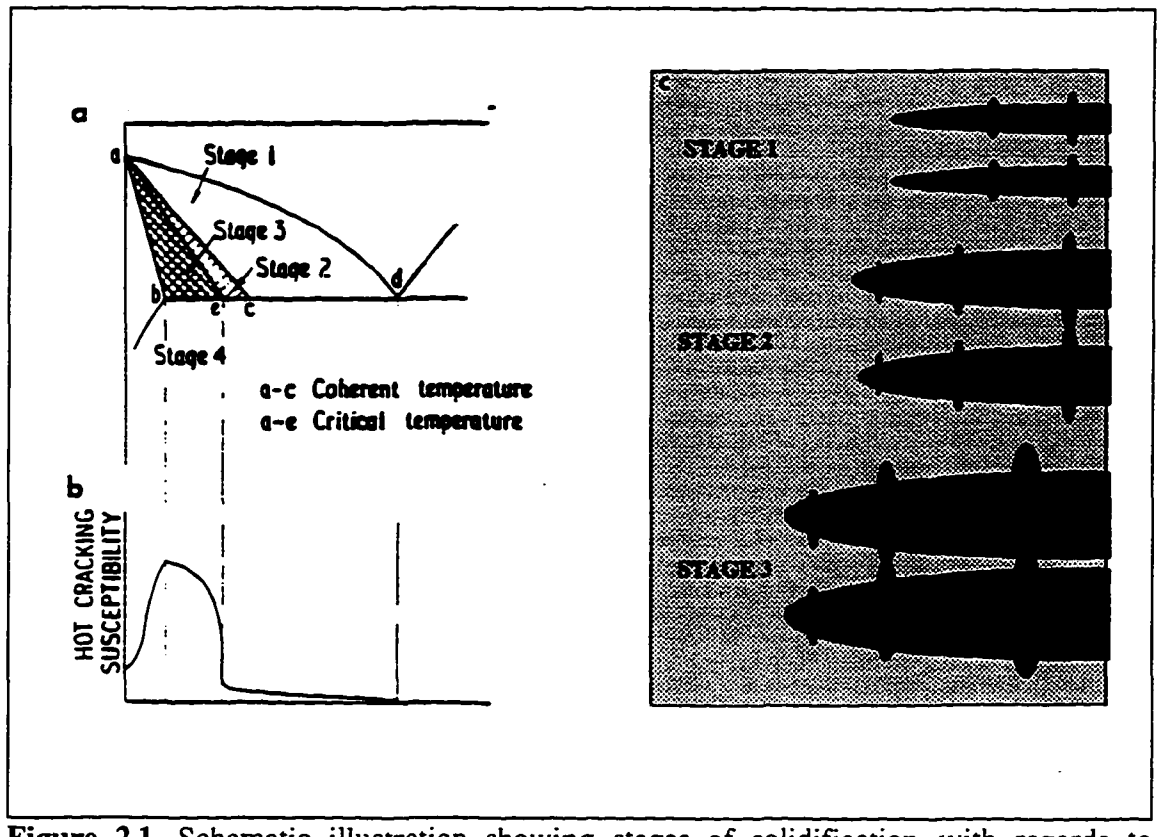

Figure 2.1. Schematic illustration showing stages of solidification with regards to dendrite/liquid morphology and cracking susceptibility.

In stage 3, the boundaries are well developed and the passage of liquid to the interdendritic volumes is strongly restricted. In this condition, any cracks that form are less likely to be back-filled by liquid and crack susceptibility is the highest as a result. Stage 4 corresponds to temperatures below the solidus where solidification is complete. Thus, stage 3 represents the critical temperature range where cracks are most likely to form and subsequently persist upon cooling. It is difficult to determine at exactly what point crack healing is prevented and the associated critical temperature range where cracks are most likely to form. In general, however, an increase in the overall solidification temperature range will widen stage 3, resulting in more exposure of the solidifying alloy to the critical range and leading to increased crack susceptibility. This phenomena has been observed experimentally for a wide range of alloy systems [e.g., 2.7,2.8].

The equilibrium solidification temperature range varies with composition and the relation between crack susceptibility and composition according to Boreland [2.3] is shown schematically in Figure 2.1b. The equilibrium solidification temperature range is highest at the maximum solid solubility limit (C_{sm}), and, according to the phenomenological mechanism proposed above, crack susceptibility is also a maximum at this point. Boreland described the effect of composition and alloy partitioning on widening of the solidification temperature range and concomitant cracking tendency by the Relative Potency Factor (RPF). The RPF is defined as

$$RPF = \frac{(T_l - T_s)}{C_o} = m_l \frac{(k-1)}{k} \qquad (2.1)$$

where T_l and T_s are the liquidus and solidus temperatures, respectively, C_o is the nominal alloy composition, m_l is the slope of the liquidus, and k is the distribution coefficient. When the RPF is multiplied by the nominal composition, the equilibrium solidification temperature range is obtained. Thus, solute additions which partition preferentially to the liquid phase during solidification (i.e., exhibit very low k values) are most detrimental to solidification cracking. Again, this general effect has been repeatedly observed under experimental conditions. Typical examples include P and S in ferritic and austentic steels [2.9], along with B, Nb, Si, and C in Ni-base alloys [2.7, 2.10]. However, it must be noted that the RPF is based on equilibrium solidification conditions where solute diffusion is assumed infinite in both the solid and liquid. In processes such as welding where solid state diffusion is often prevented, the solidification temperature range is not accurately given by the equilibrium phase diagram. Under these conditions, the liquid composition will be enriched, possibly to a eutectic composition, and the solidus can be lowered to the eutectic temperature, resulting in further widening of the solidification temperature range. This is discussed in more detail in the next section.

2.1.2 EFFECT OF SOLUTE SEGREGATION

As mentioned above, the cooling rate during weld metal solidification is typically high enough to prevent solid state diffusion in many alloy systems. This inherent feature of the welding process increases microsegation, which increases the tendency to form solidification cracks. The general effect of microsegregation is discussed qualitatively in this section and will be reviewed quantitatively in section 2.2 where various solute

redistribution models are reviewed.

The effect of incomplete solid state diffusion during solidification is illustrated schematically in Figure 2.2 [2.11]. Here, the liquidus and solidus are simplified as straight lines so that the distribution coefficient, k (= C_s/C_l, where C_s and C_l are the solid and liquid compositions), is independent of temperature. The condition shown is for $k < 1$, where solute is rejected to the liquid during solidification and $C_s < C_l$ at any temperature. This is the normal case, since solute elements are accommodated much easier into the random atomic arrangement of the liquid compared to the rigid atomic structure of the solid.

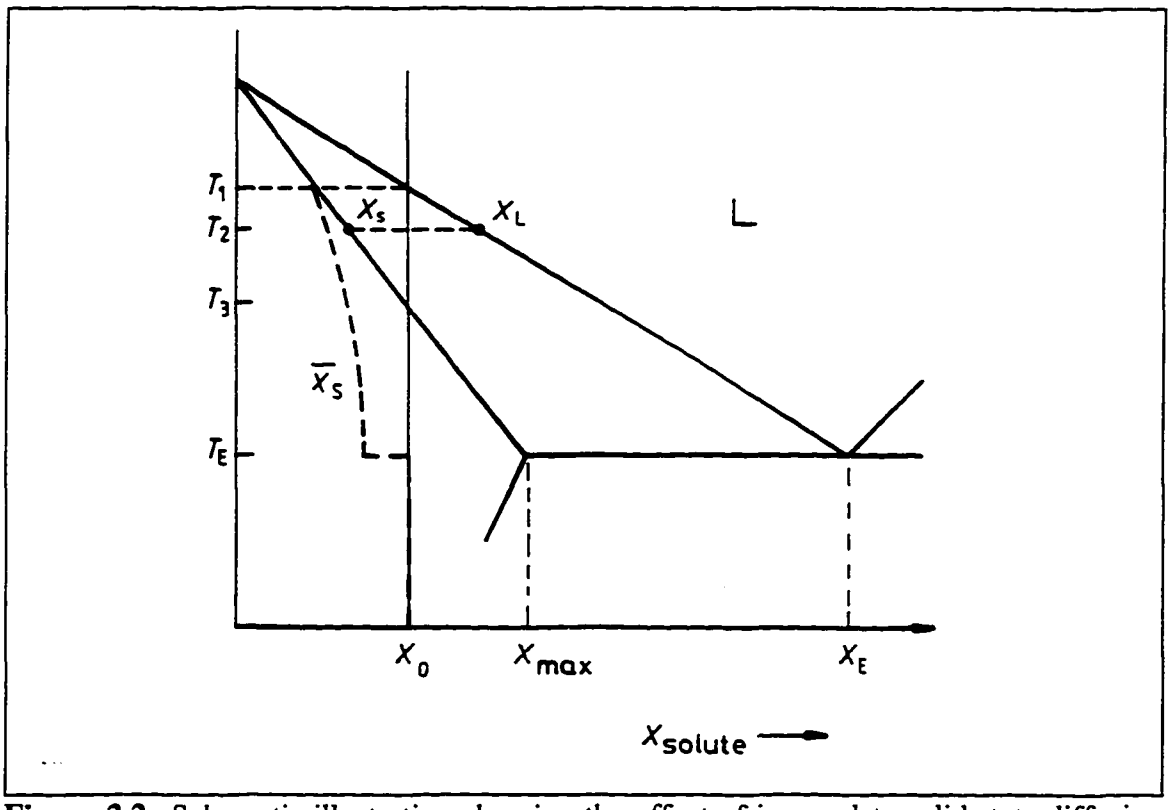

Figure 2.2. Schematic illustration showing the effect of incomplete solid state diffusion during solidification on the solidus temperature.

The first liquid to solidify at T_l will have composition kC_o, where C_o is the nominal composition. If solidification occurred under equilibrium conditions, the solid composition would increase as temperature decreased, following the solidus line as solute is redistributed in the solid by diffusion. However, under high cooling rate conditions typical of welding, solid state diffusion is hindered or completely prevented and, for many alloy systems (e.g., substitutional solutes in FCC solvents-see section 2.2.2.3), the as-solidified solid composition typically does not change. In this condition, the solid dissolves less solute than that given by the phase diagram and there is an enrichment in the liquid solute composition as a result. The actual mean composition of the solid is then given by the dotted line in the Figure 2.2. Since T_l decreases with increasing solute for $k < 1$, solute enrichment in the liquid promotes an extension of the solidification temperature range relative to the equilibrium range. In fact, the liquid is often enriched to the eutectic temperature. In view of the discussion above on the effect of the solidification temperature range, it is obvious that solute segregation exacerbates crack susceptibility by widening the solidification temperature range.

Referring again to Boreland's RPF, it is clear that this parameter is not valid under non-equilibrium solidification conditions typical of welding. As a limiting case, when the liquid is enriched to the eutectic temperature, the solidification temperature range, ΔT, is given by

$$\Delta T = T_m + m_l C_o - T_e \qquad (2.2)$$

where T_m is the melting point of the pure solvent, m_l is the liquidus slope (a negative quantity), C_o is the nominal solute content, and T_e is the eutectic temperature. Based on the discussion to this point, it is obvious that the formation of non-equilibrium eutectic in small amounts along the interdendritic boundaries will exacerbate cracking by interfering with the formation of solid/solid boundaries. However, if the liquid at the eutectic composition is present in large quantities, greater than approximately 10 volume percent [2.12,2.13], backfilling can occur up to the point where solidification is complete and the final amount of cracks present after solidification may be small. The amount of eutectic formed increases with increasing composition (see section 2.2.1.2). Thus, under non-equilibrium solidification conditions where a eutectic constituent is formed, the actual solidification temperature range decreases as C_{sm} is approached (equation (2.2)) and the amount of eutectic formed increases. Cracks may begin to heal at nominal compositions where the percent eutectic is greater than ≈10 volume percent. As a result, the actual maximum crack susceptibility is expected to occur at a value less than C_{sm}, where the solidification temperature range is relatively high and insufficient liquid is available for backfilling. Supporting evidence of this phenomenon is presented for data from the Al-Cu system in Figure 2.3 [2.14]. Figure 2.3a plots the cracking tendency as a function of percent eutectic solidification while Figure 2.3b plots the percent eutectic solidification as a function of weight percent Cu according to the Scheil equation, which has been shown to provide a fairly good description of solidification for this alloy system [2.15] (see section 2.2.1.2). The maximum solid solubility is noted as C_m in the plots. The maximum cracking tendency occurs at about $\frac{1}{2}C_{sm}$. At compositions higher than this, the

amount of eutectic approaches 10%, and back-filling is possible. Thus, the maximum crack susceptibility as a function of alloy composition is apparently achieved when a balance is struck between the temperature range and percent eutectic present at the terminal stage of solidification.

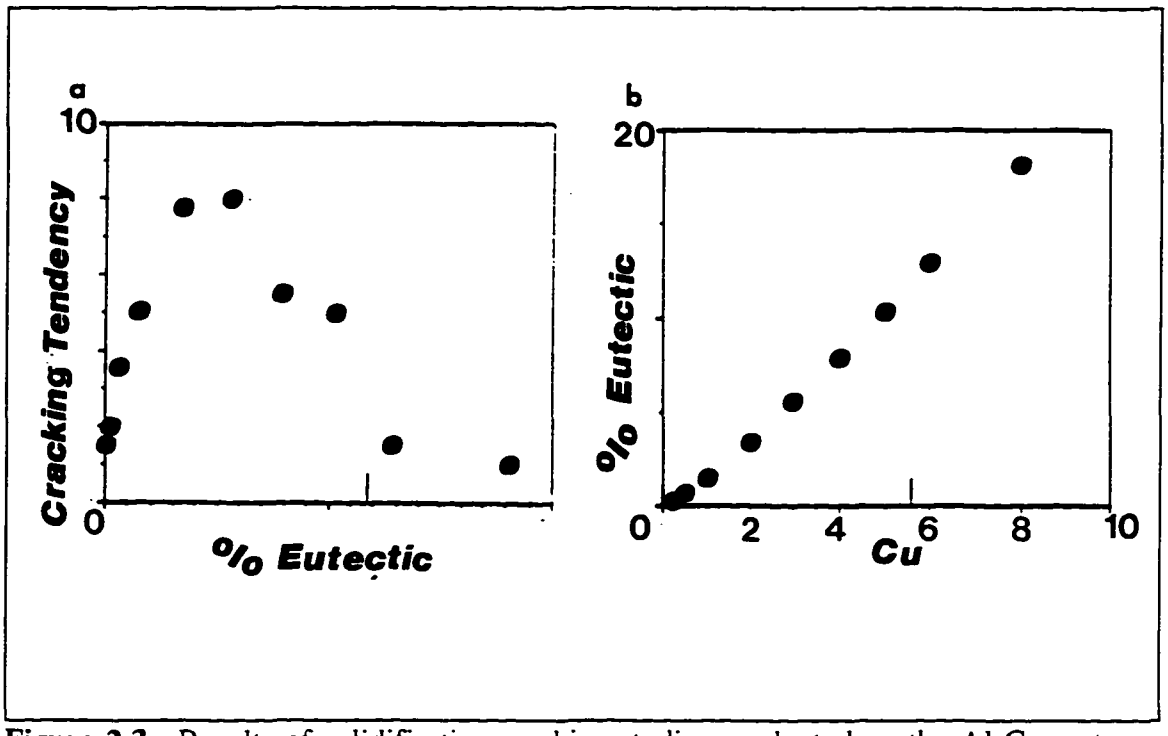

Figure 2.3. Results of solidification cracking studies conducted on the Al-Cu system.

2.1.3 EFFECT OF SOLIDIFICATION PATH

For weld metal cracking to occur during solidification, it is not a sufficient condition that the alloy exhibits a wide solidification range. It is also necessary that a liquid film exists along grain boundaries and interdendritic regions which will rupture under the imposed residual stresses. In this sense, the solidification path of the alloy is of considerable importance. Just as microsegregation was shown to exacerbate cracking

by widening the solidification temperature range, it will be illustrated in this section that microsegregation also alters the solidification path in a way which favors cracking.

Consider again the solidification path of a binary alloy under equilibrium conditions (i.e., no microsegregation) at a composition less than the maximum solid solubility, Figure 2.2. The first solid forms at composition kC_o, which is less than the bulk composition. As the temperature is decreased and the fraction of solid increased, the solid composition is adjusted to follow the solidus line. At the final stage of solidification, the solid has uniformly increased composition to C_o and the alloy exhibits a simple reaction

$$L \rightarrow \gamma \qquad (2.3)$$

However, under non-equilibrium conditions where the liquid composition can be enriched to the eutectic composition, the solidification path becomes slightly more complicated for the simple binary case.

$$\begin{array}{c} L \rightarrow L_e + \gamma \\ \downarrow T_e \\ \gamma_{max}+\beta \end{array} \qquad (2.4)$$

The liquid becomes enriched to C_e, the eutectic composition, and transforms to $\gamma+\beta$. In this condition, the microstructure is significantly different than that which would be observed under equilibrium conditions. Instead of exhibiting a single phase solid with

uniform composition, the structure possess a cored γ region and a eutectic of γ/ß, where the γ in the eutectic is at the maximum solubility limit and ß is a non-equilibrium phase. At temperatures just above the eutectic point, the liquid is distributed along interdendritic regions and is morphologically favorable for initiating solidification cracks. This phenomenon has been observed in many stainless steel and nickel based alloys [e.g., 2.6, 2.7,2.8,2.16,2.17].

2.1.4 EFFECT OF INTERFACIAL LIQUID MORPHOLOGY AND RESIDUAL STRESSES

The morphology of the interdendritic liquid is also important with regards to resisting crack formation during solidification [2.3]. The distribution of the liquid film is controlled mainly by the solid/liquid surface tension. When the surface tension is low, the liquid wets the boundary and forms a thin film which covers a large portion of the boundary. This type of morphology interferes with the formation of solid/solid boundaries, thus reducing the ability of the material to support residual stresses and increasing crack susceptibility. This effect is thought to contribute, in part, to the detrimental effects of P and S in steels [2.3] and B in Ni-based alloys [2.18]. In contrast, high surface tensions will promote spheroidization of the remaining liquid and solid/solid bridging, thus reducing cracking tendency. This concept has been utilized by Jolley and Geraghty [2.19] to increase the cracking resistance of a 18Cr-13Ni-1Nb stainless steel. In the base alloy, cracking occurred rather extensively due to the formation of a Nb rich eutectic-like constituent that formed in the interdendritic volumes. With the addition of Mg, the

eutectic-like structure was observed to become spherical and cracking was appreciably reduced.

Lastly, the magnitude of the residual stress which is present during welding must be considered. In an ideally non-constrained structure, thermal expansions and contractions due to localized heating and solidification are accommodated by small displacements and no thermal stresses are developed. However, most real structures will present some degree of restraint to thermal displacements, with the degree of restraint depending mainly on the joint design. Therefore, a given alloy system can exhibit different cracking tendencies under different joint designs. This consideration is a mechanical one and will not be discussed further here.

2.1.5 SUMMARY

Solidification cracking is strongly influenced by the solidification temperature range, solute segregation, and the solidification path. Under equilibrium conditions were no microsegregation exists, the solidification temperature range and solidification path are given by the phase diagram. In this case, the temperature range is relatively narrow (compared to non-equilibrium solidification). For binary alloys solidifying under equilibrium conditions, the solidification temperature range can be determined for a given alloy composition by the RPF, and alloying elements which partition strongly to the liquid (i.e., low k value) during solidification promote cracking.

Under non-equilibrium conditions, solute redistribution in the solid is limited or prevented completely which results in solute enrichment in the liquid. In this case, the

solidification temperature range is increased and non-equilibrium phases tend to form along interdendritic regions, both of which exacerbate fusion zone hot cracking. Thus, microsegregation of minor alloying elements during non-equilibrium conditions has a strong influence on weld cracking and deserves careful attention when assessing the effect of alloy composition on weldability. Microsegregation is affected not only by the alloy system (C_o, k, m_l), but also by the solidification parameters, (temperature gradient, G, and growth rate, R). In addition, the microsegregation profiles which are observed in weld metals at room temperature by electron microprobe (EPMA) techniques may not always correspond to the profiles which existed during solidification. A thorough understanding of weld metal microsegregation is critical when interpreting EPMA and weldability results. Therefore, various models which have been proposed for quantifying microsegregation are reviewed below with the objective of identifying the critical alloy and solidification parameters which affect solute segregation during solidification.

2.2 SOLUTE REDISTRIBUTION MODELS

In the last section it was demonstrated that microsegregation plays a key role in solidification cracking by affecting the solidification temperature range and formation of non-equilibrium phases along interdendritic regions. Thus, any study which attempts to correlate alloy composition to solidification behavior and weldability must carefully consider the physical aspects of weld metal microsegregation. The most effective way to accomplish this task is to review analytical models proposed to describe microsegregation, which is done in this section. General models to describe solute redistribution during solidification of simple planar solid/liquid interfaces are described first, with reference being made to the potential effects on weldability where appropriate. The solidification parameters which exists during welding are then reviewed with regards to break down of the planar interface, followed by a review of microsegregation models for dendritic solidification. Lastly, a summary of results from investigations directed at modelling weld metal microsegregation in particular is presented. The next section will then review solidification and weldability studies which have been conducted on pertinent Fe-Ni-Cr systems.

2.2.1 PLANAR FRONT SOLIDIFICATION

2.2.1.1 EQUILIBRIUM SOLIDIFICATION

The simplest case of solute redistribution to consider is solidification under equilibrium conditions, which assumes complete solute diffusion in the liquid and solid so that concentration gradients within each phase are not established. In this case, the

solid and liquid compositions are simply given by the phase diagram as a function of temperature. From a simple mass balance

$$C_s f_s + C_l f_l = C_o \qquad (2.5)$$

Also, since $f_s + f_l = 1$ and $k = C_s/C_l$

$$C_s = \frac{kC_o}{f_s(k-1) + 1} \qquad (2.6)$$

Although considerable solute redistribution occurs during equilibrium solidification, the assumption of complete diffusion results in a final solid with uniform composition. As most industrial solidification processes rarely occur under equilibrium conditions, particularly welding, this analytical expression is of little significance.

2.2.1.2 NO DIFFUSION IN THE SOLID/PERFECT MIXING IN LIQUID

The cooling rates typical of welding often prevent solid state diffusion, but the various forces acting on the weld pool due to the plasma jet, convection, and surface tension tend to promote good mixing in the liquid state. In this case, solute segregation can be modelled fairly accurately by the Scheil equation [2.20]. This analysis assumes that solid state diffusion is completely prevented and there is perfect mixing in the liquid. Other assumptions include: negligible undercooling before nucleation and during growth, a planar solid/liquid interface, and k is constant. As shown schematically in Figure 2.4

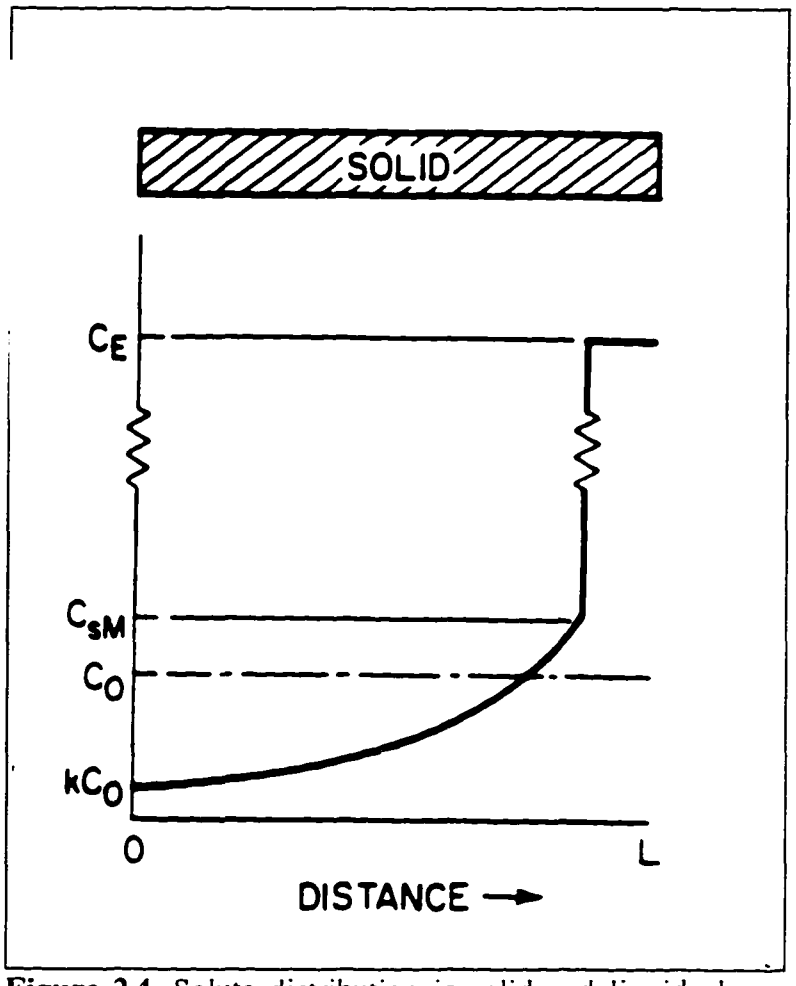

Figure 2.4. Solute distribution in solid and liquid phases during solidification assuming no solid state diffusion and complete solute mixing in liquid.

[2.21], this can analyzed by equating the small amount of solute (C_l - C_s^*) which is rejected into the liquid when a small fraction of solid df_s forms

$$(C_l - C_s^*)\, df_s = (1 - f_s)\, dC_l \qquad (2.7)$$

where C_s^* is the solid composition at the interface. Substitution of $k = C_s/C_l$ and integrating from $C_s^* = kC_o$ at $f_s = 0$ yields

$$C_s^* = kC_o(1-f_s)^{(k-1)} \qquad (2.8)$$

Similarly for the liquid composition, since $C_s^* = kC_l$ and $(1 - f_s) = f_l$

$$C_l = C_o f_l^{(k-1)} \qquad (2.9)$$

It is interesting to note that, based on equation (2.8), C_s tends to infinity as solidification nears completion ($f_s \rightarrow 1$) when $k < 1$. In physical terms, considering a simple binary eutectic system, this indicates that the liquid will be enriched in solute to the eutectic composition when $k < 1$, thus promoting a significant extension in the solidification temperature range and formation of non-equilibrium eutectic in the as-solidified microstructure. This phenomenon has been observed as a major contributing factor to solidification cracking of many Ni-rich austenitic superalloys [2.7,2.16,2.17,2.19] as well as Fe-rich austenitic stainless steel alloys [2.6,2.8]. The distribution of solute during this mode of solidification is shown schematically in Figures 2.4b and 2.4c.

Although these equations are based on a number of simplifying assumptions and represent the most extreme case of microsegregation, their simplicity and fairly good accuracy are useful for evaluating the potential role of composition and solute segregation on solidification crack susceptibility. The amount of liquid formed during the terminal stages of solidification corresponds to the amount of eutectic formed under non-equilibrium conditions. This can easily be determined by setting C_l to C_e in equation (2.9) and f_l becomes f_e

$$C_e = C_o f_e^{(k-1)} \qquad (2.10)$$

or

$$f_e = \left(\frac{C_e}{C_o}\right)^{\frac{1}{k-1}} \qquad (2.11)$$

where C_e and f_e are the eutectic composition and fraction, respectively. Figure 2.5 shows the amount of non-equilibrium eutectic predicted by equation (2.11) as a function of C_e/C_o for three k values. High amounts of eutectic are favored by low k values and nominal compositions close to the eutectic, i.e., C_e/C_o values close to unity. When large amounts of eutectic are present, back-filling of cracks may occur and crack susceptibility is low. This concept is used extensively in braze and solder alloys which have eutectic or near eutectic compositions and are essentially immune to cracking. In addition, nominal compositions close to the eutectic will possess a narrow solidification temperature range, further reducing cracking tendency. Of course in weld metals the amount of non-equilibrium eutectic is only one aspect of cracking and the amount required for back-filling is probably alloy dependent. As noted in the last section, 10 volume percent has been reported as a minimum value required for crack healing [2.12]. This is supported by experimental work on 310 stainless steel which showed that crack susceptibility was high with a eutectic-like constituent at 7 vol% but was greatly reduced when 11.3 vol% eutectic was present [2.13]. Microstructural evaluations confirmed back-filling was operable. Referring again to Figure 2.5, the most deleterious conditions appear to be the presence of strong segregants (low k) in small amounts (high C_e/C_o). In this condition, the

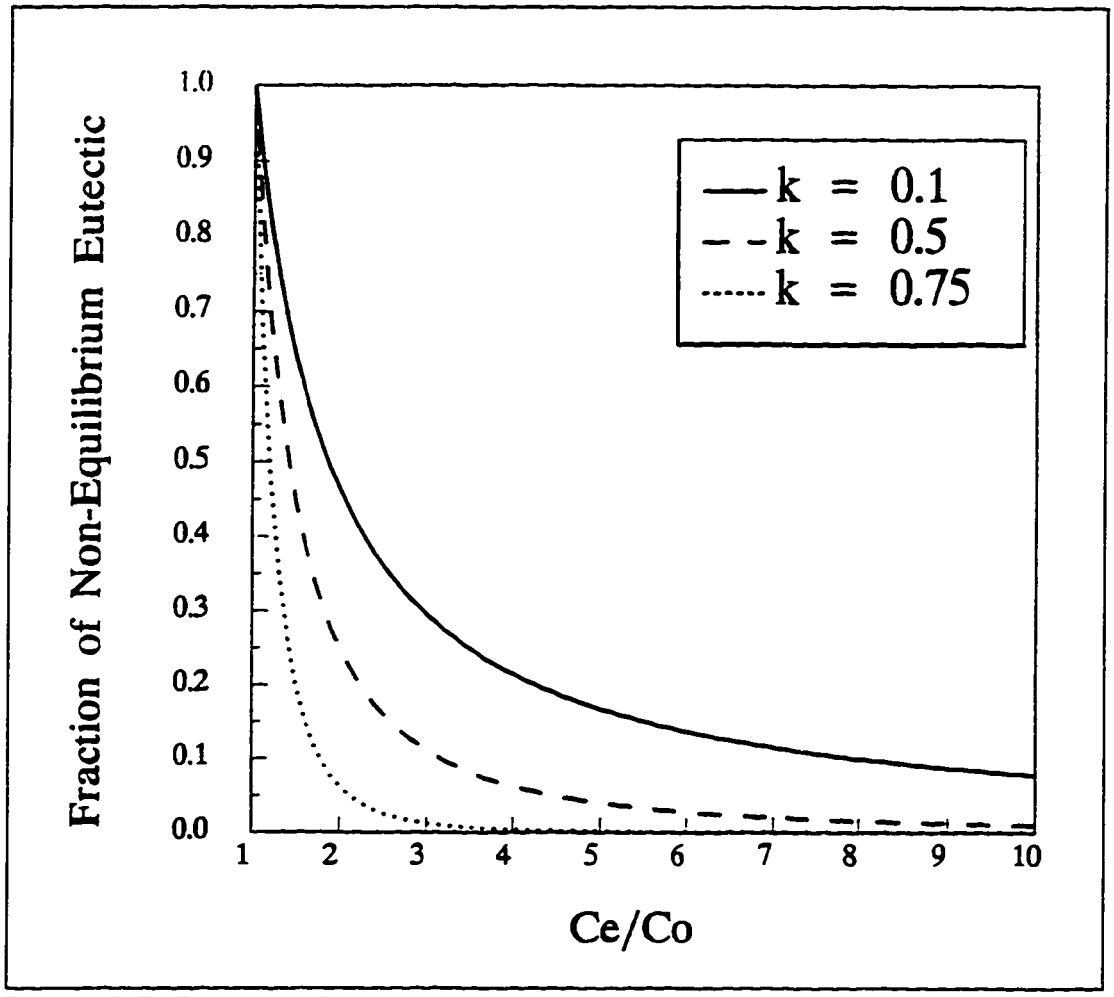

Figure 2.5. Fraction of non-equilibrium eutectic that forms during solidification according to the Scheil equation as a function of Ce/Co and k.

amount of non-equilibrium eutectic is high enough to promote cracking and low enough to prevent healing. Note that this condition also promotes a wide solidification temperature range, further enhancing crack formation.

Brooks and Baskes [2.15] have shown that the Scheil equation describes the final solute distribution fairly well in gas tungsten arc welds of Al-Cu alloys. The main limitation in the accuracy of the equation resulted from the inability to account for dendrite tip undercooling, which is due mostly to curvature effects. However, much work

has been done to develop analytical models of microsegregation which can describe the effect of tip undercooling and these models will be discussed at the end of this section.

2.2.1.3 NO DIFFUSION IN SOLID/DIFFUSIONAL MIXING IN LIQUID

The cases above assumed that diffusion and mixing of solute in the liquid phase are extensive enough to preclude concentration gradients from forming in the liquid ahead of the solid/liquid interface. However, if there is no convection in the liquid, then excess solute rejected into the liquid can only be transported away from the interface by diffusion. In this case, a solute rich boundary layer will form ahead of the solid/liquid interface which changes the final solute distribution in the solid. This is shown schematically in Figure 2.6 [2.21]. After an initial transient, the solute content in the liquid will build up to a value given by C_o/k. Since equilibrium is assumed at the solid/liquid interface, the solid will correspondingly solidify under steady state at the nominal composition at the solidus temperature. The final solute distribution is shown in Figure 2.6b, where the solid possesses the nominal solute content C_o in the steady state region and a solute dump occurs at the final transient.

In the above case, the solid and liquid compositions are given by the phase diagram at the solidus temperature. The solute content in the liquid outside the boundary layer is also at the nominal composition. Thus, the only variation in composition with distance is in the initial and final transients. The mass balance describing the solute boundary layer in the liquid is obtained by noting that the rate at which solute diffuses down the concentration gradient, $D_l(dC_l/dx)$, (D_l = solute diffusivity in liquid) must be

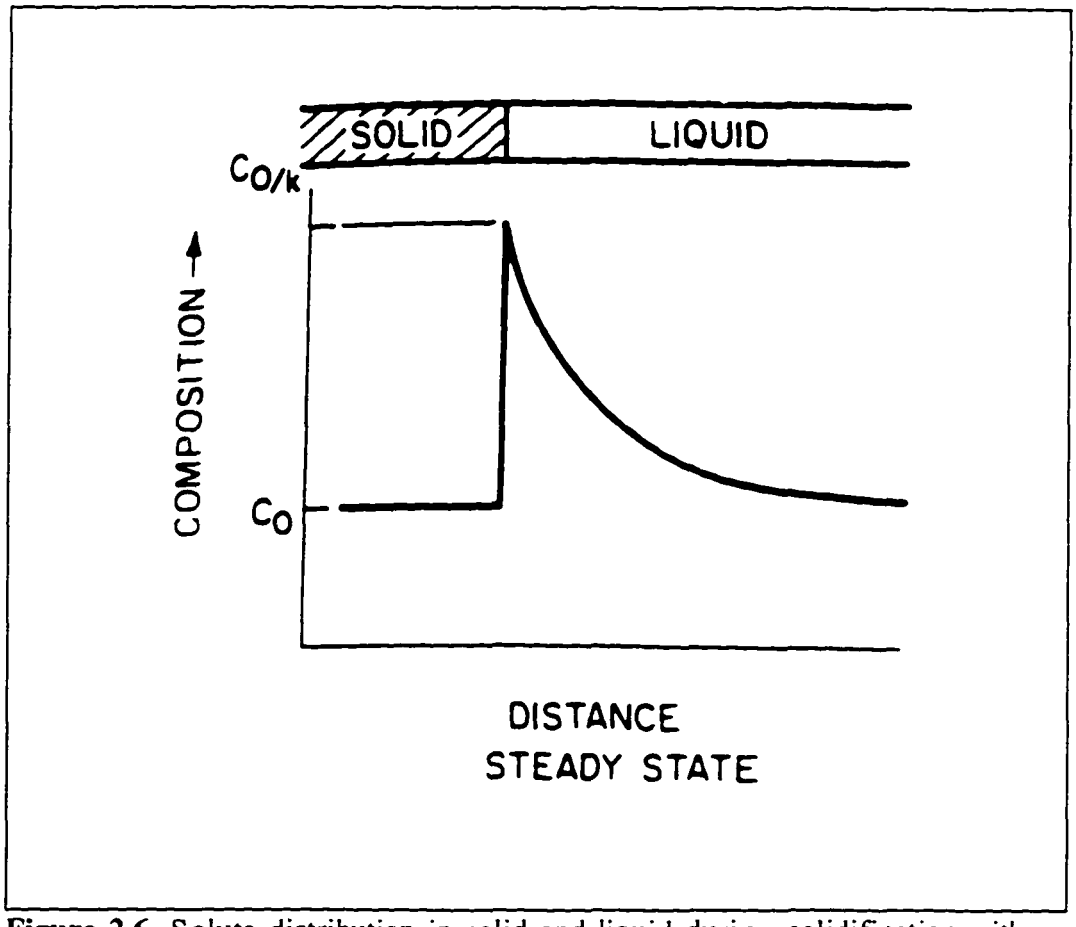

Figure 2.6. Solute distribution in solid and liquid during solidification with no solid state diffusion and solute transport in liquid by diffusion only.

balanced by the rate at which solute is rejected from the solidifying liquid, $R(C_l-C_s)$

$$D_l\left(\frac{dC_l}{dx}\right) = -R(C_l-C_s) \qquad (2.12)$$

where R is the growth rate of the interface. Using the boundary conditions that $C_l = C_o/k$ at $x = 0$ and $C_l = C_o$ at $x = \infty$ yields the following equation for the solute concentration in the liquid ahead of the solid/liquid interface

$$C_l = C_0\left(1 + \frac{1-k}{k}\, e^{-\left(\frac{Rx}{D_l}\right)}\right) \qquad (2.13)$$

Note that the final distribution of solute in the solid is characteristically different from that predicted by the Scheil equation. The Scheil analysis predicts a minimum of solute at the first solid to form (equal to kC_0) and a monotonic increase in solute as solidification proceeds. In contrast, when solute in the liquid is transported away from the interface by diffusion only, the final solute concentration is that given in Figure 2.6b. The operable solidification mode can thus be determined by performing EPMA traces across the solidified structure. Also note that, under the assumptions which apply to the Scheil equation (no solid state diffusion, perfect liquid state diffusion), the solute distribution depends only on C_0 and k. When diffusion in the liquid controls solute transport, the solute distribution depends on alloy properties (D_l) and process parameters (R).

2.2.2 MICROSEGREGATION DURING DENDRITIC SOLIDIFICATION

The analytical expressions reviewed above all assumed that the solid/liquid interface remained planar. Most alloys solidify in the cellular or dendritic mode where the planar interface is no longer stable, and this will change the resultant mass balance equations and final solute microsegregation relations. A brief description is provided below on factors which influence breakdown of the planar interface and how they affect the final microstructure in weld metals. The work done to develop models to describe solute segregation during dendritic solidification is then reviewed.

2.2.2.1 BREAKDOWN OF THE PLANAR INTERFACE

The conditions which lead to instability of the planar solid/liquid interface and formation of cellular and dendritic substructures have been recognized for many years. In this section, the quantitative analysis is only briefly reviewed in order to show how the solidification parameters vary with position in the weld metal and how this, in turn, affects the weld metal substructure. The implication of this analysis in terms of microsegregation during dendritic solidification will then be discussed in the following sections.

Figure 2.7 [2.21] shows the condition schematically. Here, it is assumed that mixing in the liquid is not complete and a solute enriched layer forms in the liquid at the interface. By knowledge of the liquidus slope, the corresponding variation in liquidus temperature with distance from the interface can be plotted as shown in Figure 2.7c. Since equilibrium at the interface is assumed, the actual temperature and liquidus temperature must be equal at the interface. However, the actual temperature gradient is controlled by the heat flow conditions. For the condition shown in Figure 2.7c, the actual temperature is above the liquidus temperature at every point. Here, the planar interface would be stable as any perturbation of solid extending past the interface into the liquid would be at a temperature above the liquidus and would melt back. If the actual temperature gradient is shallow enough to result in the conditions shown in Figure 2.7d, then the planar interface is no longer stable. In this condition, any perturbation of solid extending into the liquid phase will be at a temperature below the liquidus and will thus be undercooled and continue to grow. Therefore, the point shown in Figure 2.7c, where the

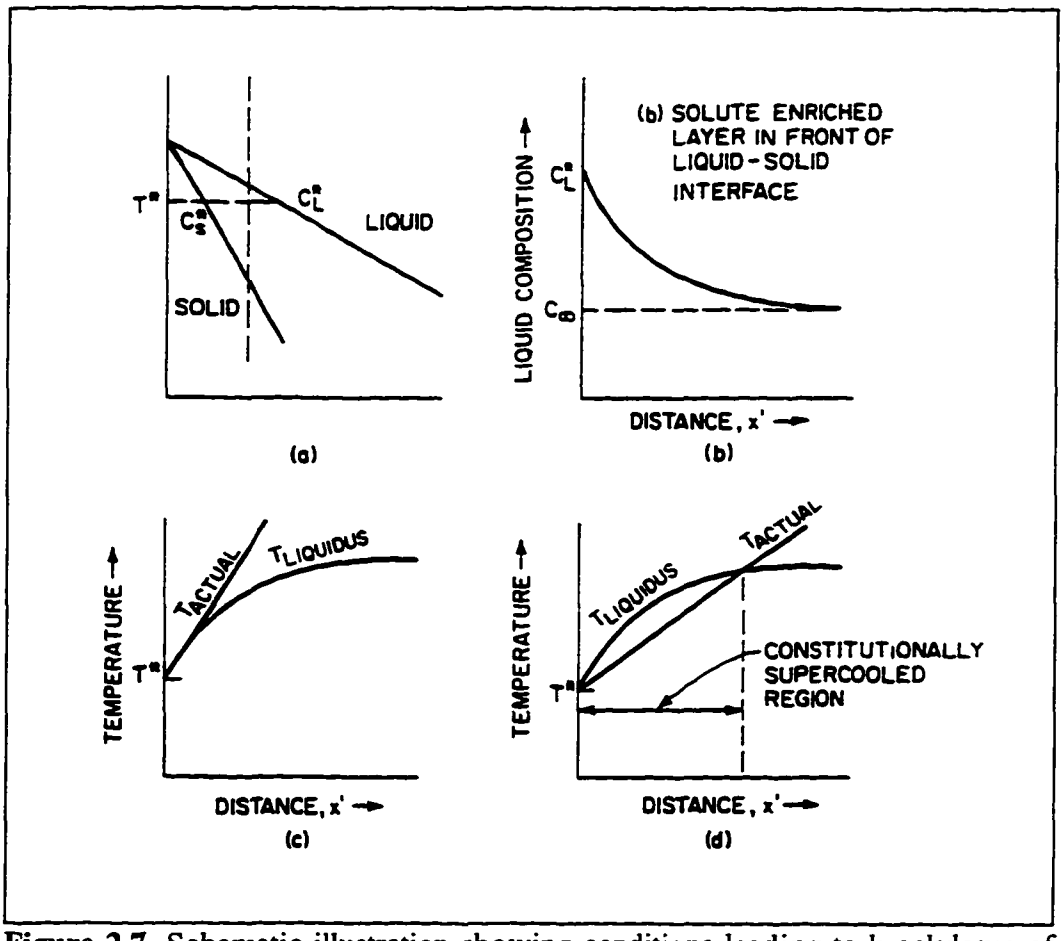

Figure 2.7. Schematic illustration showing conditions leading to breakdown of the planar solid/liquid interface.

liquidus temperature gradient and actual temperature gradient are equivalent at the interface, defines the point where the planar interface will become unstable and a cellular substructure will begin to form.

An analytical treatment of the problem [2.22] shows that the point of instability is given by

$$\frac{G_1}{R} < - \frac{m_1 C_o (1-k)}{k D_1} \qquad (2.14)$$

Here, G_l is the temperature gradient in the liquid, D_l is the diffusion coefficient of solute in the liquid, and R is the growth speed. When the inequality of (2.14) holds, the planar interface will break down into a cellular substructure. As the value of G_l/R continues to decrease, the cellular substructure will change to dendritic. In weld metal solidification, G_l and R vary with position from the fusion line. At the fusion line, R is nearly zero while G_l is very steep. At this point, depending on the alloy system (i.e., m_l, k, and C_o), a narrow region of planar solidification may be observed. As the weld centerline is approached, the growth rate increases while the temperature gradient decreases and the inequality of equation (2.14) is readily satisfied. Thus, for typical arc welding conditions, the weld metal substructure may contain narrow regions of planar and cellular solidification fronts near the fusion line, while the majority of substructure will typically be dendritic.

2.2.2.2 MICROSEGREGATION MODELS FOR DENDRITIC SOLIDIFICATION

One of the simplest ways to describe solute redistribution during cellular or dendritic growth is to apply the equations developed for planar solidification to a closed, plate-like volume element within the structure. This is shown schematically in Figure 2.8, where the assumed planar solid/liquid interface is now normal to the dendrite growth direction. Here, the major assumption made is that no mass is transported in or out of the

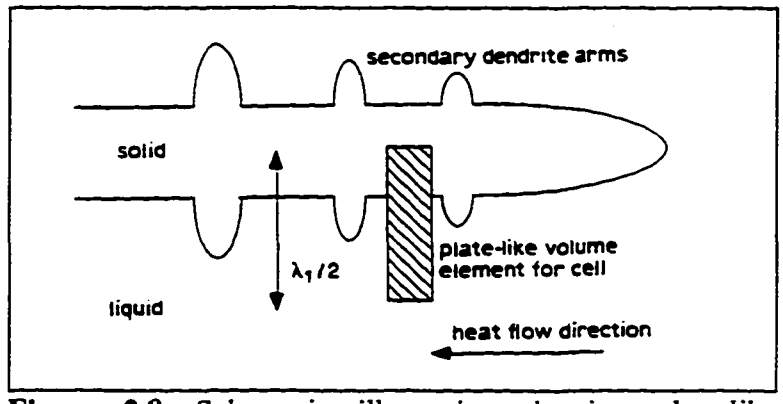

Figure 2.8. Schematic illustration showing plate-like volume element used to describe microsegregation during dendritic growth.

volume element. Under this assumption, the analytical models described above for planar interfaces can be applied to describe the solid composition, C_s, as a function of fraction solidified, f_s. Here, f_s is equal to zero at the dendrite core and unity at the midpoint between two neighboring dendrites. In some cases this approach may provide a reasonable estimation of microsegregation. However, the validity of this assumption can not be determined unless the potential influence of factors which arise due to dendritic solidification can be estimated. Analytical models developed for cellular or dendritic

solidification are described below as a means of 1) discussing the effects non-planar interfaces have on microsegregation and 2) providing relations which are useful for estimating the magnitude of these effects.

2.2.2.3 BACK DIFFUSION IN THE SOLID

In addition to assuming a planar solid/liquid interface, the important analytical treatments reviewed thus far assume no solid state diffusion during solidification and after solidification while cooling to ambient temperature. In many processes and alloy systems this is a reasonable assumption. However, situations can arise in which solid state diffusion can occur and reduce the extent of microsegregation in the final structure. In terms of the alloy system, solid state diffusion may become significant with interstitial solute elements and/or BCC solvent lattices where the diffusion rate is high. In terms of processing parameters, solid state diffusion can become important when the solidification time is long. Thus, the potential effects of solid state diffusion should be considered when attempting to model solute segregation and its potential effect on weldability.

Brody and Flemings [2.23] developed an analytical model to describe microsegregation during dendritic solidification which takes back diffusion into consideration. The volume element shown in Figure 2.8 is considered. All the general assumptions made thus far are still applied, except solute is now permitted to diffuse back towards the dendrite core under the concentration gradient which develops transverse to the dendrite during solidification. Starting with a mass balance within the volume element

$$d(f_l C_l) + d(f_s C_{s,a}) = 0 \qquad (2.15)$$

where $C_{s,a}$ is the average composition in the solid. In order to describe the final solute distribution in the solid due to both solute partitioning during solidification and solid state diffusion, the second term on the left side of equation (2.15) is represented by

$$d(f_s C_{s,a}) = C_s^* df_s + D_s A \rho_s \left(\frac{\partial C_s}{\partial x}\right)_{x_i} dt \qquad (2.16)$$

where D_s is the diffusion coefficient in the solid, ρ_s is the solid density, A is the liquid/solid interfacial area per gram, x is position from the dendrite core, x_i is the position of the solid/liquid interface, and t is time. Noting that $A = 1/\rho_s L$ (L = one half the dendrite arm spacing), and substituting equation (2.16) into (2.15)

$$d(f_l C_l) + C_s^* df_s + \left(\frac{D_s}{L}\right)\left(\frac{dt}{dx}\right) dC_s^* = 0 \qquad (2.17)$$

substituting $f_l = 1 - f_s$, noting that $d[(1-f_s)C_l] = -df_s C_l + (1-f_s)dC_l$, and rearranging

$$df_s(C_l - C_s^*) = (1 - f_s)\, dC_l + \left(\frac{D_s}{L}\right)\left(\frac{dt}{dx_i}\right) dC_s^* \qquad (2.18)$$

This mass balance places an upper bound on solid state diffusion by assuming that diffusion occurring within the dendrite does not change the composition gradient at the solid/liquid interface significantly. Equation 2.18 contains the terms dt/dx_i and Ds. Thus, in order to develop an analytical solution to this equation, the growth rate must be known as a function of time and D_s must be assumed constant. (Since D_s is an exponential function of temperature, and solidification proceeds from T_l to T_s, D_s will actually vary quite widely during solidification). By assuming the growth rate is either constant, dx/dt = a, or parabolic, $dx/dt = bt^{-1/2}$, (a and b are constants), two analytical solutions are obtained

$$for\ \frac{dx}{dt} = a: \qquad C_s^* = kC_o\left[1 - \frac{f_s}{1 + \alpha k}\right]^{k-1} \qquad (2.19)$$

$$for\ \frac{dx}{dt} = bt^{-1/2}: \qquad C_s^* = kC_o\left[1 - (1-2\alpha k) f_s\right]^{\frac{k-1}{1-2\alpha k}} \qquad (2.20)$$

where

$$\alpha = \frac{D_s t_f}{L^2} \qquad (2.21)$$

Here, t_f is the local solidification time. In order to accurately apply the mass balance in (2.18), a finite difference technique must be used to account for the change in D_s with temperature. However, the analytical solutions (2.19) and (2.20) are very useful in that the α term allows one to estimate the importance of back diffusion based on kinetic data (D_s), processing effects (t_f), and the microstructural scale (L). When $\alpha k << 1$, equations (2.19) and (2.20) reduce to the Scheil equation, indicating that solid state diffusion is insignificant and microsegregation will not be appreciably reduced by any solute diffusion back towards the dendrite core. When $\alpha k >> 1$, solid state diffusion is so fast that the solid composition will be uniform at C_o. It should be noted that these equations do not reduce to the lever rule when α tends to infinity. In this case, mass is no longer conserved within the volume element since diffusion rates are high. Clyne and Kurz [2.24] have modified the α term to ensure these relations convert to the lever rule when solid state diffusion is important. However, for the present discussion, the form of (2.19) and (2.20) will suffice.

2.2.2.4 LOCAL SOLUTE REDISTRIBUTION MODEL

The analysis above assumes that no mass is transported in or out of the volume element. This, in effect, neglects the true multi-dimensional aspect of dendritic solidification. Due to the dendritic morphology, a concentration gradient will also exist along the axial direction of the dendrites as shown schematically in Figure 2.9 [2.21]. The liquid solute concentration will be a maximum at the dendrite roots, where f_s is nearly equal to one, and decreases toward the dendrite tip, where f_s approaches zero. Solute will

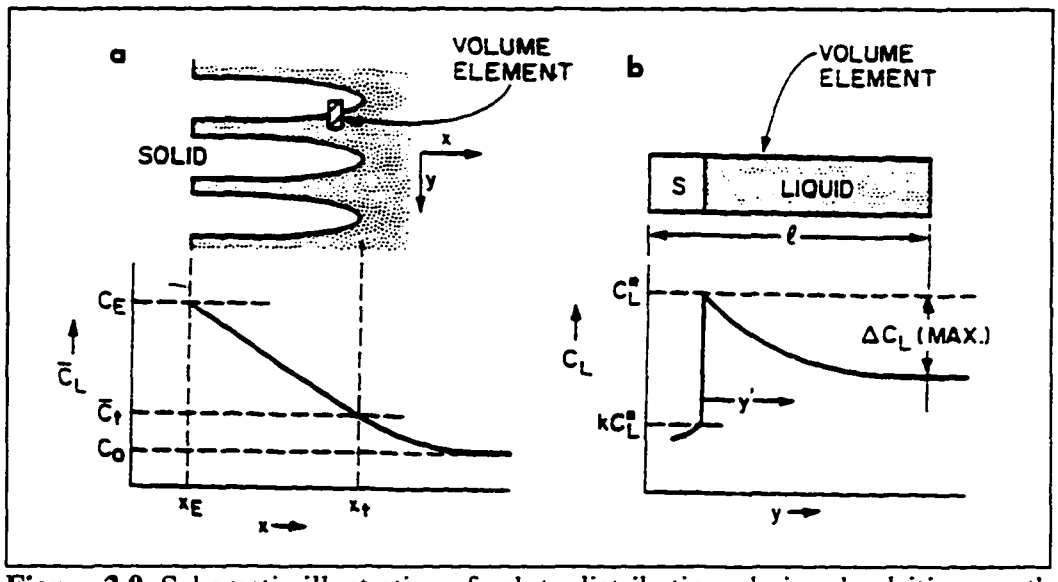

Figure 2.9. Schematic illustration of solute distributions during dendritic growth in the a) growth direction and b) transverse to the growth direction.

diffuse down this concentration gradient out ahead of the cell tips where the tip concentration is now C_t, where $C_t > C_o$ at the onset of solidification. Again assuming equilibrium at the solid/liquid interface, this solute enrichment will require a certain amount of undercooling for solidification to proceed as given by the phase diagram and shown schematically in Figure 2.10. As with solid state back diffusion, this solute enrichment has the effect of reducing the extent of segregation in proportion to the amount of undercooling (Figure 2.10).

Bower *at al.* [2.21,2.25] have developed a local solute redistribution model to describe these aspects of microsegregation during dendritic solidification. In the analysis, the important assumptions applied are: the dendrite spacing adjusts itself so that constitutional undercooling is small, undercooling due to radius of curvature effects is neglected, the liquidus slope is constant, and solid state diffusion is negligible. Taking x to now be in the dendrite growth direction, the concentration gradient along x is related

to the temperature gradient where liquid and solid coexist, G, and liquidus slope, m_l

$$\left(\frac{\partial C_l}{\partial x}\right) = \frac{G}{m_l} \qquad (2.22)$$

At steady state solidification where solute accumulation does not occur, the solute diffusing down the gradient can be related to the solute build up at the tip (C_t-C_o) and the growth rate R

$$R(C_t - C_o) = -D_l\left(\frac{\partial C_l}{\partial x}\right)_{x_t} \qquad (2.23)$$

Substituting (2.22) into (2.23), a relation can be developed for the tip composition as a function of the growth parameters (D_l, G, R) and liquidus slope m_l

$$C_t = C_o - \left(\frac{D_l G}{R m_l}\right) \qquad (2.24)$$

The dendrite tip temperature, T_t, and the dendrite tip composition, C_t, can be related through the liquidus slope by

$$T_t = T_l - (C_o - C_t) m_l \qquad (2.25)$$

Defining the undercooling associated with solute build up as $\Delta T = T_l - T_t$ and substituting

$(C_o - C_t) = (D_l G/Rm_l)$ into the relation above, the undercooling can be related to the growth parameters

$$\Delta T = T_l - T_t = \frac{D_l G}{R} \qquad (2.26)$$

The importance of this analysis lies within its ability to reveal the influence of the axial solute gradient on the final extent of microsegregation. As shown schematically by Figure 2.10, the undercooling associated with solute build up at the dendrite tip will increase the dendrite core concentration from C_c to C_t, thus reducing the overall degree of microsegregation.

From this analysis, a method can be developed to experimentally determine if tip undercooling has a significant influence on the extent of microsegregation [2.21]. An effective partition ratio, k_t, can be defined for the dendrite tips as

$$k_t = \frac{kC_t}{C_o} \qquad (2.27)$$

where k_t is related to k by

$$k_t = (1 + \frac{D_l G}{m_l R C_o}) k \qquad (2.28)$$

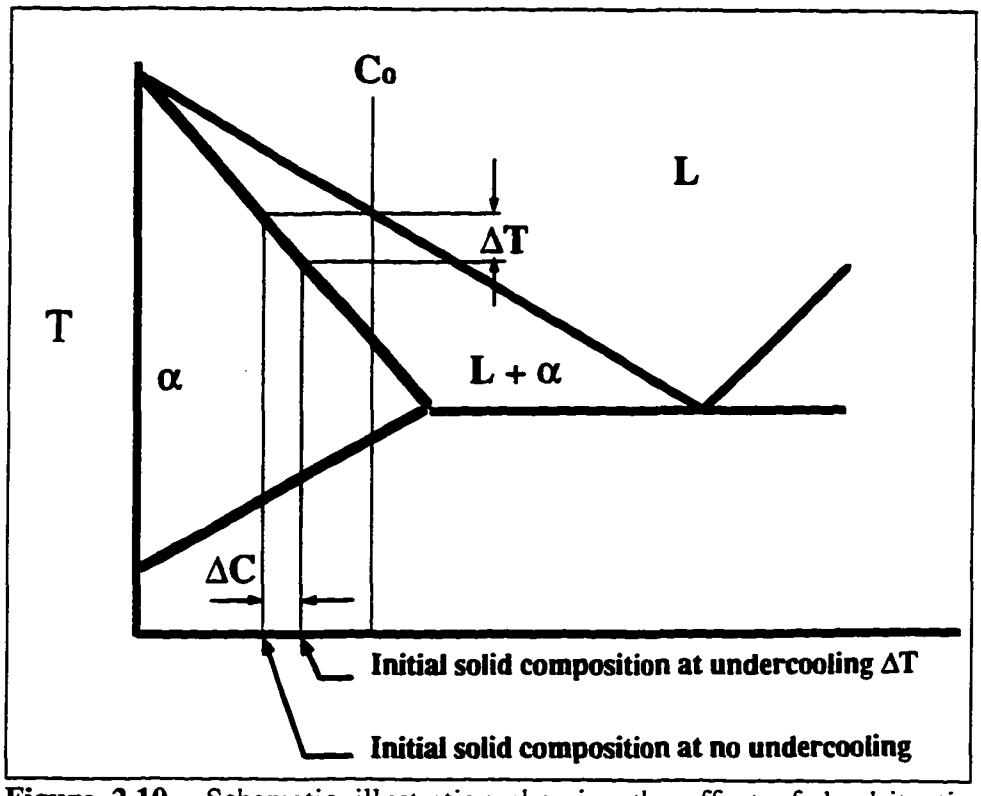

Figure 2.10. Schematic illustration showing the effect of dendrite tip undercooling on the dendrite core composition.

Experimentally, k_t is determined by quenching samples during solidification and measuring the concentration near the tip using an electron microprobe, where the tip composition is equal to kC_t. Of course, the true equilibrium partition ratio must be known to make the comparison.

By setting up the appropriate mass balance equations, Bower *et al.* [2.25] developed a final relation describing C_s^* as a function of f_s

$$C_s^* = kC_o\left[\frac{a}{k-1} + \left(1-\frac{ak}{k-1}\right)(1-f_s)^{(k-1)}\right] \qquad (2.29)$$

where $a = -(D_l G/m_l R C_o)$. When $a \approx 0$, equation (2.29) reduces to the Scheil equation. Thus, this parameter provides a means for estimating the relative influence of tip undercooling due to solute build up on the final microsegregation pattern. In applying this to weld metal solidification, R can be estimated from knowledge of the travel speed and weld geometry [2.26], D_l does not vary significantly, with an average value being $\approx 5 \times 10^{-5}$ cm^2/s [2.27], and for binary systems, m_l can be estimated from the phase diagram. However, G can be difficult to estimate in welding due to the relatively small liquid zone and concomitant steep temperature gradients. Taking the aluminum-copper system as an example, a value for G has been reported as ≈ 150 °C/cm [2.28], a typical value of R at the weld centerline (where microsegregation has the most important influence on solidification cracking) is ≈ 1 cm/s, and m_l is 3.4 °C/wt% [2.23]. Thus, for an Al-2wt%Cu alloy, the parameter has a value of ≈ 0.001 and can be neglected. This is to be expected since, based on equation (2.14), dendritic solidification inherently occurs at low values of $(G_l D_l/R)$. In weld metal solidification, the parameter will actually vary with position from the fusion line since R and G vary as a function of position from the fusion line. R is very low near the fusion line while G is very high, and the parameter may become important in this region. However, when evaluating the influence of microsegregation on weld metal solidification cracking under typical arc welding processes, this area near the fusion line can generally be neglected for two reasons. First, it is typically very narrow and secondly, solidification cracking is most prevalent at the weld centerline where G is inherently low and R is at a maximum. In any case, the parameter is alloy and process dependent and the analysis reviewed above allows its potential influence on

microsegregation to be estimated.

2.2.2.5 A GENERAL MODEL FOR MICROSEGREGATION DURING DENDRITIC SOLIDIFICATION

The two models reviewed above reveal how, under certain conditions of solidification parameters and alloy properties, the final extent of weld metal microsegregation can be reduced relative to the Scheil approximation. However, the two contributions which can reduce the extent of segregation (i.e., solid state back diffusion and tip undercooling due to solute build up) have been considered separately in these analyses. To this point, a single model does not account for each aspect simultaneously. In addition, it has been shown that tip undercooling due to radius of curvature effects can represent a significant contribution to the overall reduction in microsegregation in weld metals [2.15]. In this last section on microsegregation models, a more unified analysis which accounts for all three important aspects is considered.

The undercooling at the dendrite due to solute build up is given by equation (2.26). However, the overall tip undercooling is actually composed of four terms

$$\Delta T = \Delta T_{th} + \Delta T_K + \Delta T_c + \Delta T_r \qquad (2.30)$$

The first and second term represent undercooling due to thermal and kinetic effects, respectively, and can be ignored under conditions typical of weld metal solidification [2.26]. The third term is due to solutal effects around the dendrite tips. The fourth term

is due to radius of curvature effects which result from surface energy considerations. The surface energy of the dendrite tip posses a barrier to growth which must be overcome by undercooling. Ignoring the thermal and kinetic contributions, Burden and Hunt [2.29] derived an equation for tip undercooling which is given by

$$\Delta T = \frac{G_l D_l}{R} - \frac{m_l R r C_o (1-k)}{D_l} + \frac{2\Gamma}{r} \qquad (2.31)$$

Here, r is the dendrite radius and Γ is the Gibbs-Thomson parameter. The first term represents the diffusion of solute parallel to the dendrite out ahead of the dendrite tip, the second term accounts for solute diffusion directly from the cell tips, and the last term represents undercooling due to curvature. In order to know the undercooling, the dendrite radius must be known. Burden and Hunt assumed that growth occurred at the minimum undercooling. i.e.,

$$\frac{d\Delta T}{dr} = -\frac{m_l R C_o (1-k)}{D_L} - \frac{2\Gamma}{r^2} = 0 \quad at \text{ min. } \Delta T \qquad (2.32)$$

Solving for the value of r which corresponds to this condition and inserting this value into equation (2.31), an equation is obtained for the undercooling

$$\Delta T = \frac{G_l D_l}{R} + 2^{3/2}\left[-\frac{\Gamma m_l R C_o (1-k)}{D_l}\right]^{1/2} \qquad (2.33)$$

Solari and Biloni [2.30] extended this analysis to develop an analytical model to account for solid state back diffusion and undercooling due to solutal and curvature effects. The final mass balance is given by

$$\frac{df_l}{f_l + \alpha k} = -\frac{dC_l}{C_l(1-k) + (a-b)C_o} \qquad (2.34)$$

where the α and a terms are as previously defined and b is given by

$$b = \left(-\frac{2\Gamma R(1-k)}{m_l D_l C_o}\right)^{1/2} \qquad (2.35)$$

The final form of the relation between C_s and f_s is given as

$$C_s = kC_o\left[\frac{a-b}{k-1} + \left(1-\frac{(a-b)k}{k-1}\right)\left(1-\frac{f_s}{1+\alpha k}\right)^{k-1}\right] \qquad (2.36)$$

The general relation above reduces to particular cases under various conditions. If a = b = α = 0, the Scheil equation results and microsegregation is at a maximum. As discussed above, a is expected to be important only at the weld fusion line while α will

depend on the alloy system, microstructural scale, and local solidification time. In contrast, the parameter b may become important at the weld centerline where R is at a maximum. This is also the location where microsegregation is most likely to promote solidification cracking.

The analytical relations developed here can be limited to actual application as many of the parameters involved can vary significantly during solidification. In addition, the assumption of dendrites growing at the minimum undercooling may not be realistic [2.26], and an approach based on the minimum stability criteria [2.31] is required for better results. Nonetheless, the analyses above are very important since they identify the parameters which can influence the final weld metal microsegregation profiles. In addition, the parameters a, b, and α provide a means for estimating factors which may reduce the overall extent of microsegregation measured using electron microprobe techniques. This understanding of microsegregation phenomena and ability to estimate relative effects is very important for interpreting experimental results.

2.2.3 WELD METAL MICROSEGREGATION MODELLING

In the last section, the general models developed to describe solute segregation during solidification were reviewed. In this section, the results from several studies aimed at applying microsegregation models to weld metal solidification will be discussed.

Savage [2.32] has suggested that initial and final transients exist during cellular solidification of welds. This implies that weld metal solidification occurs with negligible solid state diffusion and solute transport in the liquid occurs by diffusion only. In this

case, equation (2.13) applies. The initial transient was estimated by assuming [2.33] that the growth rate within the volume element was approximately equal to the welding speed. Use of the welding speed for dendrite tip velocity at the weld centerline is a reasonable approximation. However, as noted by Brooks and Baskes [2.15], the growth rate of the solid/liquid interface perpendicular to the dendrite axis is considerably less than the welding speed. Use of the welding speed for this growth rate results in a gross under estimation of the initial transient. Brooks [2.15] has used more realistic growth rates for GTA welds of an Al-Cu binary alloy welded at a travel speed of 4.3 mm/s. Here, the growth rate of the solid/liquid interface within the volume element was approximately 0.00039 mm/s. Using this value of the growth rate, the initial transient was estimated to be 380 μm, which is ≈25 times the cell width (15 μm). Thus, it is unlikely that this model accurately describes weld metal microsegregation.

More recently, Brooks [2.14,2.15] has applied a model similar to that developed by Brody and Flemings, the result of which is given in analytical form by equation (2.20). This model essentially assumes that complete mixing occurs in the liquid while solute transport back towards the cell core can occur by solid state diffusion. A finite difference approach was used to adjust the diffusion coefficient with temperature during solidification. Other assumptions include: equilibrium exists at the solid/liquid interface, k is constant, no diffusion occurs parallel to the dendrite in the liquid or solid, and the cooling rate is constant. Model results were compared with experimental results for the FCC binary Al-Cu system and the BCC Fe-Nb binary system.

The microsegregation profiles from the Fe-Nb system were significantly affected

by solid state diffusion during and after solidification due to the high diffusivity of Nb in the BCC Fe lattice. Experimental and model results are shown in Figure 2.11a and 2.11b, respectively. The model results are shown for different stages of solidification to show the effect solid state diffusion has on homogenization. The model predicts the microsegregation patterns quite well. The final predicted core concentration is 2.3 wt% Nb compared to the measured value of 2.8 wt% Nb. The cell boundary concentration was predicted to be 3.8 wt% Nb, which agreed exactly with experimental results. These results show that the Brody-Flemings model provides a reasonable physical description of weld metal microsegregation. The relatively high experimentally measured core concentration which could not be predicted by the model was attributed to dendrite tip undercooling, which is discussed in more detail below with regards to the Al-Cu results.

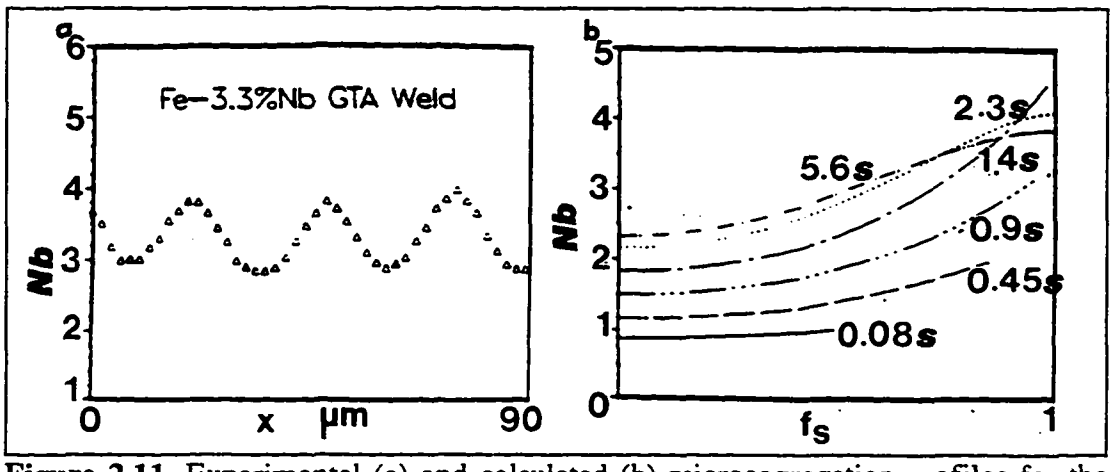

Figure 2.11. Experimental (a) and calculated (b) microsegregation profiles for the Fe-Nb system. Figure (b) shows the solute distribution at various solidification times.

The results for an Al-2wt%Cu alloy is shown in Figure 2.12. Although the model results underestimate the dendrite composition at each solid fraction, they follow the trend of the experimental data reasonably well. Solid state diffusion would provide one means to account for the discrepancy in these results. However, in order to compensate for the observed differences, it was determined that the cooling rate would have to be decreased by a factor of 300, the diffusivity would have to be increased by a factor of 300, or the cell size would have to be reduced by a factor of 17. None of these possibilities are reasonable. In general, the calculations showed that solid state diffusion has a negligible effect on microsegregation of the Al-Cu alloy system since the diffusivity of Cu in FCC Al is so low. The relatively high dendrite core compositions displayed in Figure 2.12 have been attributed to dendrite tip undercooling [2.15]. Since solid state diffusion is negligible, the model essentially reduces to the simple Scheil model, equation (2.8). However, under this condition the first fraction to solidify should be kC_o, where k = 0.17 wt% for the Al-Cu system. Here kCo = 0.34wt% for C_o = 2 wt% Cu, which is lower than the 0.75 wt% observed experimentally, the difference being attributed to dendrite tip undercooling. The mechanisms by which the tip can be undercooled have been discussed above and the analytical form of the tip undercooling equation is given by (2.33) (this relation assumes growth rate occurs at the minimum undercooling). The undercooling required to promote a dendrite core concentration in excess of kC_o can be determined by knowledge of the solidus line, m_s, by

$$\Delta T = m_s \Delta C \qquad (2.37)$$

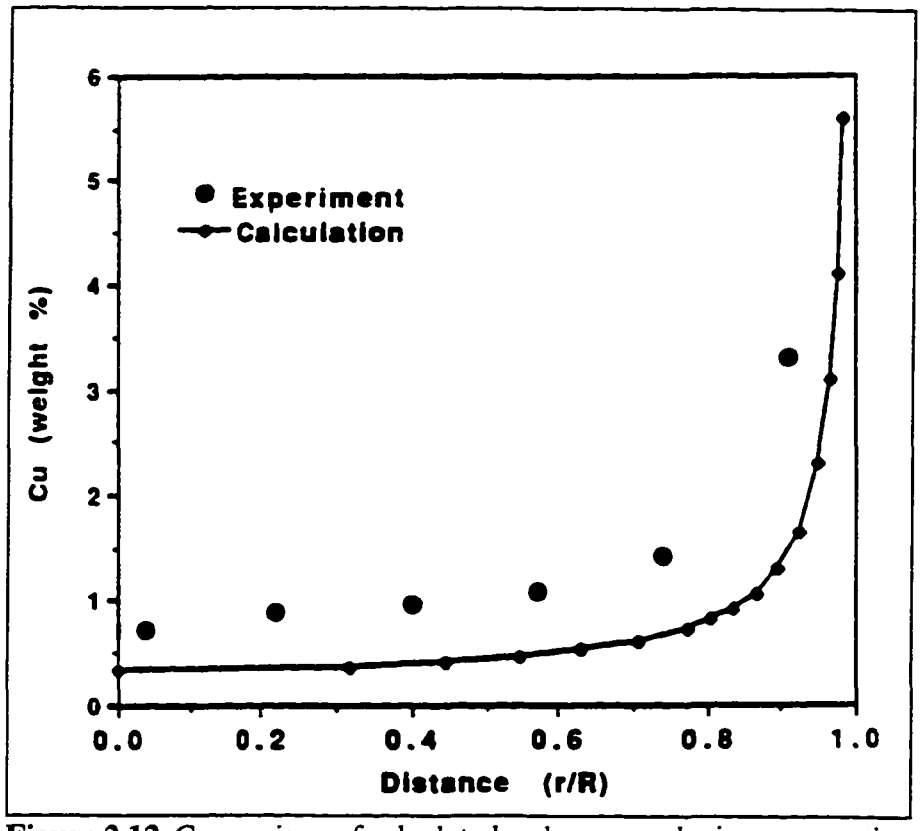

Figure 2.12. Comparison of calculated and measured microsegregation profiles for the Al-Cu system.

where ΔC is the difference between kC_o and the observed dendrite core concentration. Using a value of $m_s \approx 19.8$ K/wt% Cu, Brooks indicated the undercooling required to produce a core concentration of 0.75 wt%Cu is ≈ 8 K. Using the Burden and Hunt approach where growth is assumed to occur at minimum undercooling and ΔT is given by equation (2.33), the calculated value of ΔT is ≈ 3 K. Although this value is lower than that required to produce the measured core concentration, these experimental results were useful in elucidating the important physical aspects of weld metal microsegregation. For alloy systems where solid state diffusion is negligible (such as substitutional solutes in

FCC crystal structures), the simple Scheil equation provides a reasonable description of microsegregation after dendrite tip undercooling is taken into account. It is worth noting that EPMA results from dendritic weld microstructures of a rather large number of nickel base alloys [2.17] also show the characteristic microsegregation profiles displayed in Figure 2.12, providing further proof of the applicability of the Scheil equation. When the solute has a high diffusivity in the solid phase (such as interstitials and BCC solvent crystal structures) dendrite tip undercooling as well as solid state diffusion must be considered.

Lastly, it is worthwhile noting the work done by Elmer with regards to dendrite tip undercooling [2.34]. Here, Fe-Ni-Cr ternary alloys of varying composition which crossed the line of two fold saturation were electron beam melted and solidified at growth rates from 5.4 to 175 mm/s and temperature gradients from 87 to 46,000°C/mm. One of the main objectives of this work was to determine the influence of cooling rate on the primary solidification mode of stainless steels. Here, rather than assuming growth occurred at the minimum undercooling, the results of analyses derived from the minimum stability criteria were used. This type of analysis has been shown to yield more accurate results of the dendrite tip radius and associated undercooling [2.35]. The results are briefly reviewed here.

Esaka and Kurz [2.36,2.37] have derived a relation between the dendrite tip radius, solidification parameters, and alloy properties based on the minimum stability limit which is given by

$$R^2 - \left[\frac{D_l P_c^2 m_l (1-k)\, C_o}{\pi^2 \Gamma (I(P_c)\,(1-k) - 1)}\right] R + \left[\frac{D_l^2 P_c^2 G}{\pi^2 \Gamma}\right] = 0 \qquad (2.38)$$

where P_c is the Peclet number which is defined by

$$P_c = \frac{R r_t}{2 D_l} \qquad (2.39)$$

and $I(P_c)$ is the Ivanstov function given by

$$I(P_c) = P_c \exp(P_c)\, E_1(P_c) \qquad (2.40)$$

where E_1 is the exponential integral function. The Peclet number is related the supersaturation, Ω, which is the driving force for diffusion of solute at the dendrite tip at a given undercooling

$$\Omega = I(P_c) = \frac{\Delta C}{\Delta C^*} = \frac{C_l^* - C_o}{C_l^* (1-k)} \qquad (2.41)$$

The general approach is to use numerical methods to generate a plot of P_c versus R for a series of G values. From this information, one can determine the Peclet number which corresponds to a given growth rate and temperature gradient. The value of that

Peclet number is then used to calculate the composition of liquid at the dendrite tip, C_l^*, by equation (2.41). The undercooling due the solutal boundary layer is determined by knowledge of the liquidus slope and C_l^*

$$\Delta T_c = m_l(C_o - C_l^*) \qquad (2.42)$$

and the undercooling due to radius of curvature effects is given by the Gibbs-Thompson relation

$$\Delta T_r = \frac{2\Gamma}{r_t} \qquad (2.42)$$

The total undercooling is given by the sum of these quantities, $\Delta T = \Delta T_c + \Delta T_r$. Thus, with this approach, it is possible to determine the undercooling (ΔT) and dendrite tip composition (C_l^*) associated with solidification of a given alloy system (D_l, Γ, m_l, k, C_o) under any set of solidification conditions (G and R).

Once these values are determined from the solidification conditions, the approach developed by Sarreal *et al.* [2.38] can be used to predict solute segregation for the undercooled dendrite. Here, it is assumed that undercooling at the dendrite tip is dissipated by forming a certain fraction of primary solid phase, f_s°, given by the lever rule at the undercooled temperature

$$f_s^o = \frac{C_o - C_l^*}{C_l^*(k-1)} \qquad (2.44)$$

the remaining solid is assumed to solidify via the Scheil equation. In view of the results by Brooks presented above, this is a good assumption for weld metal solidification. The corresponding fraction of eutectic formed is given by

$$f_e = (1-f_s^o)\left(\frac{C_{sm}}{kC_t}\right)^{\frac{1}{k-1}} \qquad (2.45)$$

Elmer [2.34] used this approach to determine the undercooling associated with electron beam welding of stainless steels and calculated undercoolings as high as 30K. This information aided in interpreting changes in primary solidification mode which occurs at high growth rates and temperature gradients in stainless steels with compositions close to the line of two fold saturation.

Although this approach has been applied mainly to welding under rapid solidification conditions, such as laser and electron beam welding, the results of Brooks have shown that significant undercoolings can exist during GTA welding at relatively low welding speeds (4.3 mm/s). In addition, recent work on the optimization of arc welding processes [2.39,2.40] has shown that arc welding processes can achieve travel speeds of up to 26 mm/s and melting efficiencies equivalent to the laser and electron beam welding processes. Thus, significant undercooling may be expected even under arc welding

conditions, and this topic deserves further investigation.

2.2.4 SUMMARY

In terms of alloy parameters, microsegregation is influenced mainly by the nominal solute concentration, C_o, and the equilibrium distribution coefficient, k. For k values < 1, solute will partition to the liquid phase during solidification, with the extent of microsegregation increasing as k becomes progressively less than unity. The Scheil equation provides a simple, rather accurate analytical description of microsegregation for alloy systems in which solid state diffusion and tip undercooling is not significant. This simple relation is very useful since microsegregation can be described completely by alloy composition and the equilibrium distribution coefficient. When solid state diffusion is significant, its effect will be to reduce the extent of microsegregation by allowing solute to diffuse transverse to the dendrite axis back towards the core where the as-solidified composition is at a minimum. The relative importance of solid state diffusion can be estimated by knowledge of the local solidification time, the dendrite spacing, and the solute diffusivity in the solid.

The extent of microsegregation can also be reduced by dendrite tip undercooling. Tip undercooling occurs mainly due to solutal and curvature effects. Undercooling at the dendrite tip reduces the extent of microsegregation by increasing the as-solidified dendrite core composition, where the relation between the core concentration and undercooling is determined through knowledge of the liquidus slope. Determining the tip undercooling requires the dendrite tip radius to be known. Analytical expressions exists which relate

the tip radius to the alloy parameters (k, ml, C_o, D_l, Γ) and solidification conditions (G, R) and allow undercooling predictions to be made. Work conducted to date has shown that the Scheil equation can be applied to weld metal solidification in alloys with low solute diffusivities after effects due to tip undercooling are determined. Thus, the analytical expressions for tip undercooling, coupled with the Scheil equation, provide a useful approach to estimating microsegregation in weld metals.

2.3 PREVIOUS SOLIDIFICATION AND WELDABILITY STUDIES

2.3.1 Fe-Ni-Cr TERNARY SYSTEM

The Fe-Ni-Cr ternary system forms the basis for austenitic stainless steels and many nickel based superalloys. Because of its commercial importance, the Fe-Ni-Cr ternary system has been extensively researched. In this subsection, the solidification parameters which are representative of the two Fe-Ni-Cr base compositions pertinent to this study (approximately 10Fe-70Ni-20Cr and 50Fe-30Ni-20Cr) and Ni-X binary alloys (X=Nb, Si, C) are reviewed. This information will be useful for comparison purposes when the solidification behavior of the Fe-Ni-Cr base alloys with additions of Nb, Si, and C is evaluated.

Figure 2.13 shows the liquidus and solidus surfaces of the Fe-Ni-Cr ternary system [2.41]. A peritectic reaction at Fe-4Ni extends into the diagram and changes to a eutectic reaction at about 75%Fe. A ternary eutectic point is reached at approximately 49Cr-43Ni-8Fe. Alloys located to the Ni-rich side of the eutectic solidify as primary austenite while alloys to the chromium rich side solidify as primary ferrite. The composition of the two Fe-Ni-Cr base alloys of this study are noted on the diagrams. These alloys are sufficiently rich in Ni to exhibit primary solidification to austenite. The Fe-rich alloy (50Fe-20Cr-30Ni) exhibits a liquidus and solidus of approximately 1428°C and 1378°C, respectively, with ΔT = 50°C. The Ni rich alloy (10Fe-70Ni-20Cr) exhibits a liquidus of 1410°C and a solidus of 1367°C, with ΔT = 43°C. Thus, the Fe-Ni-Cr ternary base alloys exhibit a simple L -> γ solidification mode with a fairly narrow solidification temperature range.

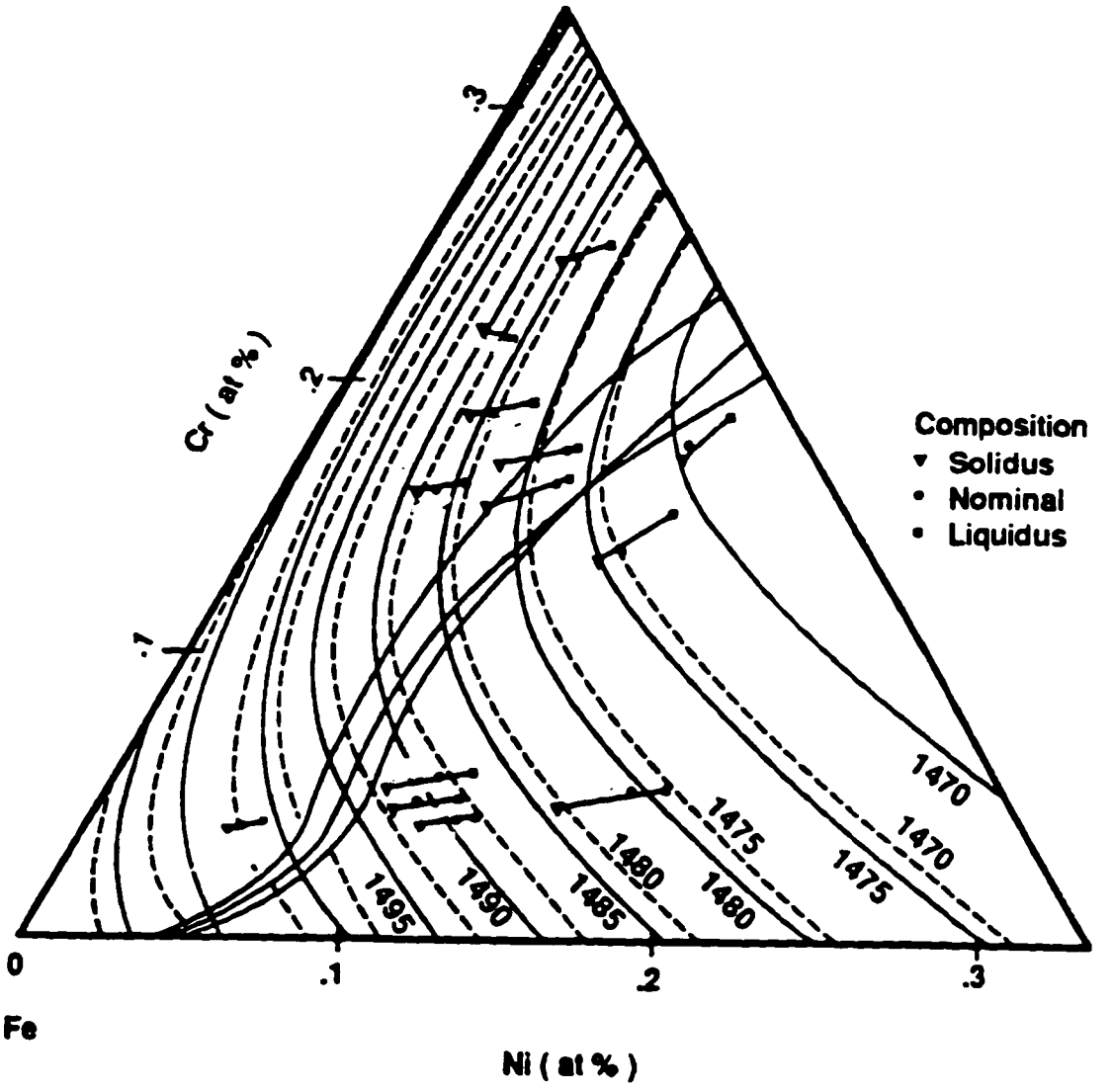

Figure 2.13. Liquidus and solidus surfaces of the Fe-Ni-Cr system.

2.3.2 Ni-X BINARY ALLOYS

As shown above, the base Fe-Ni-Cr alloys of interest to this study are sufficiently high in nickel to undergo primary solidification to an austenitic crystal structure. It is therefore useful to consider alloy solidification parameters from the binary systems between Ni-Nb, Ni-Si, and Ni-C. Although these values can not be used to represent the more complicated ternary system of Fe-Ni-Cr with simultaneous minor additions of Nb, Si, and C, they serve as a framework for interpretation of experimental results and provide a useful starting point. As discussed in the first section, solidification cracking is strongly affected by microsegregation and the concomitant increase in the solidification temperature range. In addition, the section on microsegregation modelling indicated that alloy parameters such as the liquidus slope, m_l, solidus slope, m_s, the equilibrium partition coefficient, k, and maximum solid solubility, C_{sm}, are all important parameters with regards to microsegregation and its effect on the solidification temperature range. In view of this fact, these alloy parameters will be discussed.

Table 2.1 lists the solidification parameters of interest for the binary systems. The data was taken from references [2.42-2.45]. The data reveal that each minor alloying element will partition rather strongly to the liquid phase during solidification, i.e., $k < 1$. The relative potency factor (RPF), as defined by Boreland and given by equation (2.1), is also listed for each element along with the equilibrium solidification temperature range expected for typical minimum and maximum levels of each element. The k values for each element decrease in the order $k_C < k_{Si} < k_{Nb}$, suggesting that carbon will have the most detrimental effect on weldability followed by silicon and niobium. However, the

relative amount of each element typically found in alloy systems of interest decreases in the order C < Si < Nb [2.7,2.8,2.16]. Therefore, the absolute effect of each element, as reflected in the ΔT associated with each weight percent, is similar. As previously discussed, the RPF is only valid under equilibrium conditions. However, it is a useful measure here to illustrate the combined effect of alloy solidification parameters (m_l and k) and alloy composition (C_o) on the solidification temperature range. These values will be compared with experimental results from more complicated Fe-Ni-Cr systems below.

Table 2.1. Solidification parameters for Ni-X binary alloy systems.

BINARY ALLOY SYSTEM	ALLOY SOLIDIFICATION PARAMETER						
	m_l °C/wt%	m_s °C/wt%	k	C_{sm} wt% @°C	RPF °C/wt%	ΔT, °C @ wt%	ΔT, °C @ wt%
Ni-Nb	-8.4	-11.2	0.75	20.5 @ 1270°	2.8	5.6°C @ 2wt%	14°C @ 5wt%
Ni-Si	-20	-40	0.50	9.3 @ 1125°	20	0.8°C @ 0.04wt%	10°C @ 0.50wt%
Ni-C	-70	-250	0.28	0.55 @ 1318°	180	3.6°C @ 0.02wt%	27°C @ 0.15wt%

2.3.3 NICKEL RICH ALLOY SYSTEMS

Commercially important alloys usually contain more than two elements and can not be represented by a binary phase diagram. However, many nickel base alloys terminate solidification by the formation of eutectic-like constituents in an manner analogous to a binary system, with the exception that more than one eutectic-like reaction can occur and the reactions are non-invariant. Results of detailed investigations which are useful for the present study include those of Cieslak *et al.* on the solidification and associated weldability of IN625 [2.7,2.42] and IN909 [2.43] and the IN718 investigation conducted by Knorovsky *et al* [2.16].

IN625 is actually an alloy based on the Ni-Cr-Mo system with approximately 2.5 wt% Fe, 3.5 wt% Nb, 0.005 - 0.035 wt% C, and 0.01 - 0.40 wt% Si. Nevertheless, the solidification and weldability of this alloy has been shown to be quite similar to that of IN718, which is based on the Fe-Ni-Cr ternary system with minor additions of Nb, C, and Si. The solidification of alloy 625 is largely influenced by segregation of Nb, C, and Si. Cieslak [2.7,2.42] conducted a three factor, two level, factorially designed experiment around these alloy additions, the compositions of which are shown in Table 2.2. The solidification behavior was studied with differential thermal analysis (DTA) and various microscopy techniques for phase identification. Slow heating rate (4°C/min.) and relatively fast cooling rate (20°C/min.) DTA tests were conducted. The slow heating rate scans were used to estimate the equilibrium solidus and liquidus temperatures as a function of composition. This permitted calculation of the liquidus and solidus slopes, and thus allowed determination of k values for these elements since $k = m_l/m_s$. The faster cooling

rate scans were used to reveal the formation of non-equilibrium eutectic-like reactions (and associated extension in the solidification temperature range) which may be typical of casting and welding processes when dendrite tip undercooling is not significant. Weldability was assessed using the varestraint test.

The on-heating temperatures are summarized in Table 2.3. It is readily apparent that increased alloy additions increase the equilibrium melting range. Multiple regression analysis conducted on the data yielded the liquidus, solidus, and melting temperature range as

$$T_l(°C) = 1406.8 - 108.6(C) - 27.8(Si) - 11.1(Nb) \quad (2.46)$$

$$T_s(°C) = 1385.8 - 507.4(C) - 48.6(Si) - 20.6(Nb) \quad (2.47)$$

$$\Delta T(°C) = 20.9 + 405.5(C) + 20.3(Si) + 9.4(Nb) \quad (2.48)$$

where all elemental values are in weight percent. The correlation coefficient for these linear relations was greater than 0.97, indicating they accurately describe the effects of Nb, C, and Si and that interactive effects among the elements are small. Partial derivatives of equations (2.46) and (2.47) with respect to each element yielded m_l and m_s, respectively, and k via $k = m_l/m_s$. These data are summarized in Table 2.4 and compared with their binary phase diagram quantities which were presented in Table 2.1. (Because the base alloy is not a pure solvent and therefore melts over a temperature range, these values represent approximations to k values.) It is readily apparent that the k values for

Table 2.2. Chemical compositions of alloys used to study the effect of minor variations in Nb, Si, and C on the solidification and weldability of IN 625.

ELEMENT	ALLOY NUMBER							
	1	2	3	4	5	6	7	8
Carbon	0.006	0.031	0.006	0.036	0.009	0.038	0.008	0.035
Manganese	0.02	0.02	0.02	0.03	0.03	0.03	0.03	0.03
Phosphorus	0.005	0.005	0.005	0.005	0.006	0.006	0.006	0.006
Sulfur	0.002	0.002	0.002	0.003	0.003	0.003	0.004	0.003
Silicon	0.03	0.03	0.35	0.39	0.03	0.03	0.38	0.46
Chromium	22.10	21.95	21.63	21.57	21.81	21.83	21.65	21.68
Molybdenum	9.54	9.61	9.60	9.63	9.81	9.81	9.68	9.67
Titanium	0.06	0.06	0.06	0.06	0.06	0.06	0.06	0.06
Niobium	0.01	0.01	0.02	0.02	3.61	3.60	3.57	3.53
Iron	2.56	2.55	2.18	2.59	2.30	2.31	2.26	2.29
Nickel	bal	bal	bal	bal	bal	bal	bal	bal

Table 2.3. Liquidus, solidus, and solidification temperature ranges of experimental IN625 alloys determined by slow heating (0.067°C/s) DTA scans.

ALLOY NO.	LIQUIDUS, °C	SOLIDUS, °C	ΔT, °C
1	1406.5 ± 1.3	1380.0 ± 1.4	26.5 ± 0.6
2 (C)	1403.0 ± 1.0	1369.3 ± 2.5	33.7 ± 1.5
3 (Si)	1395.5 ± 1.3	1366.5 ±1.3	29.0 ± 1.6
4 (C,Si)	1390.8 ± 0.5	1347.5 ± 1.7	43.3 ± 1.3
5 (Nb)	1363.3 ± 0.5	1308.0 ± 2.2	55.3 ± 2.4
6 (Nb,C)	1362.0 ± 0.8	1289.3 ± 2.6	72.8 ± 3.2
7 (Nb,Si)	1356.0 ± 0.8	1287.8 ± 2.4	68.3 ± 2.5
8(Nb,Si,C)	1352.0 ± 0.0	1275.7 ± 0.6	76.3 ± 0.6

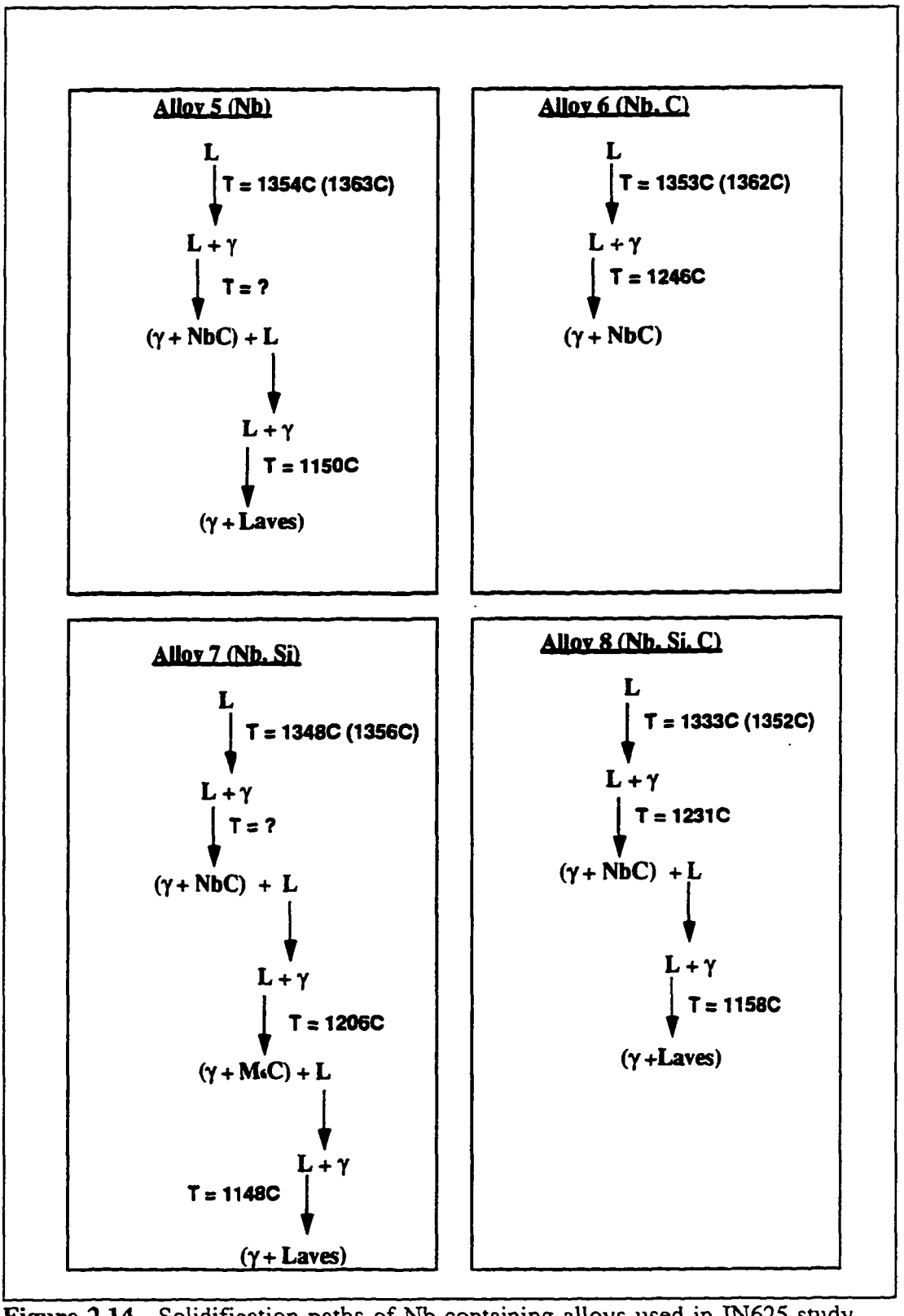

Figure 2.14. Solidification paths of Nb-containing alloys used in IN625 study.

Nb and C are significantly lower in alloy 625 compared to the respective binaries between Ni. This indicates that the solubility of these elements is decreased by the presence of other elements dissolved in the matrix such as Fe, Cr, and Mo. In dissimilar metal welds between Ni-rich alloys and iron-base alloys, the iron content can be very high (≈50 wt%) due to dilution and may reduce the solubility even further. In addition, carbon dilution from Fe-C alloys can raise the weld metal carbon concentration to ≈0.16 wt%, which is more than a factor of four greater than the high carbon level used in Cieslak's studies. Based on the discussions from the previous sections on solidification cracking and microsegregation, equation (2.48) and Table 2.4 suggest that composition variations in dissimilar metal welds between (Nb,Si,C)-containing Ni-Base alloys and Fe-C alloys may have a significant negative impact on solidification behavior and associated weldability.

The solidification paths associated with each alloy in Table 2.2 containing Nb are summarized in Figure 2.14. The Nb-free alloys terminated solidification by a simple L -> γ transformation without any eutectic-like reaction, thus illustrating the strong potential of Nb to promote secondary phases of Laves and carbides when present in relatively small quantities. The temperature values in parenthesis represent the equilibrium melting (on-heating) liquidus values and are always higher than solidification (on-cooling) temperatures due to undercooling required for nucleation. These values are listed because of their importance in weld metal solidification. The weld metal nucleates solidification epitaxially from the base metal, which requires virtually no undercooling [2.44]. Thus, the equilibrium melting temperature is often thought to be the accurate measure of the weld metal liquidus on solidification, and the difference between this value and the terminal

solidification reaction represents the weld metal solidification range. (However, undercooling during growth can occur during solidification as discussed in the previous section.) In general, the reaction paths indicate that C promotes formation of NbC while Si promotes the Laves phase, $(Fe,Cr,Ni)_2Nb$. Since the Laves phase forms at the lowest temperature, it can significantly widen the solidification temperature range.

Table 2.4. Comparison of k values for Nb, Si, and C in IN625 and binary systems.

ELEMENT	Ni-X BINARY	ALLOY 625
Nb	0.75	0.54
Si	0.50	0.57
C	0.28	0.21

Figure 2.15 shows the maximum crack length at 2.5% augmented strain as a function of the equilibrium melting temperature from each alloy of the 625 study. As expected, the increased additions of Nb, Si, and C and their associated increase in the melting temperature range have a deleterious effect on weldability, which is in general agreement with the discussion on solidification cracking discussed previously. In addition to the effect of melting temperature range, Alloys 1-4 solidified as primary γ with no terminal eutectic-like constituents, which also contributes to their superior weldability. It is interesting to note, however, that no direct correlation was observed between the solidification temperature range and maximum crack length for the Nb-containing alloys. This result can be rationalized by noting that other factors, such as the amount and morphology of second phases, can also influence the hot cracking tendency.

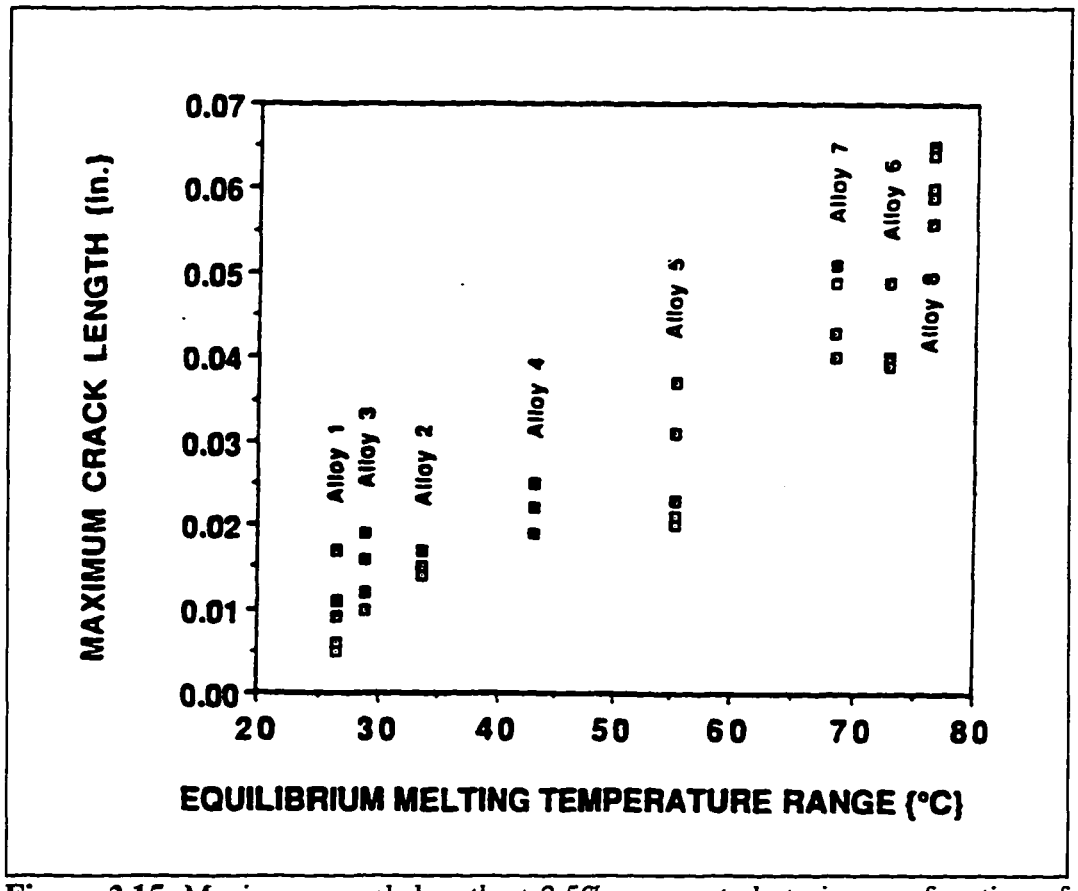

Figure 2.15. Maximum crack length at 2.5% augmented strain as a function of equilibrium melting temperature range for experimental IN625 alloys.

The strong effect of Nb on the formation of secondary solidification constituents has been observed in other nickel base alloys. Knorovsky [2.16] observed that Nb was the major solute controlling the solidification behavior of alloy 718. The proposed solidification path and composition of this alloy are listed in Figure 2.16. In terms of relative Nb, Si, and C contents, this alloy is similar to alloy 625 (Nb,Si) in Table 2.2 and Figure 2.14. Each alloy exhibits a L -> (γ + NbC) and L -> (γ + Laves) reaction, with the (γ + NbC) eutectic-like constituent forming in small quantities in each system. The presence of M_6C in the 625 (Nb,Si) alloy has been attributed to the higher Si content

[2.42]. Neglecting the small amount of NbC formation, Knorovsky developed a pseudo-binary solidification diagram for alloy 718 based on Nb segregation and the L -> (γ + Laves) eutectic. The reaction temperatures and compositions were determined through microscopy techniques (EPMA and AEM) and DTA data to assemble the diagram shown in Figure 2.17. A value of k for Nb at the initiation of solidification was determined by measuring the dendrite core Nb concentration, which represents C_s in equation (2.8) when $f_s = 0$, (assuming no dendrite tip undercooling) leaving k as the only unknown. A value for k was also obtained at the end of solidification by measuring the maximum solid solubility of Nb ($C_{sm,Nb}$ = 9.3 wt%), which resides in γ within the (γ + Laves) eutectic, and the composition of the liquid at the eutectic reaction, which is given by the average Nb concentration of the eutectic as determined by EPMA (C_e = 19.1 wt% Nb). The ratio of these quantities yields a value for k at the end of solidification. It is interesting to note that k was not statistically different at the beginning to end of solidification (k_{Nb}≈0.50) and was similar to k_{Nb} in alloy 625 determined by Cieslak (Table 2.4).

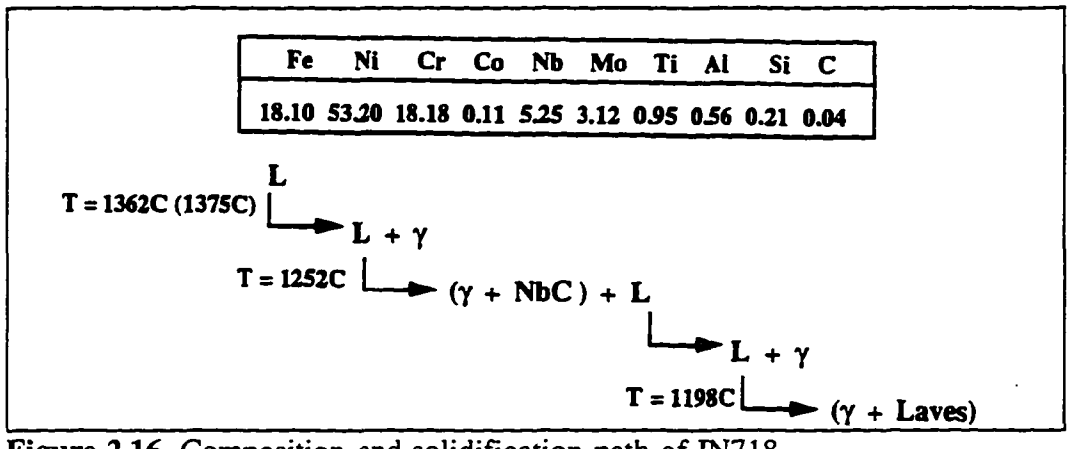

Figure 2.16. Composition and solidification path of IN718.

To summarize the diagram construction in Figure 2.17, points 1 and 2 represent the on-heating solidus and liquidus points, respectively, at the nominal composition (determined by DTA), point 3 is Cs as $f_s = 0$ (determined by EPMA), points 4 and 5 represent the average eutectic (EPMA) and maximum γ compositions (AEM), respectively, and point 6 represents the Nb content of the Laves within the eutectic

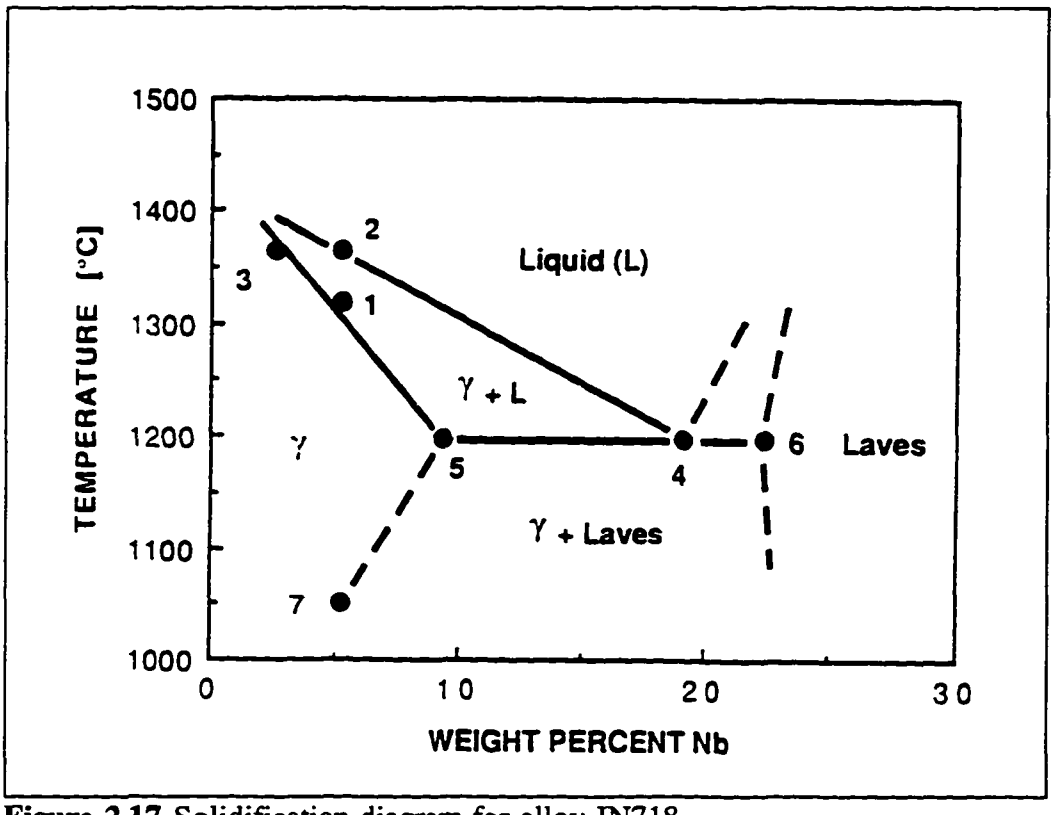

Figure 2.17 Solidification diagram for alloy IN718.

(AEM). Point 7 was taken from solubility data of Nb in alloy 718 as proposed by Eiselstein [2.45]. The maximum solubility of Nb in alloy 718 was determined by Knorovsky at 9.3 wt%, in contrast to pure nickel which can dissolve up to ≈20.5 wt% Nb (Table 2.1). As with the results of the 625 study, this indicates Nb solubility is significantly decreased by the presence of additional alloying elements. The solidification

diagram assembled by this approach provides a convenient method for approximating the behavior of a complicated alloy system in a straight forward manner.

Figure 2.18 shows the maximum crack length as a function of applied strain for IN718. Comparison is made with 304 stainless steel and Hastelloy C-4. Hastelloy C-4 is a nickel based alloy which solidifies as single phase γ with no terminal eutectic-like

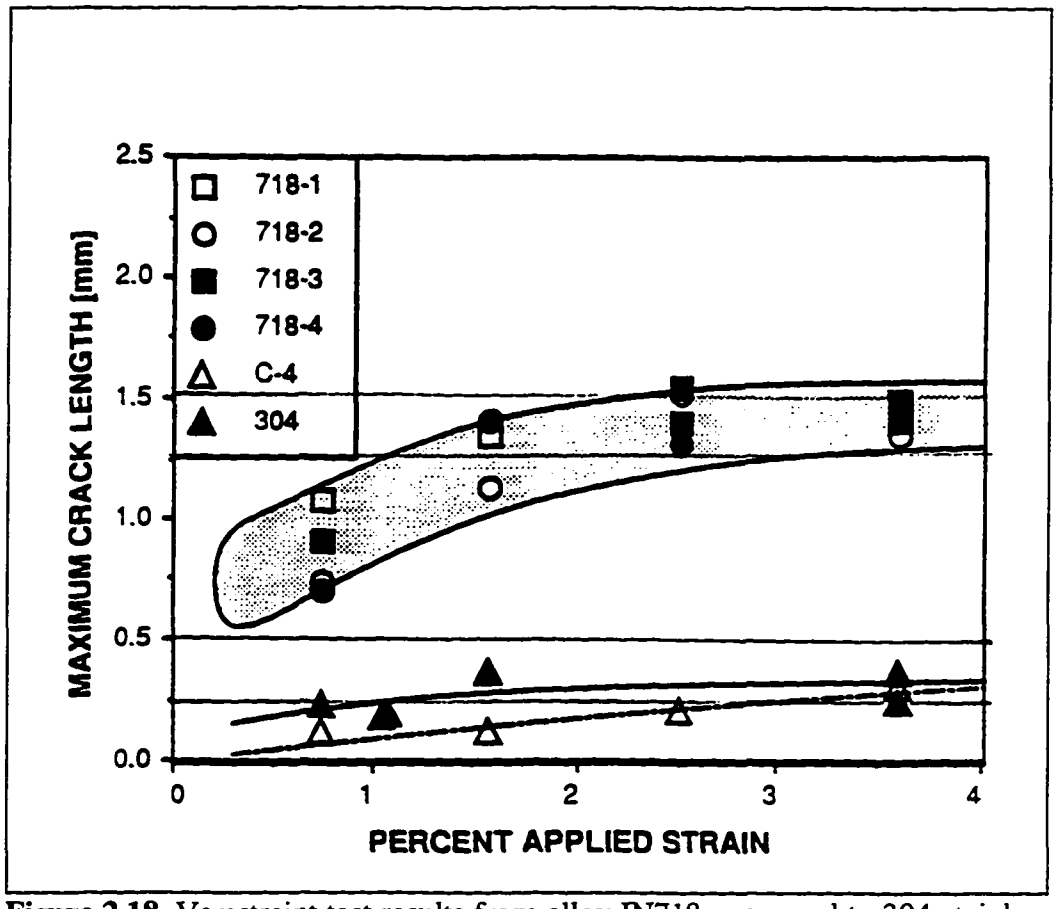

Figure 2.18. Varestraint test results from alloy IN718 compared to 304 stainless steel and Hastelloy C-4.

formation and a solidification temperature range of ≈ 70°C [2.46]. As a result, its weldability is very good. In contrast, IN718 solidifies over a temperature range of ≈ 165°C and terminates solidification by forming 7-11 wt% of combined γ/Laves + γ/NbC

eutectic constituents due to microsegregation of mainly Nb, and its weldability is adversely affected from these factors.

Lastly, the solidification behavior of IN909, an Fe-Ni-Co alloy with minor additions of Nb (≈5 wt%), Ti (≈1.5 wt%) and Si (0.50 wt%) is very similar to that of IN625 and IN718 [2.43]. The solidification path of IN909 as determined by DTA is shown in Figure 2.19. The alloy terminates solidification at 1198°C by the formation of a γ/Laves eutectic-like constituent. The initial distribution coefficients of several elements in IN909 and IN718 as determined by EPMA are listed in Table 2.5. The similarity in k values for Nb and Si among the three alloys considered (IN625, IN718, IN909) is rather surprising when the difference in major alloying elements between these two alloys is considered. The maximum solid solubility of Nb in IN909 was determined to be 9.4 wt%, which is essentially identical to that in IN718 (9.3 wt% Nb). Thus, the behavior of Nb and Si is very similar during solidification of a rather wide range of Ni-based alloys.

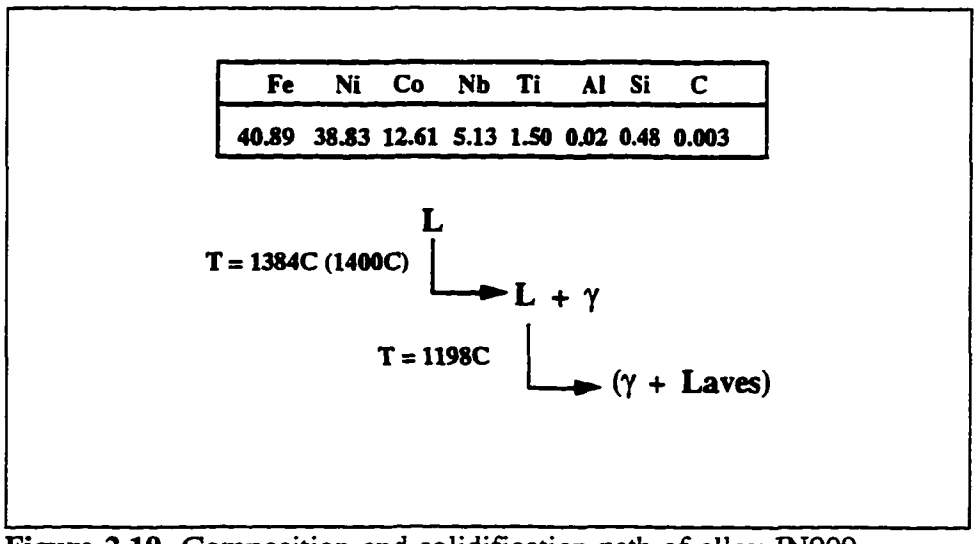

Figure 2.19. Composition and solidification path of alloy IN909.

Table 2.5. Initial distribution coefficients, k, of several elements in alloys IN909 and IN718 as determined by EPMA.

ELEMENT	ALLOY IN909	ALLOY IN718
Niobium	0.49	0.48
Silicon	0.67	0.67
Titanium	0.65	0.63
Iron	1.10	1.04
Nickel	0.97	1.00
Chromium	--	1.03
Cobalt	1.02	--
Molybdenum	--	0.82
Aluminum	--	1.00

2.3.4 IRON RICH ALLOY SYSTEMS

Ni-rich Fe-Ni-Cr alloys which contain Nb, Si, and C are utilized extensively in dissimilar metal weld combinations. The most common examples include weld overlay applications on Fe-C steel substrates and the joining of carbon steel to austenitic stainless steel for high temperature service. In these applications, the dilution that occurs during welding substantially increases the Fe concentration in the weld metal at the expense of Ni. As a result, the final weld metal chemistry is similar to the 300 series austenitic stainless steels. In this regards, it is useful to examine work conducted on austenitic steels containing Nb, Si, and C as these alloys may be expected to behave like dissimilar welds between Ni-rich superalloys and Fe-based alloys.

Nakao *et al.* [2.8] investigated the effect of Nb and C additions on the hot cracking sensitivity of IN519, an alloy with a base composition of 50.5Fe-24Cr-24Ni-

1.5Nb. In this work, C and Nb were varied in a factorial fashion, where C was varied from 0.02 - 0.50 wt% and Nb was varied from trace amounts to 3.0 wt%. The solidification behavior was assessed using DTA (cooling portion only) and the cracking sensitivity was evaluated using spot varestraint testing. X-ray diffraction of extraction replicas was employed for identification of secondary solidification constituents.

The results of the phase identification work is summarized in Table 2.6 (phases in parenthesis exhibited weak diffraction patterns) and can be summarized as follows:

- With trace amounts of Nb, only $M_{23}C_6$ and M_7C_3 form
- NbC forms consistently whenever Nb and C are both present
- The Laves phase forms when C is at very low levels
- The C content required to form $M_{23}C_6$ apparently increases as the Nb content is increased
- M_7C_3 forms at high C contents (> 0.4 wt%)

These results are in general agreement with the work conducted by Cieslak *et al.* on IN625, where NbC was always observed to form when Nb and C were present and Laves formed only at low C levels. In Nakao's work, the NbC reaction initiated in the range of 1280 to 1350°C, with the higher temperatures being promoted by increased Nb contents. The Laves phase occurred at ≈1260 -1290°C. These results are also in agreement with those of Cieslak, where NbC formed at temperatures which were higher than the Laves phase.

Table 2.6. X-Ray diffraction results conducted on experimental IN519 alloys.

Carbon wt%	Niobium, wt%				
	0%	1.0%	1.5%	2.0%	3.0%
≈ 0%	---	NbC Laves	---	Laves	Laves
0.1 %	$M_{23}C_6$	NbC ($M_{23}C_6$)	NbC	NbC (Laves)	NbC Laves
0.2 %	$M_{23}C_6$	NbC ($M_{23}C_6$)	NbC ($M_{23}C_6$)	NbC	NbC Laves
0.25 %	---	---	NbC ($M_{23}C_6$)	---	---
0.3 %	$M_{23}C_6$	NbC $M_{23}C_6$	NbC $M_{23}C_6$	NbC ($M_{23}C_6$)	NbC
0.35 %	---	---	NbC $M_{23}C_6$	---	---
0.4 %	M_7C_3	NbC $M_{23}C_6$	NbC $M_{23}C_6$	NbC $M_{23}C_6$	NbC
0.5 %	M_7C_3	NbC M_7C_3 ($M_{23}C_6$)	NbC M_7C_3 ($M_{23}C_6$)	NbC $M_{23}C_6$	NbC $M_{23}C_6$

The effect of composition variations and concomitant solidification reactions on the hot cracking sensitivity is displayed in Figure 2.20. Figure 2.20a shows that the solidification temperature range approaches a minimum as the Nb/C atomic percent ratio tends towards unity. As a result of this behavior, the crack susceptibility is minimized at compositions where the Nb/C atomic percent ratio is near one (Figure 2.20b). In terms of phase formation, this occurs when NbC is the only constituent to form since it forms at the highest temperature and thus minimizes the solidification temperature range. The formation of NbC has also been observed in weld metals of 347 stainless steel by Lundin

et al. [2.6] and Nb-doped 310 stainless steel by Ogawa and Tsunetomi [2.47]. Ogawa reported a reaction temperature for NbC at ≈ 1315°C, which is within the range observed by Nakao.

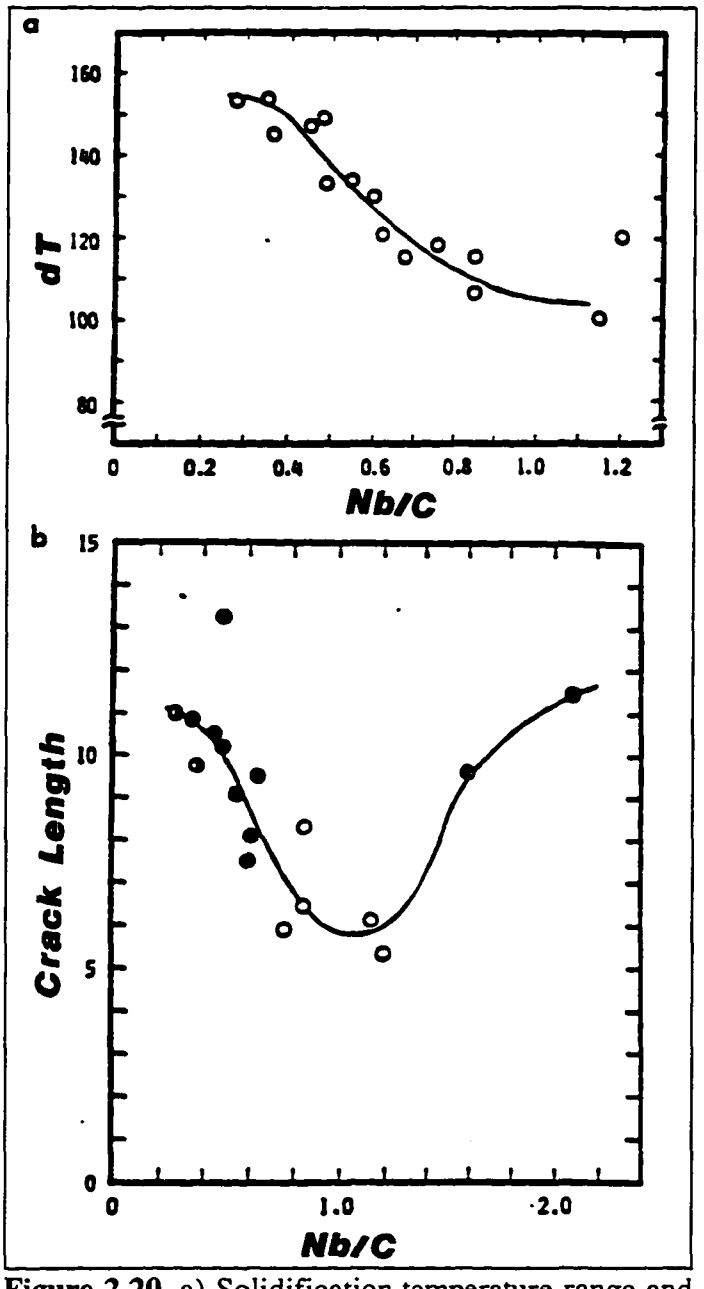

Figure 2.20. a) Solidification temperature range and b) Total crack length as a function of Nb/C atomic ratio for experimental IN519 alloys.

2.3.5 DISSIMILAR METAL WELDS

As previously mentioned, dissimilar metal welds are frequently required in industrial applications. In the case where a single base metal and filler wire combination are utilized, the final weld metal composition can vary from that of the base metal to that of the filler metal, depending on the extent of dilution. The dilution, in turn, depends on the processing parameters. A method has recently been proposed for predicting weld metal dilution levels from knowledge of thermal efficiency factors, which permits one to estimate weld metal composition *a priori* [2.48]. However, no detailed work has been conducted on the solidification reactions and resultant weldability of dissimilar metal welds even though several investigators have identified dissimilar weld combinations which are quite susceptible to solidification cracking [2.49-2.53]. The limited amount of work conducted to date has shown that solidification reactions which occur in the autogenous weld metals discussed above may be operable.

Patterson and Milewski evaluated the hot cracking susceptibility of dissimilar metal welds between 304L and IN625 [2.51]. Weld metal dilution was observed to increase the cracking susceptibility compared to the base materials. A eutectic-like structure was observed in the interdendritic volumes and Auger electron spectroscopy revealed Nb enrichment at the crack surfaces. Cieslak *et al.* [2.50] conducted TEM on second phase constituents which formed on the same dissimilar metal weld combination and identified a eutectic-type structure between Laves and austenite. Based on the discussion above, it is not surprising to find that Laves phase promoted cracking in the final weld metal. Robitz [2.52] evaluated the solidification cracking of IN625 claddings

(apparently on C-steel). It was found that Nb, Si, C, Fe, Mo, P, and S all increased crack susceptibility, although no detailed results were reported. Lastly, Cieslak found that NbC was responsible for extensive solidification cracking between 15-5PH and HP9-4-20 laser welds [2.49]. The 15-5PH alloy had 0.39 wt% Nb and 0.54 wt% Si while the Nb and Si contents of the HP9-4-20 were 0.02 wt% and 0.11 wt%, respectively. In contrast, welds between PH13-8Mo (0.02 wt% Nb, 0.02 wt% Si) and HP9-4-20 were crack-free.

2.3.6 SUMMARY

In the first section of this review it was shown that solidification cracking is affected mainly by solute segregation as it influences the solidification temperature range and formation of eutectic-like constituents at the terminal stages of freezing. From the review section above on pertinent alloy systems, it is clear that solutes of Nb, Si, and C segregate rather strongly during solidification and have a pronounced effect on crack susceptibility. The effects of these minor alloy additions has been investigated in detail for several Ni-based alloy systems. In these materials, the liquid becomes enriched during solidification to the point where second phases of carbides and/or Laves can form with an accompanied increase in the solidification temperature range. Similar effects have been observed in Fe-rich systems, although detailed solidification studies have not been conducted. Dissimilar metal welds between (Nb,Si,C)-containing Ni alloys and Fe-C alloys can possess a broad range in chemical composition depending on dilution, and several investigators have reported significant cracking problems between this dissimilar metal combination. However, no detailed investigations have been conducted to examine

this problem, and this area requires further attention if Ni-base alloys are to be used successfully in critical applications as filler metals and cladding alloys with Fe-base materials.

2.4 RESEARCH OBJECTIVES

The major objectives of this research are:

1. Develop a matrix of experimental alloys which properly simulate the wide variation in composition and solidification behavior observed in commercial Ni base and Fe base superalloys containing Nb, Si, and C.

2. Determine alloy solidification parameters and develop a solidification model which can be used to quantitatively determine the relation between alloy composition, solute redistribution, and microstructural development.

3. Use the established relations between alloy composition and microstructural evolution to determine the influence of composition on fusion zone solidification cracking susceptibility.

3. EXPERIMENTAL PROCEDURE

3.1 EXPERIMENTAL ALLOY DESIGN

A four factor, two level set of experimental alloys was designed to simulate commercial alloys of interest to this study. The target compositions of the alloys are summarized in Table 3.1. The alloys exhibit factorial variations in Fe (in exchange for Ni), Nb, Si, and C at two levels. The high nickel alloys (Alloys 1 - 8) simulate Nb, Si, and C variations in nickel base alloys and low dilution welds between nickel base alloys and carbon steels (low iron content). The high iron alloys (Alloys 9 - 16) simulate Nb, Si, and C variations in iron base alloys and dissimilar metal welds between nickel base alloys and carbon steels made at high dilution levels. The high and low target levels of Nb, Si, and C are set as follows (all values in wt%): $2 < Nb < 5$, $0.02 < C < 0.15$, and $0.10 < Si < 0.60$. These limits were chosen to represent low and high composition values of wrought alloys and filler metals as well as composition limits which can arise due to dilution from carbon steels. The Cr content is selected at 20 wt%, which is typically used in many commercial alloys for good corrosion resistance.

Table 3.1. Target chemical compositions of experimental Fe-Cr-Ni ternary alloys with minor additions of Nb, Si, and C. All values in weight percent.

ALLOY	Fe	Cr	Ni	Nb	Si	C
1	10	20	Bal.	2	0.10	0.02
2	10	20	Bal.	2	0.10	0.15
3	10	20	Bal.	2	0.60	0.02
4	10	20	Bal.	2	0.60	0.15
5	10	20	Bal.	5	0.10	0.02
6	10	20	Bal.	5	0.10	0.15
7	10	20	Bal.	5	0.60	0.02
8	10	20	Bal.	5	0.60	0.15
9	Bal.	20	30	2	0.10	0.02
10	Bal.	20	30	2	0.10	0.15
11	Bal.	20	30	2	0.60	0.02
12	Bal.	20	30	2	0.60	0.15
13	Bal.	20	30	5	0.10	0.02
14	Bal.	20	30	5	0.10	0.15
15	Bal.	20	30	5	0.60	0.02
16	Bal.	20	30	5	0.60	0.15

The alloys were prepared at Sandia National Laboratory by investment casting. All samples were melted and poured in vacuum to produce six bars of each composition with approximate dimensions of 170 mm x 25 mm x 6.3 mm. Table 3.2 lists the actual compositions of the alloys determined by wet chemical analysis techniques. Several additional alloys with intermediate C contents (Alloys 1.5, 3.5, 7.5, and 11.5) were added based on preliminary weldability results. These alloys were fabricated by arc melting at Oak Ridge National Laboratory. Two high Nb alloys (Ni-1 and Fe-1) were also added to

produce alloys with high quantities of eutectic-type constituents. These alloys were produced at Lehigh University from high purity powders (> 99.99 wt%) by gas tungsten arc melting. The alloys exhibit a wide range in Nb, Si, and C contents which is desired for this research. The levels of P and S are controlled to low levels so that they will not affect the weldability results.

Although the alloys exhibit the desired composition ranges, the oxygen contents are relatively high in the alloys made at SNL and produced oxides in the alloys. The maximum solid solubility of oxygen in Ni is on the order of 0.01 wt% [3.1], which is below all the values listed in Table 3.2. Thus, the alloys are expected to contain oxides at these oxygen levels. The oxides present two potential difficulties. First, they may tie up the important solute elements of interest (Nb, Si, and C), effectively reducing the matrix composition. This could interfere with accurate determination of liquidus and solidus slopes from the differential thermal analysis (DTA) data. Secondly, as shown in Figure 3.1a, an oxide film developed on many of the alloys during welding which hindered accurate crack length measurements on the varestraint samples. These factors are discussed below.

Table 3.2 Actual alloy compositions. All values in weight percent.

Alloy	Fe	Ni	Cr	Nb	Si	C	P	S	O
1	10.49	68.53	18.90	1.93	0.08	0.017	0.004	0.003	0.050
1.5	10.75	67.95	19.21	2.00	0.03	0.052	0.004	0.003	ND
2	11.12	68.20	19.12	1.95	0.06	0.132	0.004	0.002	0.043
3	10.70	68.11	19.02	1.82	0.38	0.010	0.004	0.003	0.083
3.5	10.39	66.80	19.29	1.94	0.41	0.075	0.004	0.003	ND
4	10.72	67.60	19.08	1.91	0.40	0.155	0.004	0.001	0.031
5	10.84	65.79	18.98	5.17	0.05	0.013	0.005	0.010	0.057
6	10.88	65.22	18.89	4.87	0.08	0.161	0.005	0.007	0.044
7	10.70	65.53	19.30	4.86	0.52	0.010	0.005	0.009	0.082
7.5	10.82	63.93	18.54	4.92	0.46	0.081	0.005	0.004	ND
8	10.80	64.96	18.90	4.72	0.52	0.170	0.005	0.007	0.051
Ni-1	7.71	55.03	18.23	17.79	1.03	0.08	ND	ND	ND
9	46.03	33.56	19.31	1.66	0.10	0.003	0.006	0.003	0.060
10	46.69	32.80	19.70	1.66	0.01	0.108	0.006	0.002	0.060
11	45.38	32.80	19.53	1.77	0.57	0.004	0.006	0.002	0.037
11.5	47.38	31.05	19.64	1.84	0.67	0.116	0.006	0.001	ND
12	45.28	32.39	19.89	1.93	0.61	0.079	0.006	0.002	0.037
13	44.55	31.24	19.63	4.42	0.02	0.015	0.007	0.003	0.057
14	44.05	31.93	19.52	4.51	0.08	0.210	0.006	0.002	0.051
15	45.40	30.03	19.54	4.88	0.66	0.010	0.007	0.003	0.042
16	44.47	30.89	19.45	4.77	0.64	0.216	0.006	0.002	0.037
Fe-1	40.87	27.89	19.69	10.63	0.63	0.081	ND	ND	ND

ND - Not determined

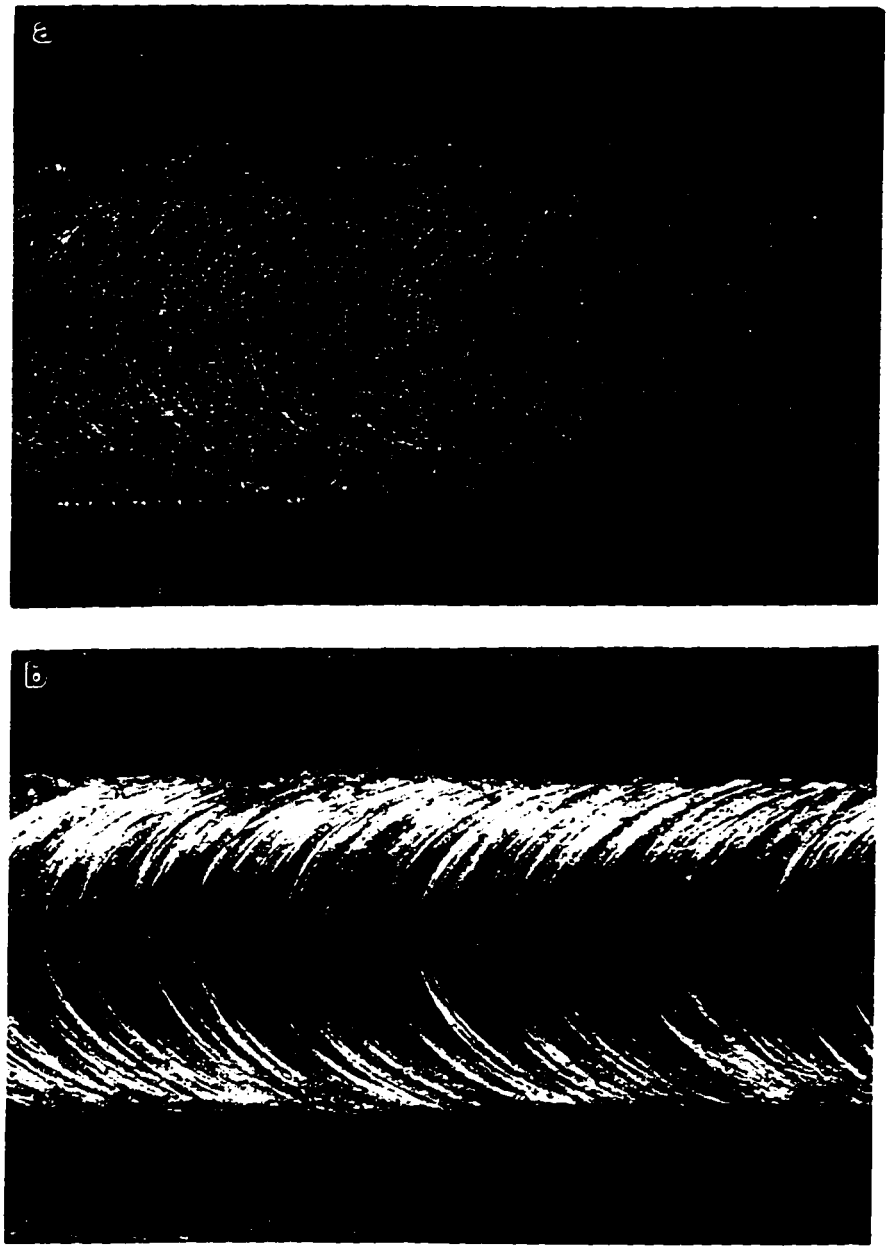

Figure 3.1. a) Stereomicroscope photograph of oxide on varestraint sample before cleaning procedure is applied. b) After cleaning procedure.

Electron Probe Micro-Analysis (EPMA) was conducted on oxides within all the even number alloys to determine their chemical composition (details of the EPMA procedure are described below). As shown by Figure 3.2, the oxides are typically 5-10 μm, which is larger than the sampling diameter of the electron probe (≈1-2 μm). Thus, EPMA can be utilized for accurate measurement of the oxide compositions. Preliminary results from Energy Dispersive Spectrometry (EDS) indicated the oxides contained mainly Cr, which suggested they were chromium oxide. Therefore, pure Cr_2O_3 was used as a standard for determining the chromium and oxygen contents. Pure elemental standards were used for all other elements.

The EPMA results are summarized in Table 3.3. Each value is an average from five measurements made on oxides within each even number alloy. The values in parentheses are standard deviations. Also listed is the weight percentage of oxides in the alloys. The oxide weight percentages are calculated assuming all the oxygen is consumed to form oxides and thus represents an upper bound value of oxide content. (The upper bound oxide content is given by the ratio of weight fraction oxygen in the alloy to weight fraction oxygen in the oxide.) Note that the oxides are never present in quantities greater than 0.25 wt%. The table also lists the Nb and Si content of each alloy along with the total amount of Nb and Si lost to the oxide. The amount of element lost to the oxide is given by the product of weight fraction oxide in the alloy and weight fraction element in the oxide. Except for the oxides in Alloys 12, 14, and 16 which are Nb-rich, the compositions suggest the oxide is Cr_2O_3 (ideal oxygen content of 31.5 wt% O). The amount of element lost to the oxides is also given as a percentage of the total element

content in the alloy. There are only four cases where the amount of Nb or Si lost to the oxide exceeds 1% of the total element amount and it never exceeds 2%. In most cases the loss is well below 1%. Thus, the amount of Nb and Si lost to the oxides will be considered negligible in this work.

Table 3.3. Compositions and calculated weight fraction of oxides in high carbon alloys. All composition values shown are in weight percent. Values in parentheses represent standard deviation values from five measurements.

Alloy->	2	4	6	8	10	12	14	16
Fe	0.2 (0.1)	0.3 (0.1)	0.3 (0.1)	0.4 (0.4)	0.6 (0.2)	1.2 (0.3)	1.1 (0.1)	1.1 (0.1)
Ni	1.4 (0.1)	1.6 (0.2)	1.4 (0.1)	2.4 (2.1)	0.3 (0.1)	0.7 (0.1)	0.5 (0.1)	0.7 (0.1)
Cr	60.7 (2.4)	55.4 (2.3)	60.5 (1.1)	60.8 (1.5)	64.6 (0.5)	34.1 (3.5)	25.2 (0.8)	31.0 (1.3)
O	34.0 (1.0)	34.9 (1.2)	34.1 (0.3)	33.1 (0.8)	32.8 (0.3)	34.6 (1.5)	28.8 (0.6)	30.5 (0.6)
Nb	0.5 (0.1)	0.3 (0.2)	0.8 (0.1)	0.9 (0.4)	1.2 (0.1)	22.4 (4.5)	44.1 (0.4)	34.4 (2.0)
Si	0.2 (0.2)	0.2 (0.1)	0.2 (0.1)	0.2 (0.1)	0.3 (0.2)	5.1 (1.0)	0 (0)	1.2 (0.6)
Al	2.3 (1.5)	7.0 (1.4)	2.8 (1.1)	2.0 (0.5)	0.3 (0.3)	1.4 (0.3)	0.4 (0.1)	0.4 (0.1)
Wt % Oxide	0.1	0.2	0.1	0.2	0.2	0.1	0.2	0.1
Nb in Alloy (wt%)	1.53	1.53	4.57	4.59	1.68	1.99	3.98	4.03
Nb lost to Oxide (wt%)	0.0006	0.0003	0.001	0.001	0.002	0.02	0.07	0.04
Percent Nb lost to Oxide	0.1	0.1	0.1	0.1	0.1	1.3	1.9	1.0
Si Content in Alloy (wt%)	0.16	0.40	0.08	0.52	0.25	0.61	0.23	0.49
Si lost to Oxide (wt%)	0.0002	0.0002	0.0002	0.0003	0.0005	0.006	0.001	0.001
Percent Si lost to Oxide	0.1	0.1	0.3	0.6	0.2	1.0	0.5	0.2

Figure 3.2. Light optical photomicrograph of typical oxide observed in alloys.

An oxide cleaning procedure was developed to eliminate the oxide film which formed on the varestraint samples. Three overlapping autogenous gas tungsten arc (GTAW) welds, approximately 4.5 mm in width, were placed on the center of each varestraint sample as shown schematically in Figure 3.3 (welding parameters: 95 A, 10 V, 3.3 mm/s travel speed). The surface oxide was removed after each pass using a low speed miniature abrasive wheel with 60 grit SiC paper. This procedure reduced the oxygen content by removing the oxide which floated to the weld pool surface. After the three passes were applied, a fourth pass was placed at the center of the "cleaned" area during the varestraint test which produced a bright weld surface for accurate crack length measurements. An example of the clean weld surface produced with this technique is shown in Figure 3.1b.

3.2 WELDABILITY EVALUATIONS

The weldability (i.e., resistance to solidification cracking) of each alloy was evaluated using the varestraint test [3.2, 3.3]. This instrument is shown schematically in Figure 3.4. A weld is established on a sample by a GTAW torch which travels in the direction indicated in the figure. When the torch reaches point "A", the sample is forced to bend over a die block to a predetermined radius which induces a strain on the solidifying sample equal to t/2R, where t is the specimen thickness and R is the radius of the die block. The augmented strain simulates the residual thermal and shrinkage strains which rupture the interdendritic liquid films during the terminal stages of solidification. As discussed in Chapter 2, the cracking susceptibility of a given alloy depends on the residual strain and material factors such as the solidification temperature

range, the amount of terminal liquid, and the terminal liquid morphology (surface tension). By inducing cracks in various alloy compositions under a controlled strain level, material considerations are the only factors which remain to produce different cracking behaviors.

The as-cast samples were machined to typical sub-size varestraint specimens (165 mm x 25 mm x 3.2 mm). The welding parameters used for the varestraint evaluations are summarized in Table 3.4. In order to acquire adequate statistics, three tests were conducted on each alloy at an augmented strain of 2.5% to simulate highly restrained welds. The maximum crack length (MCL) was used as the indicator of cracking susceptibility and was measured using a light optical microscope at 100X. The physical interpretation of the MCL is shown schematically in Figure 3.5. During welding, a liquid + solid region will exist behind the weld pool. It is this liquid + solid region which, because of nil strength, is susceptible to cracking under the influence of strain. The temperature gradient behind the weld pool is depicted in the lower figures, where temperature decreases with increasing distance from the solid/liquid interface. The interface between the liquid weld pool and solid + liquid region is located at a position where the actual temperature intersects the liquidus temperature of the alloy. Similarly, the interface between the solid + liquid region and completely solidified weld is positioned where the actual temperature intersects the terminal solidus temperature of the alloy. Thus, composition variations which promote low temperature eutectic-type reactions at the terminal stages of solidification will widen the solidification temperature range and aggravate the cracking tendency by expanding the crack susceptible solid + liquid region.

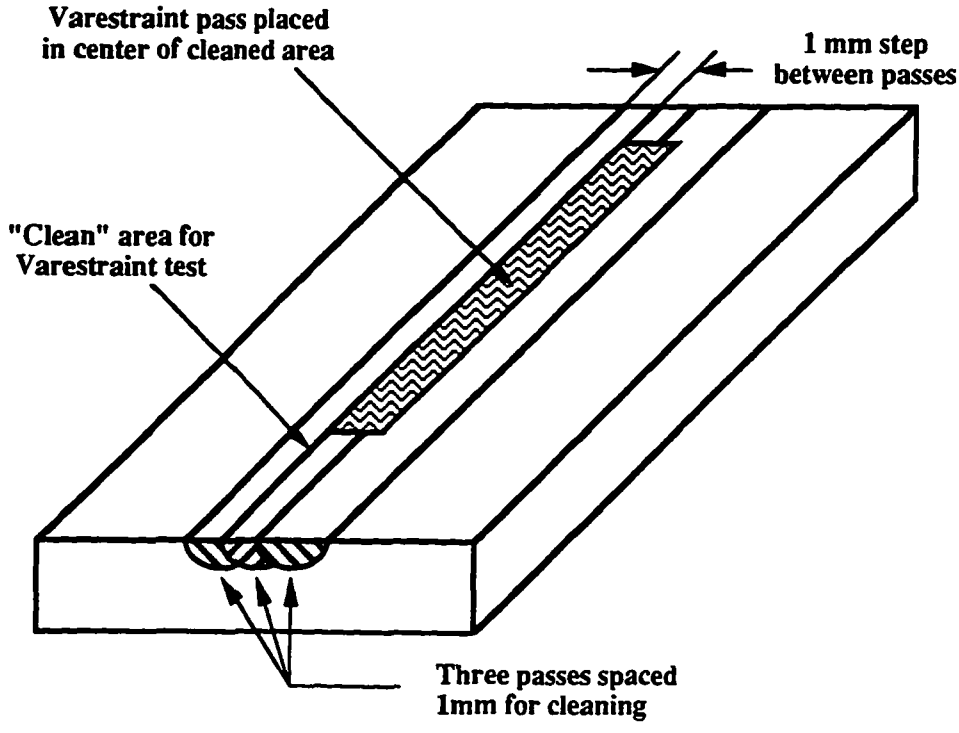

Figure 3.3. Schematic illustration of oxide cleaning procedure used to produce clean weld surfaces for crack length measurements.

Table 3.4. Summary of varestraint welding parameters and conditions

Welding Current - 95 Amperes	Shielding Gas - High Purity Argon
Arc Voltage - 10 V (≈2.5 mm arc gap)	Electrode Type - W-2ThO_2
Travel Speed - 3.3 mm/s	Electrode Tip Angle - 60°
Sample Size - 165mm x 25mm x 3.2mm	Electrode Diameter - 3.2mm
Augmented Strain - 2.5%	Air Pressure - 80 psi

3.3 DIFFERENTIAL THERMAL ANALYSIS

The liquidus, solidus, and temperatures of eutectic-type reactions were measured using differential thermal analysis (DTA). Attempts were made to homogenize/solution heat treat all samples to single phase austenite for accurate solidus temperature measurements. The samples were placed in an evacuated quartz tube and heat treated for temperatures and times up to 1300 °C and 60 hours. Despite these rather long, high temperature heat treatments, most alloys could not be heat-treated to produce single phase austenite. The solvus temperature for Ni-16Cr-8Fe alloys [3.4] and Fe-25Ni-20Cr alloys [3.5] containing Nb and C are given by

$$\ln[(Nb)(C)^{0.81}] = 7.5 - \frac{14,000}{T} \qquad (Ni\text{-}16Cr\text{-}8Fe) \qquad (3.1)$$

$$\log(Nb \cdot C) = 4.07 - \frac{8,358}{T} \qquad (Fe\text{-}25Ni\text{-}20Cr) \qquad (3.2)$$

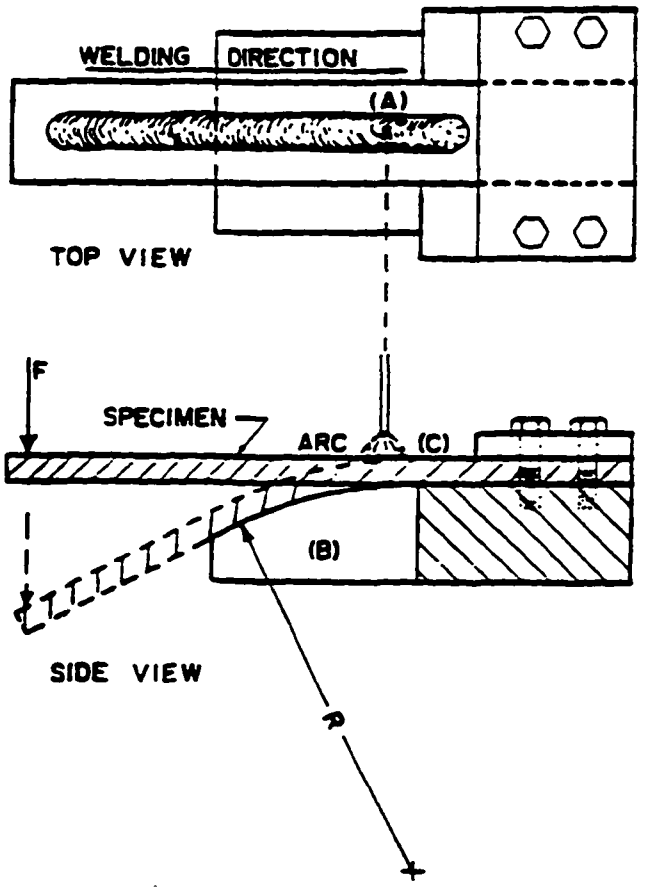

Figure 3.4. Schematic of varestraint tester used for solidification cracking tests.

Here, T is the solvus temperature (in K) and the Nb and C contents are expressed in weight percentages. Since the matrix compositions for these relations are close to those of the current work (using eq. (3.1) for Alloys 1-8 and eq. (3.2) for Alloys 9-16), these solubility product relations should provide a good estimate of the solvus temperatures required to achieve a single phase austenitic structure. The calculated solvus temperature (in °C) for each alloy is listed in Table 3.5. DTA measurements showed that these calculated solvus temperatures were above the temperature of the $L \rightarrow \gamma + NbC$ eutectic type reaction (1305°C to 1360°C) and often near or above the liquidus temperature (1380°C to 1430°C). This indicates that the combined Nb and C content exceeds the maximum solid solubility and no single phase austenite field exists for the high C alloys. For the Fe base alloys, it was not possible to obtain single phase samples even for most of the low C alloys. Thus, solidus temperatures were only measured on Ni base Alloys 1, 1.5, 3, 3.5, 5, and 7 where homogeneous single phase samples could be produced.

DTA was conducted on a Netzsch STA 409 differential thermal analyzer using 500 to 550 mg samples. The DTA system was calibrated to melt within 2°C of the melting point of pure Ni (1455°C). Samples were melted and solidified under flowing argon in alumina crucibles using pure Ni as the reference material. Preliminary tests were first conducted to establish the liquidus temperature of each alloy. After these preliminary tests, the liquidus and solidus (where possible) temperatures were determined by heating samples slowly at a rate of 5°C/minute to approximately 10°C above their liquidus temperature. The samples were than solidified at a relatively fast cooling rate of 20°C/minute to determine temperatures of eutectic type reactions which occur under

non-equilibrium solidification conditions. Reaction temperatures were taken as deviations from the local baseline. All reported reaction temperatures are an average from at least three tests, and the order of testing was randomized.

Table 3.5 Calculated solvus temperatures for each alloy based on Nb and C contents. Ni-Base alloy solvus temperatures were calculated using eq. 3.1 and iron base alloy solvus temperatures were calculated using eq. 3.2.

Alloy	Solvus Temp., °C (eq. 3.1)	Alloy	Solvus Temp, °C (eq. 3.2)
1	1107	9	1038
1.5	1248	10	1462
2	1379	11	1070
3	1044	11.5	1490
3.5	1294	12	1437
4	1401	13	1319
5	1220	14	1768
6	1619	15	1280
7	1177	16	1787
7.5	1489		
8	1623		

3.4 WELD-QUENCH EXPERIMENTS

In order to determine the extent of microsegregation, it is necessary to measure the composition profiles (using EPMA) across the dendritic substructure in the as-solidified condition. Solid state diffusion may occur during and after solidification which can possibly hinder accurate measurements of the as-solidified segregation patterns. Weld-

quench experiments were conducted in order to avoid this potential problem. Alloys 8 and 16 were welded using the same process (GTAW) and parameters as the varestraint tests noted above. However, during this autogenous weld, a high pressure water spray was directed at the weld pool to quench the dendrite tips growing into the advancing liquid weld pool. Composition profiles of quenched dendrites were then obtained by EPMA and compared to profiles obtained on welds with no forced cooling which cooled at ≈660 °C/s.

3.5 MICROSTRUCTURAL CHARACTERIZATION

Light Optical Microscopy (LOM) was conducted on DTA samples polished through 0.04μm colloidal silica and electrolytically etched in a 10% chromic acid + 90% water solution at 3 volts. Scanning Electron Microscopy was conducted on weld metals (using the same preparation procedure) using a JEOL 6300 Field Emission Gun Scanning Electron Microscope (FEG-SEM) at an accelerating voltage of 15kV. The varestraint samples were mounted in thermal setting epoxy to provide a planar view of the solidification cracks which intersected the specimen surface. After mounting, the surfaces were lightly ground with 600 grit SiC paper to remove a very thin layer of surface material and provide a flat area in the crack region for subsequent polishing and etching. Quantitative Image Analysis (QIA) was conducted on autogenous GTA welds and selected DTA samples. Area fractions of total eutectic type contents and, where possible, individual γ/NbC and γ/Laves eutectic type constituents were measured on each sample with at least ten SEM photomicrographs. Area fractions were assumed to be equivalent

to volume fractions.

Electron Probe Micro-Analysis (EPMA) was conducted on a JEOL 733 Probe at an accelerating voltage of 15kV and beam current of 20 nA. All EPMA samples were mounted in thermal setting epoxy, polished flat to a 0.3μm finish using an alumina slurry, ultrasonically cleaned in acetone, and carbon coated prior to analysis. The K_α lines were used for Fe, Ni, Cr, and Si while the L_α line was used for Nb. Raw data were reduced to weight percentages using the ZAF algorithm [3.6]. The crystal structure of secondary phases in welds of Alloys 6 and 13 were determined by collecting Backscattered Electron Kikuchi Patterns (BEKP) in an SEM at Sandia National Laboratory. The details of this procedure are described in [3.7].

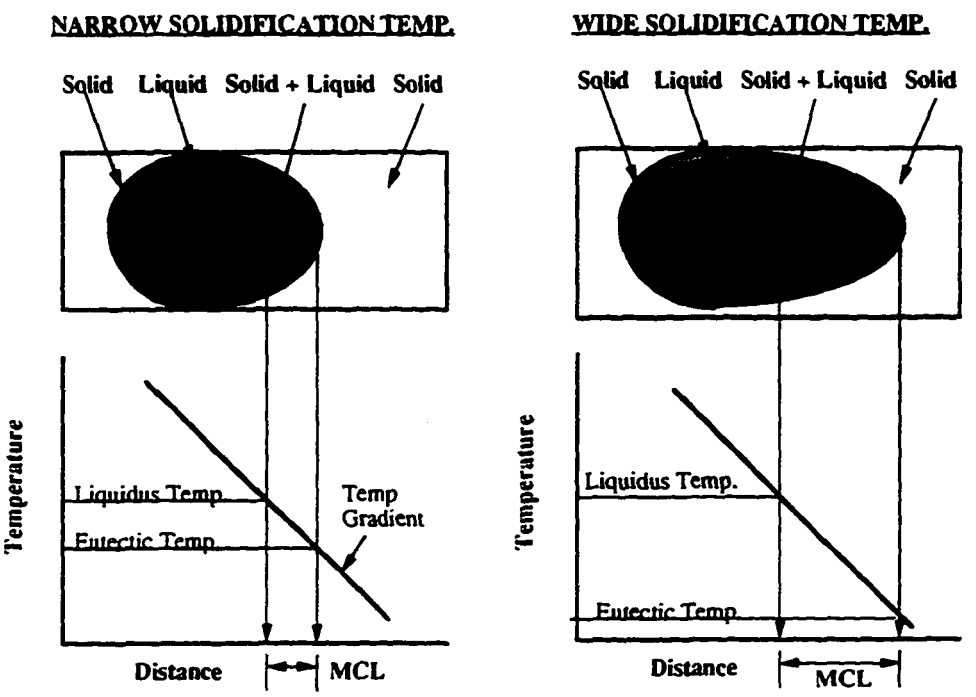

Figure 3.5 Physical interpreataion of the maximum crack length measurement.

4. GENERAL SOLIDIFICATION BEHAVIOR

4.1 SOLIDIFICATION MICROSTRUCTURES

The microstructures of varestraint samples, weld metals, and DTA specimens were examined as a starting point for developing a detailed understanding of the solidification behavior of these alloys. Attention was focused on the varestraint samples in order to make preliminary identifications of secondary phases which form during solidification while simultaneously assessing the relation between microstructure and solidification cracking susceptibility. SEM photomicrographs of the varestraint samples are presented in Figures 4.1 through 4.20. These photomicrographs were all taken in the vicinity of solidification cracks produced during varestraint testing. These collection of photomicrographs, together with the EPMA and BEKP data (below), form the basis for identifying the secondary phases which form in each alloy. They will also be utilized again in Chapter 6 to determine the relation between microstructure and weldability.

In addition to the primary austenite dendrites, the alloys generally form one or both of two secondary phases during solidification. The first type of secondary phase typically exists as thin lamella in a eutectic-type arrangement with the austenite matrix. This phase is readily evident in all the high C (even-numbered alloys). The other type of secondary phase exists as isolated particles at low volume fractions (e.g., Alloy 6 - Figure 4.8) while, at higher volume fractions, is present in a lamellar-type arrangement with the austenite matrix (e.g., Alloy 15, Figure 4.19). Examination of microstructures in DTA samples, which solidify at much lower cooling rates, showed identical results. Typical DTA microstructures are shown in Figures 4.21 through 4.28. Examination of weld metals

at locations remote from solidification cracks also showed similar features (e.g., Alloys 13 and 16 - Figures 4.29 and 4.30). The high Nb alloys (Ni-1 and Fe-1) exhibit these phases in high amounts (Figures 4.31 and 4.32).

Due to the relatively slow cooling rates (0.33 °C/s), the secondary phases which form in DTA samples exhibit regions which are 2-5 μm in diameter and can thus be analyzed by EPMA. Typical compositions of the first type of secondary phase (e.g., labeled "NbC" in Figures 4.22 and 4.24) present in DTA samples of several alloys are summarized in Table 4.1. (All reported EPMA measurements are the average and standard deviation from at least five measurements. Values reported with no standard deviation are single measurements acquired for confirmation.) The Nb content of this phase varies between 83.6 to 89.5 wt% Nb and is consistent with niobium carbide (NbC), which has a stoichiometry range of approximately 88 - 91 wt% Nb in the binary Nb-C system [4.1]. The slightly lower values of Nb measured in the NbC here are probably due to the presence of other metal elements (Fe, Ni, Cr), which may substitute for Nb. Backscattered electron kikuchi patterns collected from this phase in the weld metal of Alloy 6 revealed an fcc crystal structure, which is also consistent with the NbC phase [4.1].

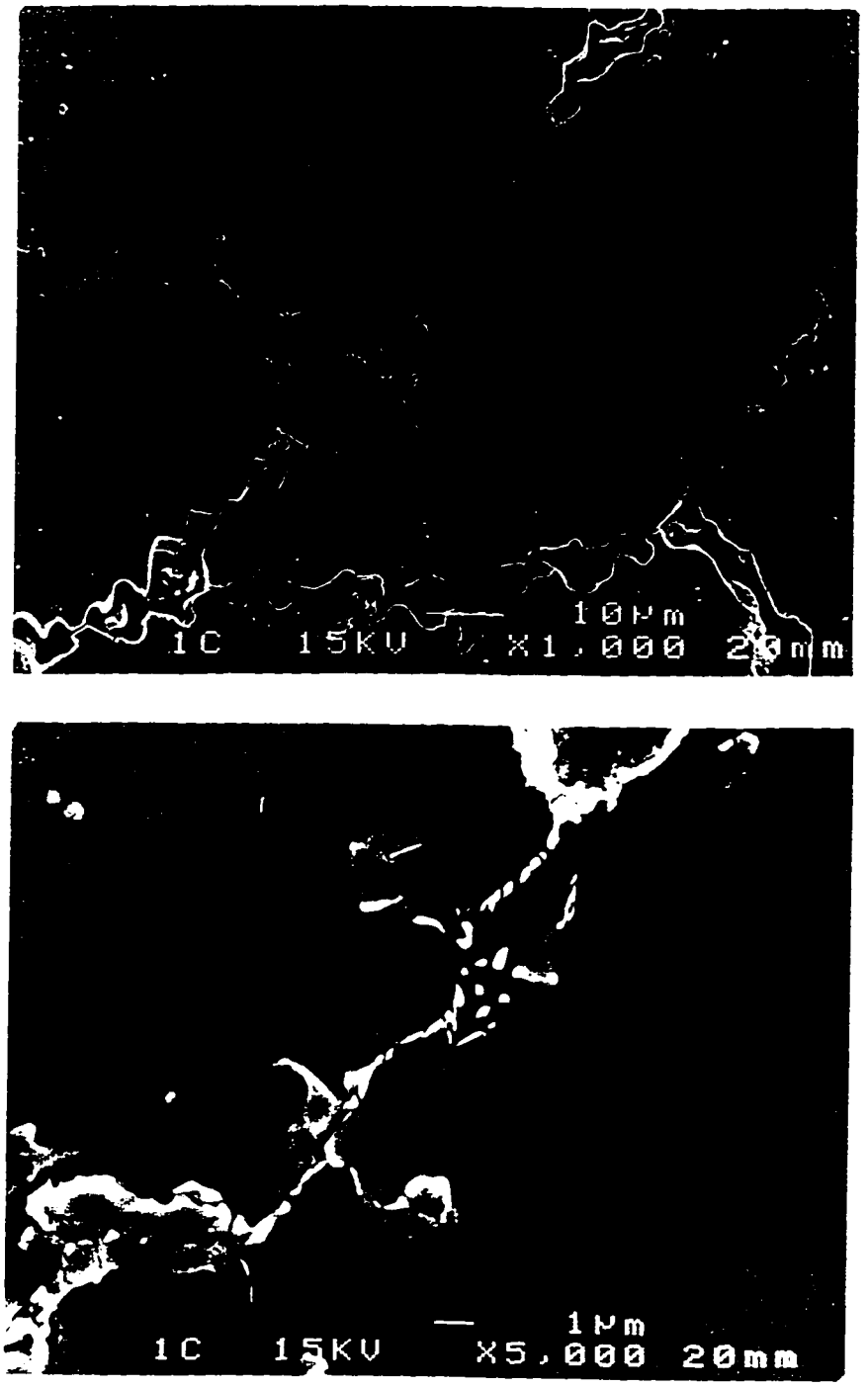

Figure 4.1. SEM photomicrographs of Alloy 1 varestraint sample.

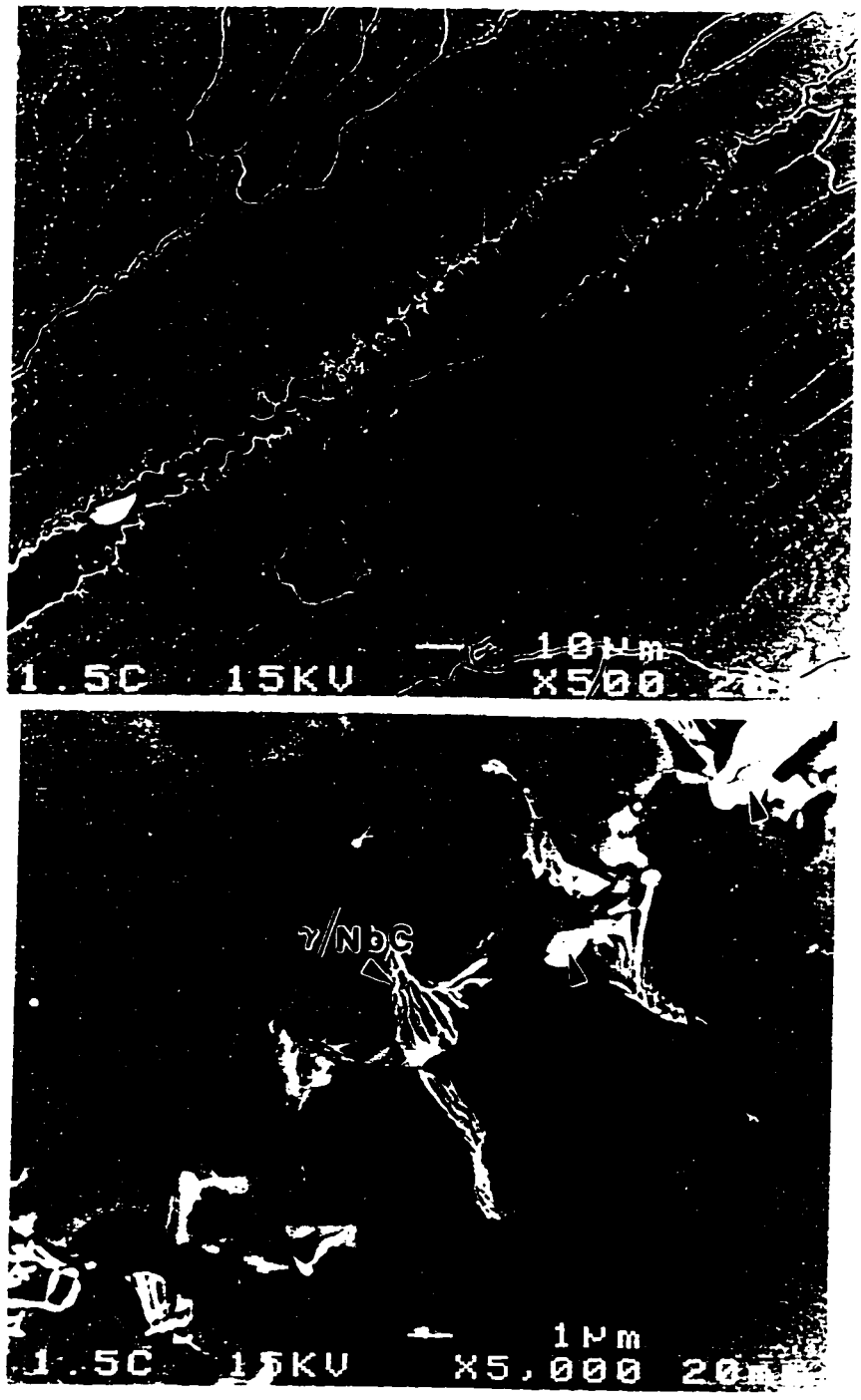

Figure 4.2. SEM photomicrographs of Alloy 1.5 varestraint sample.

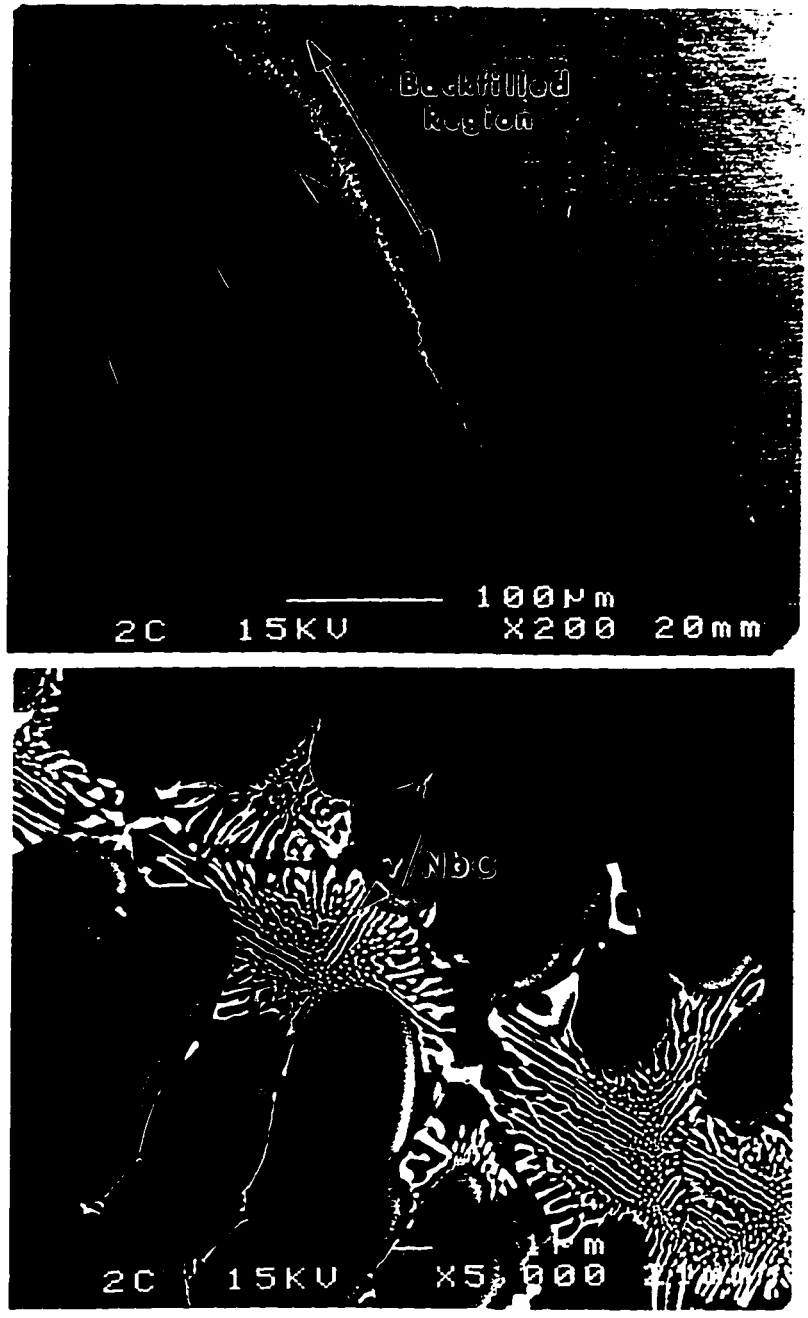

Figure 4.3. SEM photomicrographs of Alloy 2 varestraint sample.

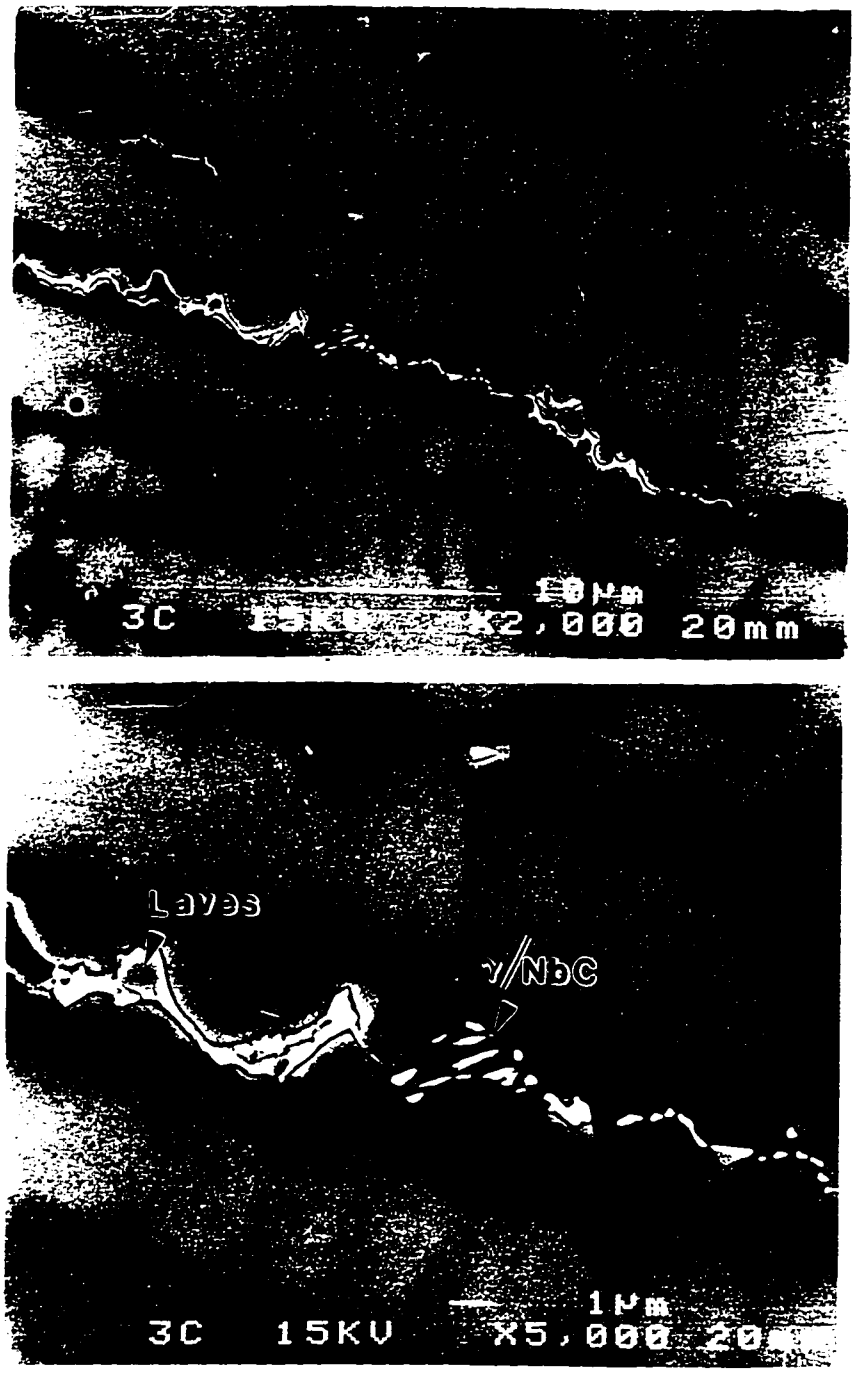

Figure 4.4. SEM photomicrographs of Alloy 3 varestraint sample.

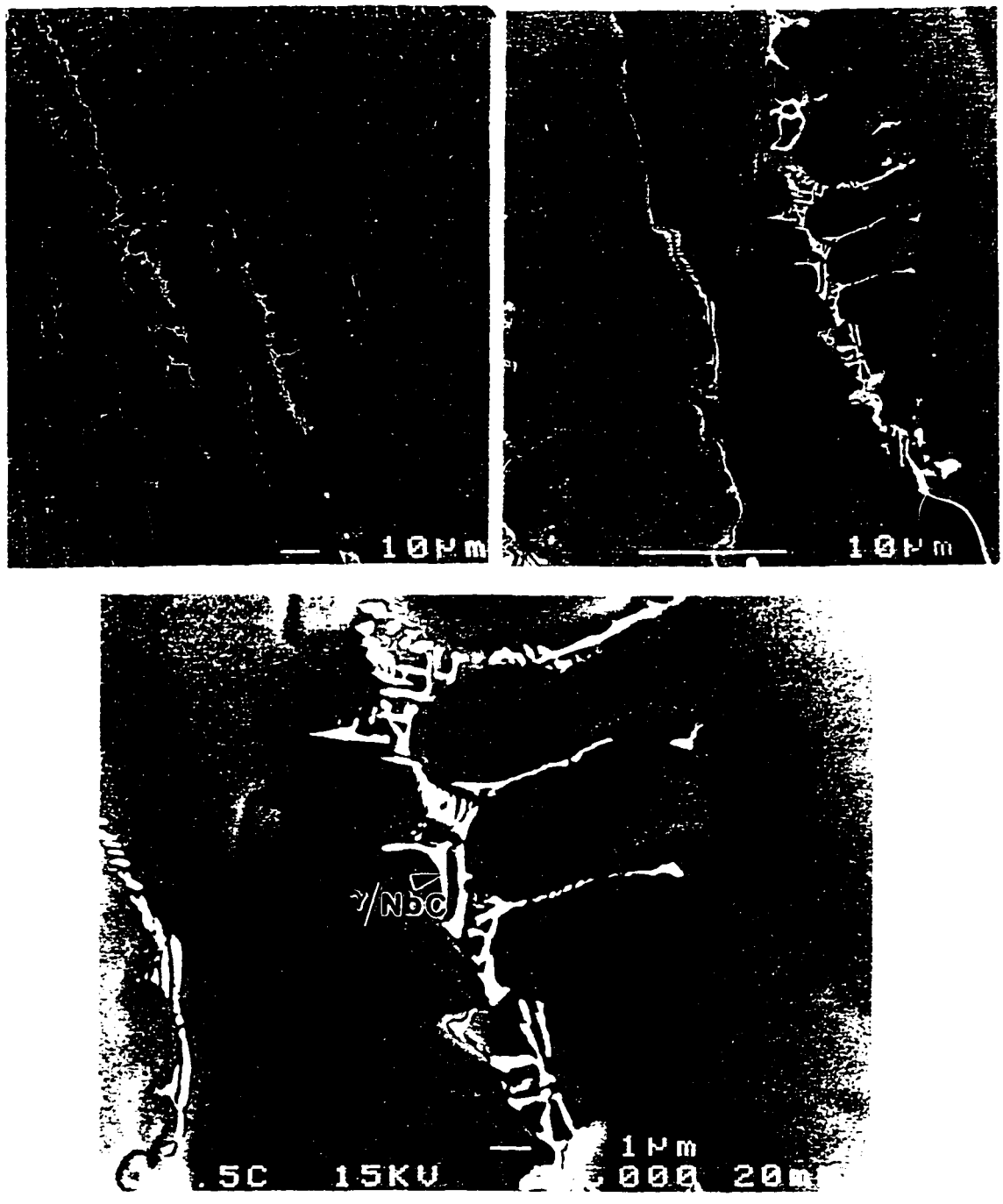

Figure 4.5. SEM photomicrographs of Alloy 3.5 varestraint sample.

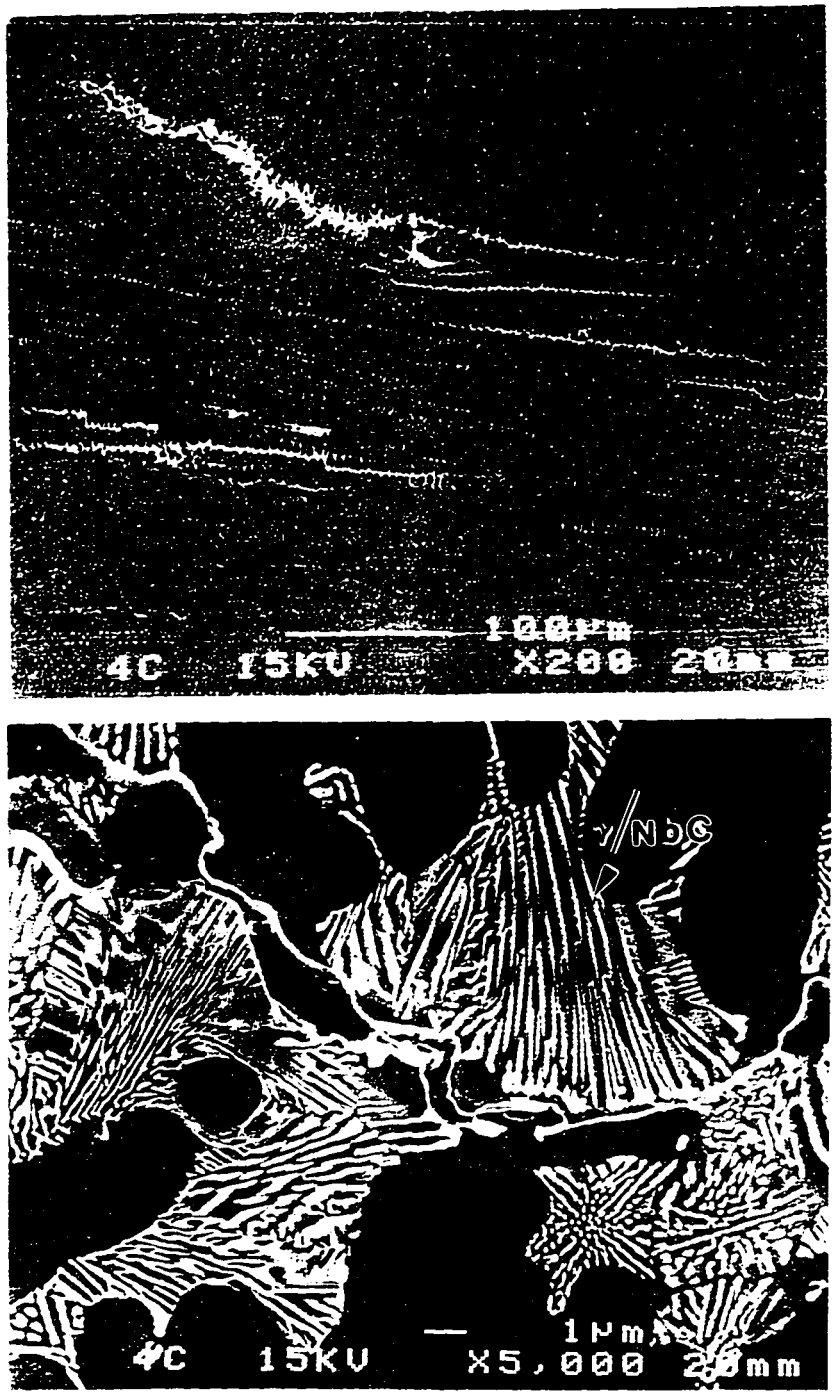

Figure 4.6. SEM photomicrographs of Alloy 4 varestraint sample.

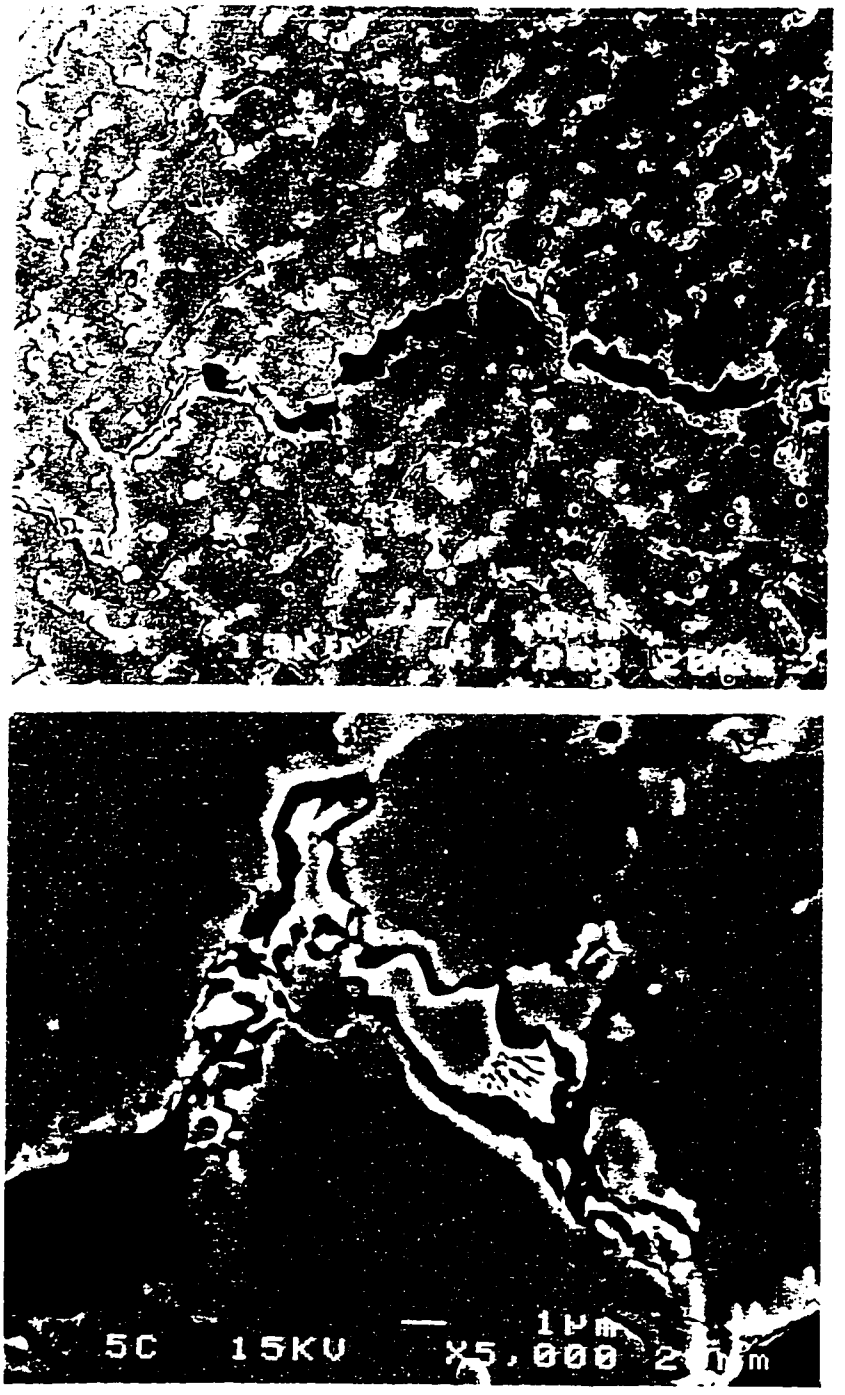

Figure 4.7. SEM photomicrographs of Alloy 5 varestraint sample.

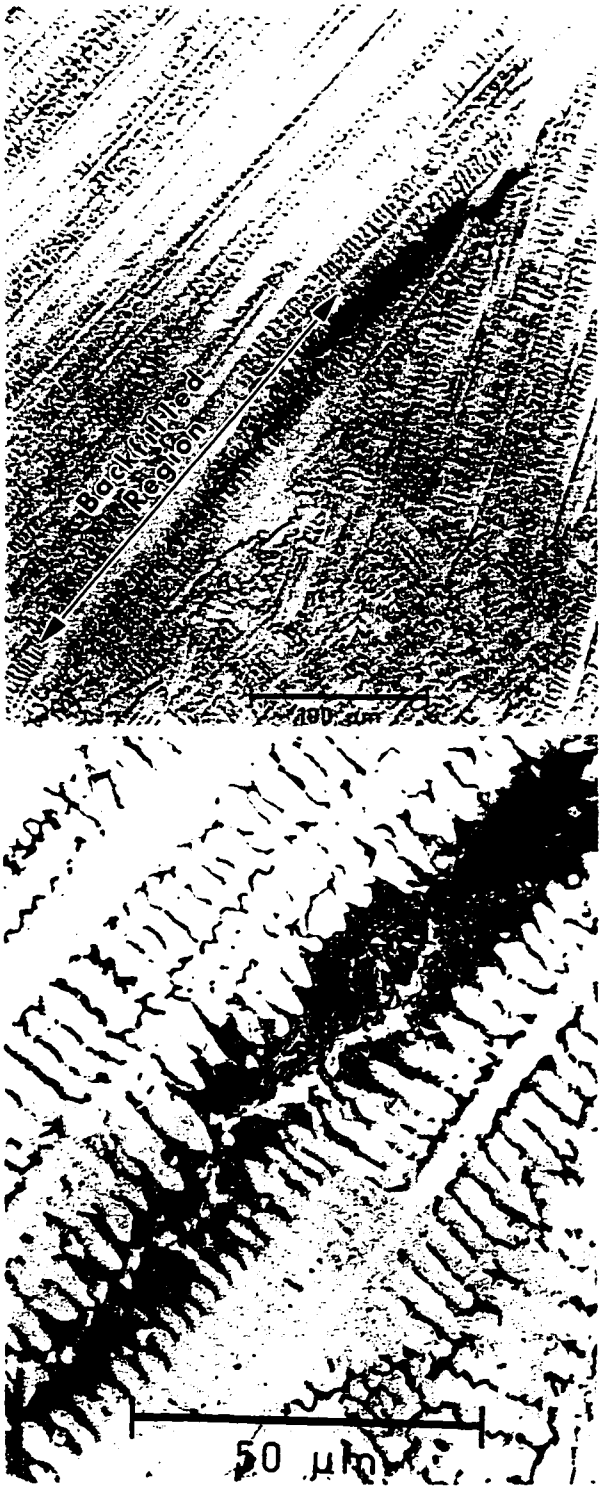

Figure 4.8. LOM photomicrographs of Alloy 6 varestraint sample.

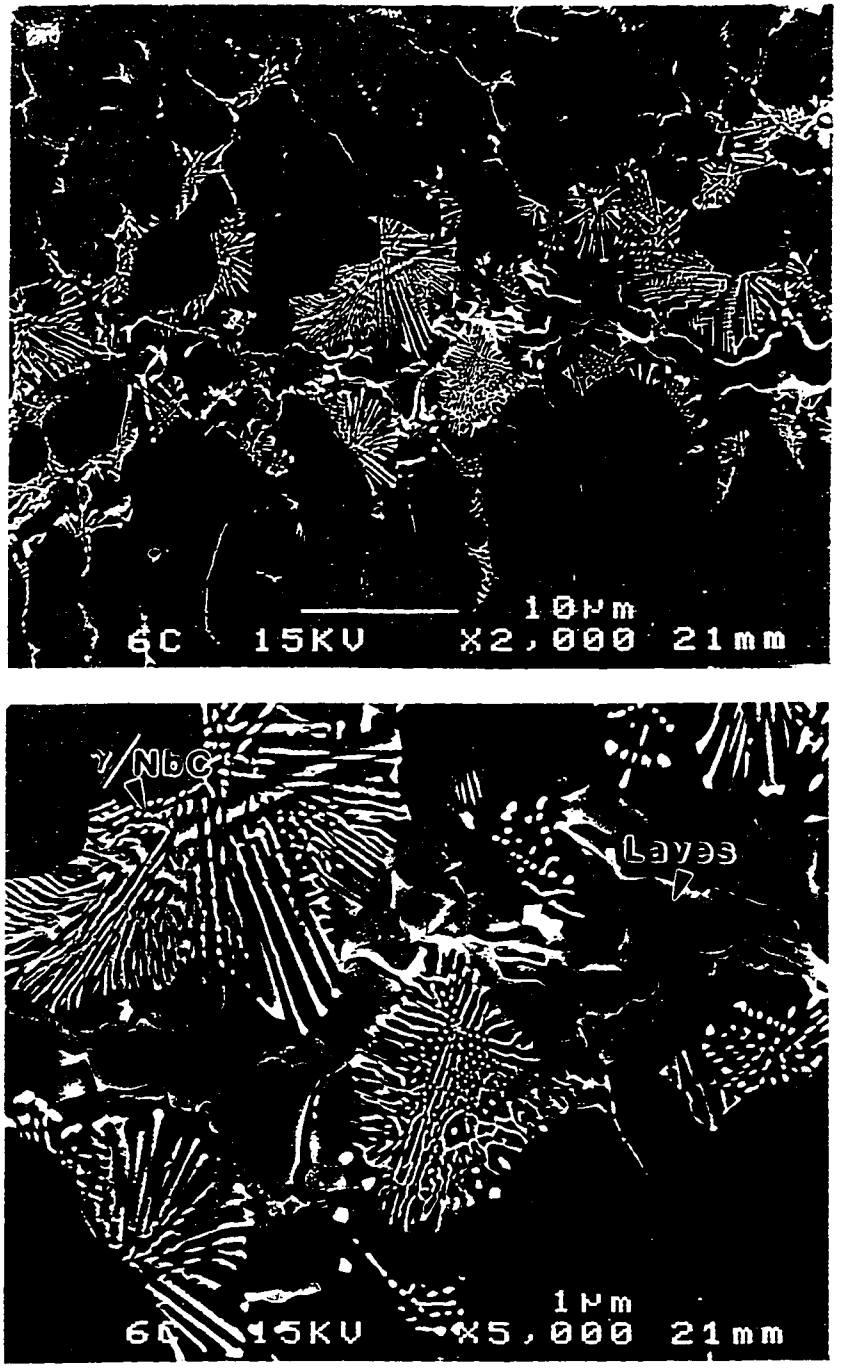

Figure 4.8. - continued - SEM photomicrographs of Alloy 6 varestraint sample.

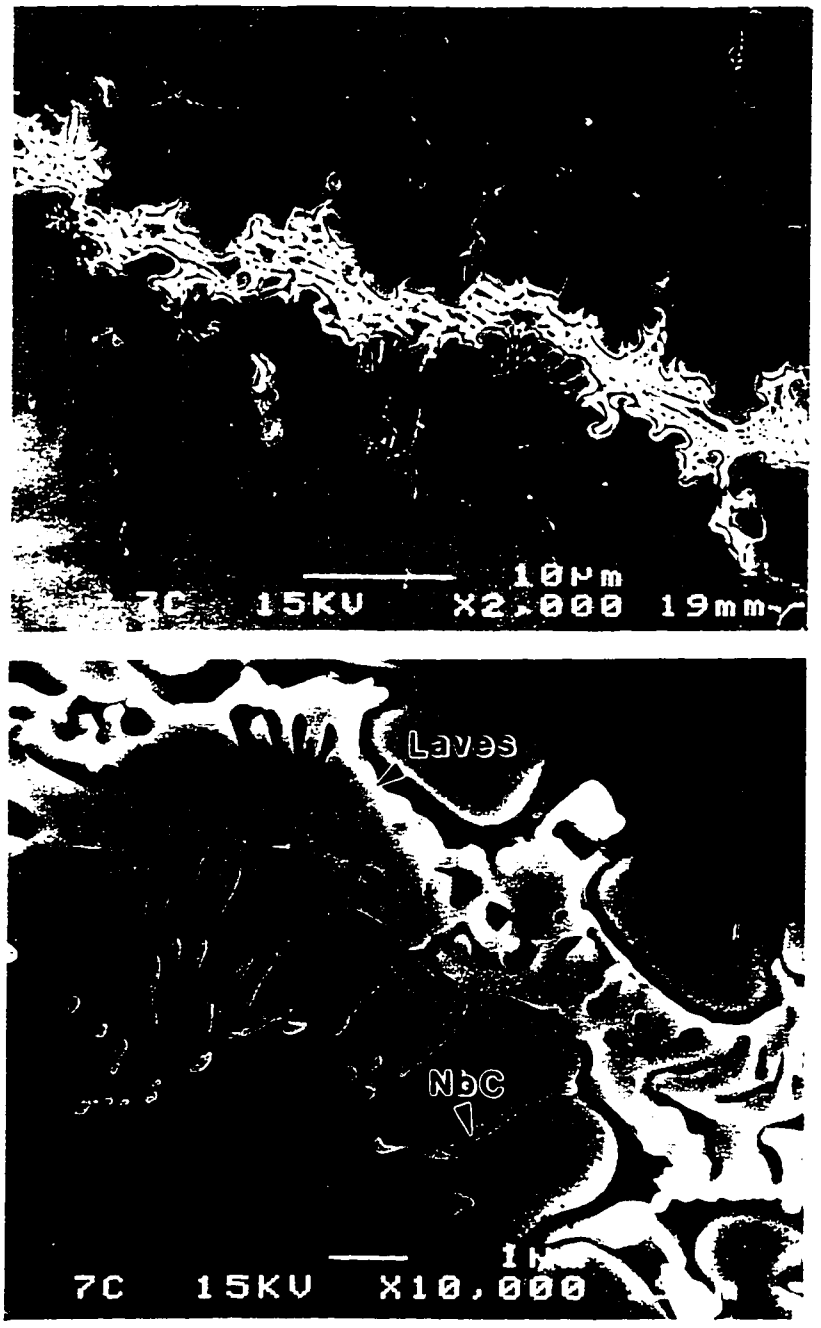

Figure 4.9. SEM photomicrographs of Alloy 7 varestraint sample.

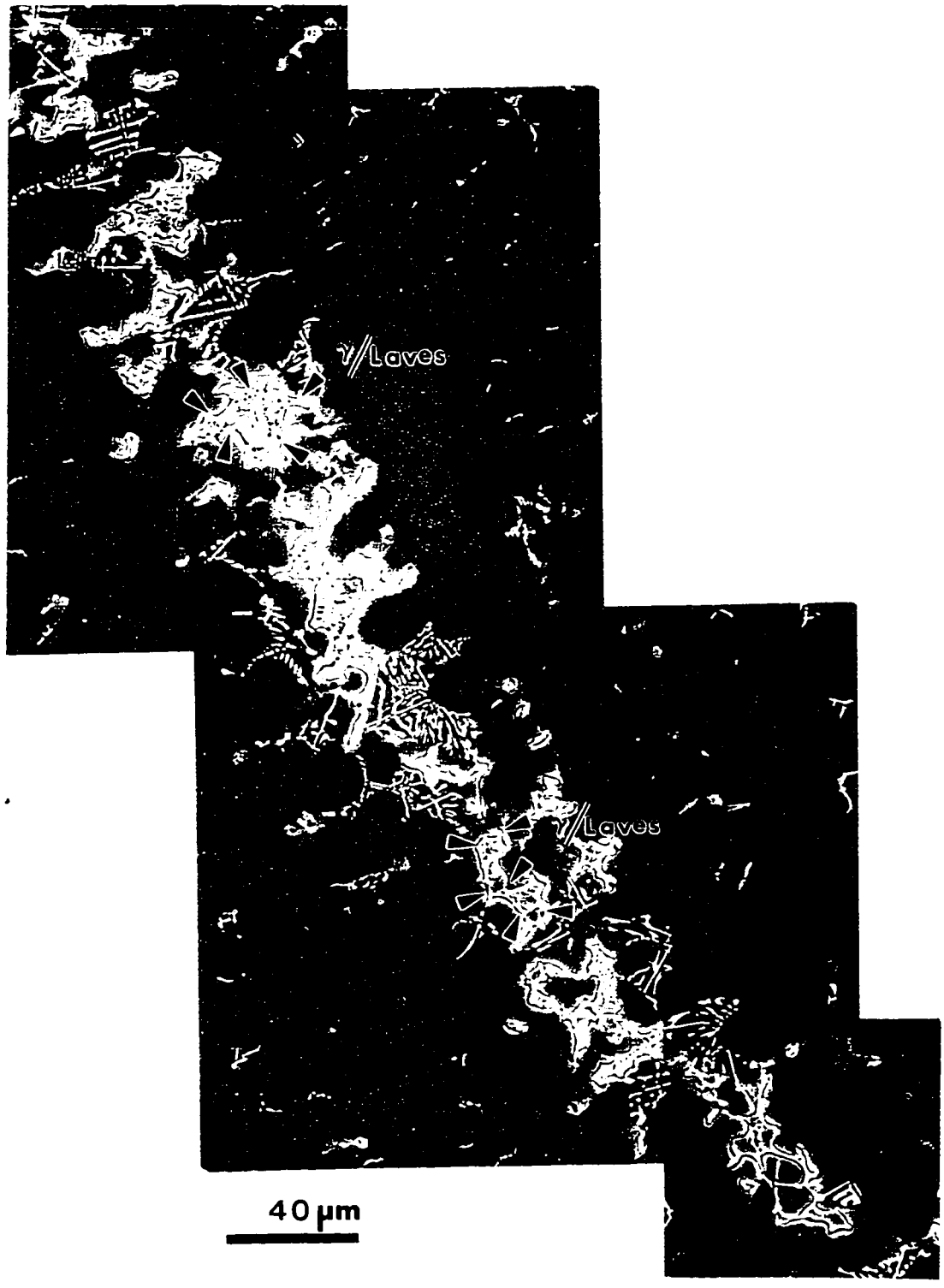

Figure 4.10. SEM photomicrographs of Alloy 7.5 varestraint sample.

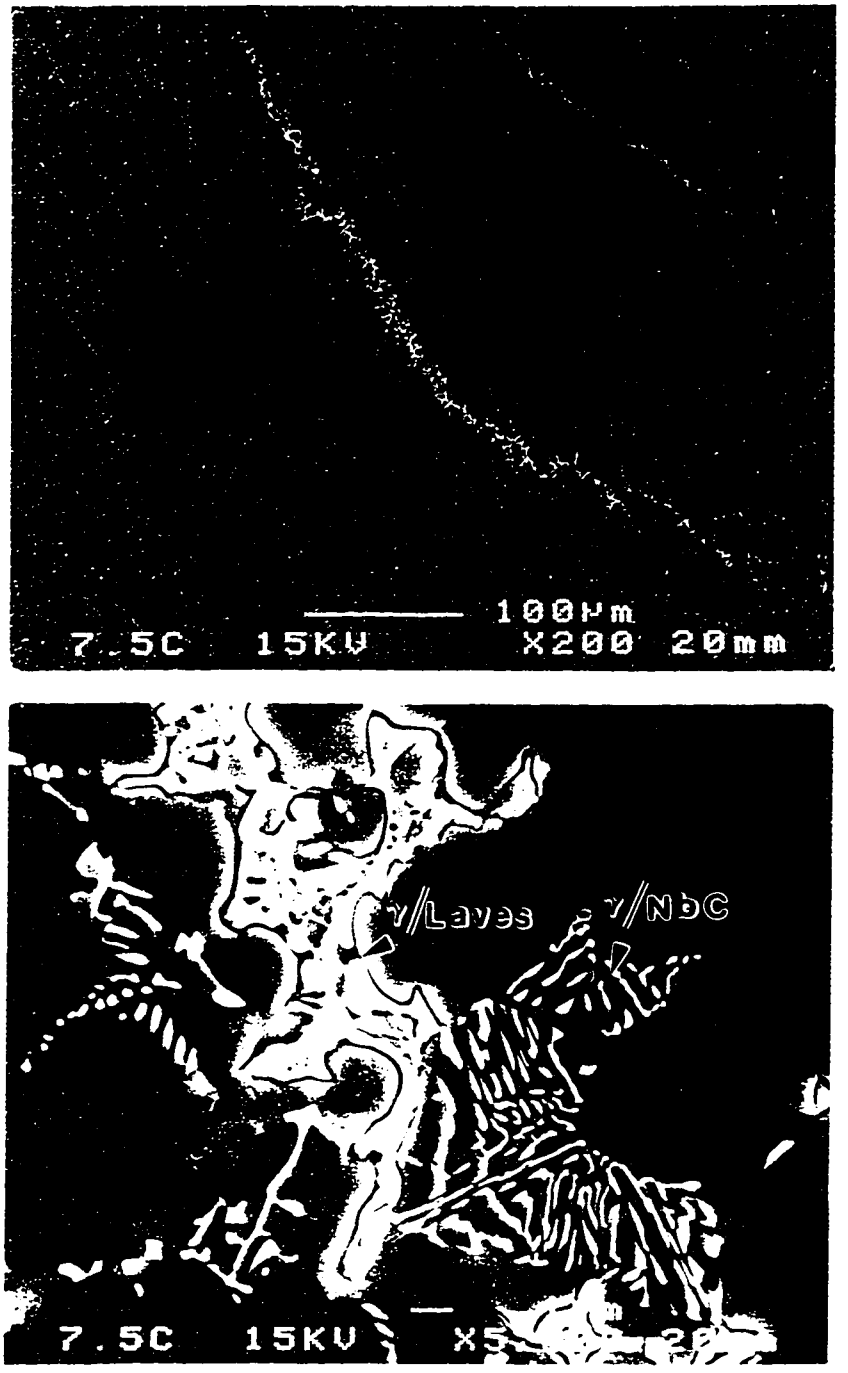

Figure 4.10. - continued - SEM photomicrographs of Alloy 7.5 varestraint sample.

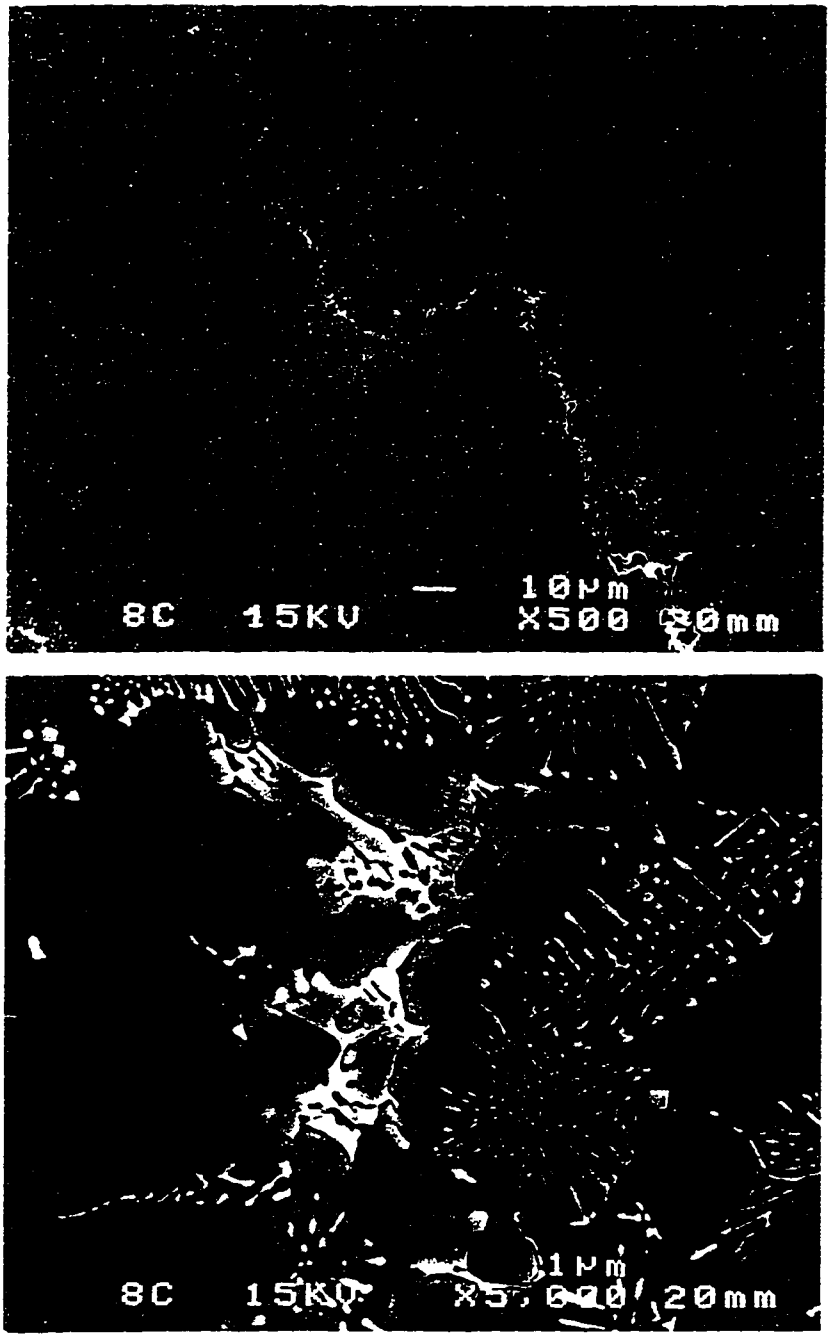

Figure 4.11. SEM photomicrographs of Alloy 8 varestraint sample.

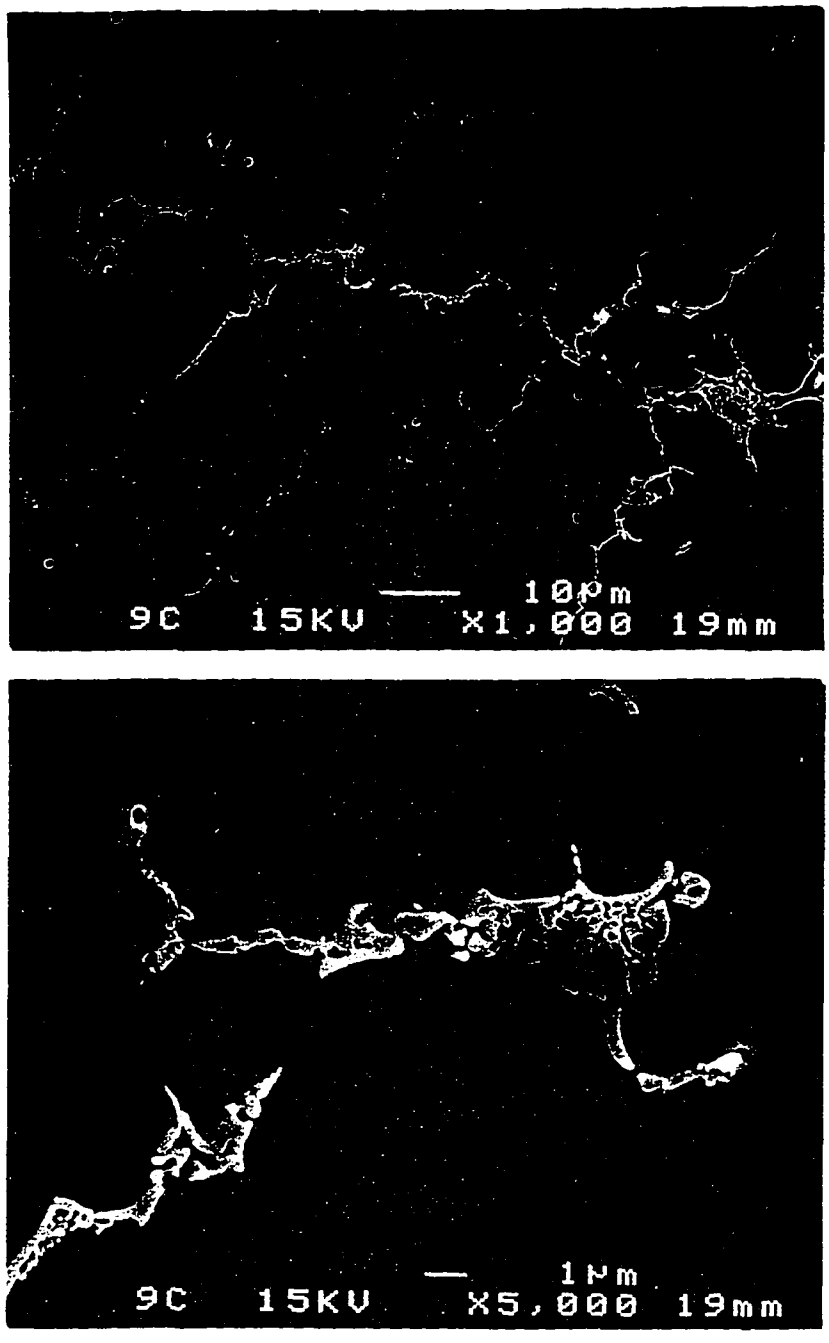

Figure 4.12. SEM photomicrographs of Alloy 9 varestraint sample.

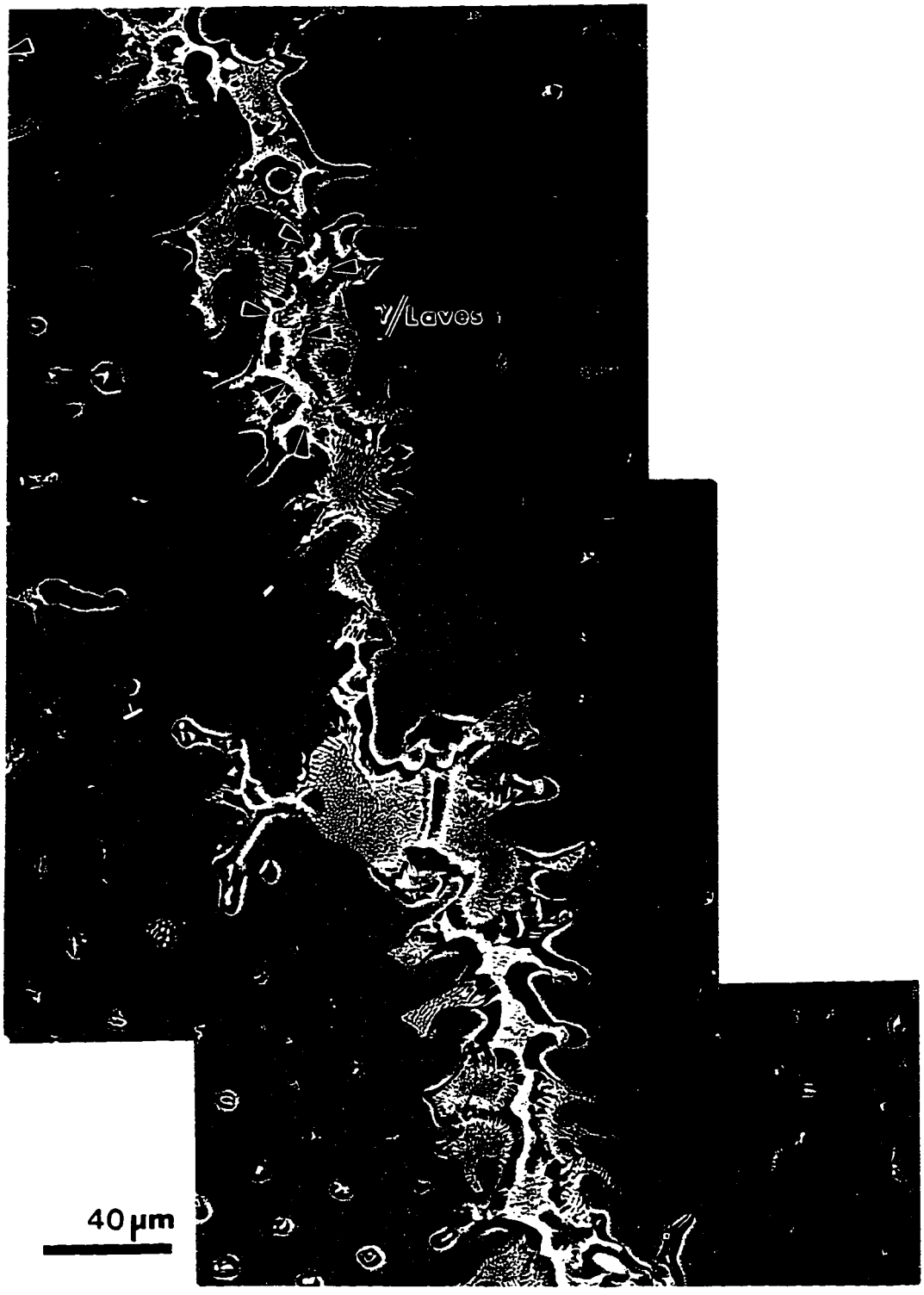

Figure 4.13. SEM photomicrographs of Alloy 10 varestraint sample.

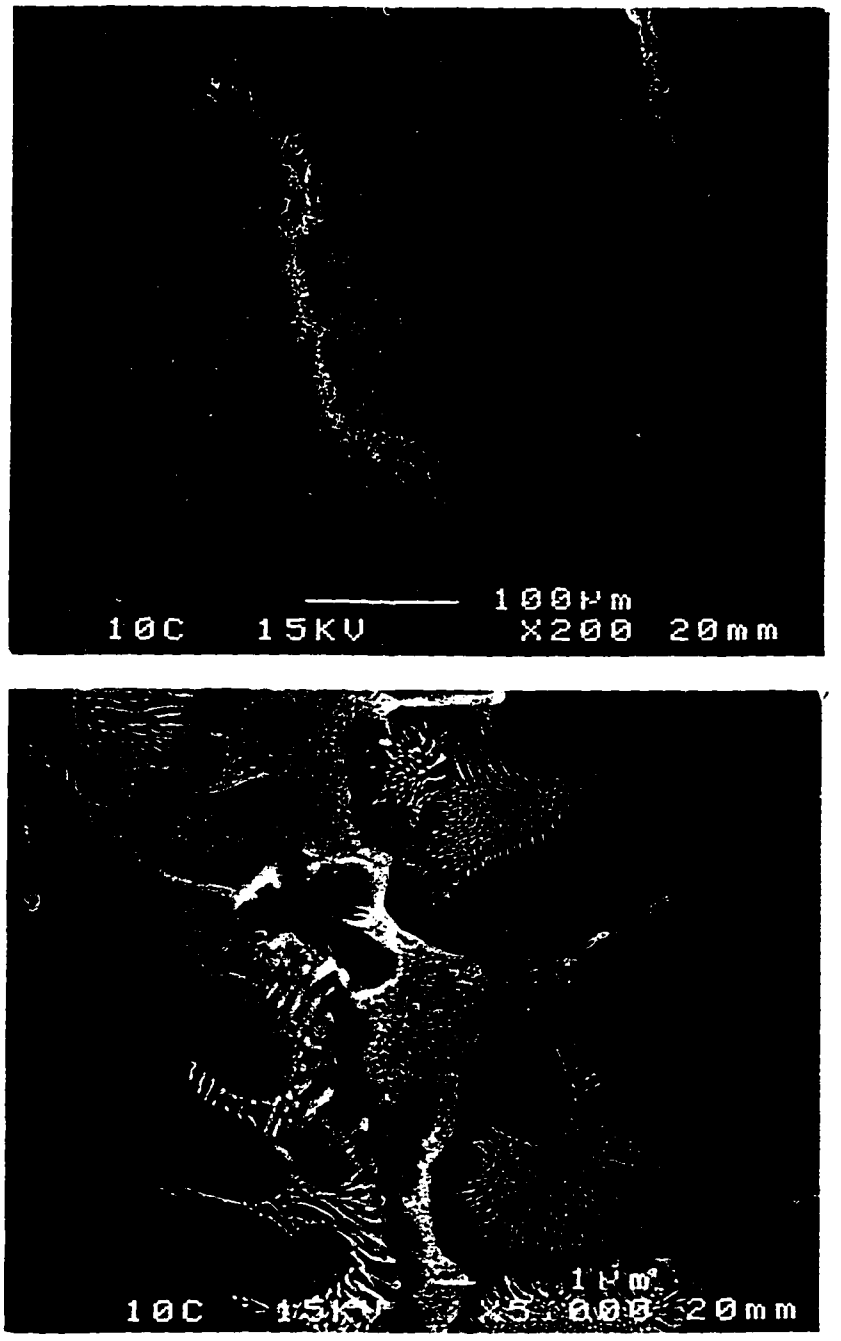

Figure 4.13. - continued - SEM photomicrographs of Alloy 10 varestraint sample.

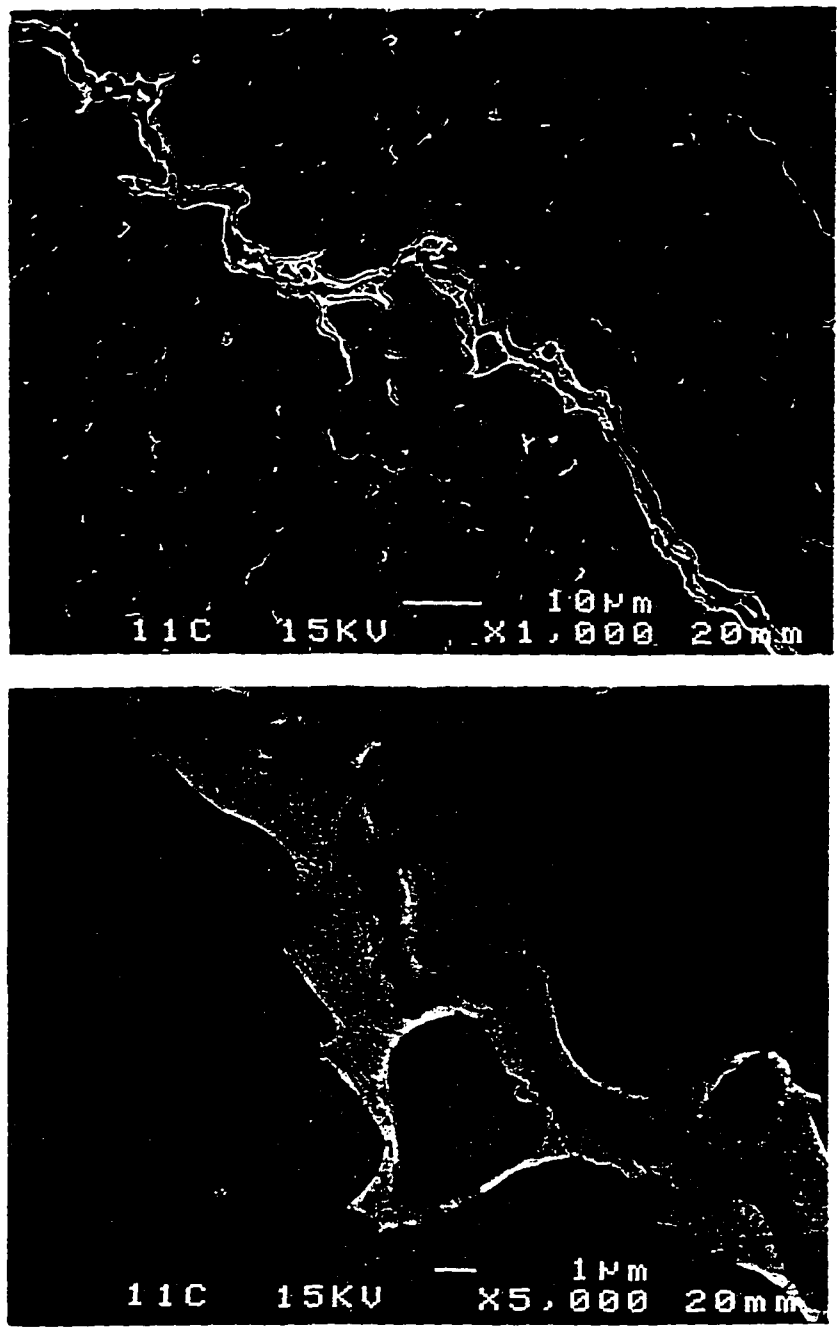

Figure 4.14. SEM photomicrographs of Alloy 11 varestraint sample.

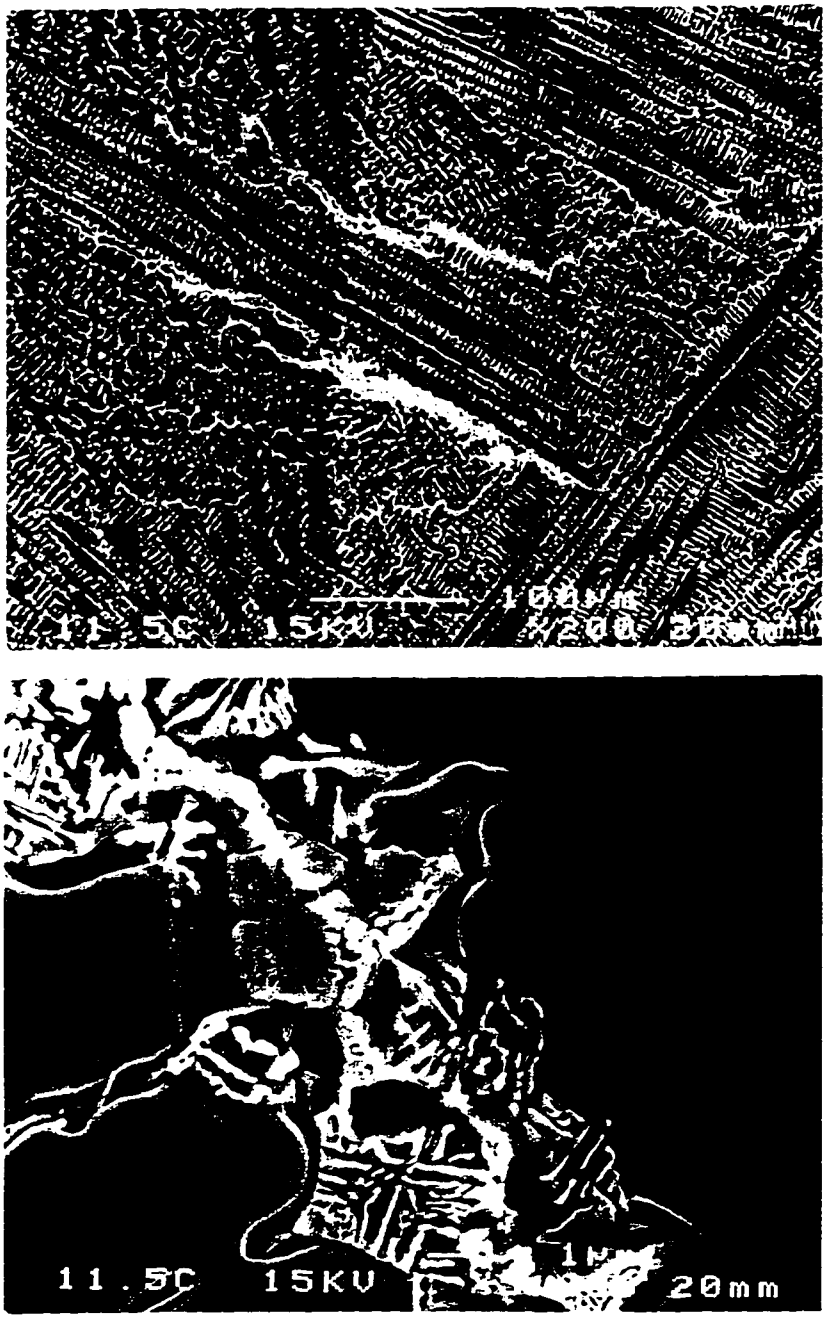

Figure 4.15. SEM photomicrographs of Alloy 11.5 varestraint sample.

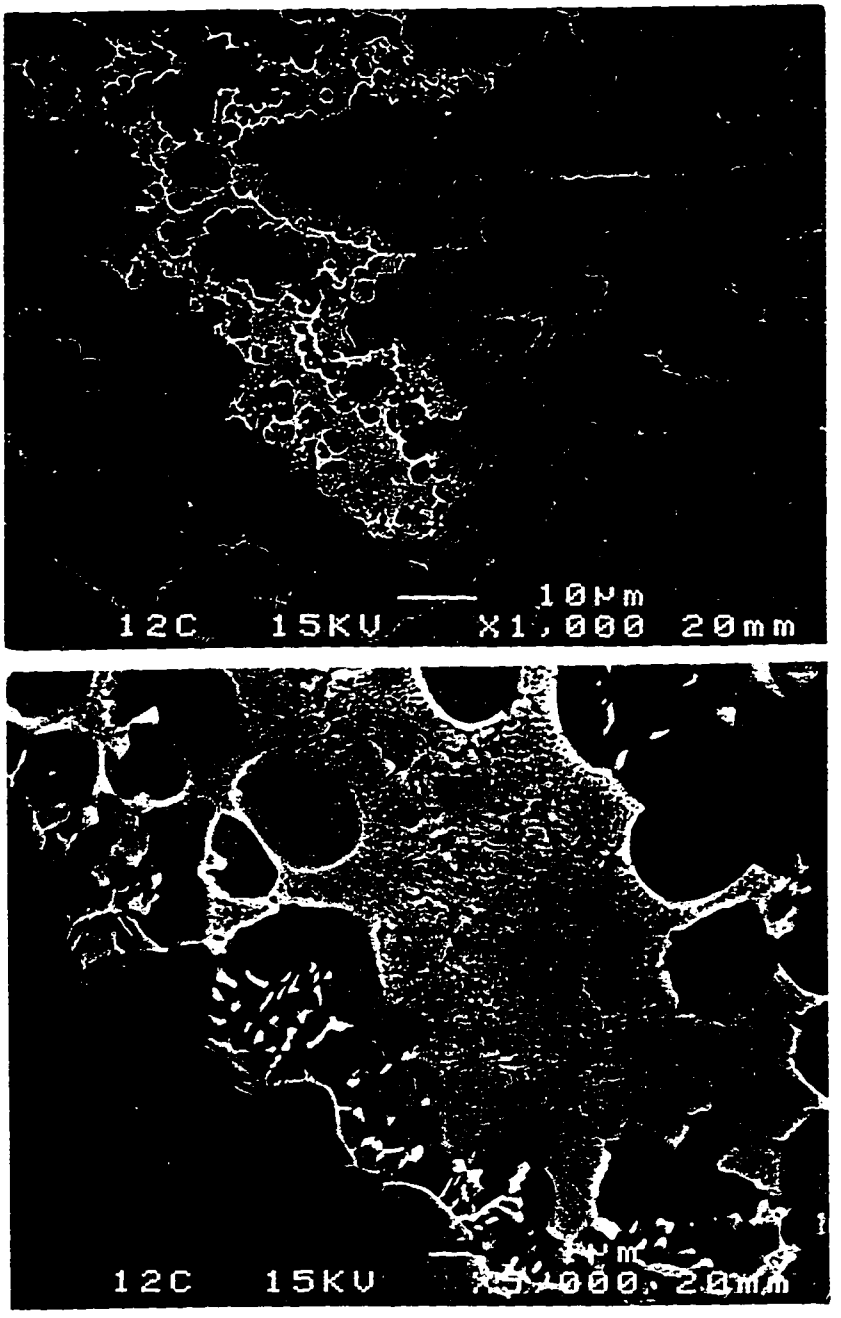

Figure 4.16. SEM photomicrographs of Alloy 12 varestraint sample.

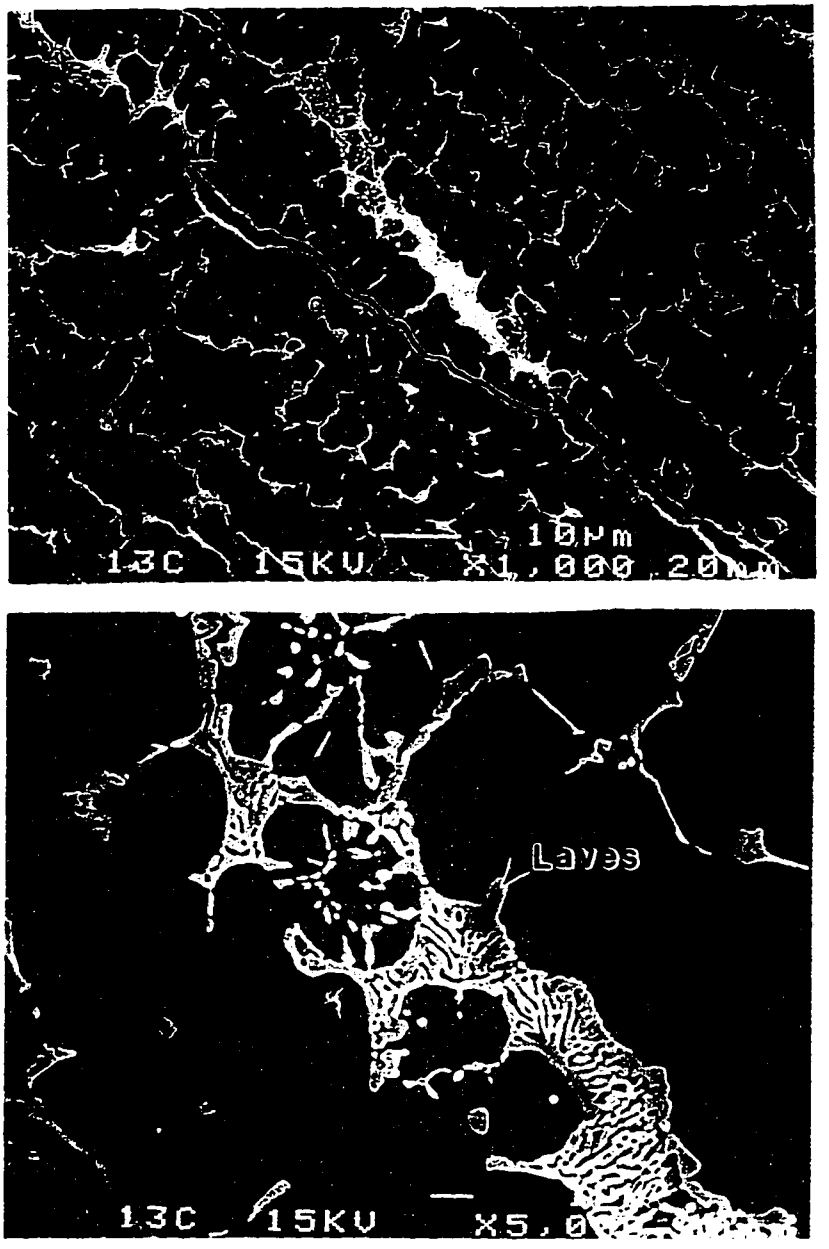

Figure 4.17. SEM photomicrographs of Alloy 13 varestraint sample.

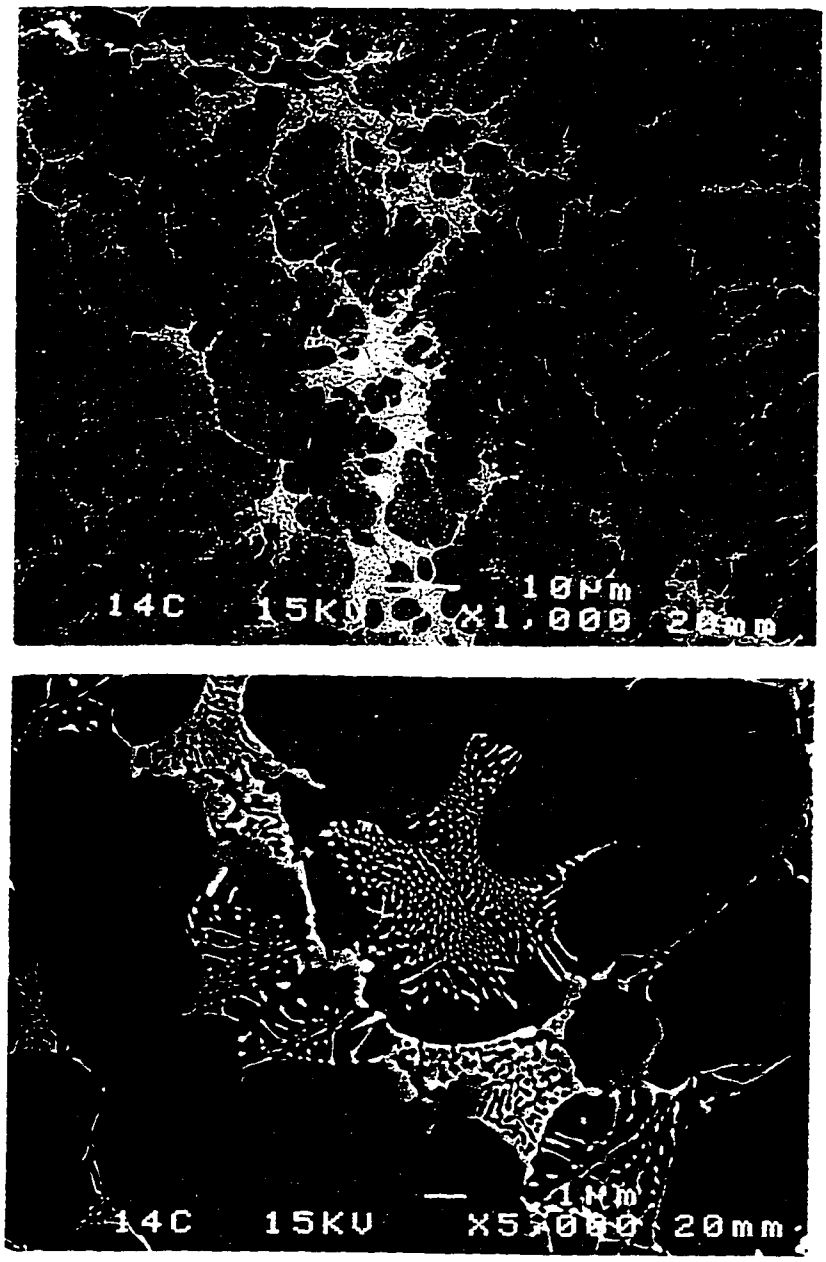

Figure 4.18. SEM photomicrographs of Alloy 14 varestraint sample.

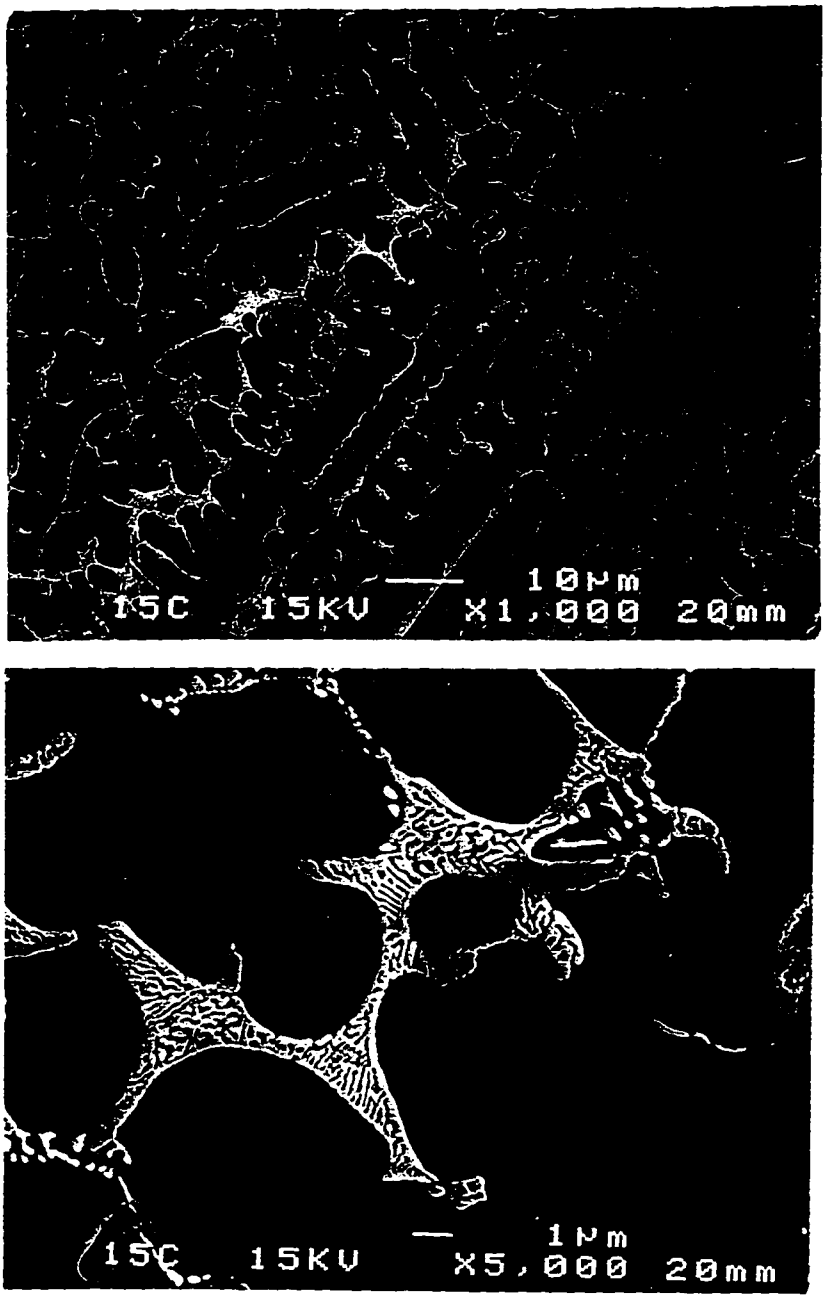

Figure 4.19. SEM photomicrographs of Alloy 15 varestraint sample.

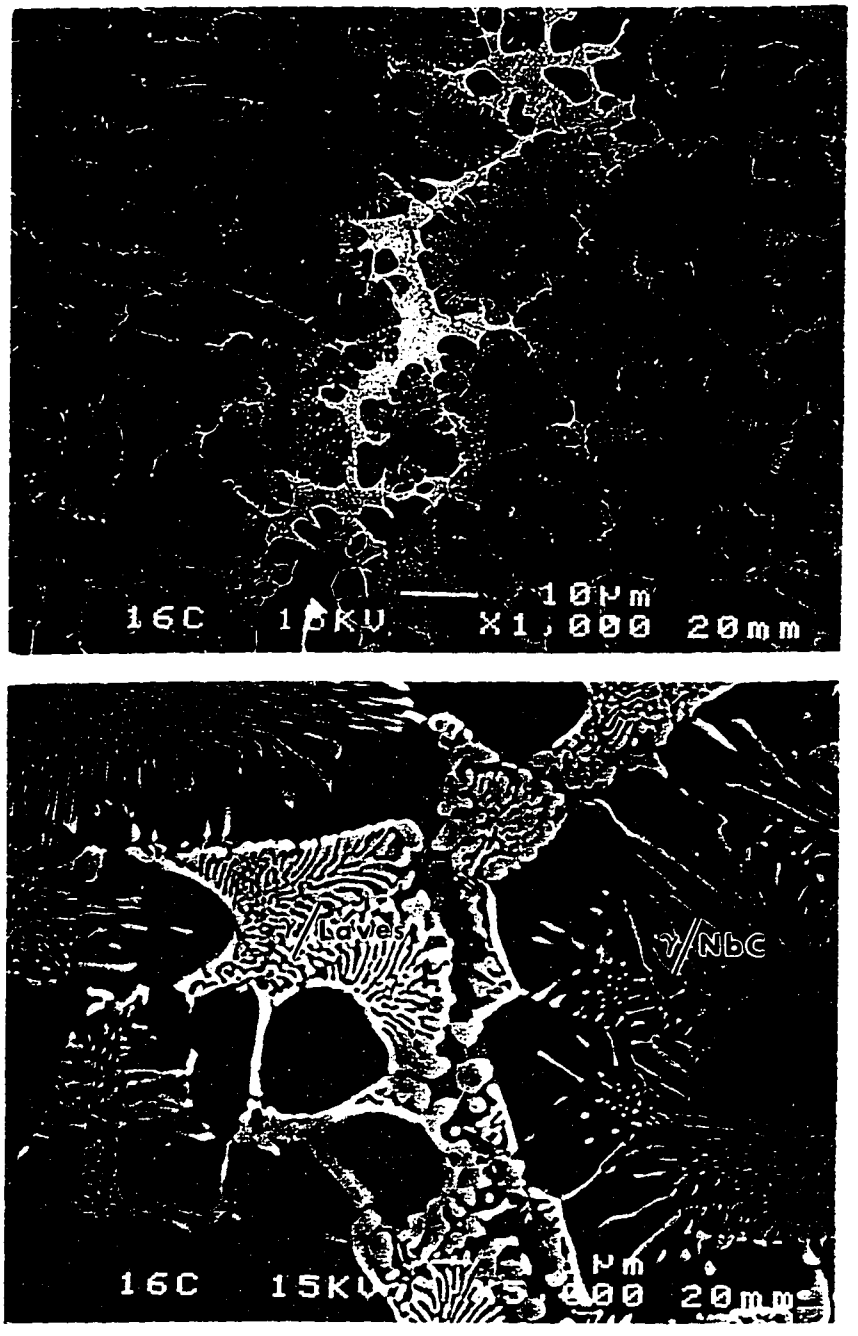

Figure 4.20. SEM photomicrographs of Alloy 16 varestraint sample.

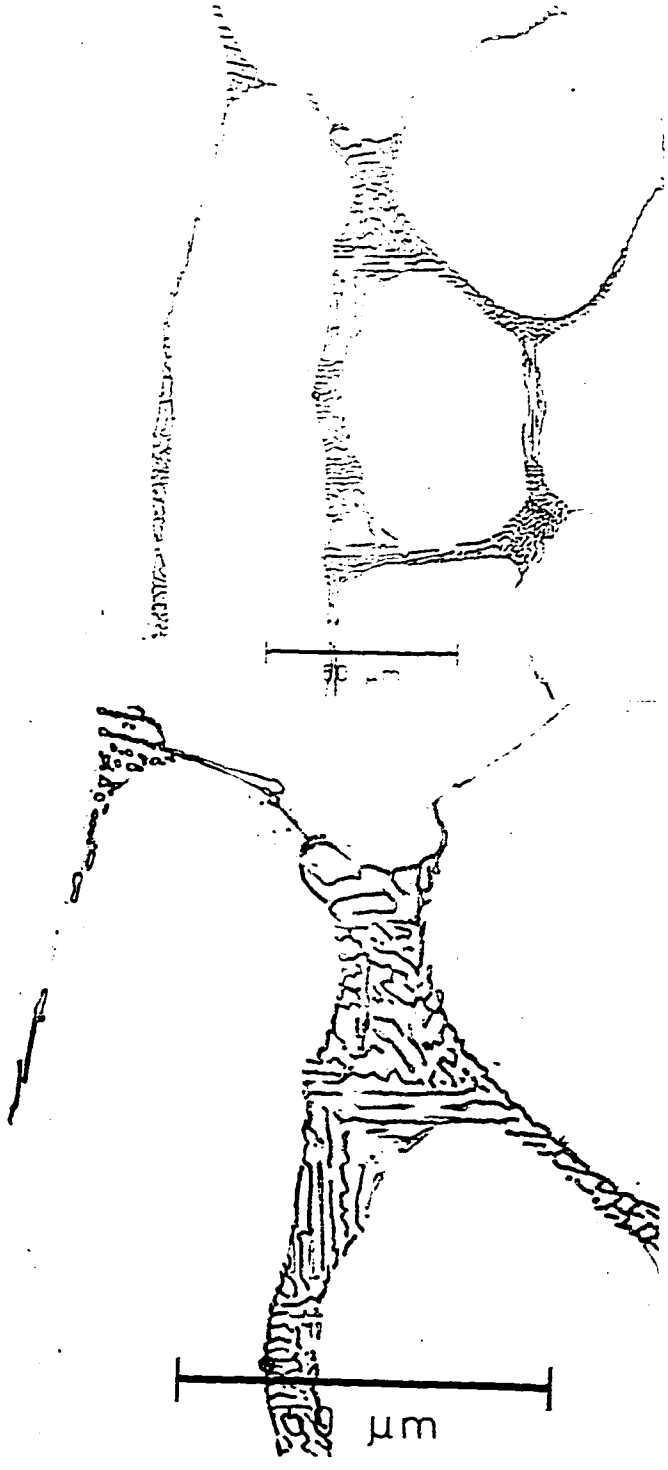

Figure 4.21. LOM photomicrographs of Alloy 2 DTA sample.

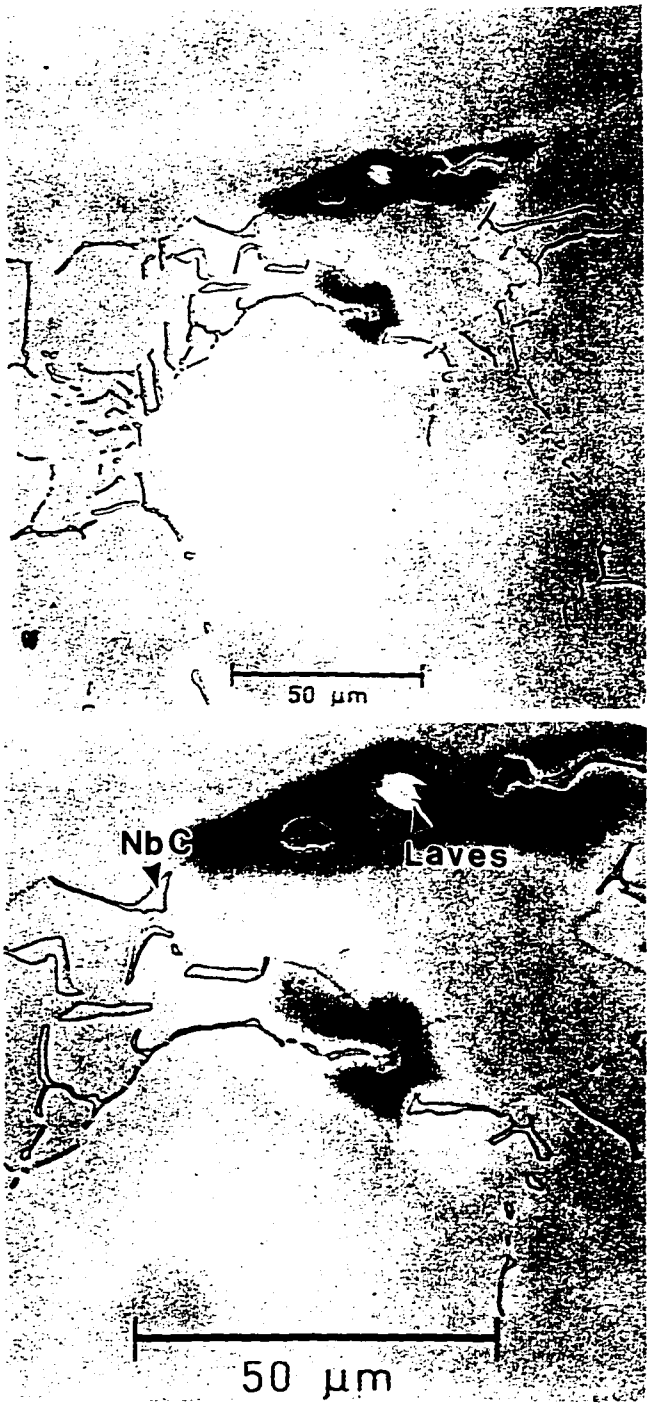

Figure 4.22. LOM photomicrographs of Alloy 6 DTA sample.

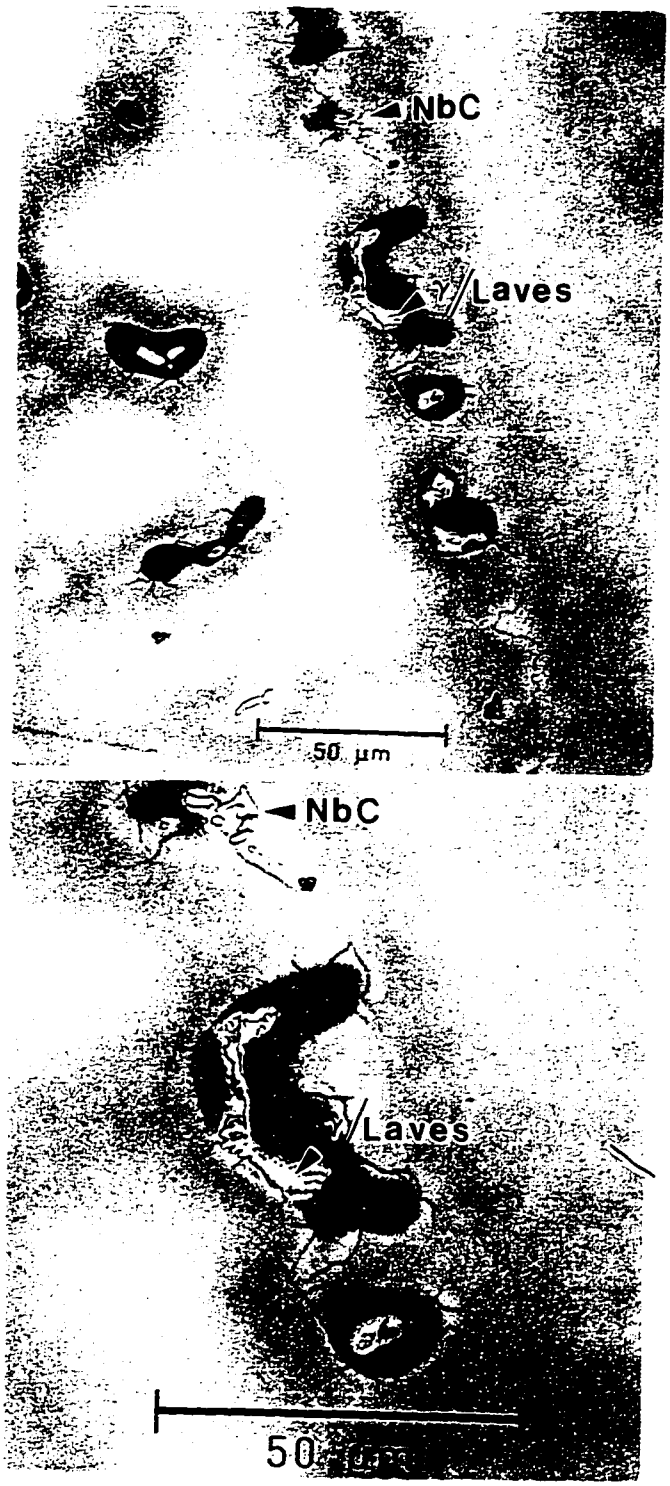

Figure 4.23. LOM photomicrographs of Alloy 7 DTA sample.

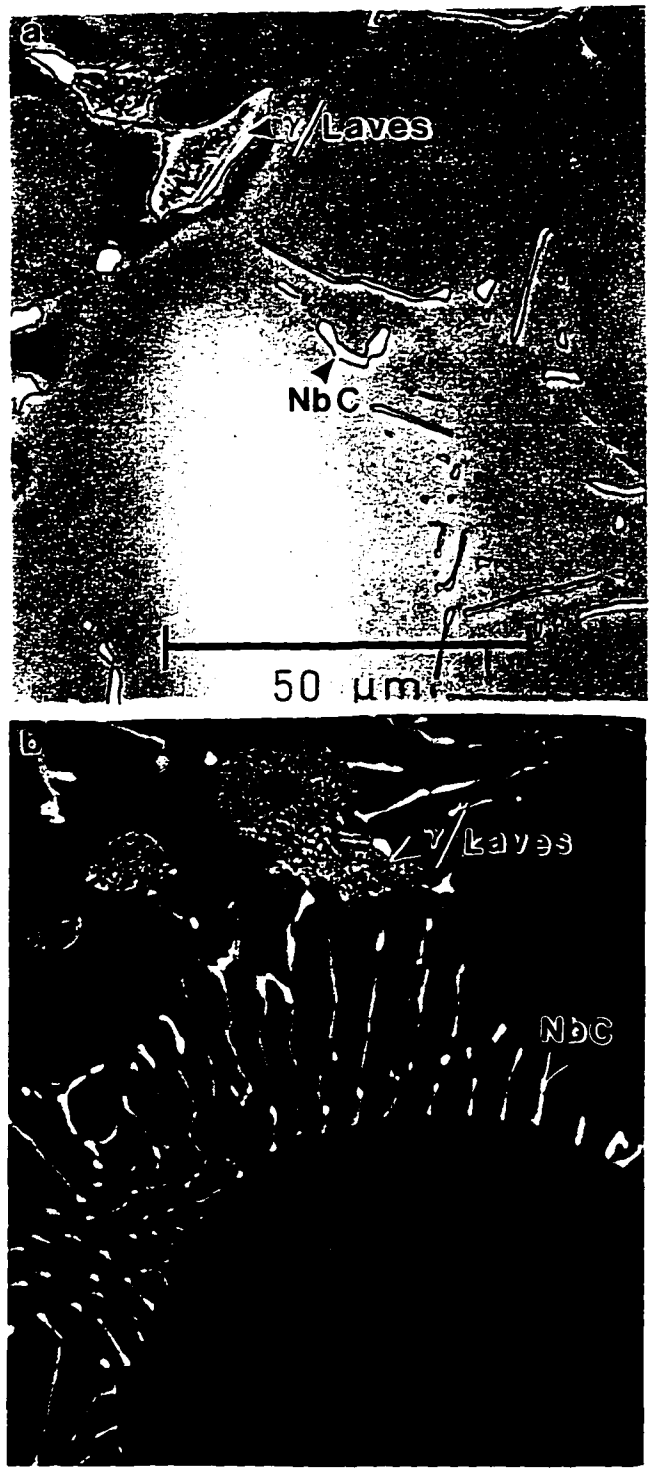

Figure 4.24. LOM (a) and BSE (b) photomicrographs of Alloy 8 DTA sample.

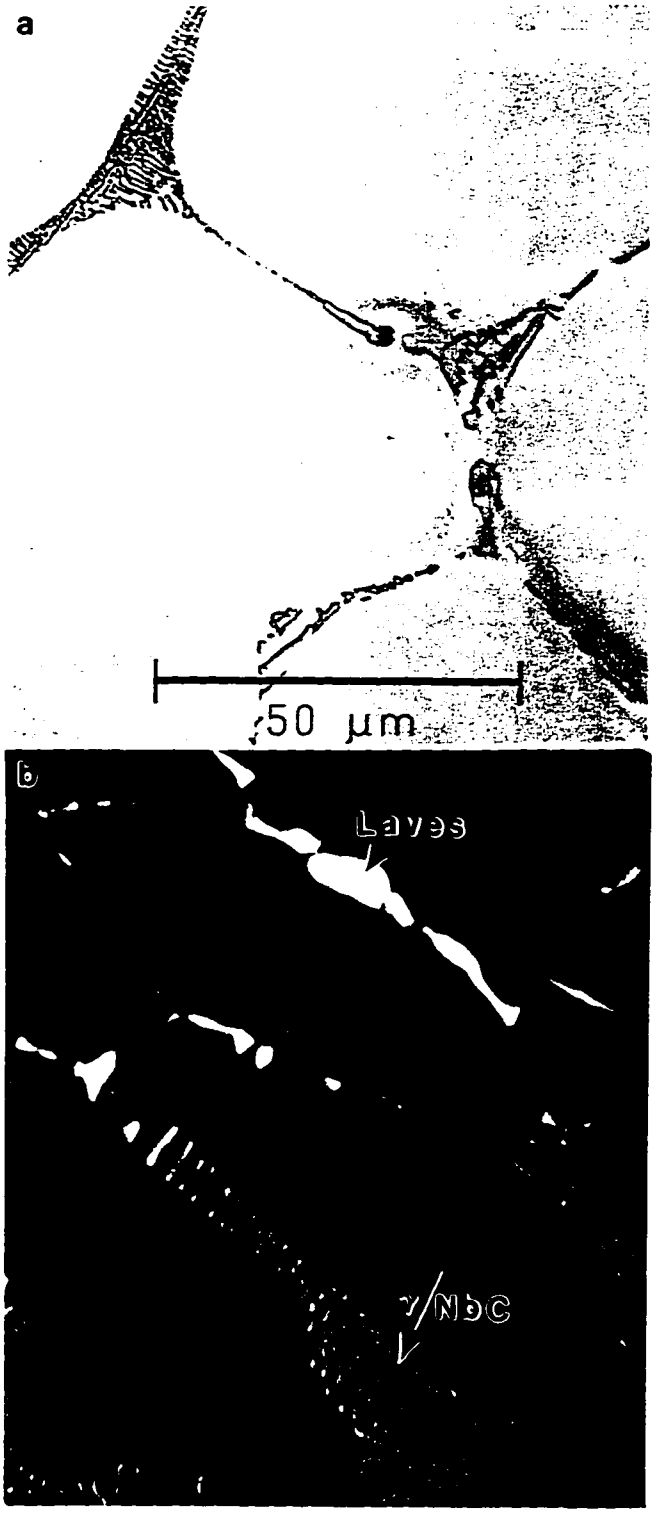

Figure 4.25. LOM (a) and BSE (b) photomicrographs of Alloy 12 DTA sample.

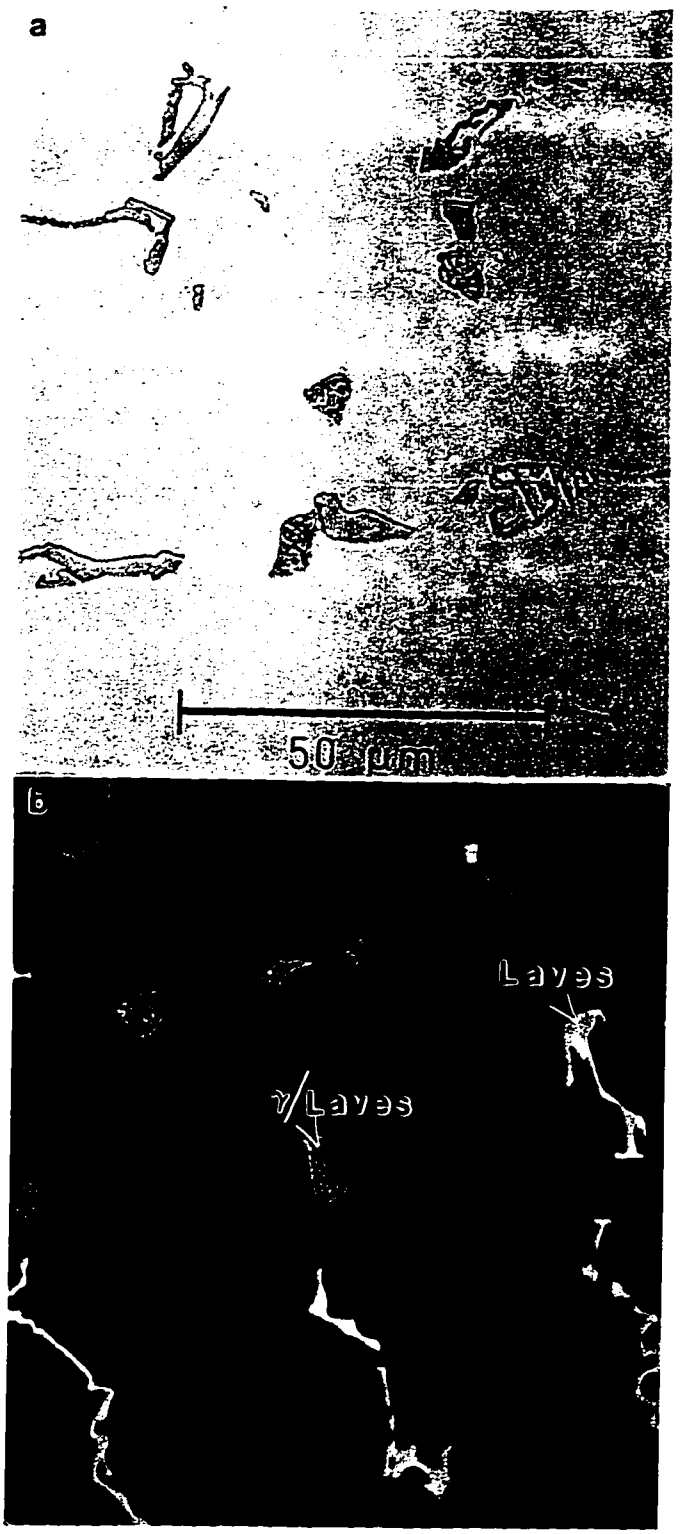

Figure 4.26. LOM (a) and BSE (b) photomicrographs of Alloy 13 DTA sample.

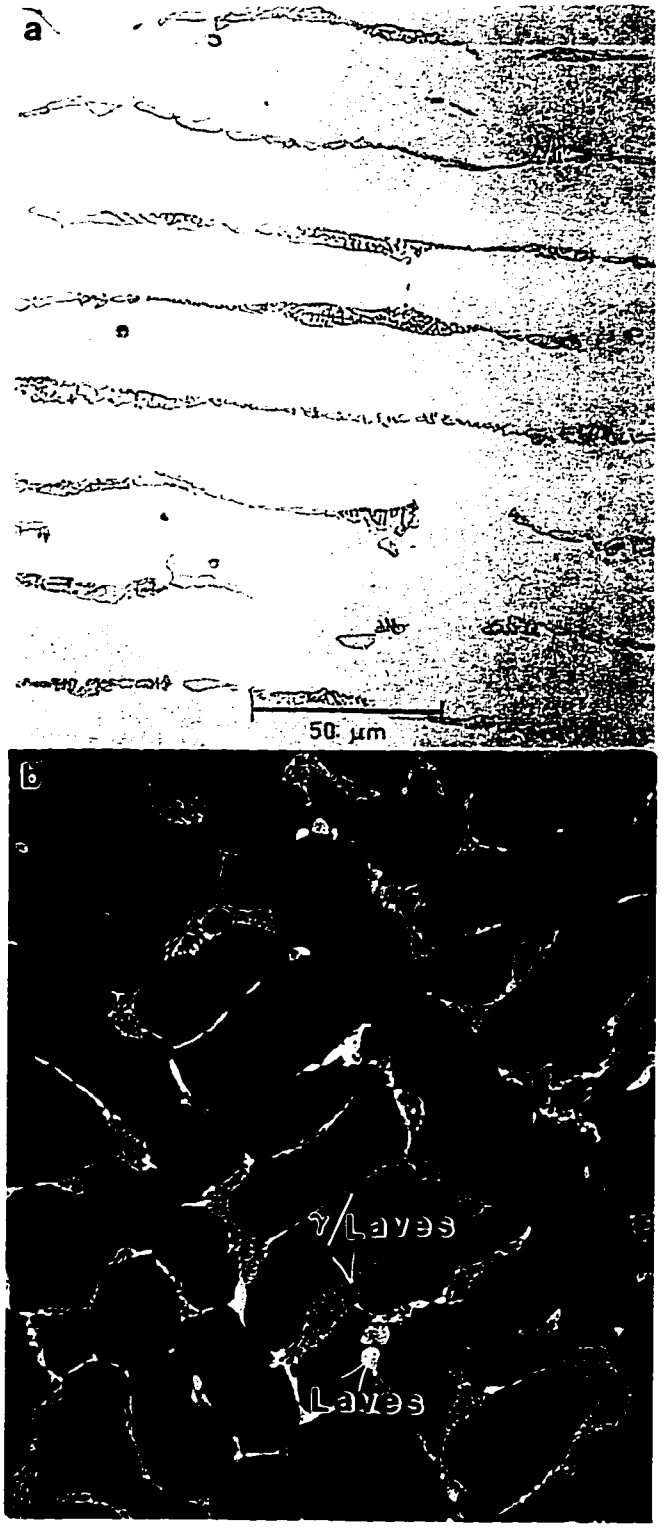

Figure 4.27. LOM (a) and BSE (b) photomicrographs of Alloy 15 DTA sample.

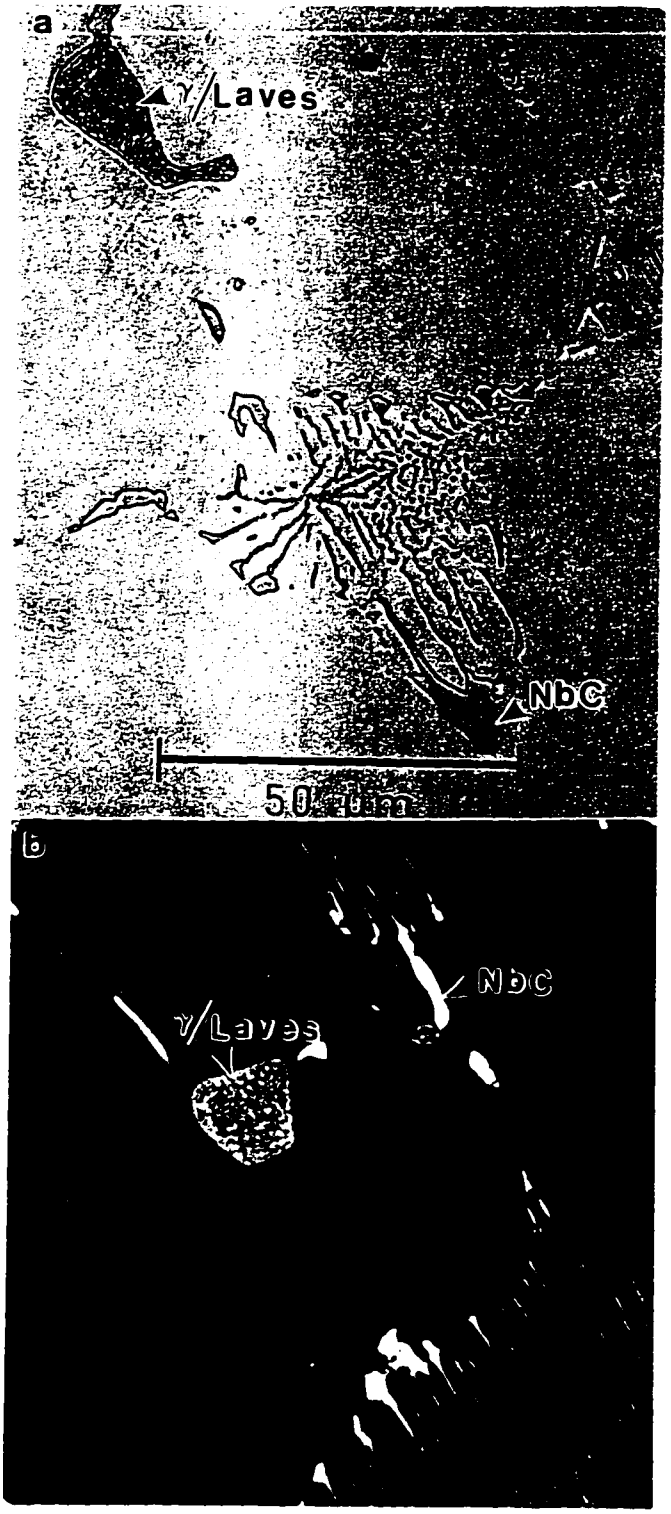

Figure 4.28. LOM (a) and BSE (b) photomicrographs of Alloy 16 DTA sample.

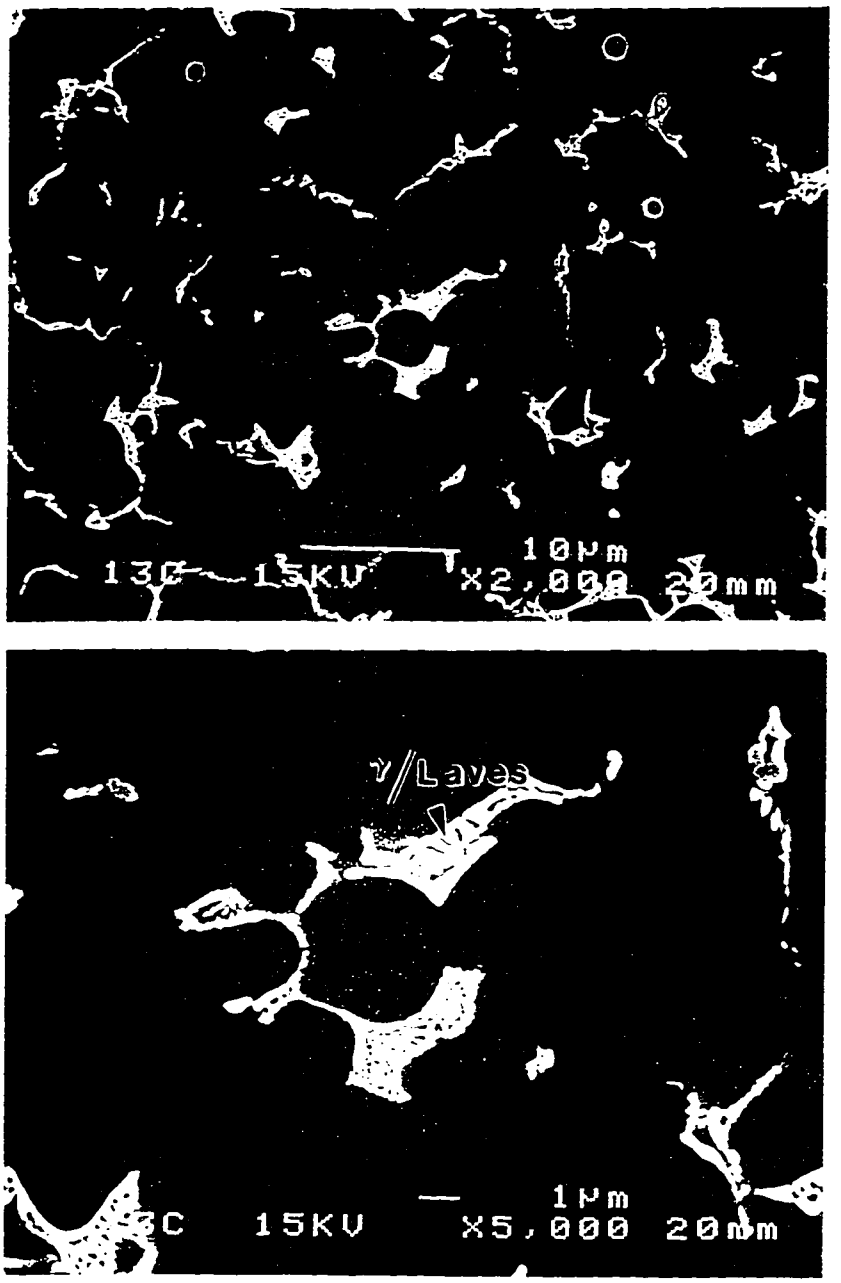

Figure 4.29. SEM photomicrographs of Alloy 13 weld metal microstructure.

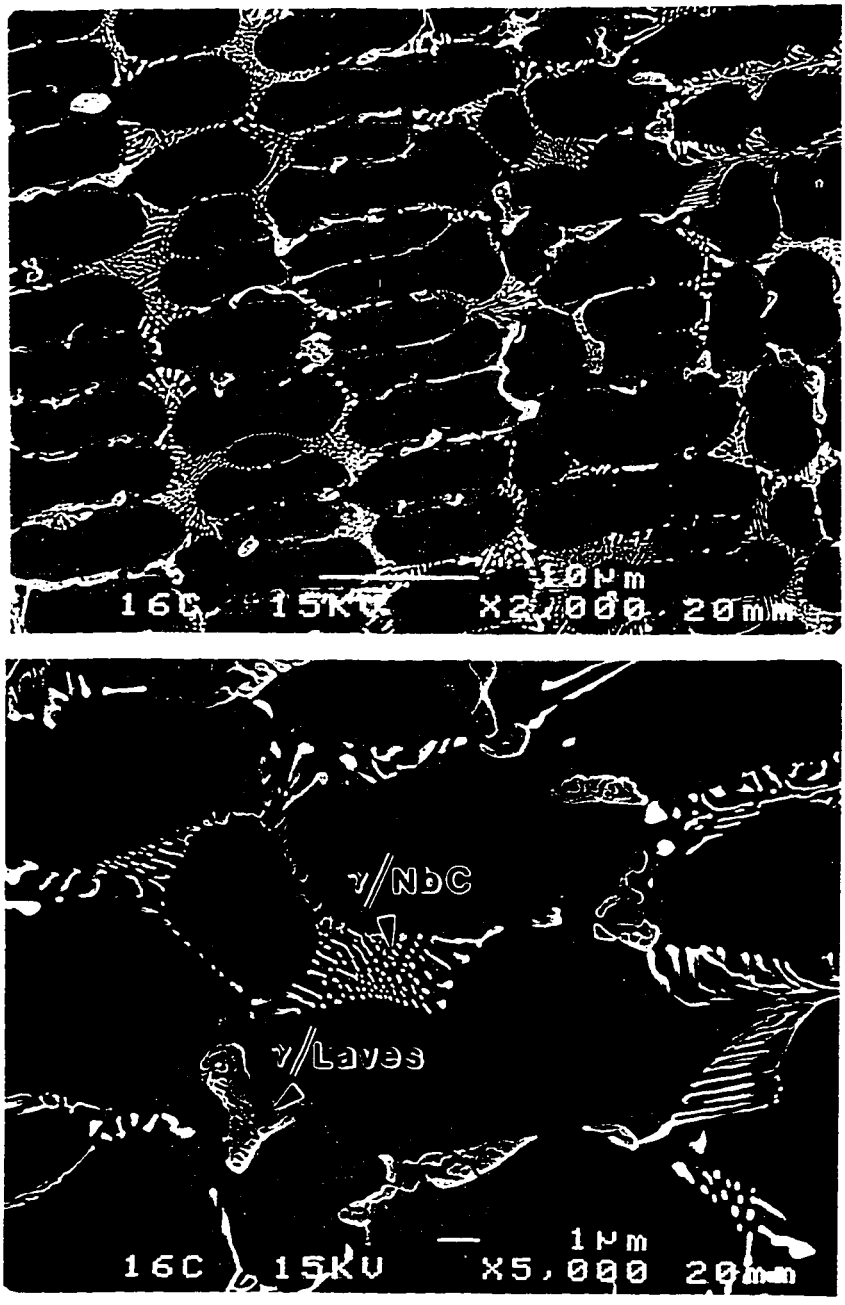

Figure 4.30. SEM photomicrographs of Alloy 16 weld metal microstructure.

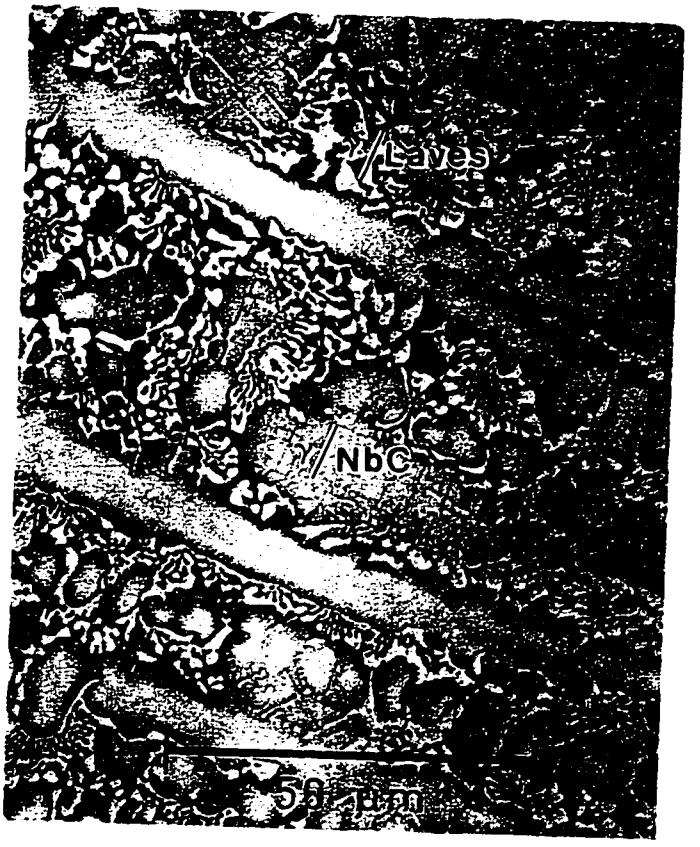

Figure 4.31. LOM photomicrograph of Alloy Ni-1.

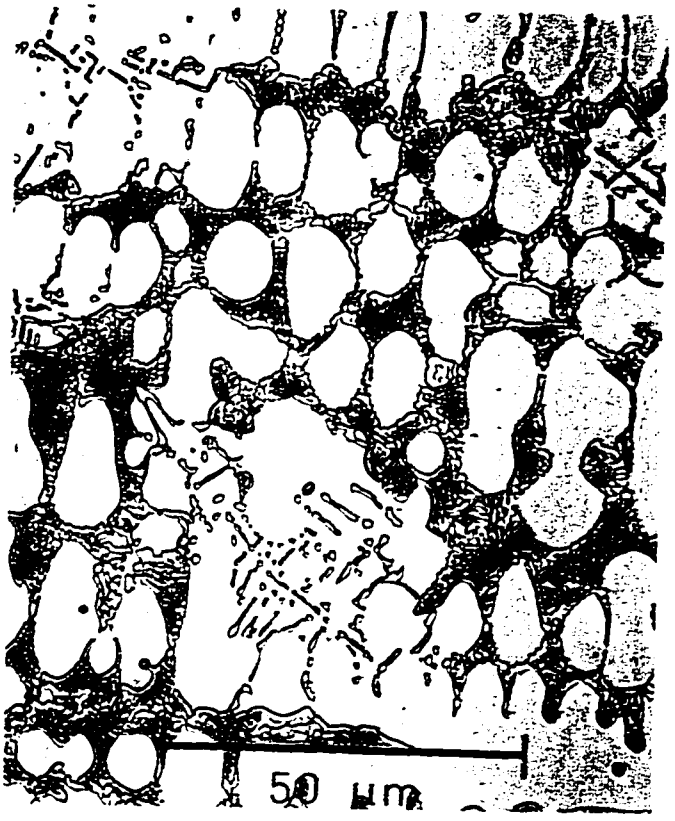

Figure 4.32. LOM photomicrograph of Alloy Fe-1.

Table 4.1 Compositions of NbC in DTA samples (metal elements only). All values in weight percent.

Alloy	Fe	Ni	Cr	Nb
3.5	0.5 ± 0.1	3.3 ± 0.1	1.8 ± 0.1	83.6 ± 0.8
6	0.4 ± 0.1	2.9 ± 0.3	1.1 ± 0.2	87.5 ± 2.0
8	0.5 ± 0.1	3.0 ± 0.7	1.3 ± 0.5	86.9 ± 1.5
9	1.3 ± 0.1	1.1 ± 0.1	1.7 ± 0.4	87.7 ± 0.4
10	3.9	1.0	2.1	87.4
14	1.8 ± 0.9	1.2 ± 0.6	1.1 ± 0.5	89.5 ± 0.3
16	1.2 ± 0.2	1.1 ± 0.2	0.9 ± 0.2	88.0 ± 0.5

Typical EPMA measurements on the other secondary phase (e.g., labelled "Laves" in Figures 4.25 through 4.27) are summarized in Table 4.2. Comparison is made to the Laves phase identified by EPMA and transmission electron microscopy in commercial superalloys by other investigators [4.2, 4.3]. The Nb content of this phase varies between 29.1 and 36.4 wt%, which is similar to the Nb content observed in the Laves phase of commercial alloys of 29.0 to 34.1 wt% Nb. Backscattered electron kikuchi patterns from the Laves phases labelled in Figures 4.8 (Alloy 6) and 4.17 (Alloy 13) revealed a hexagonal crystal structure, which is also consistent with the Laves phase. This phase is typically surrounded by a dark halo after etching which can assist in identification.

Table 4.2 Composition of Laves phase identified in DTA and GTA melt alloys. All values in weight percent.

Alloy	Fe	Ni	Cr	Nb	Si	Co	Mo	Ti
5	2.8 (0.3)	63.1 (0.4)	4.9 (1.0)	29.1 (1.3)	0.1 (0.1)	--	--	--
Ni-1	5.5 (0.2)	46.5 (1.0)	12.6 (0.1)	33.7 (1.2)	1.7 (0.2)	--	--	--
13	25.9 (1.5)	25.3 (0.8)	11.1 (0.1)	35.7 (1.1)	0.5 (0.1)	--	--	--
14	25.5 (1.5)	26.0 (0.4)	12.2 (1.2)	36.0 (0.3)	0.7 (0.1)	--	--	--
15	26.5 (0.9)	24.1 (1.5)	11.3 (0.1)	36.4 (0.4)	1.8 (0.2)	--	--	--
16	23.9 (0.4)	26.1 (0.6)	11.5 (0.2)	36.0 (0.2)	2.6 (0.1)	--	--	--
Fe-1	25.5	23.9	12.5	36.1	2.0	--	--	--
T-Span [4.2]	18.1	18.4	2.4	34.1	1.1	25.7	--	1.5
IN909 [4.3]	20.2	30.5	--	33.0	2.2	11.2	--	2.1
IN718 [4.3]	10.6	39.4	11.2	29.0	1.7	--	7.5	0.8

The morphology of the NbC and Laves phases generally depends on the amount of each phase (which, in turn, is a function of composition) and the cooling rate. In the high C alloys (even-numbered alloys), the NbC always exists as a well defined eutectic-type morphology with the austenite matrix in the both the DTA and weld metal microstructures. At low C contents, the DTA samples typically exhibit the NbC as isolated particles (e.g., Alloy 7 DTA sample - Figure 4.23) while, in the higher cooling rate welds, the NbC can form in the lamellar arrangement with the austenite matrix (e.g.,

Alloy 7 varestraint sample - Figure 4.9). The γ/NbC eutectic-type morphology can also be observed in the varestraint samples of Alloy 1.5, 3, 3.5, and 7.5. It is important to note that the NbC phase was observed in all of the alloys used in this study. Alloy 1 presents the only possible exception to this, where the isolated particles observed in both the varestraint and DTA samples were too small to analyze by EPMA.

The Laves shows somewhat similar behavior. When present in very low quantities, the Laves forms as isolated particles in both the DTA and weld metals (e.g., Alloy 6 - Figures 4.8 and 4.22). At higher volume fractions, the Laves is observed in a eutectic-type morphology in the Ni base DTA and weld metal microstructures (e.g., Alloys 7 and 8). The Fe base DTA samples show unusual behavior, where the Laves is present in both the isolated and eutectic-type morphologies within the same sample (e.g., Figure 4.26). EPMA measurements of these eutectic-type structures in the DTA samples, presented later, confirmed they are indeed the γ/Laves constituent. The Laves phase was present in all the Fe base alloys. For the Ni base alloys, no Laves was observed in Alloys 2, 3.5, or 4 during microstructural examination or EPMA analysis. Confident assessments for Laves could not be made for Alloys 1 and 1.5, but the small particles (labelled by arrowheads in Figure 4.2) in Alloy 1.5 may be Laves. The remaining Ni base alloys (3, 5, 6, 7, 7.5, and 8) all exhibited the Laves phase. The type of secondary phases observed in each alloy is summarized in Table 4.3.

The total volume percentages of eutectic type constituents (γ/NbC + γ/Laves) and individual volume percentages of each eutectic type constituent in the alloys are summarized in Table 4.3 and shown in graphical form in Figures 4.33 and 4.34. The

γ/Laves contents in Alloys 7.5, 8, and 11.5 were acquired from backscattered electron images of DTA samples where the γ/NbC and γ/Laves constituents could be distinguished. All other results were acquired from at least ten secondary electron SEM photomicrographs acquired along the centerline of welds prepared under the same processing parameters used during varestraint testing. It should be noted that, in the low Nb/low C alloys (Alloys 1, 1.5, 3, 3.5, 9, and 11), the secondary phases do not always form a well-defined lamellar structure with γ. Thus, only the NbC or Laves portion of the eutectic-type structure is often included in the measurement. As a result of this effect, the reported data for these alloys are expected to represent a lower bound to the actual total eutectic-type volume percentages. For total voulme percentage measurements, Fe and Ni base alloys with similar levels of Nb, Si, and C are matched for comparison. The results from individual constituent measurements (where such distinctions were possible) are aligned to make similar comparisons. Some of the comparisons should be considered semi-quantitative since, as noted in Figure 4.34, NbC and Laves phases were present at levels too low for individual quantification in some of the alloys.

Table 4.3. Phase identification summary and quantitative image analysis results.

Alloy	Phases Present	Total Eutectic-Type Constituent (Volume Percent)	γ/NbC (Volume Percent)	γ/Laves (Volume Percent)
1	?	0.8 ± 0.2	---	---
1.5	NbC [1]	1.6 ± 0.4	---	---
2	NbC	5.2 ± 1.5	5.2 ± 1.5	0
3	NbC, Laves	1.2 ± 0.7	---	---
3.5	NbC	3.0 ± 0.4	3.0 ± 0.4	0
4	NbC	7.3 ± 1.3	7.3 ± 1.3	0
5	NbC, Laves	2.5 ± 1.1	~0[2]	~2.5 ± 1.1
6	NbC, Laves	13.3 ± 2.5	~13.3 ± 2.5	~0[3]
7	NbC, Laves	2.7 ± 0.4	~0[2]	~2.7 ± 0.4
7.5	NbC, Laves	7.5 ± 0.5	5.2 ± 0.5	2.3 ± 0.5
8	NbC, Laves	15.2 ± 1.6	13.7 ± 1.6	1.5 ± 0.7
9	NbC, Laves	3.8 ± 0.5	~0[2]	~3.8 ± 0.5
10	NbC, Laves	9.0 ± 1.0	~9.0 ± 1.0	~0[3]
11	NbC, Laves	2.5 ± 0.4	~0[2]	~2.5 ± 0.4
11.5	NbC, Laves	7.3 ± 1.1	6.6 ± 1.1	0.7 ± 0.1
12	NbC, Laves	6.7 ± 1.7	4.4 ± 1.7	2.3 ± 0.8
13	NbC, Laves	12.9 ± 1.4	~0[2]	~12.9 ± 1.4
14	NbC, Laves	23.8 ± 1.6	18.8 ± 1.6	5.0 ± 0.6
15	NbC, Laves	15.5 ± 1.4	~0[2]	15.5 ± 1.4
16	NbC, Laves	23.6 ± 2.1	17.5 ± 2.1	6.1 ± 0.7

1 - May contain Laves also
2 - NbC or γ/NbC present in too low an amount to accurately quantify.
3 - Laves or γ/Laves present in too low an amount to accurately quantify.

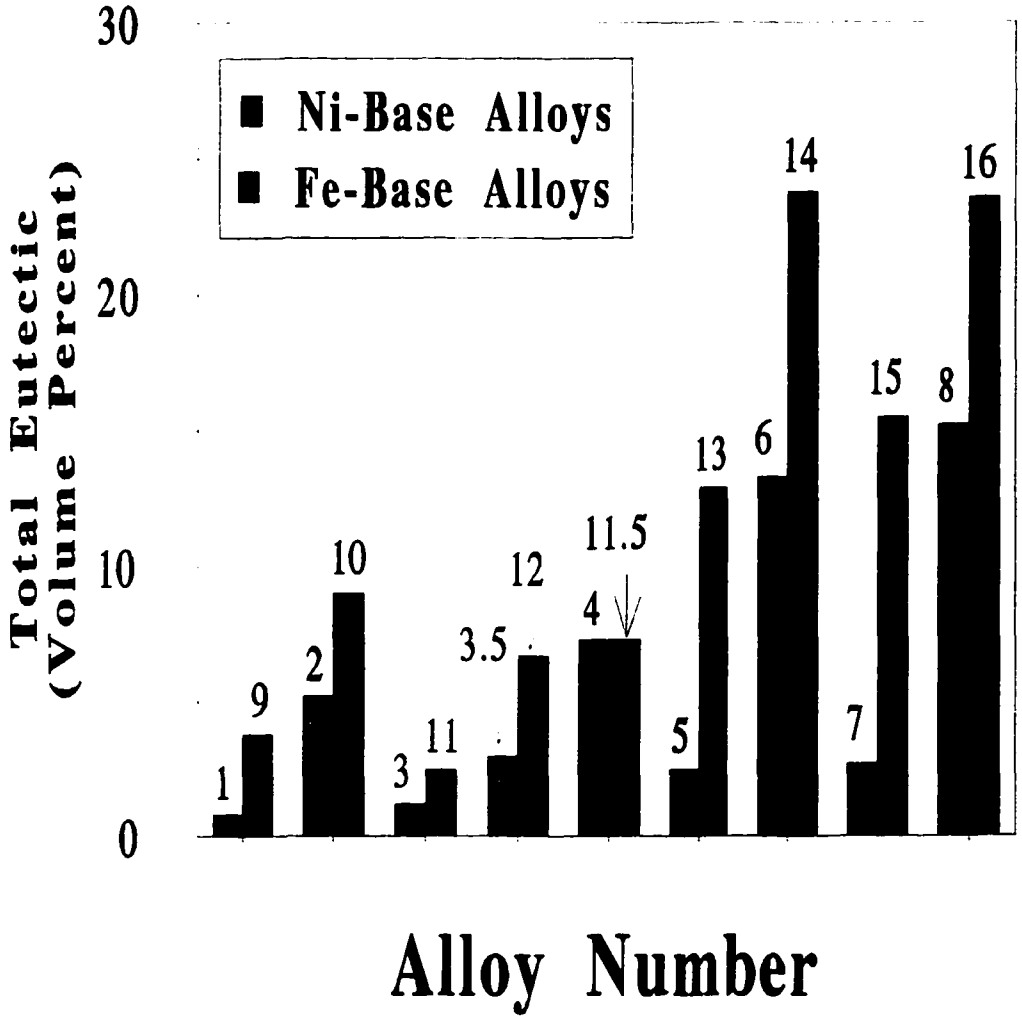

Figure 4.33 Total amount of eutectic-type constituents (γ/NbC + γ/Laves) measured in each alloy.

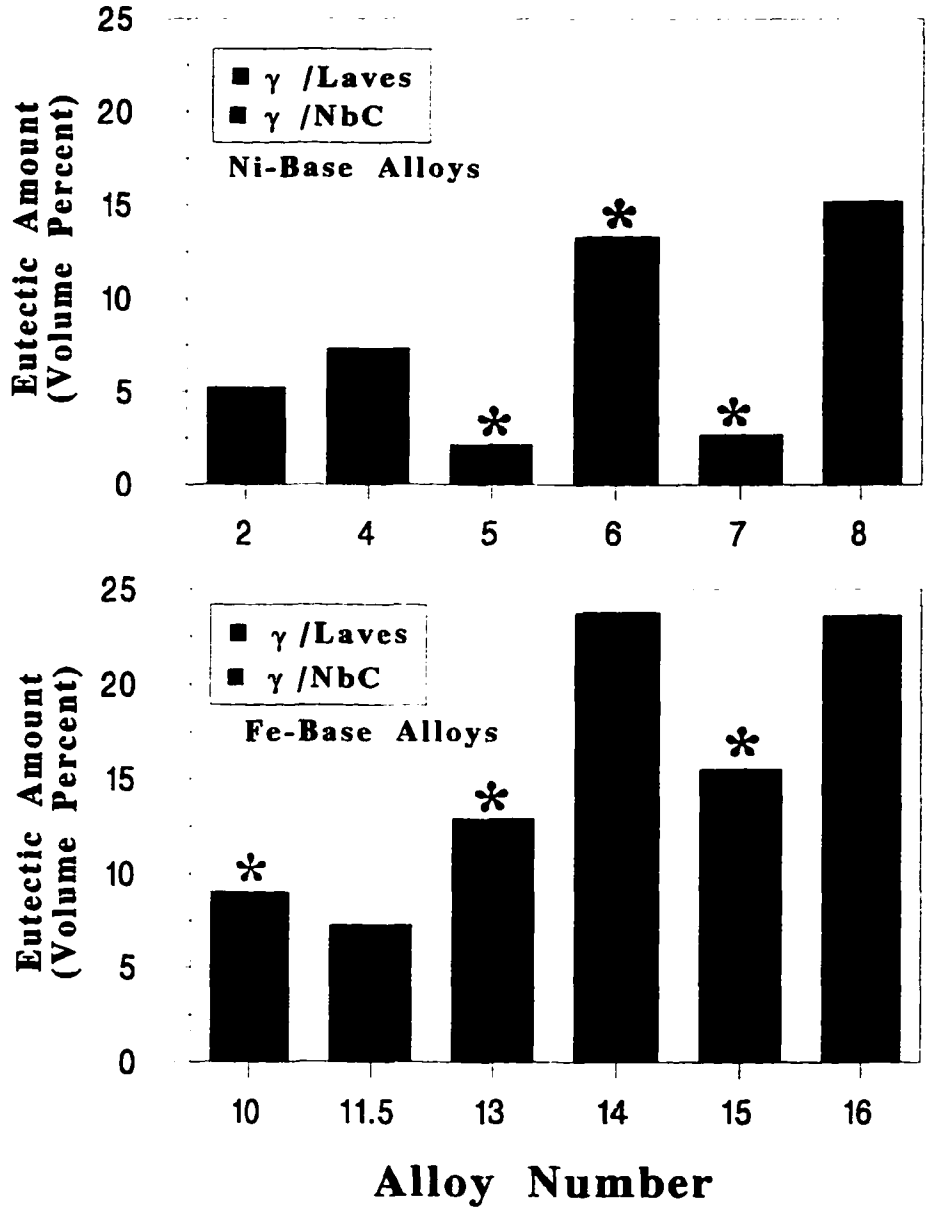

* - Contains very small amount of Laves phase which could not be quantified

* - Contains very small amount of NbC phase which could not be quantified

Figure 4.34. Individual amounts of γ/NbC and γ/Laves eutectic-type constituents measured in selected alloy.

There are several important effects of Fe, Nb, Si, and C displayed in Figures 4.33 and 4.34. First, at similar levels of minor alloy additions (Nb, Si, and C), the iron base alloys generally form significantly higher levels of total eutectic-type constituents. Measurements of the individual eutectic-type constituents (Figure 4.34) indicates that this response can be attributed mostly to the formation of higher amounts of γ/Laves. It is worth noting that no Laves phase exists in the simple Ni-Nb binary phase diagram while the Fe-Nb system forms the Laves phase over a composition range of 38 to 50 wt% Nb over a broad temperature range of 600°C to 1400°C [4.4]. The Cr-Nb system also forms the Laves phase over a similar composition range (45 to 52 wt% Nb at 1000°C) [4.4]. The Ni-Nb system forms Ni_3Nb over the composition range of approximately 33 to 38 wt% Nb (at 1200°C). The addition of Fe to Ni-Nb alloys is well known to promote Laves phase at the expense of the Ni_3Nb phase [4.5]. Thus, Fe additions to the austenite matrix, at the expense of Ni, can be expected to promote the formation of more γ/Laves as observed here. The addition of Si has a similar effect, as the amount of γ/Laves always increases with increasing Si within a given matrix composition (compare Alloy 5 to 7, 6 to 8, 13 to 15, and 14 to 16). The Laves promoting tendency of Si has also been documented in superalloys [4.6]. Nb additions promote higher amounts of total eutectic. This is to be expected, since each of the secondary phases which form in the eutectic-type structures (NbC and Laves) are both highly enriched in Nb. At high C levels, Nb additions generally promote more γ/NbC (compare Alloy 2 to 6, 4 to 8, 10 to 14, 11.5 to 16). When the C and Fe levels are both high, Nb additions will increase the amounts of both the γ/NbC and γ/Laves constituents (compare Alloys 10 to 14 and 11.5 to 16).

Finally, it is readily apparent that alloys with high C levels (even-numbered alloys) form large amounts of the γ/NbC eutectic-type constituent.

The presence of these two phases has been observed in a large number of commercial superalloys, including Alloys IN625 [4.7], IN718 [4.8], IN909 [4.3], IN903 [4.9], IN519[4.10], Thermo-Span [4.2], and IN625 weld overlays [4.11, 4.12]. Alloys IN718, IN909, and Thermo-Span all contain ~ 5 wt% Nb with relatively low C levels of 0.003 to 0.05 wt% C and exhibit the Laves phase as the predominant secondary solidification constituent, with NbC typically forming in smaller quantities. This is very similar to the results obtained here (e.g., Alloys 5, 7, 13, and 15). IN903 contains ~ 3 wt% Nb, 0.03 wt% C, and ~0.07 wt% Si. At this composition, NbC is observed as the major secondary phase, with Laves forming in trace amounts [4.9]. Considering the low Si and intermediate C content, it is not surprising to find NbC as the major secondary phase in this alloy. Cieslak conducted a detailed investigation on the effects of Si and C additions to IN625. As found in this work, Si additions promoted the Laves phase while C promoted NbC. In one case, the addition of C led to the formation of only the γ/NbC constituent and no Laves formed at all. A similar effect was observed in Alloys 2, 3.5, and 4 in this work. The solidification behavior of IN625 weld overlays on C steel have also been examined. These results are useful as they reveal the effect of Fe additions to the nominal IN625 composition. When IN625 is joined to a 0.13 wt% C steel at 25% dilution [4.11], the Fe is raised from 4 to 28 wt% and only the γ/Laves constituent is observed. However, when IN625 is joined to a higher C steel (0.25wt% C), both the γ/NbC and γ/Laves eutectic-type structures are observed [4.12]. The alloys in this

research properly simulate these wide ranges of effects displayed by individual commercial alloys systems. Thus, the systematic variations in composition that are utilized here to develop a detailed solidification model should be readily applicable to commercially important superalloys.

4.2 SOLIDIFICATION REACTION SEQUENCES

In this section, the sequence of eutectic-type reactions which occur during solidification are determined by combining the results of DTA cooling curves and the microstructural characterization results discussed in the previous section. When conducting DTA cooling scans, it is desirable to utilize a cooling rate which simulates reactions occurring during typical non-equilibrium solidification processes (e.g., casting and arc welding). In this sense, high cooling rates are favorable. However, at high cooling rates, there is often a significant lag between the point (in time and temperature) at which the reaction occurs and the point at which the temperature rise from the reaction (due to the enthalpy release) is detected by the DTA thermo-couple [4.14]. Relatively high cooling rates of 20°C/min are typically used in solidification studies of Nb-bearing superalloys [4.2, 4.3, 4.11], but the influence of this DTA test parameter has not been reported in terms of the potential effect on accuracy due to lag time. Thus, brief experiments were conducted to assess this possible effect, the main results of which are shown in Figure 4.35.

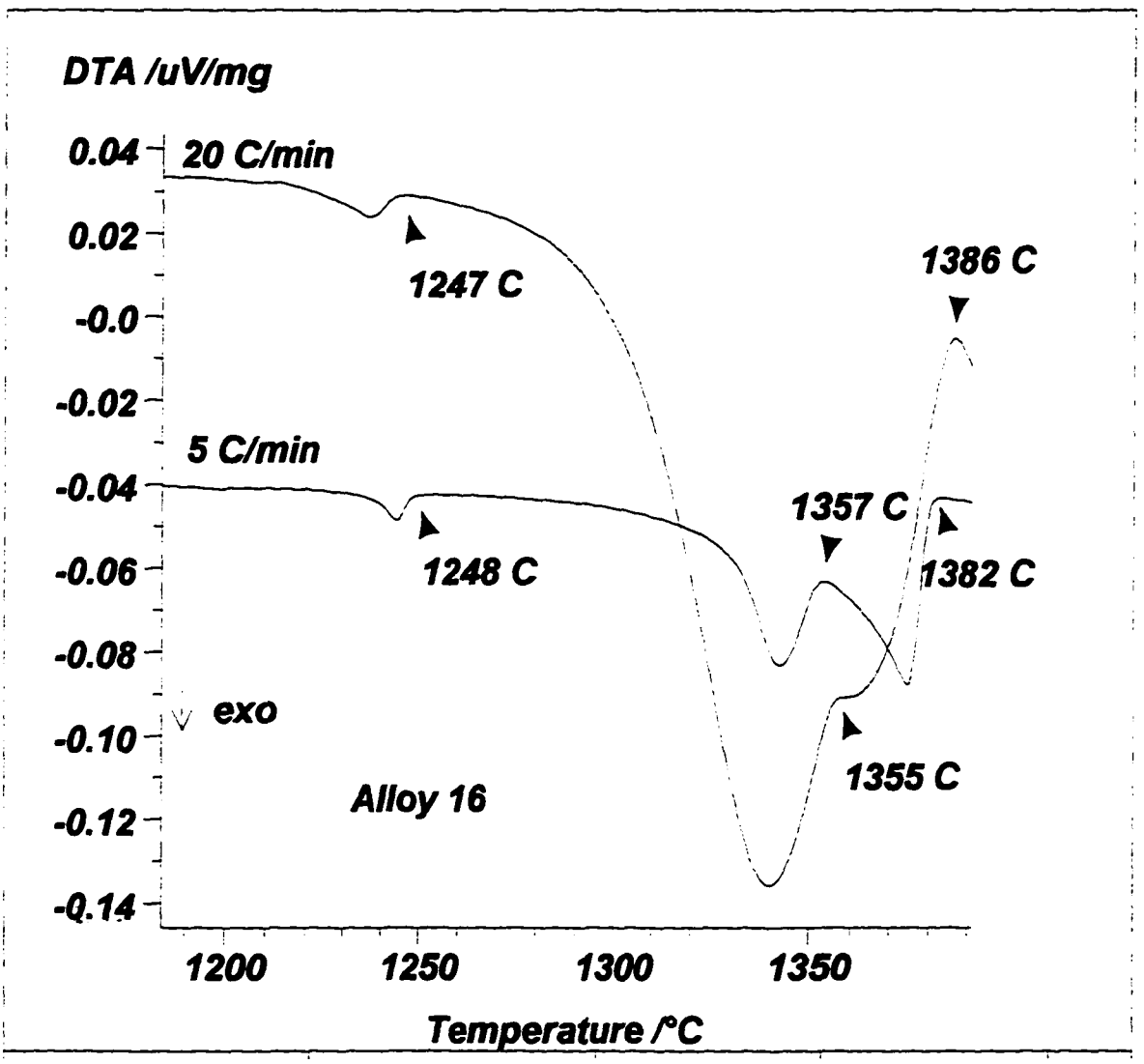

Figure 4.35. Cooling portion of a DTA scan conducted on Alloy 16 at 5°C/min and 20°C/min.

This figure shows the cooling portion of a DTA scan conducted on Alloy 16 at a relatively slow cooling rate of 5°C/min and a more commonly used fast cooling rate of 20°C/min. The plot displays the output signal of the DTA (in μV/mg - the voltage signal from the thermo-couple normalized by the weight of the sample) as a function of temperature. As discussed in more detail below, this alloy exhibits two exothermic eutectic-type reactions on cooling: one near 1356°C and one near 1248°C. Although the two curves were acquired at different cooling rates, each identifies reaction temperatures which are essentially identical. The only difference among the curves lies within the peak heights, where the higher cooling rate produces more pronounced peaks. At higher cooling rates, the enthalpy release rate from the sample is higher which produces a larger temperature difference between the sample and standard. This larger temperature difference is manifested as a larger output voltage between the sample and standard thermocouples. Thus, the 20°C/min cooling rate has the advantage of increased sensitivity while simultaneously providing a level of accuracy comparable to the slower 5°C/min cooling rate. Thus, all solidification scans were conducted at 20°C/min.

4.2.1 Ni-BASE ALLOYS

Typical DTA solidification traces for the Ni-base alloys are shown in Figures 4.36 through 4.39. Figure 4.36 shows the scan acquired on Alloy 3. On cooling from above the liquidus temperature, a large exothermic peak is initiated at 1408°C which is associated with solidification of the primary austenite dendrites. (More accurate measurements of liquidus temperatures are reported from heating curves in the next

section.) Although a small amount (1.2 ± 0.7 vol. %) of eutectic-type constituent formed in this alloy, no secondary peak could be discerned in the DTA scan. This behavior was typical for all the Ni-base alloys containing less than 0.052 wt% C and less than 2.7 vol.% total eutectic-type constituent (e.g., Alloys 1, 1.5, 3, 5, and 7). At these low quantities of eutectic-type constituents, there is apparently insufficient energy released during the reaction to produce a temperature difference between the standard and sample which can be detected by the DTA system. Thus, terminal solidification reaction temperatures could not be determined for these alloys.

Figures 4.37 and 4.38 show DTA scans of Alloys 4 and 8, respectively. In addition to the large exothermic peak from the primary austenite dendrites, distinct secondary exothermic peaks are initiated at 1331°C for Alloy 4 and 1326°C for Alloy 8. These peaks are rather broad, suggesting the corresponding reactions occur over a wide temperature range. These type of secondary peaks were observed for the remaining Ni-Base alloys, which all contain C contents above 0.075 wt% and eutectic-type constituents above 3 vol. %. (e.g., 2, 3.5, 4, 6, 7.5, and 8). As listed in the QIA results (Table 4.3), γ/NbC forms as the only eutectic-type constituent in Alloys 2, 3.5, and 4 and is the major constituent in Alloys 6, 7.5, and 8. Thus, these secondary peaks are associated with the $L \rightarrow (\gamma + NbC)$ reaction, and the first deviation from the local baseline is taken as the initiation of this reaction.

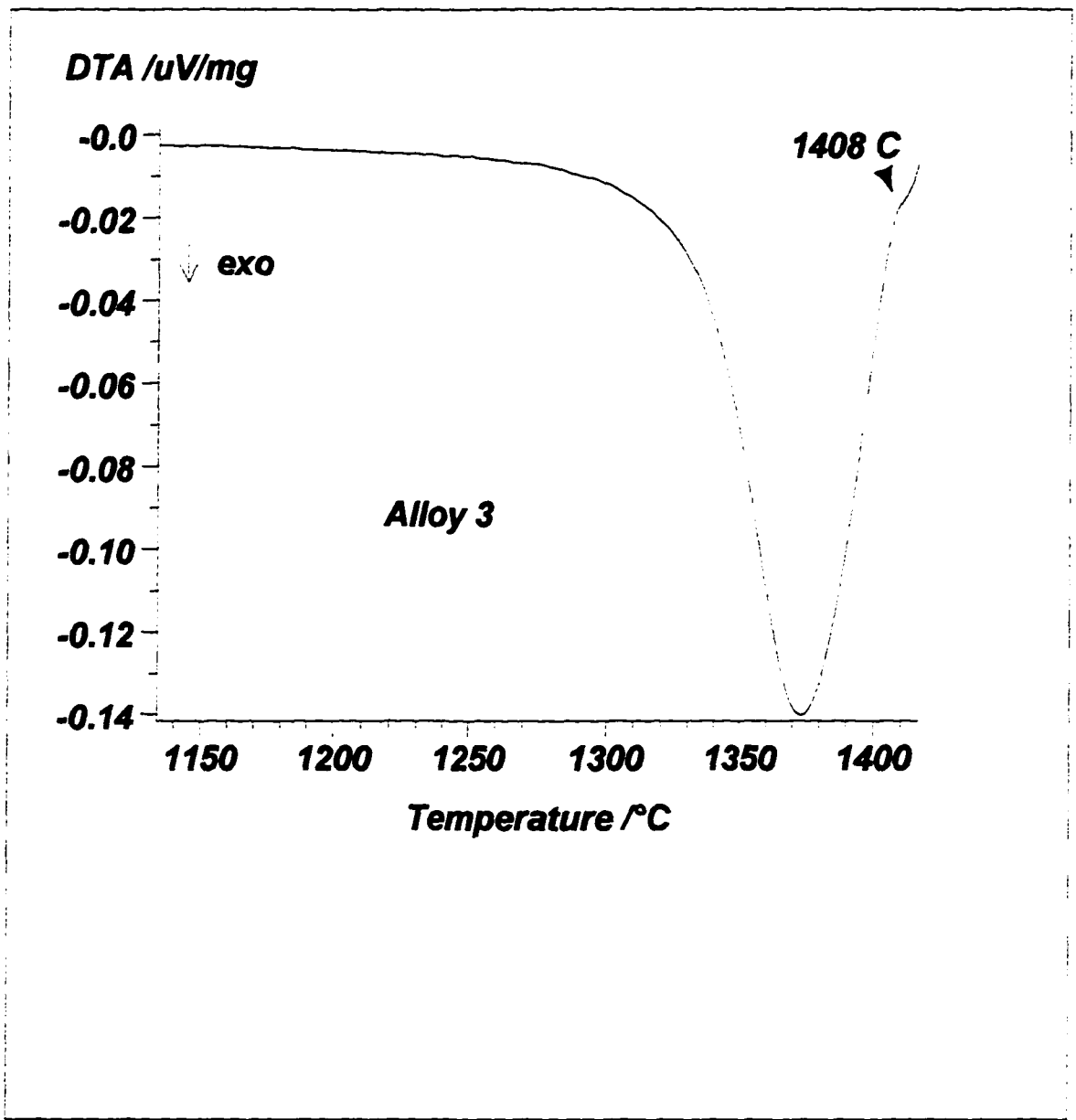

Figure 4.36. DTA solidification scan of Alloy 3.

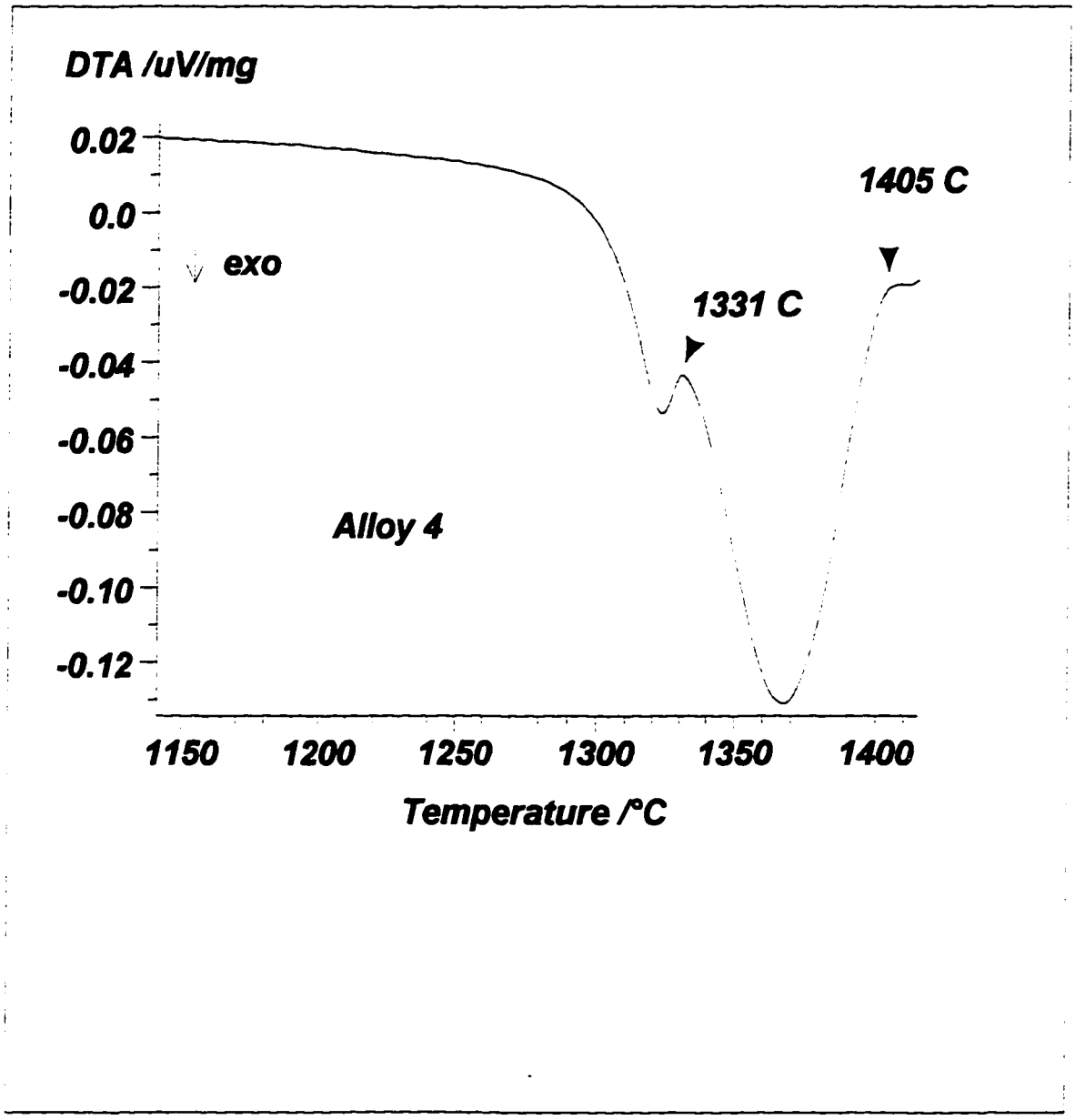

Figure 4.37. DTA solidification scan of Alloy 4.

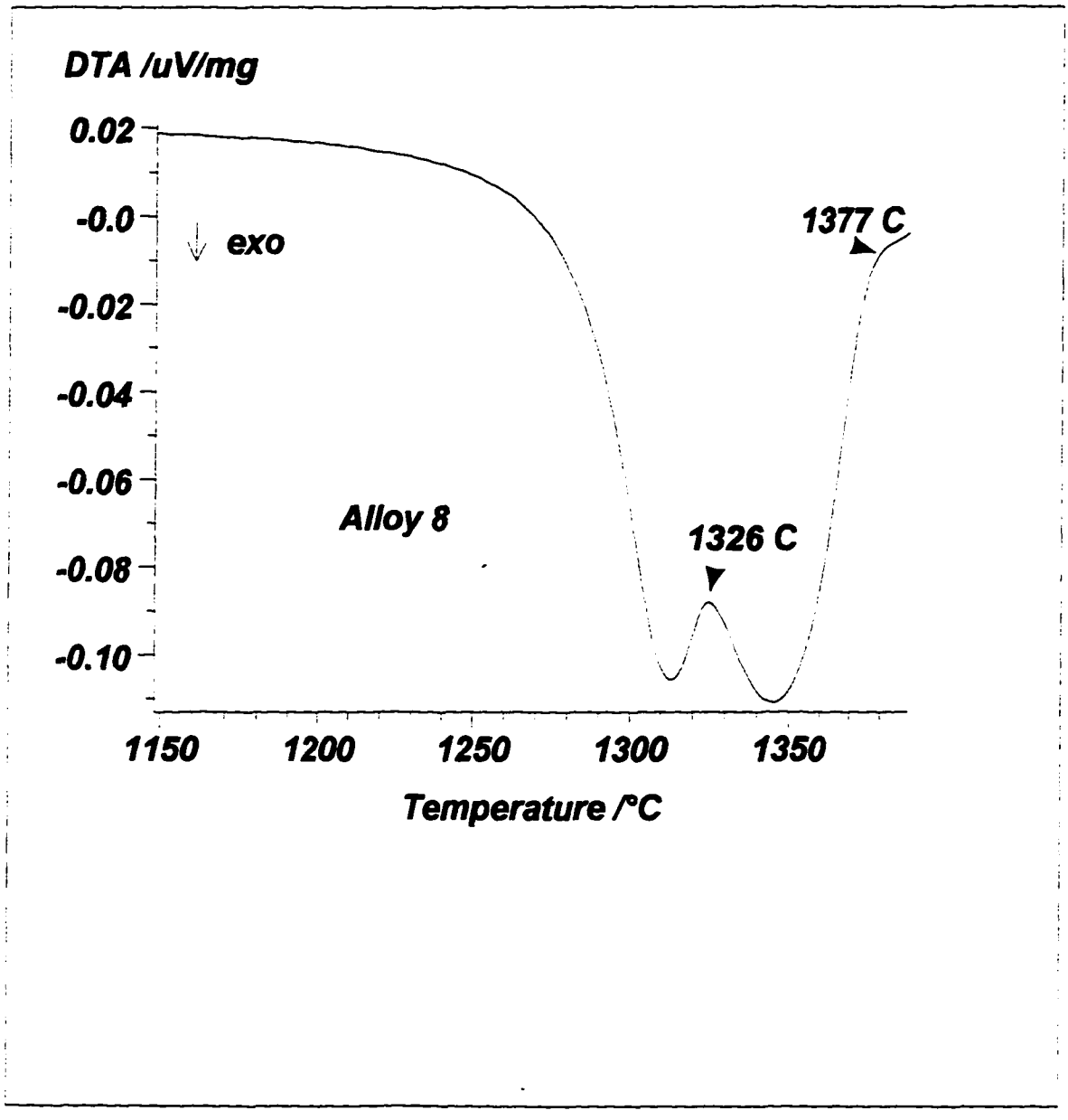

Figure 4.38. DTA solidification scan of Alloy 8.

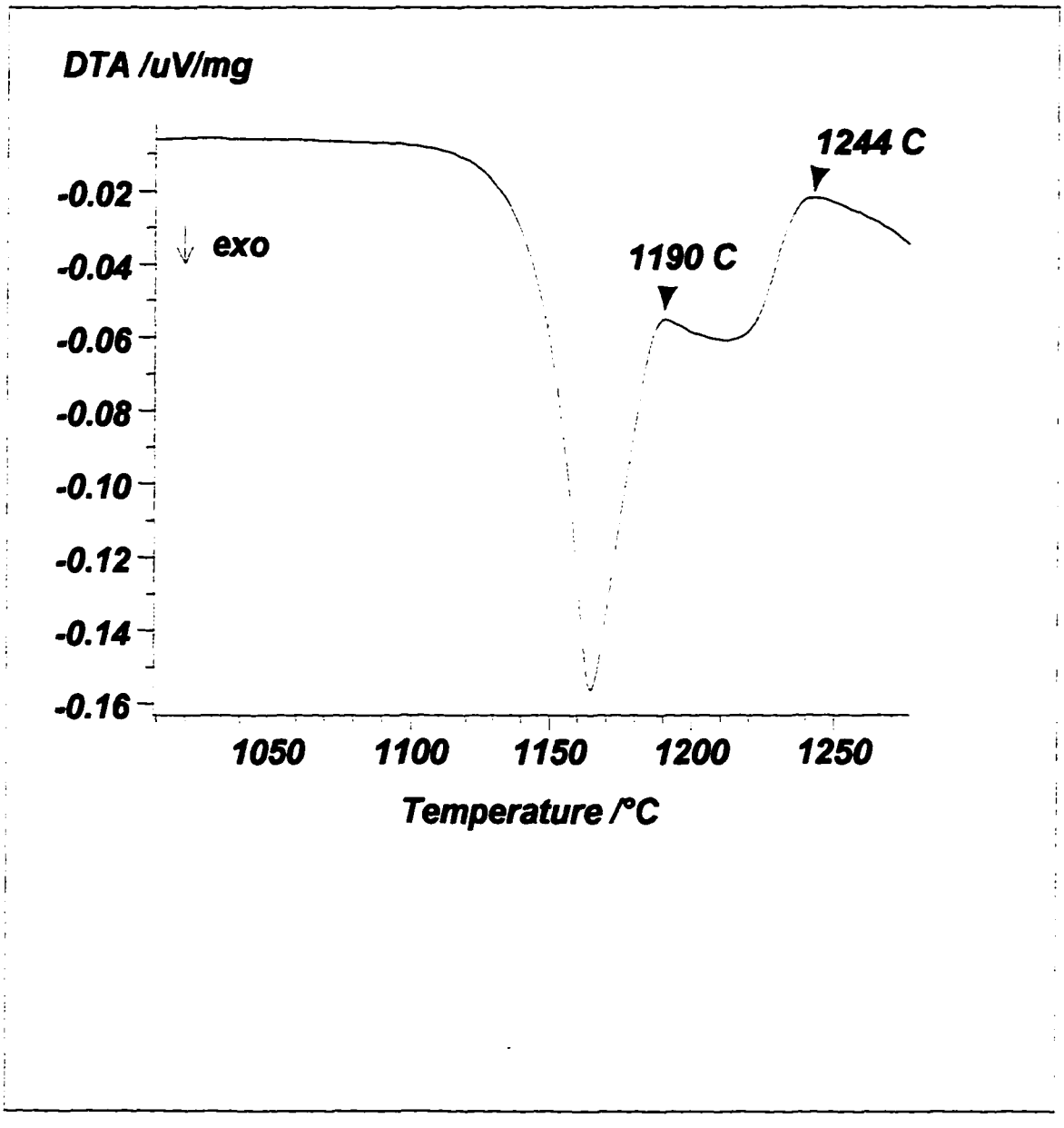

Figure 4.39a. DTA solidification scan of Alloy Ni-1.

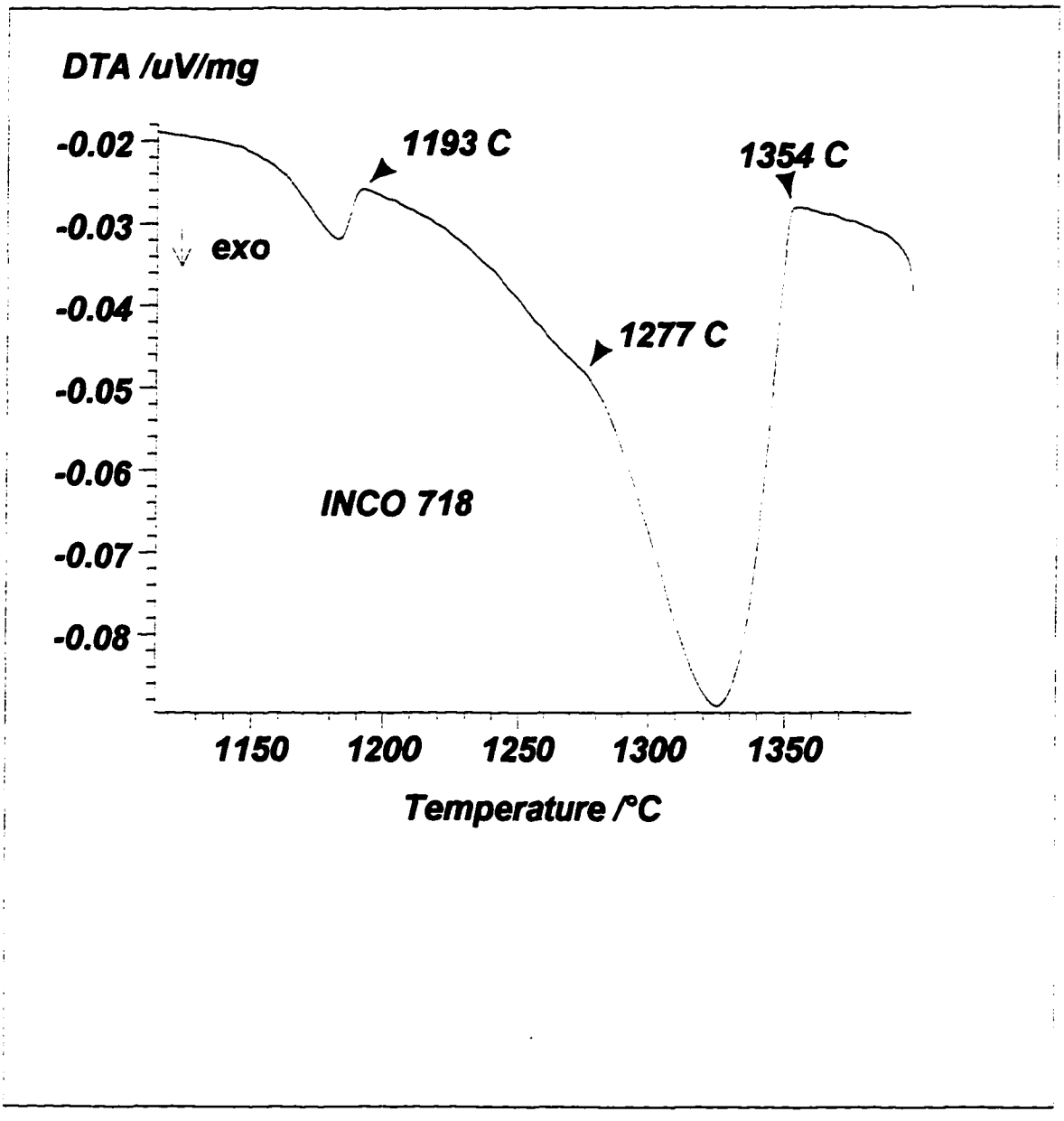

Figure 4.39b. DTA solidification scan of Alloy IN718.

The secondary peaks from these alloys exhibit differences in integrated peak areas and reaction start temperatures. These differences are summarized in Table 4.4, where the reported reaction temperatures are an average from three measurements. The alloys are listed in order of increasing γ/NbC amount. Note that the integrated peak area generally increases in the same order as the γ/NbC volume percent. This is to be expected, since the integrated area is representative of the total energy released during solidification which, in turn, is proportional to the amount of solid (i.e., γ + NbC) which forms. This consistency between the QIA and DTA results provides further confirmation that the DTA peaks are correctly matched to the L → (γ + NbC) reaction. The differences in reaction temperatures among the alloys result mainly from variations in their solidification paths, which is controlled by the nominal alloy composition and distribution coefficients for the solute elements (Nb, C, and Si). These details are discussed in more detail in the next chapter.

The DTA solidification scan for Alloy Ni-1 is presented in Figure 4.39 along with a similar scan for commercial alloy IN718. The solidification sequence of IN718 has been investigated in detail by Knorovsky *et al.* [4.8]. After solidification of the primary dendrites, the alloy exhibits both the L → (γ + NbC) and L → (γ + Laves) reactions, with the Laves forming in much higher amounts than NbC. Knorovsky *et al.* report temperatures for the L → (γ + NbC) and L → (γ + Laves) reactions of 1252°C and 1198°C, respectively. The L → (γ + Laves) reaction temperature was essentially the same for scans conducted during heating and cooling. The L → (γ + NbC) reaction temperature of 1252°C was reported from scans acquired on heating. The IN718 scan shown in Figure

4.39b is in very good agreement with the Knorovsky *et al.* data. On cooling, the L → (γ + NbC) and L → (γ + Laves) reactions are detected at 1277°C and 1193°C, respectively. The L → (γ + Laves) reaction temperature is within 5°C of that reported by Knorovsky *et al.* The L → (γ + NbC) reaction temperature acquired on cooling in this work is 25°C higher than that acquired by Knorovsky during heating. This is to be expected. The L → (γ + NbC) reaction is well known to occur over a broad temperature range [4.8], and thus the onset of the reaction determined during cooling should be higher than the onset of the reaction measured during heating.

The cooling scan of Ni-1 displays a large exothermic peak at 1190°C. As shown in Figure 4.31, this alloy contains mostly γ/Laves, with smaller amounts of γ/NbC and primary austenite. Thus, the large peak initiated at 1190°C is readily matched to the L → (γ + Laves) reaction, which is in very good agreement with the same reaction temperature measured in IN718. This result is rather useful, as it provides an estimation of the L → (γ + Laves) reaction temperature in the Ni base alloys which could not be determined in Alloys 1 through 8 due to the small amount of γ/Laves which forms in these alloys. Based on the DTA scans presented thus far, it is readily apparent that the L → (γ + NbC) reaction occurs before the L → (γ + Laves) reaction during solidification. This sequence of reactions is well documented for commercial alloy systems as well [4.3, 4.7, 4.8].

It is somewhat surprising to find only one peak occurring at higher temperatures in the Ni-1 cooling scan (1244°C), since both primary austenite and NbC are present in Alloy Ni-1. As discussed in more detail later, this alloy is very close to the line of two fold saturation which separates the γ and NbC primary phase fields. Thus, the primary

$L \rightarrow \gamma$ reaction and $L \rightarrow (\gamma + NbC)$ eutectic-type reaction are very close to each other in terms of reaction temperature. This, coupled with the fact that the NbC and primary γ both form in small quantities in Alloy Ni-1, preclude unequivocal matching of the deviation at 1244°C to either of these two solidification reactions.

Table 4.4. Summary of secondary solidification reaction temperatures in Ni base alloys.

Alloy	$L \rightarrow (\gamma + NbC)$ Start Temperature (°C)	γ/NbC Amount (vol. %)	Integrated Peak Area ($\mu V \cdot s/mg$)
3.5	1322 ± 1.4	3.0 ± 0.4	0.2
2	1341.5 ± 0.7	5.2 ± 1.5	0.5
7.5	1305.5 ± 0.7	5.2 ± 0.5	0.4
4	1330.0 ± 1.3	7.3 ± 1.3	0.8
6	1332.0 ± 1.4	13.3 ± 2.5	1.6
8	1328.0 ± 2.8	13.7 ± 1.6	2.1

4.2.2 Fe-BASE ALLOYS

Typical DTA traces for the Fe base alloys are presented in Figures 4.40 through 4.44. The DTA scan for Alloy 9 (Figure 4.40) displays a large exothermic peak associated with formation of the primary γ dendrites. No smaller peaks were detected at lower temperatures. A similar scan was recorded for Alloy 11. These alloys both have very low C contents and form less than 3.8 vol. % of total eutectic-type constituent. Thus, no secondary reaction temperatures could be identified in these alloys. The DTA cooling scan for Alloy 12 is shown in Figure 4.41. This scan was typical for Alloys 10 and 11.5 as well. On cooling from above the liquidus temperature, primary γ begins to form at 1417°C, followed by a secondary reaction initiating at 1349°C. γ/NbC is the major

constituent observed in these three alloys. Thus, this secondary peak is associated with the L → (γ + NbC) reaction. The DTA cooling scan for Alloys 13 and 15 were similar (Figure 4.42). After the large exothermic peak from formation of the γ dendrites, each alloy exhibits a small exothermic deviation from the local baseline (at 1332°C for Alloy 13), followed by a larger peak (at 1247°C for Alloy 13). γ/Laves is the major constituent formed in these alloys, while γ/NbC forms in much smaller quantities. Thus, the small deviation occurring first on cooling is associated with the L → (γ + NbC) reaction and the lower temperature peak represents the L → (γ + Laves) reaction. Alloy 16 (Figure 4.43) exhibited a large secondary reaction peak at 1356°C from the L → (γ + NbC) reaction (γ/NbC is the major constituent in this alloy), followed by a smaller peak at 1246°C from the L → (γ + Laves) reaction. The DTA scans recorded from two separate tests on Alloy Fe-1 are shown in Figure 4.44. On cooling from above the liquidus, primary γ dendrites form in the range of 1339°C to 1346°C. There is a small, but reproducible, deviation from the local baseline at 1325°C which is interpreted as the L → (γ + NbC) reaction. Solidification is terminated with the L → (γ + Laves) reaction at 1266°C. The reaction temperatures and peak areas for the Fe base alloys are summarized in Table 4.5. As with the Ni base alloys, the reaction which produces the larger amount of eutectic-type constituent also produces the larger peak area, providing further confirmation that the DTA peaks are matched to the appropriate solidification reaction. This solidification sequence, where the L → (γ + NbC) reaction occurs before the L → (γ + Laves) reaction, is also consistent with that observed for the experimental Ni base alloys in this work and similar commercial superalloys [4.3, 4.7, 4.8]. The broad shape of the L → (γ + NbC)

peak indicates this reaction occurs over a wide temperature range while the rather narrow peak associated with L $\rightarrow$ (γ + Laves) indicates this reaction occurs over a small temperature range. This characteristic of each reaction has also been observed in commercial superalloy systems [4.2, 4.3, 4.8, 4.11].

At similar levels of solute elements, the solidification reactions in the Fe base alloys are consistently higher than those in the corresponding Ni base alloys. The compositions of the γ/NbC and γ/Laves eutectic-type constituents in the weld metals of several alloys are summarized in Table 4.6 and 4.7. As noted in earlier work by Knorovsky *et al.* [4.8], the eutectic-type constituents which form in welds exhibit fine structures which are suitable for composition measurements by EPMA. The majority of measurements were acquired on weld metals where composition modifications during post solidification cooling are avoided due to the high cooling rates. Several measurements were also made on the fine eutectic-type γ/Laves structure which formed in DTA samples (see results for Alloys 13 and 16 in Table 4.7). Not surprisingly, the Fe contents of the eutectic-type constituents in the Fe base alloys are considerable higher than those in the Ni base alloys. Considering that the melting temperature of Fe is higher than that of Ni, the higher reaction temperatures for the Fe base alloys are to be expected. As noted earlier, the Laves phase in the Fe base DTA samples was often present as both coarse, isolated particles and a fine eutectic-type structure in the same DTA sample, suggesting that an unidentified eutectic-type constituent may be present. However, the similarity in composition displayed in the DTA and weld metals for Alloys 13 and 16 confirms that the fine structure is indeed the γ/Laves constituent in the DTA sample.

Table 4.5. Summary of secondary solidification reaction temperatures in Fe base alloys.

Alloy	L → (γ + NbC) reaction			L → (γ + Laves) reaction		
	Start Temp. (°C)	γ/NbC (vol.%)	Peak Area (μV·s/mg)	Start Temp. (°C)	γ/Laves (vol. %)	Peak Area (μV·s/mg)
10	1357.5 (0.7)	9.0 (1.0)	0.4	--	--	--
11.5	1347.5 (2.1)	6.6 (1.1)	0.8	--	--	--
12	1348.0 (1.4)	4.4 (1.7)	0.4	--	--	--
13	1332.5 (0.7)	ND	0.1	1249.5 (3.5)	12.9 (1.4)	0.7
14	1360.8 (2.2)	18.8 (1.6)	3.0	1243.0 (2.1)	5.0 (0.6)	0.7
15	1289.5 (0.8)	ND	0.1	1256.3 (1.2)	15.5 (1.4)	1.8
16	1355.2 (1.7)	17.5 (2.1)	3.3	1248.2 (4.8)	6.1 (0.7)	0.2

ND - Present in quantities too low for accurate quantification

Table 4.6 γ/NbC Compositions. All values in wt%.

Alloy/ Sample	Fe, wt%	Ni, wt%	Cr, wt%	Nb, wt%	Si, wt%
Alloy 6 Weld	8.4 ± 0.2	58.7 ± 0.7	19.5 ± 0.2	13.3 ± 0.8	0.1 ± 0.02
Alloy 8 Weld	8.9 ± 0.3	58.7 ± 0.5	19.4 ± 0.2	12.5 ± 0.6	0.5 ± 0.02
Alloy 14 Weld	40.2 ± 0.7	28.5 ± 0.7	20.3 ± 0.3	10.9 ± 0.7	0.1 ± 0.02
Alloy 16 Weld	40.5 ± 0.5	28.6 ± 0.3	19.7 ± 0.2	10.8 ± 0.7	0.5 ± 0.02

Table 4.7 γ/Laves Compositions. All values in wt%.

Alloy/ Sample	Fe, wt%	Ni, wt%	Cr, wt%	Nb, wt%	Si, wt%
Alloy 7 DTA	4.9 ± 0.2	59.4 ± 0.8	10.2 ± 1.0	24.3 ± 0.7	1.7 ± 0.1
Alloy 7.5 DTA	4.9 ± 0.2	58.1 ± 1.7	11.4 ± 0.8	23.5 ± 1.3	2.0 ± 0.1
Alloy 8 DTA	4.4 ± 0.2	60.3 ± 0.5	11.3 ± 0.3	21.5 ± 0.5	2.5 ± 0.2
Ni-1 GTA Melt	7.0 ± 0.1	52.2 ± 0.4	16.7 ± 0.2	23.1 ± 0.5	1.0 ± 0.1
Alloy 13 Weld	31.4 ± 1.8	29.8 ± 1.1	16.6 ± 0.6	21.1 ± 1.3	0.3 ± 0.1
Alloy 13 DTA	31.2 ± 0.9	30.4 ± 0.5	17.3 ± 0.2	20.9 ± 1.0	0.3 ± 0.1
Alloy 14 Weld	31.0 ± 1.1	29.5 ± 0.8	16.8 ± 0.7	22.4 ± 2.4	0.3 ± 0.1
Alloy 15 Weld	32.7 ± 0.5	29.7 ± 1.0	16.7 ± 0.4	20.1 ± 0.9	0.9 ± 0.1
Alloy 16 Weld	32.7 ± 0.4	30.8 ± 0.7	16.9 ± 0.1	18.3 ± 0.7	1.3 ± 0.1
Alloy 16 DTA	28.6 ± 1.9	33.4 ± 1.4	16.5 ± 0.9	19.8 ± 1.2	1.7 ± 0.1
Fe-1 GTA Melt	37.7 ± 0.3	26.2 ± 0.4	18.0 ± 0.1	17.2 ± 0.1	0.9 ± 0.1

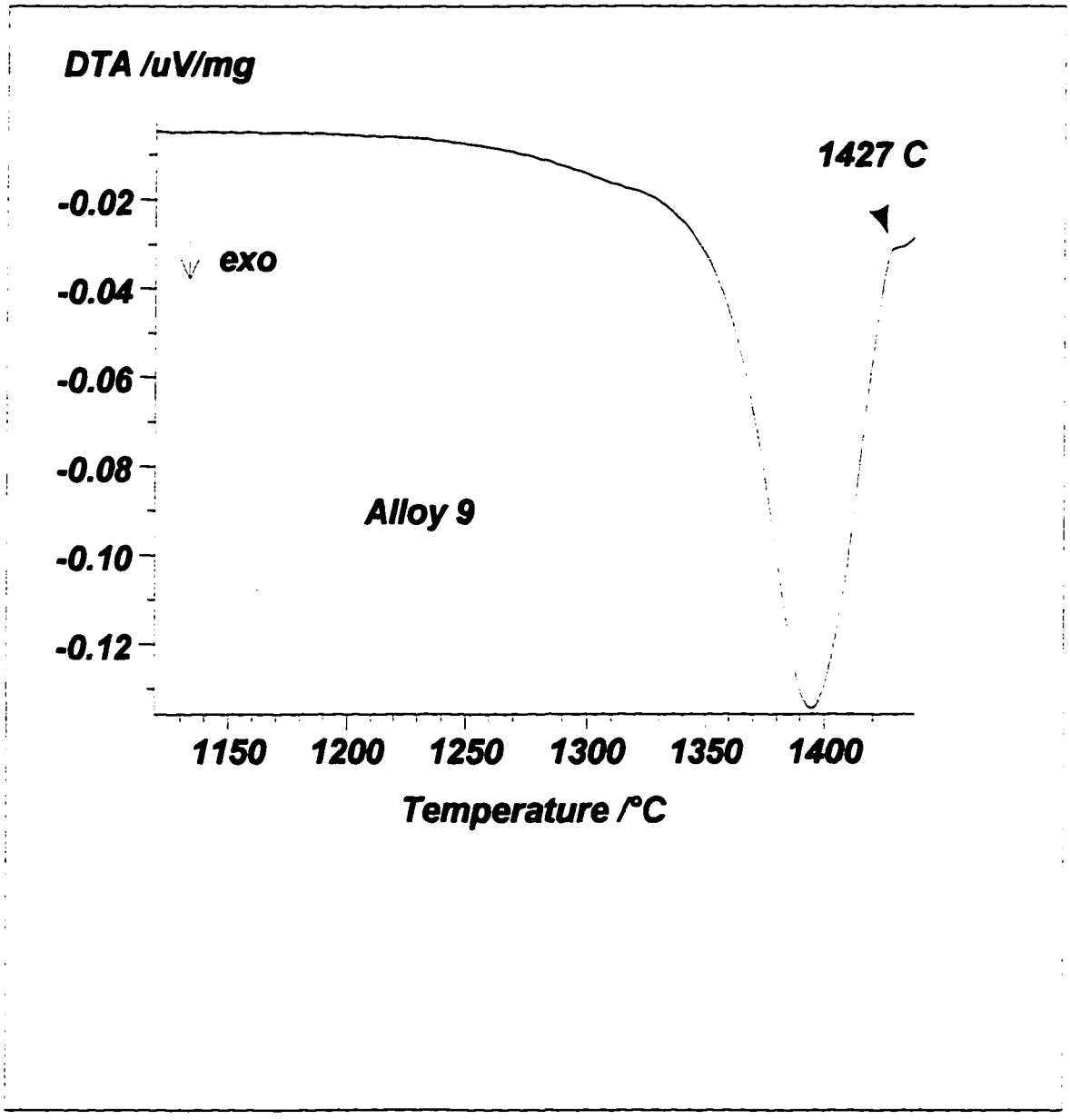

Figure 4.40. DTA solidification scan of Alloy 9.

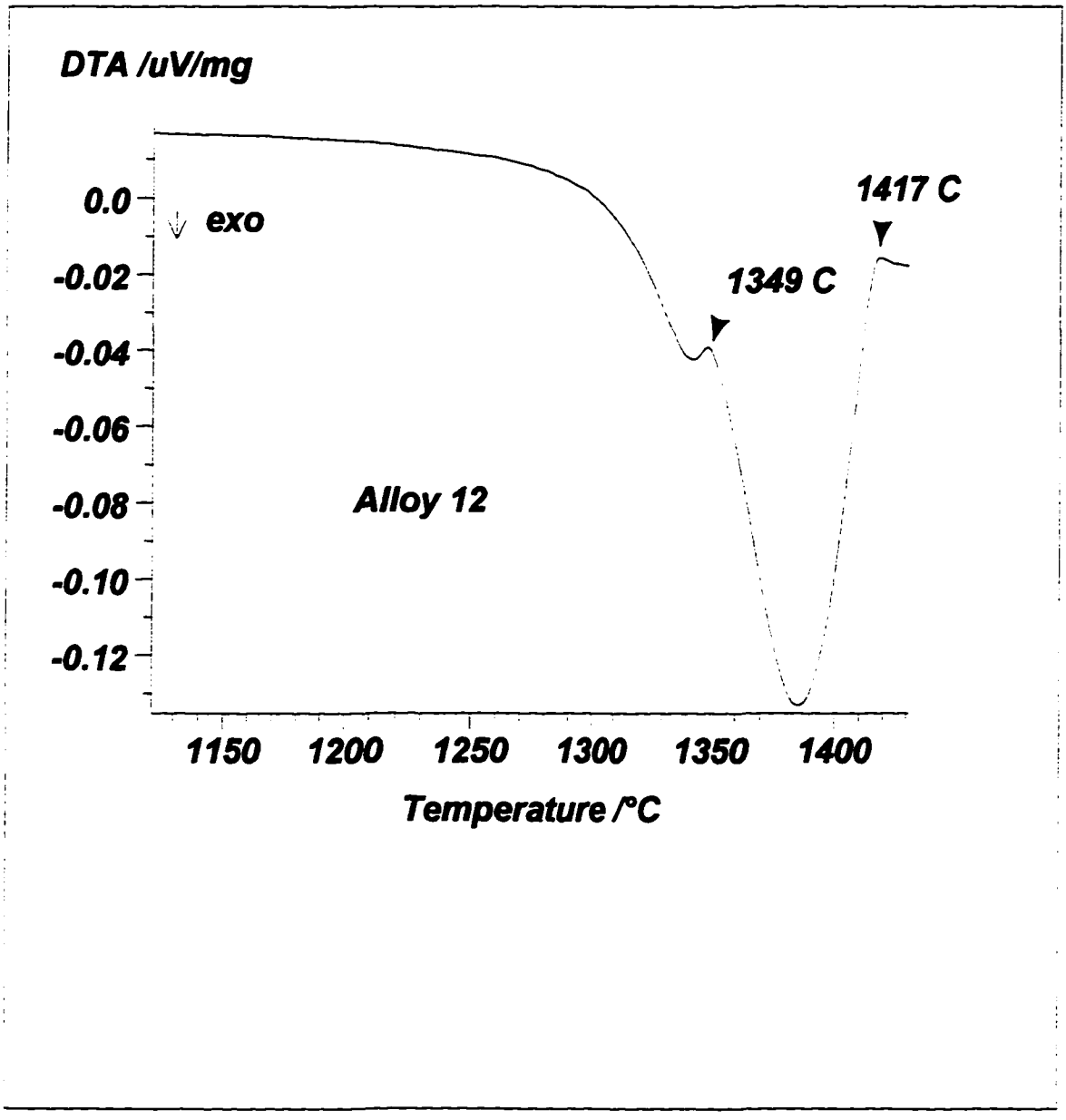

Figure 4.41. DTA solidification scan of Alloy 12.

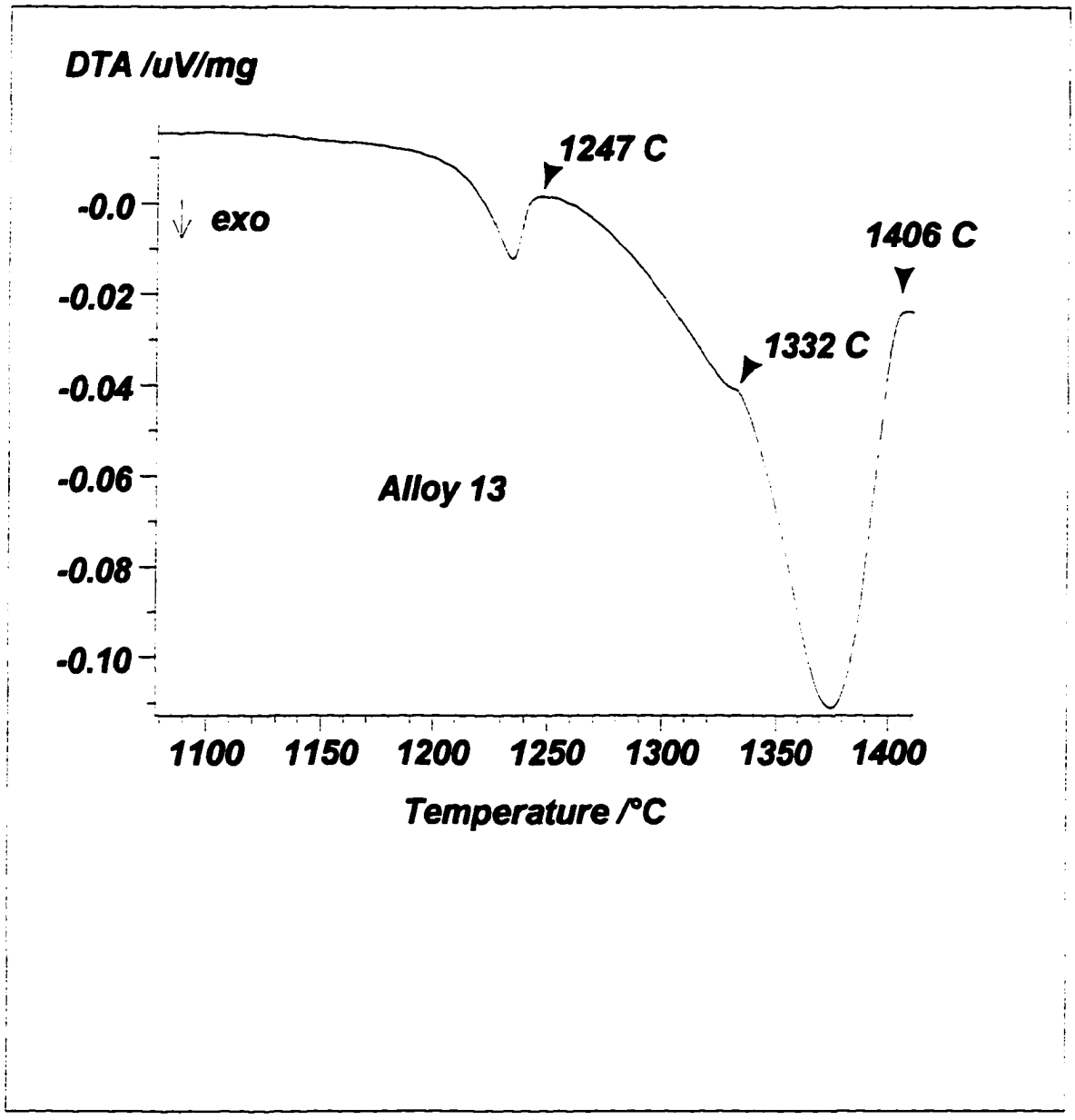

Figure 4.42. DTA solidification scan of Alloy 13.

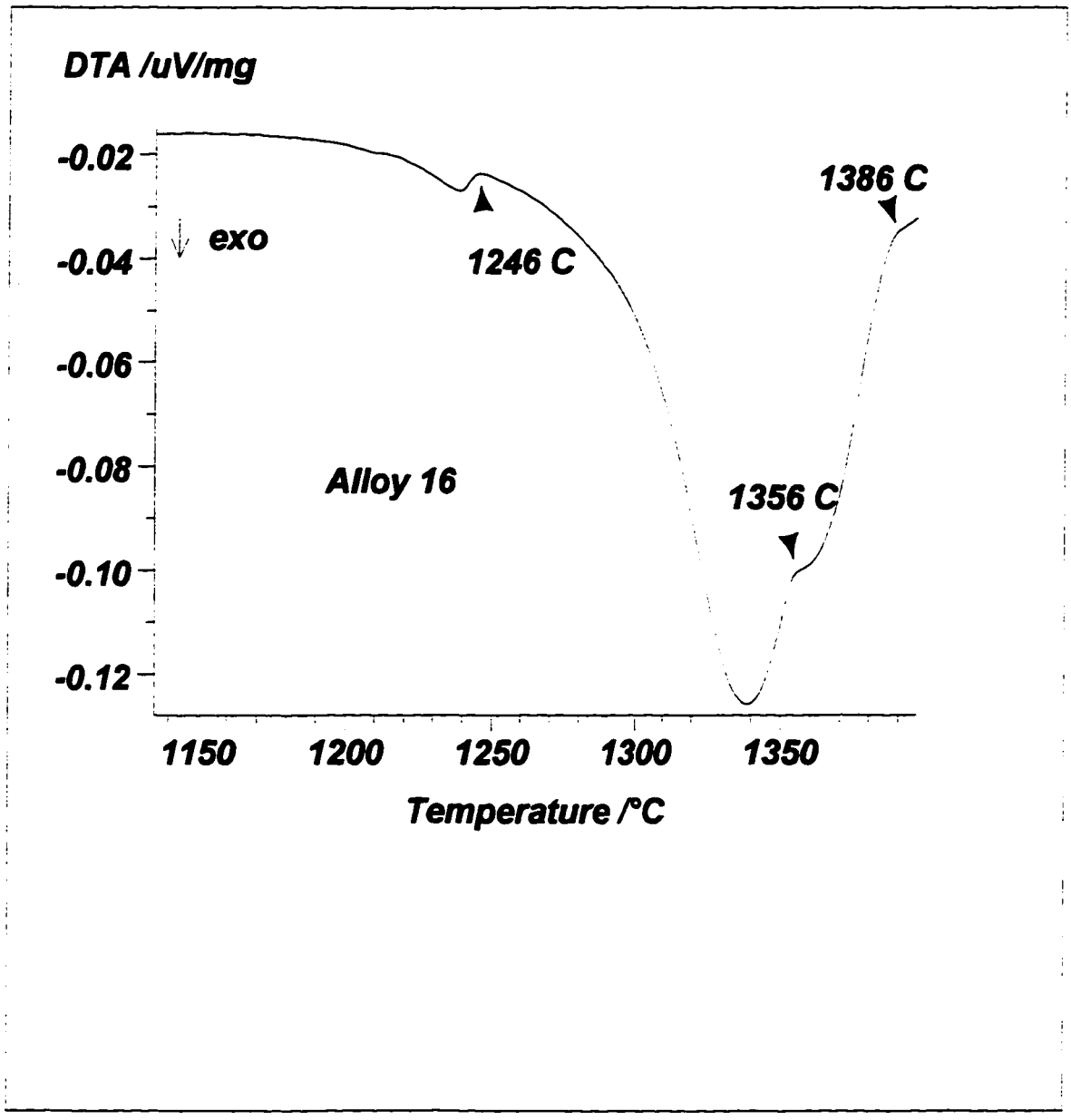

Figure 4.43. DTA solidification scan of Alloy 16.

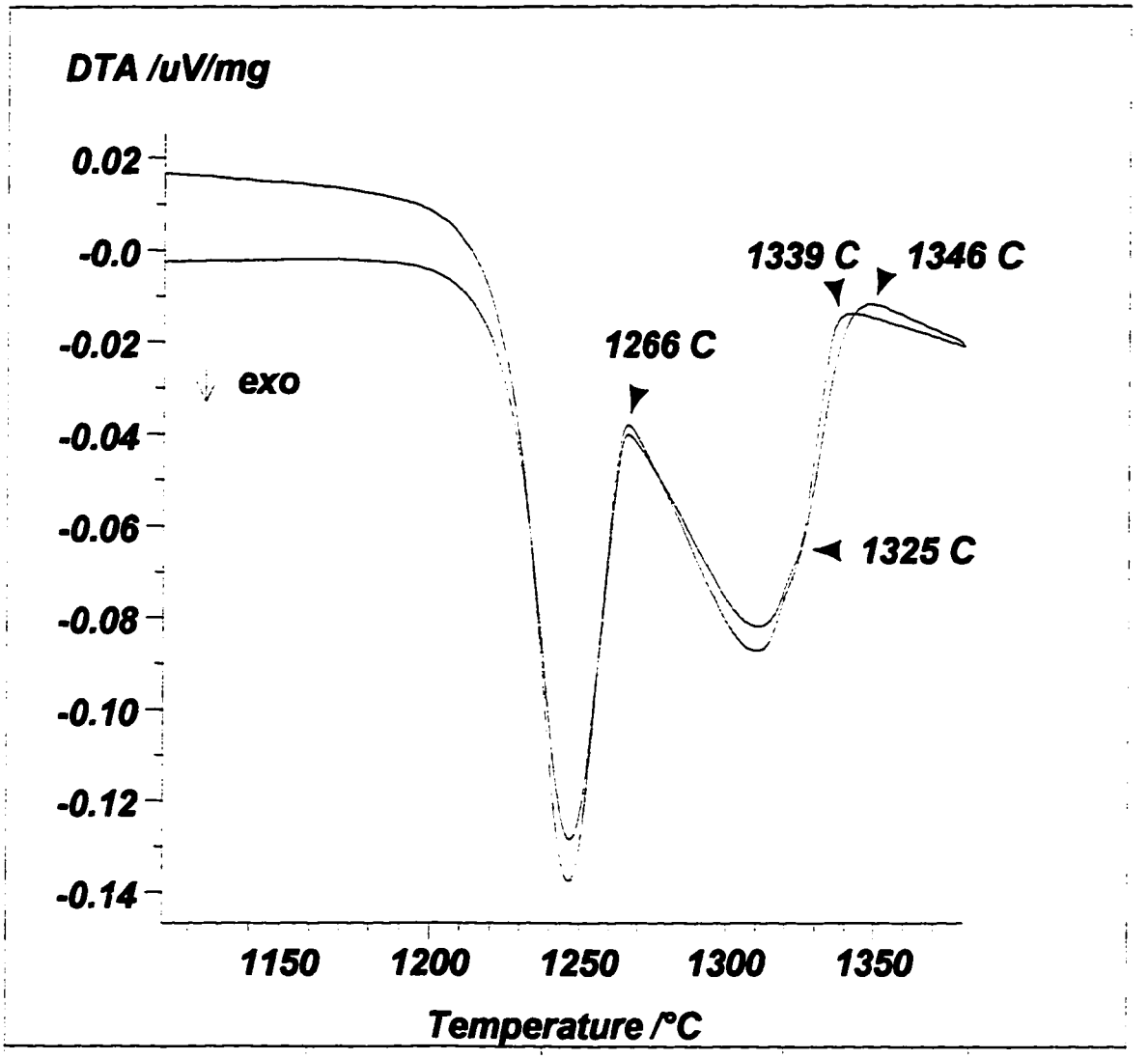

Figure 4.44. DTA solidification scan of Alloy Fe-1.

4.2.3 ANALOGY TO THE Ni-Nb-C SYSTEM

As noted in Table 4.3, all the alloys in this study exhibited the NbC phase (except for Alloy 1, where no confident phase identification could be made). The Laves phase was observed in all alloys except 2, 3.5, and 4 (it may be present in Alloy 1.5). It is interesting to note the similarity in secondary phases formed during solidification in these alloys and those expected in the ternary Ni-Nb-C system. The liquidus projection for the Ni-Nb-C system was estimated by Stadelmaier and Fiedler [4.15], and the Ni-rich corner of this diagram is reproduced in Figure 4.45. It should be noted that this diagram is only an estimate which was obtained by observing the primary solidification phase in a number of ternary Ni-Nb-C alloys. The accuracy of the boundaries separating each primary phase field is unknown as few alloys were investigated with compositions close to the reported boundaries. Nevertheless, the projection provides a useful starting point for more detailed analysis of the experimental alloys used in this study.

The liquidus projection exhibits three primary phase fields which are of interest here: γ, NbC, and Ni_3Nb. A primary C (graphite) phase field exists at high C contents which is not of interest. As previously noted, additions of Fe, Cr, and Si to the Ni-Nb system are well known to promote Laves at the expense of Ni_3Nb in commercial superalloys as well as the experimental alloys utilized in this work. Thus, by replacing Ni_3Nb with Laves, the Ni-Nb-C liquidus projection can be utilized as a guide in developing a qualitative description of the solidification reactions in these alloys [4.15a].

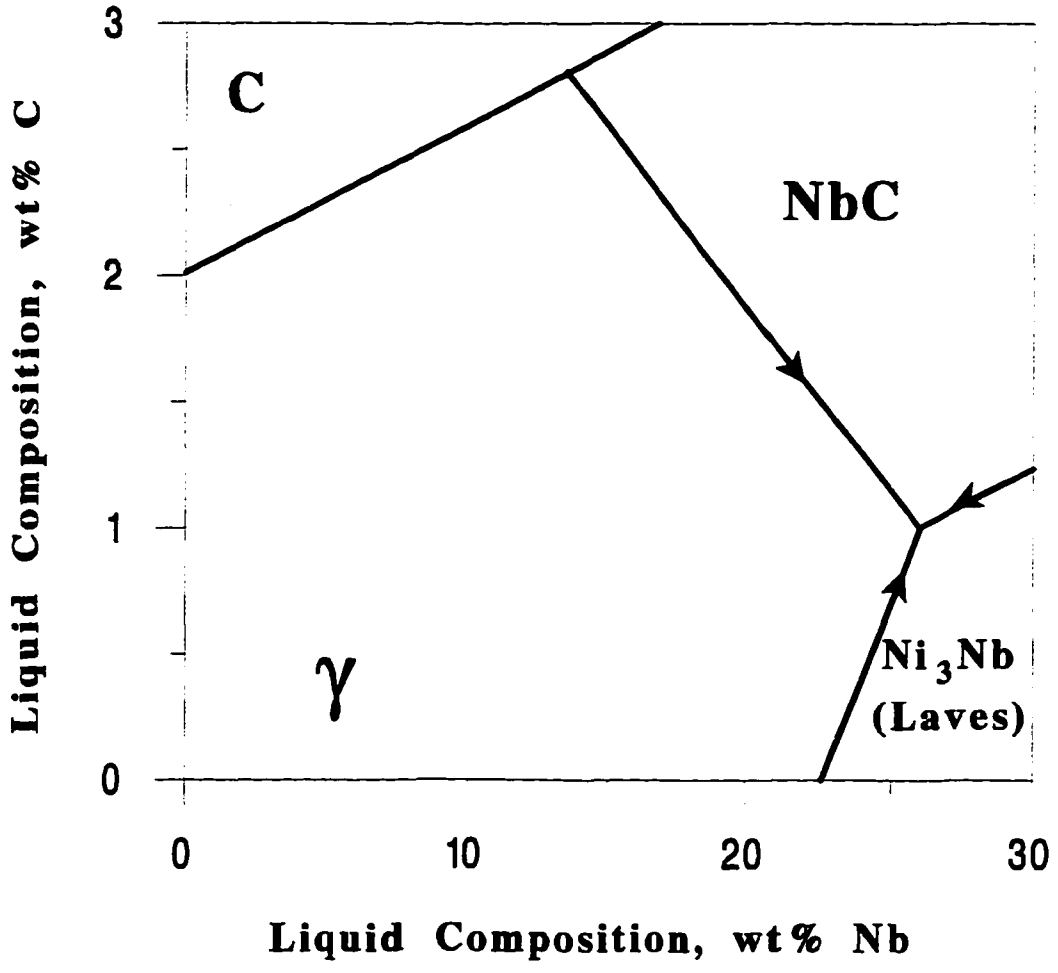

Figure 4.45. Liquidus surface for the Ni-Nb-C ternary system.

Combining the microstructural characterization results with the DTA data, it can be concluded that all the alloys in this study display one of two solidification sequences. For alloys 2, 3.5, and 4, solidification begins with formation of primary γ dendrites which, upon forming, reject Nb and C to the liquid. (As discussed in more detail later in this chapter, the distribution coefficients for Nb and C are less than unity for these alloy systems, indicating they segregate to the liquid during solidification.) Thus, as solidification proceeds, the liquid composition moves away from the Ni corner, becoming progressively richer in Nb and C until the line of two fold saturation between γ and NbC is reached. At this point, the maximum solubility of Nb and C in the austenite matrix is exceeded and the γ and NbC form simultaneously from the liquid by a eutectic-type reaction as the liquid composition travels down the line of two fold saturation. This initial solidification sequence explains the broad exothermic peaks exhibited in the DTA scans, where the $L \rightarrow (\gamma + NbC)$ reaction occurred over a wide temperature range. Due to its' high C content (~9.5 wt%), the formation of NbC depletes the liquid of C while the Nb content of the liquid continues to increase. For Alloys 2, 3.5, and 4, solidification is completed along the line of two fold saturation between γ and NbC, as no Laves phase was observed in these alloys.

The completion of solidification prior to reaching a minimum in the liquidus surface (i.e., the proposed ternary eutectic point of four phase L-γ-NbC-Laves equilibrium in Figure 4.45) is rather unique. Flemings [4.16] points out that, for the case of two solutes with negligible diffusion rates in the solid, the liquid composition should become progressively enriched in solute until a local minimum is reached on the liquidus surface,

at which point the remaining liquid will transform to solid. The continued enrichment in liquid composition is a direct result of insignificant solute diffusion in the solid. This is readily evident by inspection of the Scheil equation (eq. 2.9), which predicts that the liquid composition, C_l, tends towards infinity as the remaining fraction liquid, f_l, goes to zero. Although the diffusivity of Nb in austenite is expected to be negligible [4.8, 4.11], the diffusion rate of C is likely to be high enough to significantly alter the solidification reaction from the ideal case proposed by Flemings, and solidification is completed before a local minimum is reached. This phenomenon will be analyzed in quantitative detail in the next chapter.

The initial reaction sequence is similar for the remaining alloys, except that solidification does not terminate with the L $\rightarrow$ (γ + NbC) reaction. Instead, the liquid composition continues to travel down the line of two fold saturation between γ and NbC, becoming progressively enriched in Nb (and depleted in C). According to the proposed Ni-Nb-C liquidus projection, solidification should terminate with the ternary L $\rightarrow$ (γ + NbC + Laves) reaction where the liquidus surface is at a minimum. Under this condition, the Laves and ternary γ and NbC phases should be intermixed. However, this type of structure is not observed in any of the alloys which form both the NbC and Laves phases (e.g., examine Alloys 8, 14, and 16). Instead, the γ/NbC and γ/Laves eutectic-type constituents are always distinctly separated. This suggests that the pseudo-ternary liquidus projection for the alloys in this work are more properly represented by a class II reaction [4.17].

In this case, the local minimum on the liquidus surface occurs where the line of two fold saturation separating the γ and Laves phases intersects the Ni-Nb binary side of the diagram. The solidification sequence for alloys with this type of surface would occur as follows. After primary γ solidification, the liquid composition travels along the line of two fold saturation separating the γ and NbC phases during the $L \rightarrow (\gamma + NbC)$ reaction. This process continues until the class II reaction is reached, at which point the NbC stops forming as the $L \rightarrow (\gamma + NbC)$ reaction is replaced by the $L \rightarrow (\gamma + Laves)$ reaction. Solidification is completed at the Ni-Nb binary side of the diagram by the $L \rightarrow (\gamma + Laves)$ reaction. This solidification sequence accounts for the two spatially separate γ/NbC and γ/Laves eutectic-type constituents which are observed experimentally.

Note that the $L \rightarrow (\gamma + Laves)$ reaction is present in the high Nb nickel base alloys and all the iron base alloys, but not the high C/low Nb nickel base alloys (Alloys 2, 3.5, and 4). Reference to the Ni-Nb-C liquidus surface indicates that, in order for the $L \rightarrow (\gamma + Laves)$ to occur, the liquid must become sufficiently enriched in Nb so that the class II reaction is reached. As discussed in more detail in the next chapter, alloys that have nominal compositions with high C/Nb ratios will exhibit a primary $L \rightarrow \gamma$ solidification path which extends far into the C rich side of the liquidus surface. Thus, the liquid composition of these alloys must "travel" a relatively long distance along the γ/NbC two fold saturation line before the class II reaction is reached and γ/Laves can form. During this process, Nb in the liquid is consumed by the $L \rightarrow (\gamma + NbC)$ reaction. If the Nb content of the alloy is low to begin with, then solidification can go to completion before the class II reaction is reached. As a result, no γ/Laves eutectic-type constituent forms.

This explains the lack of Laves phase in the Ni base alloys with high C/Nb ratios (Alloys 2, 3.5, and 4). The presence of Laves phase in Fe base alloys with similar C/Nb ratios is apparently due to the Laves forming tendency of Fe. The quantitative results displayed in Figure 4.34 show that, for similar Nb levels, the Fe base alloys form more of the γ/Laves constituent than the comparable Ni base alloys. In other words, less Nb is required to form a given level of Laves when the Fe content of the alloy is high. This effect would explain the formation of Laves in the Fe base alloys with high C/Nb ratios.

The Ni-Nb-C liquidus projection, together with results from DTA and microstructural characterization, provide a qualitative interpretation of the solidification behavior of these alloys. This information forms the basis for developing a model for quantitative prediction of microstructural evolution during solidification. The main objective of such a model is to predict the composition and relative fractions of all phases forming during the entire solidification process. Several key elements are required to construct such a solidification model. These include solidification parameters related to both the alloy system and processing conditions, a liquidus surface to identify the lines of two fold saturation separating primary phases fields, and an appropriate solute redistribution model which accurately describes solutal transport in the liquid and solid during solidification. The remainder of this chapter is dedicated to determining the first two elements of the solidification model: alloy/process solidification parameters and diagrams representing ternary-type liquidus projections. Since the alloy systems in this research contain six elements (Fe,Ni,Cr,Nb,Si,C), the term "ternary liquidus projection" can not be properly applied. In addition, the experimental data utilized to construct such

projections will be derived from welds prepared under non-equilibrium conditions. Thus the term "pseudo-ternary solidification surface" more appropriately describes these diagrams. The potential effects of solute diffusion in the solid is also quantitatively treated both theoretically and, where possible, experimentally. This information forms the basis for developing the appropriate solute redistribution model. In the next chapter, this information is then applied to develop a solute redistribution model for these experimental superalloys. A conventional model, which is well recognized in the solidification literature, is first outlined as a starting point. This model is then modified to account for particular characteristics of the alloy systems under study in this investigation. Results of the model are then compared to experimental measurements.

4.3 SOLIDIFICATION PARAMETERS

The solidification parameters which are important for quantitative modelling of microstructural evolution include parameters related to both the alloy system and processing conditions. In terms of the alloy system, the distribution coefficients and diffusivities for the pertinent solutes in the solid must be known for the solidification model to be developed in this study. Important solidification parameters related to the process include the temperature gradient, cooling rate, and growth rate of the solid/liquid interface. All of these parameters will now be determined for the alloys and processing conditions applicable to this study.

4.3.1 PROCESSING SOLIDIFICATION PARAMETERS

The temperature gradient, G, solid/liquid interface growth rate, R, and cooling rate, ε, are related by

$$\epsilon = GR \qquad (4.1)$$

Thus, knowledge of any two of these parameters permits calculation of the third. The relation in eq. (4.1) is most easily interpreted in solidification conditions of welding by noting that the temperature gradients surrounding the weld pool move at a rate which is governed by the travel speed of the heat source. As the temperature gradients (dT/dx) move a small distance (dx) over an incremental time (dt), (where dx/dt is related to the heat source travel speed) the temperature at any point changes by dT, producing a corresponding cooling rate, dT/dt. Thus, the product of the temperature gradient and growth speed is numerically equivalent to the cooling rate.

As shown schematically in Figure 4.46, the travel speed of the heat source, S, and the solid/liquid interface growth rate can be related by

$$R = S \cos \theta \qquad (4.2)$$

At the weld centerline, cos θ = 1 and the growth rate of the solid/liquid interface is equivalent to the travel speed of the heat source. Under steady-state conditions, this equality must hold. Otherwise, the size of the weld pool would vary during welding. For

example, if R was less than S at the weld centerline, then the weld pool would gradually increase in length as welding progressed. The fact that the weld pool length remains constant confirms that R = S at the weld centerline. Deviations form this behavior can occur at very high travel speeds [4.18]. Small corrections may be also needed to account for the fact that the actual growth rate direction may not be precisely perpendicular to the solid/liquid interface [4.19]. Such minor factors need not be considered in the estimations which will be made here.

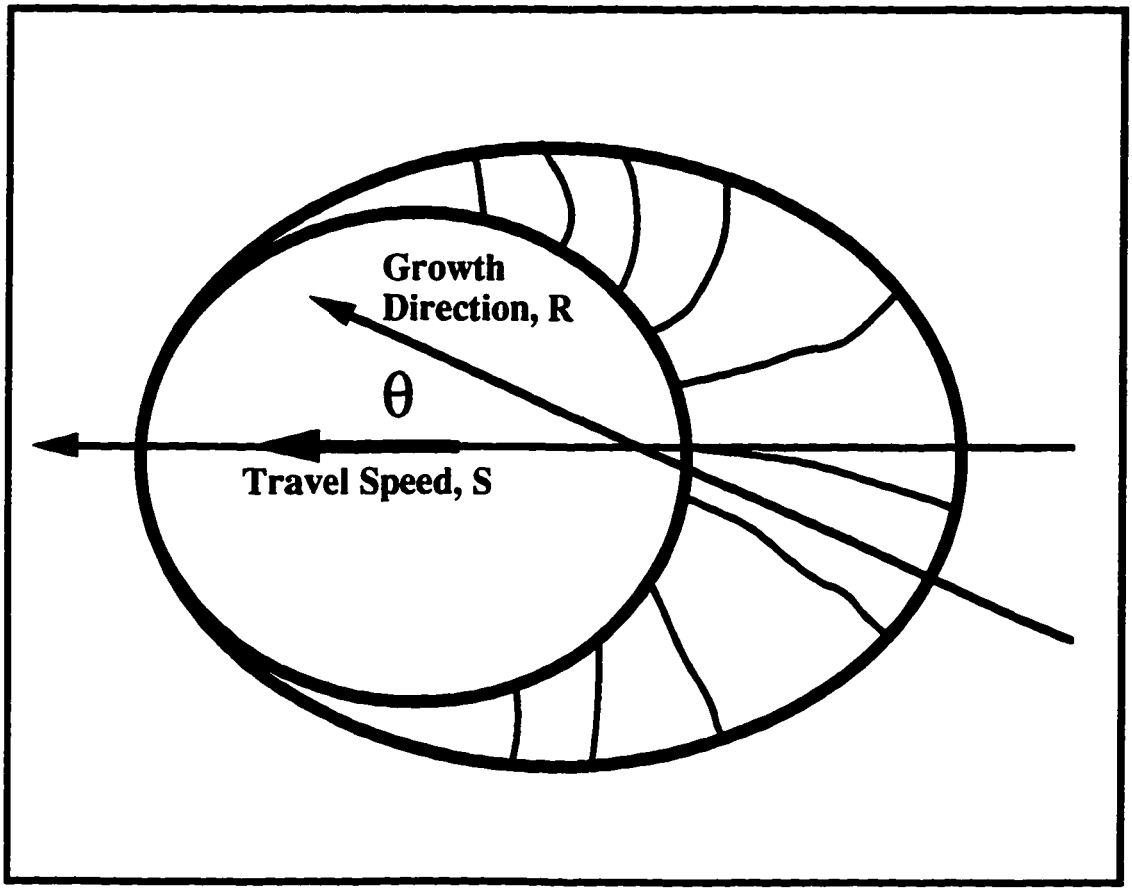

Figure 4.46.Relation between heat source travel speed and S/L interface growth rate

In this work, the cooling rate is the key parameter which must be determined. The cooling rate controls the time available for possible back diffusion of solute into the solid during solidification which, in turn, affects the amount of solute rejected to the liquid. The cooling rate of the weld metals prepared in this study are estimated by experimental and analytical methods below. These results are then used to determine the relative back diffusion potential of Nb and C.

The cooling rate in the welds can be determined experimentally through measurements of the dendrite arm spacing, λ, using the following semi-empirical relation developed for type 310 stainless steel [4.20]:

$$\lambda = 80\varepsilon^{-0.33} \qquad (4.3)$$

where λ is in μm and ε is the cooling rate in °C/s. Type 310 stainless steel has a nominal composition of Fe-21Ni-25Cr, which is close to the matrix composition of the Fe-base alloys used in this work (Fe-32Ni-19Cr). Thus, by measuring the dendrite arm spacing in Alloys 9 through 12, the cooling rate can be estimated via eq. (4.3).

Table 4.8 summarizes the results of dendrite arm spacing measurements on Alloys 9 through 16. These measurements were conducted on dendrites near the weld centerline. As expected, there is no significant difference in the λ values from individual alloys. The average λ of all the alloys is 9.2 ± 0.8 μm, and the values exhibit a range of 8.4 to 10.4 μm. Use of these values in eq. (4.3) indicates that, under these processing conditions, the welds in Alloys 9 through 16 cool at a rate of 460 to 860 °C/s (average = 660 °C/s). The potential for using these cooling rate values for the Ni base alloys is discussed below.

Table 4.8 Summary of dendrite arm spacing measurements.

Alloy	λ, μm	Alloy	λ, μm
9	10.2 ± 0.8	13	8.5 ± 1.1
10	9.4 ± 1.3	14	9.4 ± 1.0
11	10.4 ± 0.9	15	9.0 ± 1.6
12	8.6 ± 2.2	16	8.4 ± 1.3
Average of all measurements: λ = 9.2 ± 0.8 μm Range: λ = 8.4 to 10.4 μm			

The cooling rate in the welds can also be estimated analytically via the Rosenthal heat flow equation [4.20a]

$$T - T_o = \frac{\eta_a VI}{2\pi kr} \exp\left[\frac{-S(r-x)}{2d}\right] \qquad (4.4)$$

where T is temperature, T_o is the initial temperature, k is thermal conductivity, η_a is the arc efficiency, VI is the arc power, d is thermal diffuivity, S is the travel speed, and r is the radial distance from the heat source, given as $r = (x^2 + y^2 + z^2)^{1/2}$. Eq. (4.4) defines the temperature (T) at any location (r) from the heat source. As previously mentioned, the cooling rate of interest to this study is that at the weld centerline. This location is particularly important since the growth rate of the solid/liquid interface, R, is equivalent to the travel speed, S, at this point. In addition, the maximum crack length measured during varestraint testing typically occurs at the weld centerline because the solid + liquid region behind the weld pool is the largest at this location. For these reasons, the dendrite

arm spacing measurements and quantitative image analysis (discussed in the previous section) were both conducted along the weld centerline.

At the weld centerline, y = z = 0, r = x, and eq. (4.4) simplifies to

$$T - T_o = \frac{\eta_a VI}{2\pi kx} \qquad (4.5)$$

The temperature gradient along the weld centerline is given by the partial derivative of (4.5) with respect to x

$$G = \frac{\partial T}{\partial x} = -\frac{2\pi k\ (T - T_o)^2}{\eta_a VI} \qquad (4.6)$$

As noted in eq. (4.1), the cooling rate is given by the product of temperature gradient (G) and growth rate (R) and, at the weld centerline R = S (eq. 4.2). Thus, at the weld centerline

$$\epsilon = GS = -\frac{2\pi k\ S(T - T_o)^2}{\eta_a VI} \qquad (4.7)$$

Eq. (4.7) is useful to this study in two ways. First, it provides an analytical expression for estimating the cooling rate at the weld centerline when the welding

parameters are known. The welding parameters are summarized in Table 3.4. Second, eq. (4.7) indicates that, in terms of material properties, the cooling rate should be controlled by the thermal conductivity. Figure 4.47 shows the thermal conductivity for 310 stainless steel [4.21] and Inconel X [4.22] as a function of temperature. As previously mentioned, 310 stainless steel has a nominal composition close to that of Alloys 9 through 16. Thus, the thermal conductivity values for 310 stainless steel shown in Figure 4.47 should be close to those of the Fe base alloys in this study. Inconel X has a nominal alloy composition of Ni-16Cr-7Fe, which is close to the Ni base alloys. Considering the similarities in thermal conductivities between the two alloy types, combined with the fact that the cooling rate is controlled by thermal conductivity through eq. (4.7), the cooling rate estimation made on Alloys 9 through 16 via dendrite arm spacing measurements should provide a good representation of the cooling rate in Alloys 1 through 8 as well.

The limitations of eq. (4.7) must be understood before it is used for quantitative cooling rate calculations. This relation was derived assuming that thermo-physical properties do not vary with temperature and melting does not occur. Thus, variations in thermal conductivity with temperature (Figure 4.47) and the enthalpy required for melting (and subsequently released during solidification) are ignored. Nevertheless, the relation provides an order-of-magnitude estimation of the cooling rate and serves as a check on the cooling rate values determined through dendrite arm spacing measurements.

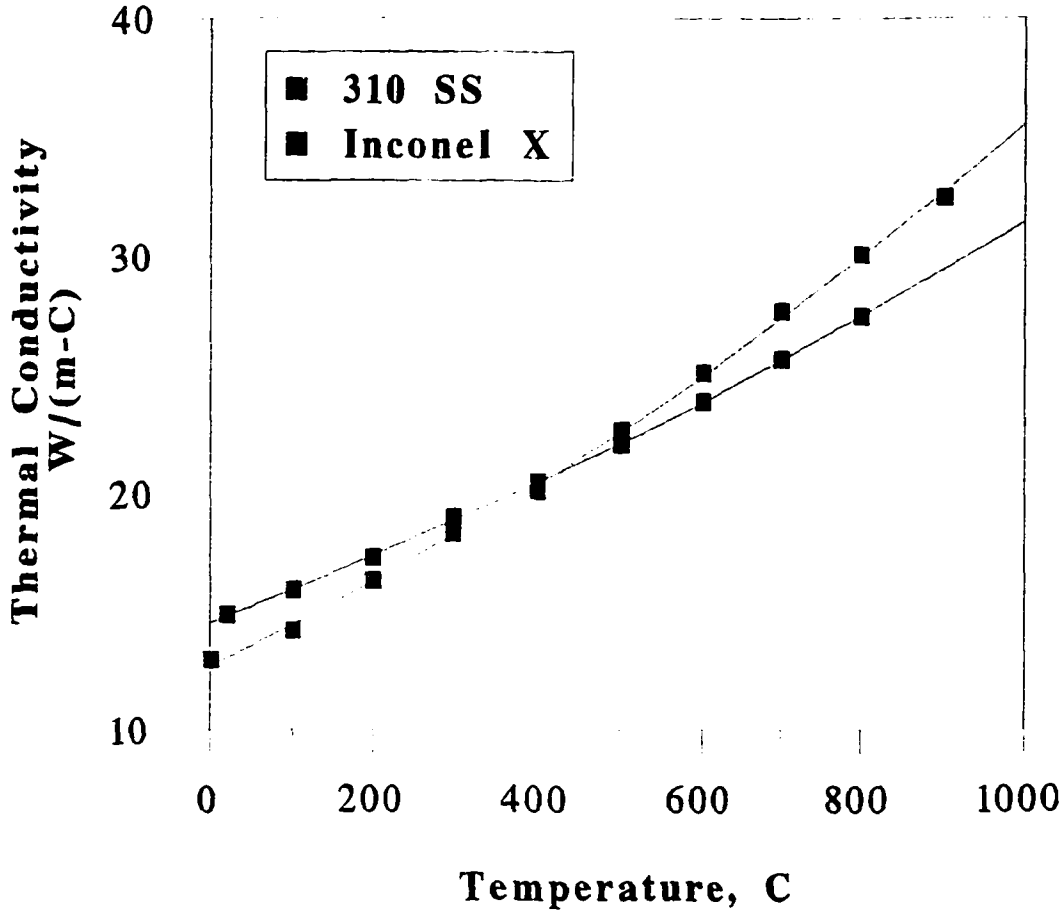

Figure 4.47. Thermal conductivity for 310 stainless steel and Inconel X as a function of temperature.

The temperature surrounding the weld pool varies from the liquidus to ambient. Thus, heat flow around the weld pool, and the corresponding cooling rate, is controlled by the full range of thermal conductivity values displayed in Figure 4.47. In view of this, an "average" thermal conductivity value of 25 W/(m•°C) is selected to represent the actual range which is operable during welding. Use of this value in eq. (4.7) along with the welding parameters listed in Table 3.4, and a value of $\eta_a = 0.8$ for the GTAW process at 95 A [4.23], the cooling rate at 1200°C and 1400°C (the solidification range of these alloys) is approximately 940 °C/s and 1290 °C/s, respectively. These values are in reasonable agreement with those determined via eq. (4.3) of 460 °C/s to 860 °C/s and serve as a check on the cooling rates determined through dendrite arm spacing measurements. The cooling rate determined through the dendrite arm spacing values will be utilized in preference to the calculated values from eq. (4.7), since they are derived from experimental data and require no assumptions concerning constant thermo-physical properties.

4.3.2 ALLOY SOLIDIFICATION PARAMETERS

4.3.2.1 EQUILIBRIUM DISTRIBUTION COEFFICIENTS

For a solute which exhibits linear liquidus and solidus slopes, the distribution coefficient is defined by

$$k_i = \frac{m_{l,i}}{m_{s,i}} = \frac{C_{s,i}}{C_{l,i}} \qquad (4.8)$$

where m_l and m_s are the liquidus and solidus slopes, respectively, and C_s and C_l are the solid and liquid composition at any point during the solidification process. The subscript i refers to the *ith* solute in the system. The liquidus and solidus slopes, and hence distribution coefficient, can be measured by conducting DTA on alloys with systematic variations in solute content.

Liquidus and solidus temperatures were determined by conducting slow heating rate (5°C/min) DTA scans on each alloy. As discussed in Chapter 3, accurate solidus temperatures could only be measured on Alloys 1, 1.5, 3, 5, and 7. Figure 4.48 shows a heating curve for Alloy 3 which is typical for all these alloys that were homogenized prior to testing. On heating, a large endothermic peak associated with melting of the austenite matrix is initiated at 1366°C. Consistent with conventional DTA interpretations [4.14, 4.24], the liquidus temperature is represented by the maximum on the peak occurring at 1413°C. The DTA heating trace for Alloy 12, which was typical of the remaining alloys, is presented in Figure 4.49. As discussed in the previous sections, Alloy 12 forms the γ/NbC eutectic-type constituent during solidification. Thus, this constituent is present in the as-cast sample utilized for DTA testing. On heating, the γ/NbC liquation reaction is initiated at 1329°C and is complete at 1364°C. Upon continued heating, the liquidus temperature is reached at 1419°C. Liquidus and solidus temperatures for all the alloys used in this work are summarized in Table 4.9. The average and standard deviation of each reaction temperature were determined from at least three measurements, and the order of testing was randomized. The Ni base and Fe base alloys are matched to make comparisons among alloys with similar solute levels.

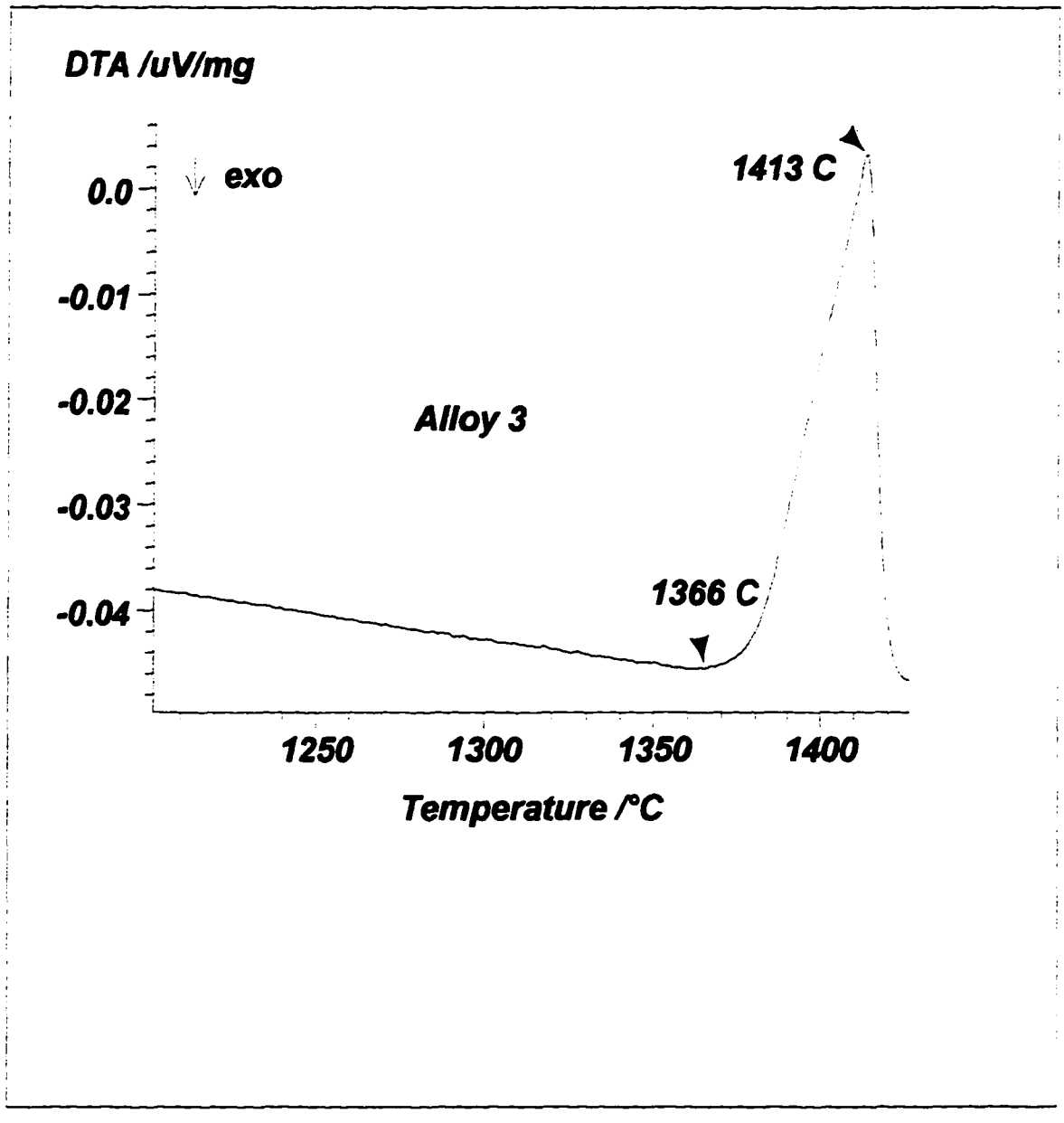

Figure 4.48. DTA melting scan of Alloy 3.

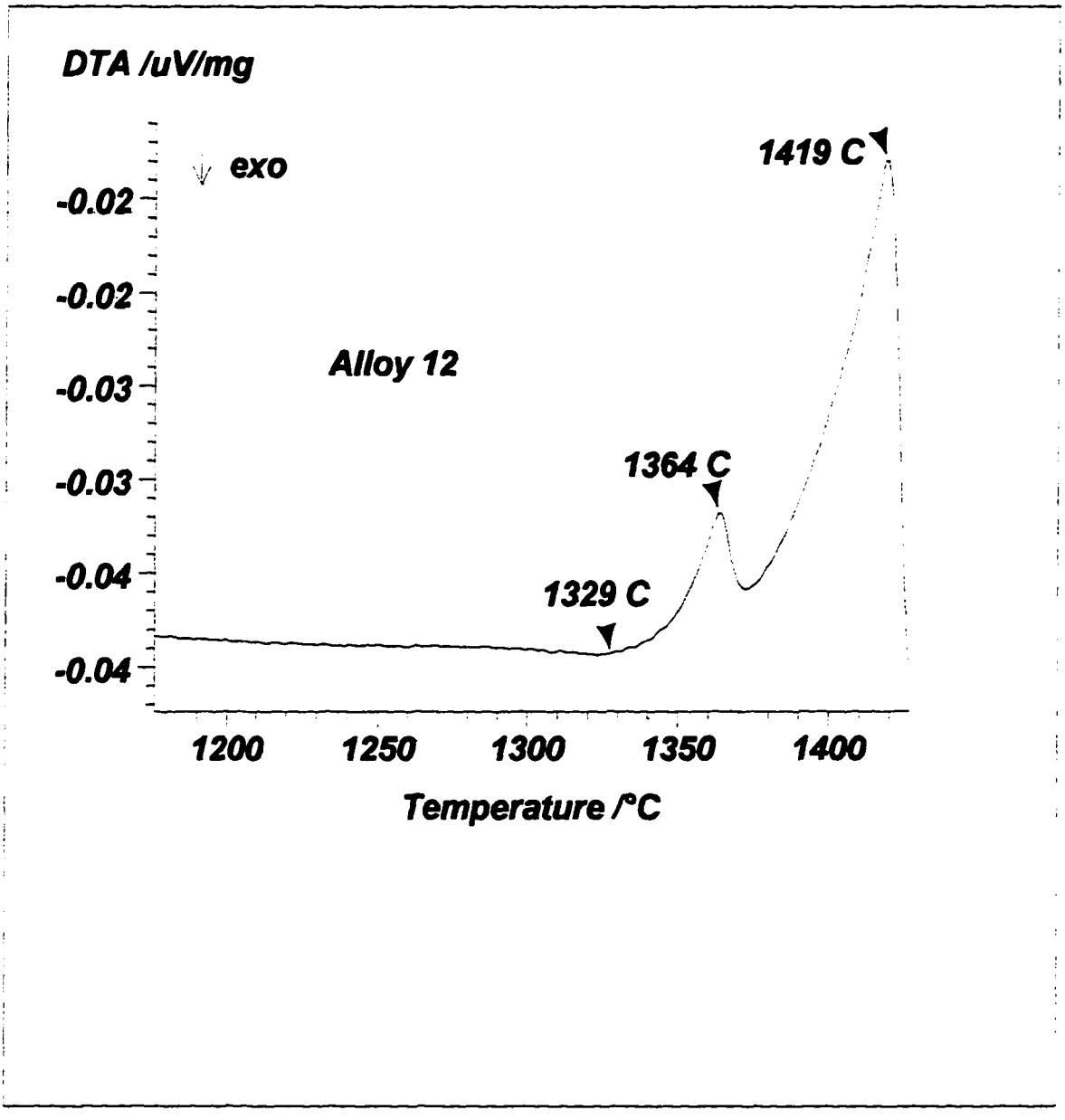

Figure 4.49. DTA melting scan of Alloy 12.

It is readily apparent that the Fe base alloys exhibit higher liquidus temperatures than the corresponding Ni base alloys. A similar trend was observed for the eutectic-type reactions which occur during solidification and is expected based on the higher melting point of Fe. More importantly, the data show that the addition of each solute element (Nb, Si, and C) lowers the liquidus and solidus temperatures (refer to Table 3.2 for alloy compositions). The effect of each element on the solidus and liquidus temperature can be expressed quantitatively by conducting multiple linear regression analysis on the DTA data. From this analysis, the following linear equations were obtained:

Ni Base Alloys:

$$T_s = 1413.6 - 17.9(wt\%Nb) - 36.2(wt\%Si) - 126(wt\%C) \quad \pm 1.2^{\circ}C \quad (4.9)$$

$$T_l = 1437.7 - 8.3(wt\%Nb) - 23.4(wt\%Si) - 34.1(wt\%\ C) \quad \pm 2.8^{\circ}C \quad (4.10)$$

Fe Base Alloys:

$$T_l = 1447.5 - 10.3(wt\%Nb) - 7.6(wt\%Si) - 38.2(wt\%\ C) \quad \pm 1.7^{\circ}C \quad (4.11)$$

Figure 4.50 plots the measured reaction temperatures versus those calculated using eqs. (4.9) through (4.11). The difference in measured and calculated temperatures never exceeds 2.8°C and is usually less than 1°C. Thus, the simple linear regression equations provide an accurate representation of the solutal effects. This result implies that

interactive effects among the solutes are negligible, as no cross product terms are required in the linear regression equations.

The liquidus slope of the *ith* element in any multi-component system is given by

$$m_{l,i} = \frac{\partial T_l}{\partial i} \qquad (4.12)$$

where T_l represents the liquidus equation. Similarly, the solidus slope is given by

$$m_{s,i} = \frac{\partial T_s}{\partial i} \qquad (4.13)$$

where T_s represents the solidus equation. Reference to eqs. (4.12) and (4.13) indicates that the coefficients in the liquidus and solidus linear regression equations take on rather important meanings, as they are numerically equivalent to the liquidus and solidus slopes for each solute in the respective matrix. Further, the ratio of the liquidus to solidus slope can now be readily calculated to determine the distribution coefficient of each solute (for the Ni base alloys only). These solidification parameters are summarized in Table 4.10. Note that the distribution coefficients for all the solutes in the Ni base alloys are less than unity. This indicates that these elements partition to the liquid during solidification. Since $k = C_s/C_l$, lower k values denote a stronger segregation tendency towards the liquid. Comparison of these values to literature data is made in a subsequent section.

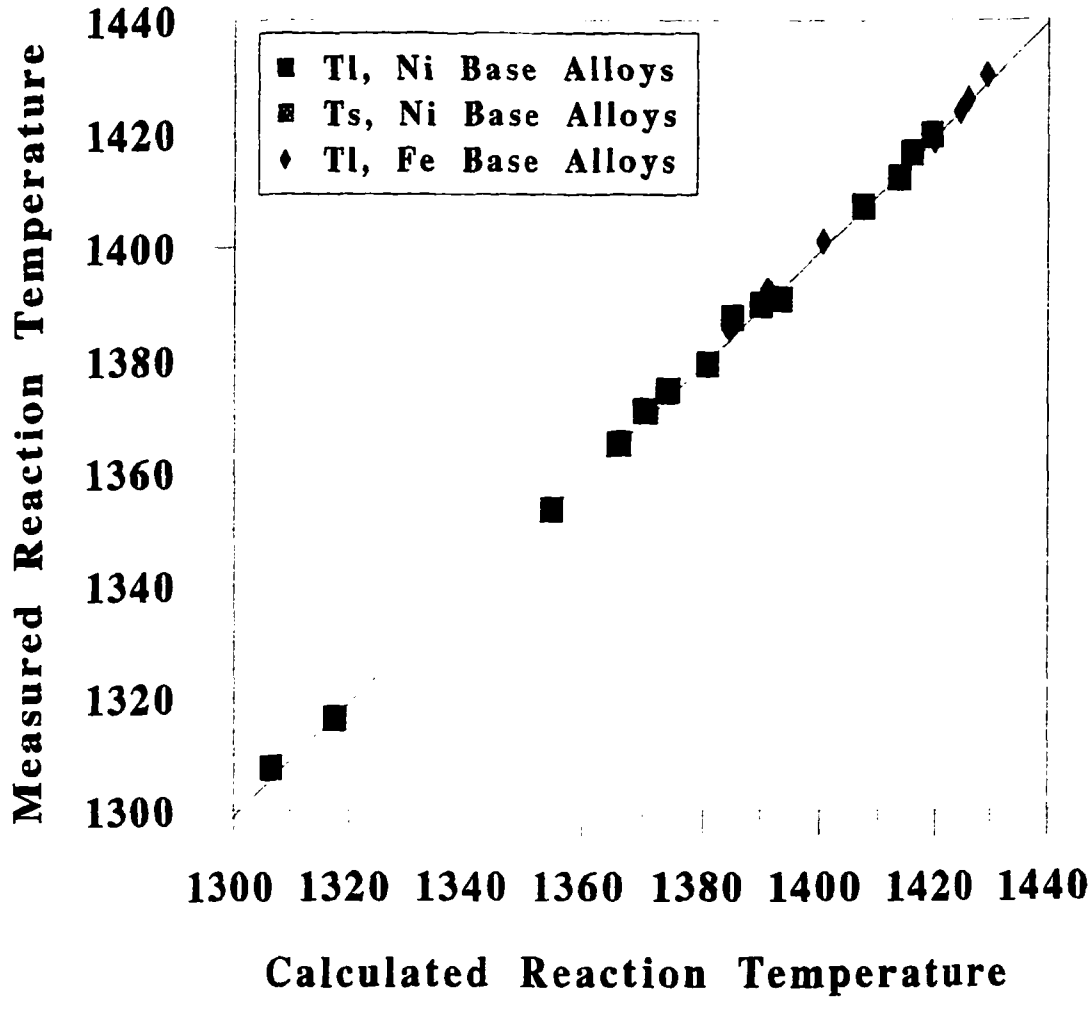

Figure 4.50. Comparison of measured reaction temperatures versus those calculated using eqs. (4.9) through (4.11).

Table 4.9 Summary of liquidus and solidus temperatures (all values in °C)

Alloy	Solidus	Liquidus	Alloy	Liquidus
1	1374.4 (0.5)	1420.0 (1.7)	9	1430.4 (0.9)
1.5	1371.0 (1.0)	1418.0 (0.3)	--	--
2	--	1416.7 (1.2)	10	1426.1 (0.8)
3	1365.3 (1.5)	1412.3 (0.6)	11	1423.9 (1.1)
3.5	1353.5 (0.7)	1410.5 (0.7)	12	1418.8 (0.2)
4	--	1407.3 (0.6)	11.5	1419.6 (1.2)
5	1316.5 (0.7)	1391.0 (1.0)	13	1401.1 (0.7)
6	--	1390.0 (1.0)	14	1392.0 (0.3)
7	1307.7 (1.5)	1387.7 (1.5)	15	1392.6 (0.6)
7.5	--	1382.0 (1.4)	--	
8	--	1379.3 (0.6)	16	1385.6 (0.3)

Table 4.10. Summary of solidification parameters determined through DTA data.

Solute	Ni Base Alloys			Fe Base Alloys
	Liquidus Slope, $m_{l,i}$ (°C/wt%)	Solidus Slope, $m_{s,i}$ (°C/wt%)	Distribution Coefficient ($m_{l,i}/m_{s,i}$)	Liquidus Slope, $m_{l,i}$ (°C/wt%)
Nb	-8.3	-17.9	0.46	-10.3
Si	-23.4	-36.2	0.65	-7.6
C	-34.1	-126	0.27	-38.2

4.3.2.2 SOLUTE DIFFUSIVITY CONSIDERATIONS

A. ANALYTICAL ANALYSIS

The Brody-Flemings model [4.25], described previously in section 2.2.2.3, can be used to estimate the significance of solid state diffusion which, for a parabolic growth rate, is given by:

$$C_s^* = kC_o[1 - (1-2\alpha k) f_s]^{\frac{k-1}{1-2\alpha k}} \qquad (4.14)$$

$$f_s = \left(\frac{1}{1 - 2\alpha k}\right)\left[1 - \left(\frac{T_m - T}{T_m - T_l}\right)^{\frac{1 - 2\alpha k}{k-1}}\right] \qquad (4.15)$$

$$\alpha = \frac{D_s t_f}{L^2} \qquad (4.16)$$

Here, D_s is the diffusivity of solute in the solid (assumed constant in the derivation of (4.14)), t_f is the local solidification time, and L is half the dendrite arm spacing. T_m is the melting point of the pure solvent and T_l is the liquidus temperature of the alloy. The back diffusion potential is dependent on the diffusion distance (L), the cooling rate during solidification which, in turn, controls the time available for diffusion (t_f), and the diffusivity of solute in the solid (D_s). If the diffusion distance of the solute is very short in relation to half the dendrite arm spacing ($\alpha << 1$), then solid state diffusion is negligible and equation (4.14) reduces to the Scheil equation. At higher values of α,

solute diffusion becomes significant and deviations from the Scheil equation can be expected.

The α parameter was calculated for Nb and C in order to estimate the significance of back diffusion for these two elements. These calculations require knowledge of the local solidification time (t_f) the dendrite arm spacing (2L), and the solute diffusivity (D_s). Assuming a constant cooling rate during solidification, the local solidification time is given by the ratio of solidification temperature range to cooling rate:

$$t_f = \frac{\Delta T}{\varepsilon} \qquad (4.17)$$

For most of the Ni base alloys, the DTA data showed that solidification terminated at ~1190°C with formation of the γ/Laves constituent. The highest liquidus temperature measured for the Ni base alloys (Alloy 1) was 1420°C. Similarly, the highest liquidus for the Fe base alloys is 1430°C, while solidification is complete with the $L \rightarrow (\gamma + \text{Laves})$ reaction at ~1240°C. Thus, ΔT for the alloys used in this study is ~200°C. With a solidification temperature range of 200°C and a cooling rate of 660°C/s, the local solidification time, t_f, is 0.3 sec.

The value of D_s chosen for estimating the significance of back-diffusion will obviously vary significantly with the temperature chosen. Calculations were made at both the highest liquidus and lowest terminal solidus for each matrix composition in order to bound the possible range of α. Values of D_s for Nb in a Ni base alloy were not available

in the literature. As an estimate, D_s values were determined from the diffusion data for Nb in γ Fe [4.26]: D_o = 7.5 x 10^7 μm/sec. and Q = 264 kJ/mol. D_s values for C were determined from the data by Bose and Grabke [4.27], where D_o values and activation energies were determined in a range of Fe-Ni alloys with varying carbon contents (0.05 wt% to 0.20 wt%). Carbon content was found to have no significant effect on the diffusion data. The values differed slightly with the matrix composition. The following values were used: 30Fe-70Ni (representative of Alloys 1-8): D_o = 8 x 10^6 μm/sec., Q = 135 kJ/mol, and 75Fe-25Ni (representative of Alloys 9-16): D_o = 5 x 10^6 μm/sec., Q = 125 kJ/mol. Table 4.11 summarizes the α values calculated for Nb and C at the limits of solidification. For these calculations, L = λ/2 = 4.6 μm and t_f = 0.3 sec.

Table 4.11. Summary of α values for Nb and C.

Solute	Temperature, °C	Ds, μm^2/sec.	α
Nb	T = 1430	0.60	0.009
	T = 1190	0.03	0.0004
C in 30Fe-70Ni matrix	T = 1420	550	7.8
	T = 1190	120	1.7
C in 75Fe-25Ni matrix	T = 1430	730	10.3
	T = 1240	240	3.4

These results suggest that, since $\alpha_{Nb} << 1$, Nb diffusion in the solid can be neglected under these conditions. This has been proposed in other research as well [4.8, 4.11], and experimental evidence supporting this is provided in the next section. In contrast, C diffusion needs to be considered in more detail as the calculated α values are well in excess of unity.

Klyne and Kurz [4.28] have demonstrated that the Brody-Flemings model (eqs. 4.15, 4.16, and 4.17) is valid provided solid state diffusion is relatively slow. They show that the model breaks down at α values above approximately 0.1 since, in the presence of a fast diffusing element, solute is no longer conserved within the volume element considered in derivation of the Brody-Flemings model. This is readily apparent by noting that the B-F model does not reduce to the equilibrium lever rule when $\alpha \rightarrow \infty$. Klyne and Kurz have proposed a modification to the B-F model by replacing the α term with α', where

$$\alpha' = \alpha\left[1-\exp\left(-\frac{1}{\alpha}\right)\right] - \frac{1}{2}\exp\left(-\frac{1}{2\alpha}\right) \qquad (4.18)$$

Use of this value correctly reduces the B-F model to the Scheil equation when $\alpha \rightarrow 0$ and to the lever rule as $\alpha \rightarrow \infty$.

The Klyne-Kurz model was used to estimate the significance of C diffusion during solidification. The case of carbon in the 30Fe-70Ni alloys will be considered since this condition is the farthest from equilibrium (α the smallest). The t_f and L values noted

previously were used (t_f = 0.3 sec. and L = 4.6 μm). For the case of a simple binary system, T_m in eq. (4.15) is the melting temperature of the pure solvent. In this work, T_m is represented by the value of the liquidus temperature of the (Fe,Ni,Cr) "solvent", which is the value given by the liquidus temperature equation (eq. 4.10) when Nb = Si = C = 0. Thus, T_m = 1437.7 °C. Use of this model also requires a value of k for C in the (Fe,Ni,Cr) matrix. This value was determined from the DTA data in Table 4.10 as k_C = 0.27. The D_s and the corresponding α and α' values were calculated at each temperature step during solidification starting at T_l = 1420°C. Once α' was established as a function of temperature, these values were used in eq. (4.15) to calculate f_s as a function of temperature. Once f_s was established as a function of temperature, these values were used to generate the C_s/f_s curve via equation (4.14).

Figure 4.51 shows the results of the calculations. Comparisons are made with the equilibrium lever law, where C_s and f_s are given by

$$C_s = \frac{kC_o}{f_s(k-1) + 1} \qquad (4.19)$$

$$f_s = \frac{1}{1-k}\left(\frac{T_l - T}{T_m - T}\right) \qquad (4.20)$$

and the Scheil equation

$$C_s^* = kC_o(1-f_s)^{(k-1)} \qquad (4.21)$$

$$fs = 1 - \left(\frac{T_m - T}{T_m - T_l}\right)^{\frac{1}{k-1}} \qquad (4.22)$$

These two conditions provide useful comparisons as they bound the possible extent of microsegregation during solidification. The significance of Figure 4.51 lies within the similarities between the equilibrium lever law and Klyne-Kurz model when C diffusivity is considered. These results demonstrate that, even under these high cooling rate conditions, the diffusivity of C in γ is high enough such that the equilibrium lever law can be applied with introduction of little error. This result is obtained by considering the diffusivity of carbon in the Ni base alloys. The Klyne-Kurz model results would be even closer to the equilibrium curve had the higher diffusivity of C in the Fe-rich alloys been considered. This behavior of C has been suggested in other work as well [4.28]. Thus, based on these results, the equilibrium lever law, given by eqs. (4.19) and (4.20), is assumed to be valid for describing the solute partitioning behavior of C during solidification.

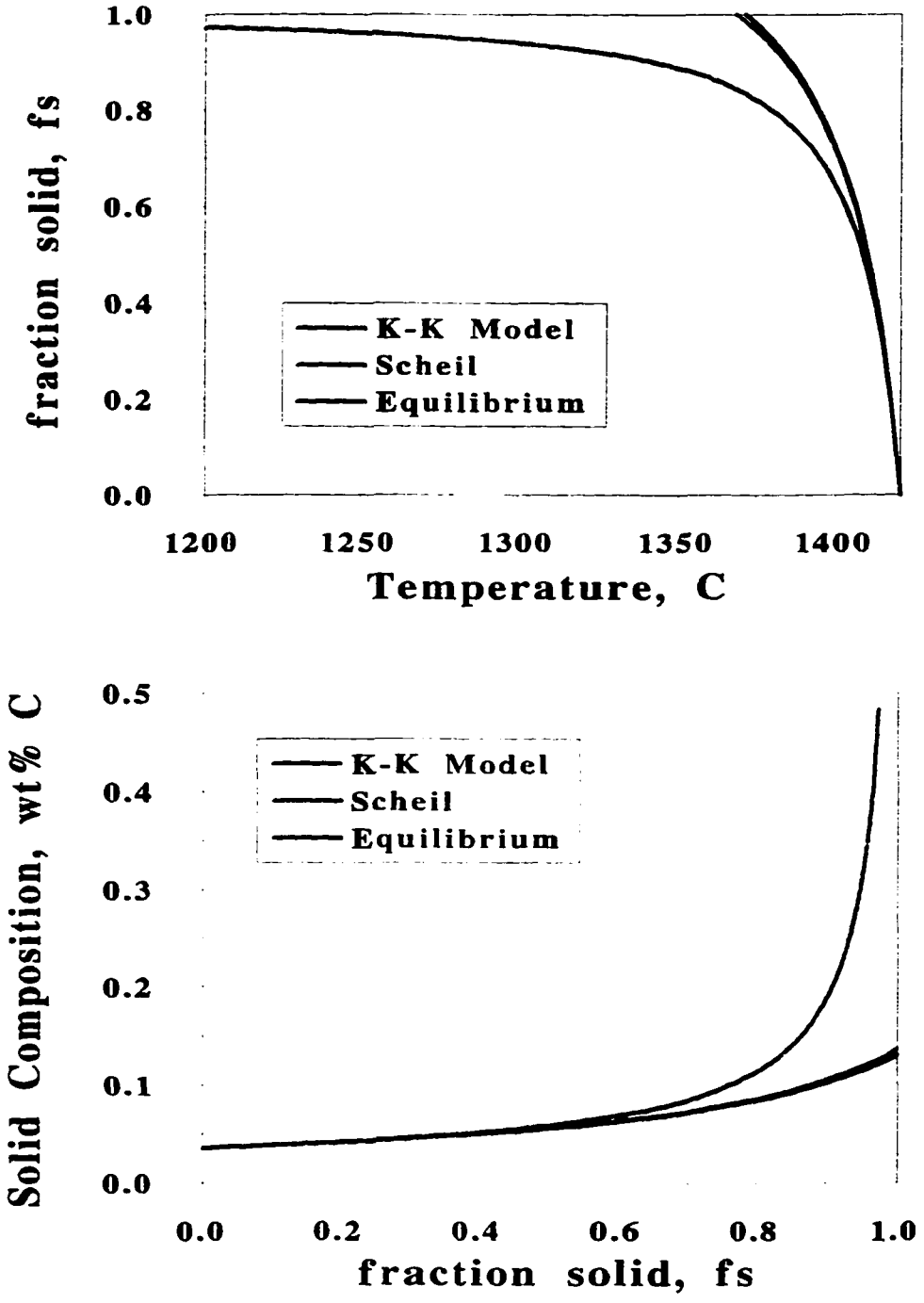

Figure 4.51. Results of solute redistribution calculations for conditions of negligible solid state diffusion (Scheil equation), equilibrium, and the Klyne-Kurz model.

B. EXPERIMENTAL VERIFICATION OF NEGLIGIBLE Nb DIFFUSION

The preceding analytical analysis indicates that diffusion of Nb in the γ dendrites can be neglected during solidification. This result can be experimentally verified by quenching experiments. With this approach, the tips of γ dendrites which are growing into the advancing liquid weld pool are quenched with a high pressure water jet. The quenching action freezes in the tip composition, which is the first solid to form. The dendrite tip composition is then measured using EPMA and compared to that of dendrite core compositions in welds which solidified under no forced cooling. If back diffusion is significant during welding, then the dendrite cores in the normally-cooled welds will exhibit a higher Nb content than the quenched dendrite tips.

Quenching experiments were conducted on Alloys 8 and 16. A typical quenched microstructure (for Alloy 8) is shown in the SEM photomicrographs of Figure 4.52. The front of quenched dendrite tips, as well as the quenched liquid, is readily evident in the figure. The quenched dendrite analyzed by EPMA is noted in the figure also. After SEM examination, this particular dendrite was marked for identification by a precision microscope scribe. The sample was then re-polished prior to EPMA in order to provide a flat surface for quantitative analysis. LOM photomicrographs showing regions of parallel dendrites analyzed by EPMA in normally-cooled welds of Alloys 8 and 16 are shown in Figure 4.53. A typical composition trace from the quenched dendrite shown in Figure 4.52 is presented in Figure 4.54. This trace was acquired perpendicular to the γ dendrite at a position approximately 8 μm from the tip. An EPMA trace conducted across normally cooled dendrites in the weld of Alloy 8 is provided in Figure 4.55. Similar plots

are provided for Alloy 16 in Figures 4.56 and 4.57.

The evolution of composition gradients in the γ dendrites is readily apparent in these figures. As previously discussed, the distribution coefficient for Nb is less than unity. Recall that $k_{Nb} = C_{s,Nb}/C_{l,Nb}$, or $C_{s,Nb} = k_{Nb}C_{l,Nb}$. At the start of solidification, the liquid composition is equivalent to the nominal composition, $C_{o,Nb}$. Thus, the first solid to form at the dendrite core, C_{core}, will exhibit a composition equal to $C_{core} = k_{Nb}C_{o,Nb}$. Since $k_{Nb} < 1$, the first solid to form will possess a composition less than the nominal alloy composition. As solidification proceeds, solute is rejected to the liquid, causing a progressive enrichment of Nb in the liquid. Assuming k_{Nb} is constant during solidification, which has been proven experimentally by Knorovsky *et al.*[4.8], the dendrite composition will gradually increase according to $C_{s,Nb} = k_{Nb}C_{l,Nb}$. Silicon displays similar behavior. This is expected, since $k_{Si} = 0.65$. The segregation potential for Si is less pronounced in the composition traces because k_{Si} is slightly higher than k_{Nb} and Si is present in only minor amounts. The "solvent" elements (Fe,Ni,Cr) generally segregate in the reverse direction, suggesting their k values are greater than unity.

Table 4.12 compares the dendrite core compositions of quenched and normally cooled welds. There is no significant difference among the dendrite core compositions of welds in the quenched or normally cooled condition. This characteristic is particularly important for Nb, as it allows use of the simple Scheil model for describing solute redistribution during solidification. It is worth noting that use of the Scheil equation for Nb has been justified both analytically (via calculation of the α parameter) and experimentally (through quench experiments).

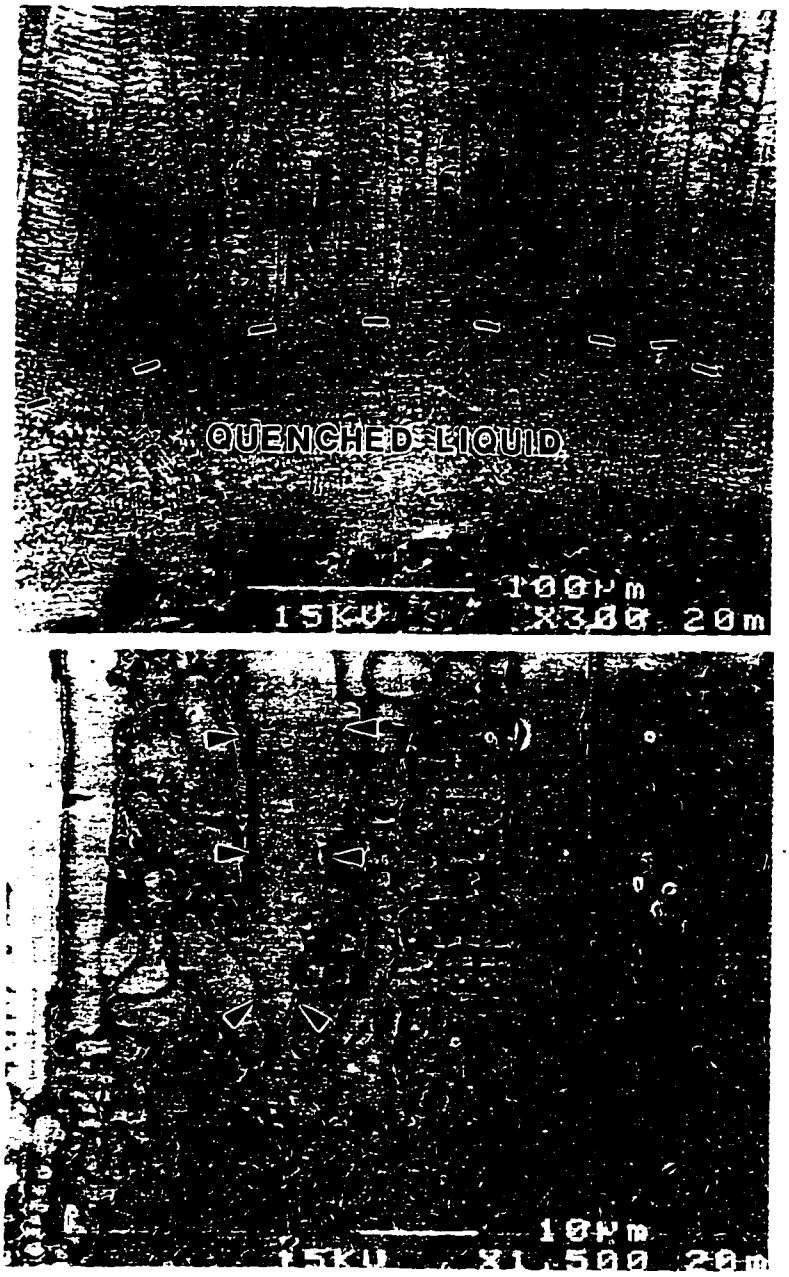

Figure 4.52. Quenched weld metal microstructure of Alloy 8.

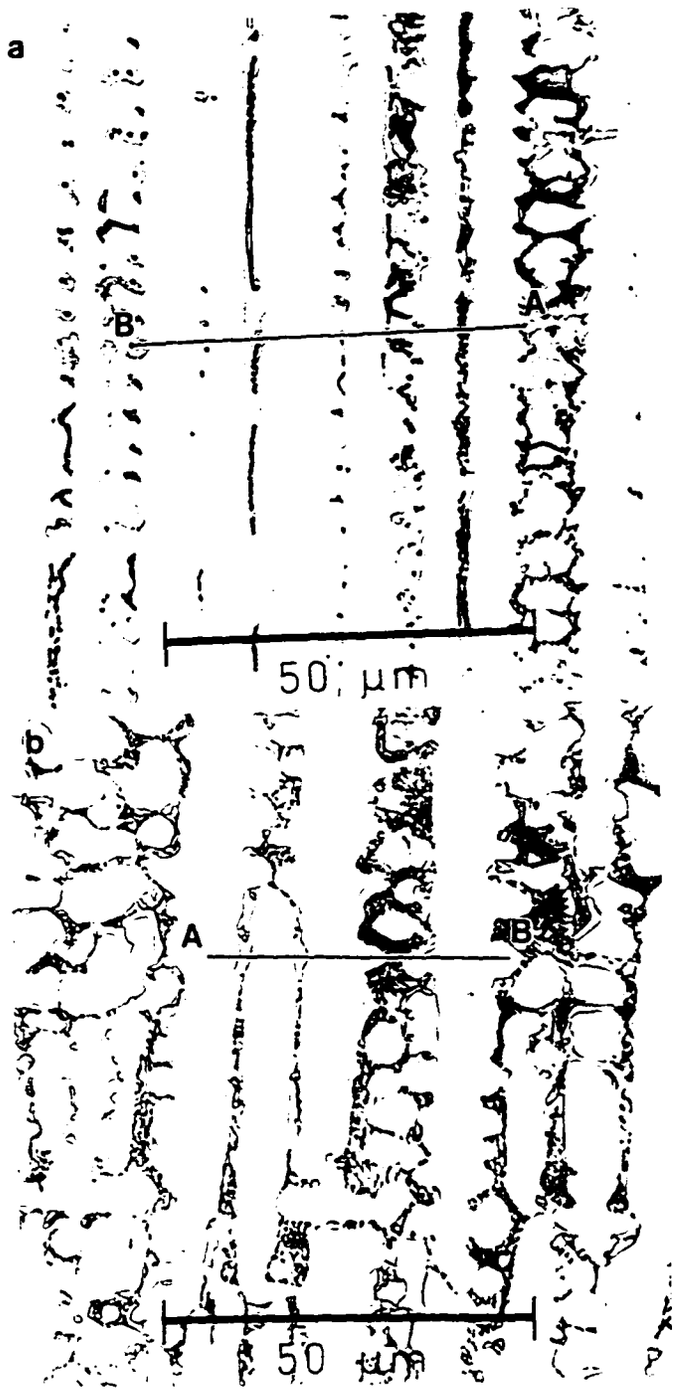

Figure 4.53. LOM photomicrographs showing regions of parallel dendrites analyzed by EPMA in normally-cooled welds of Alloys 8 (a) and 16 (b).

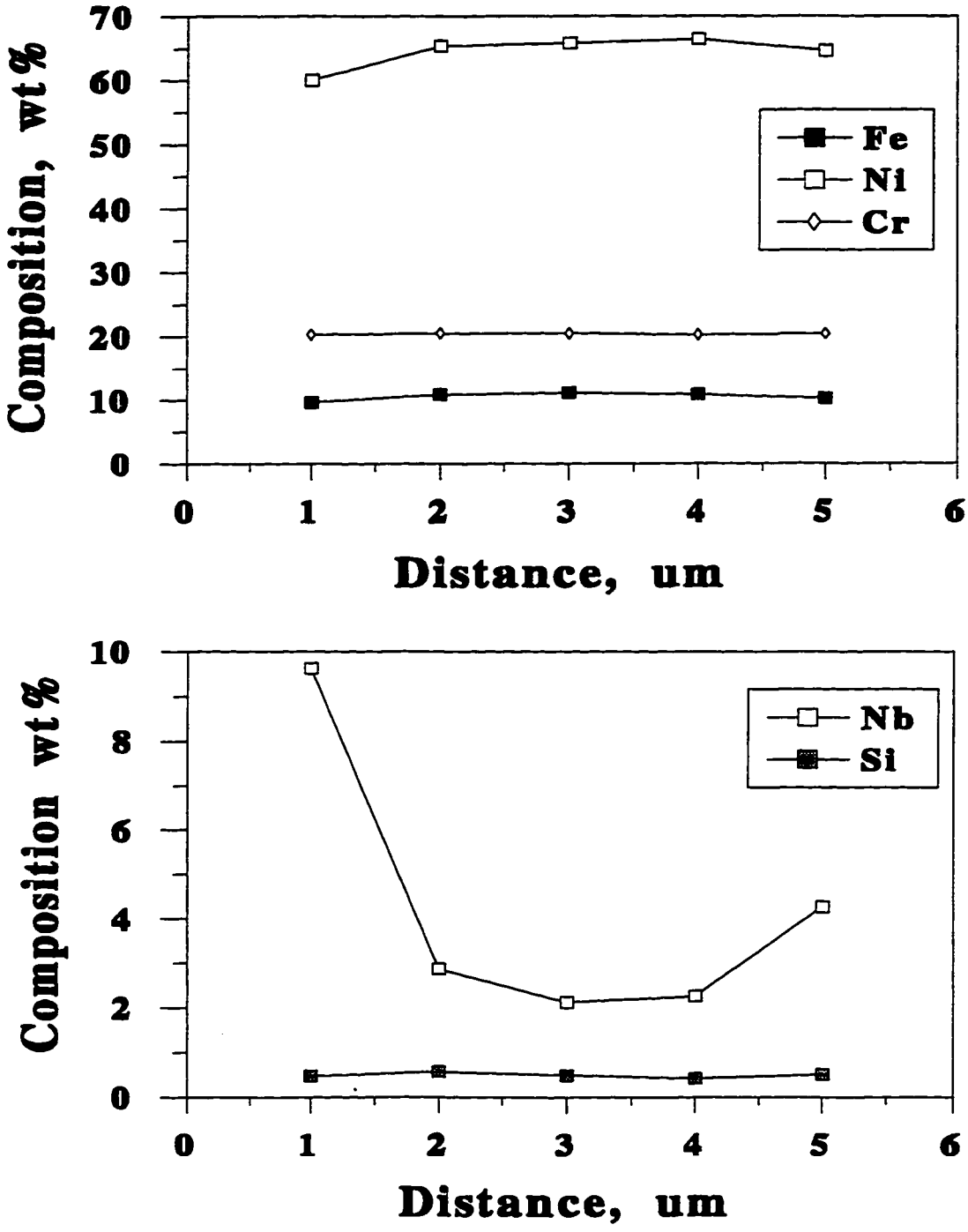

Figure 4.54. EPMA composition trace from the quenched dendrite in Alloy 8.

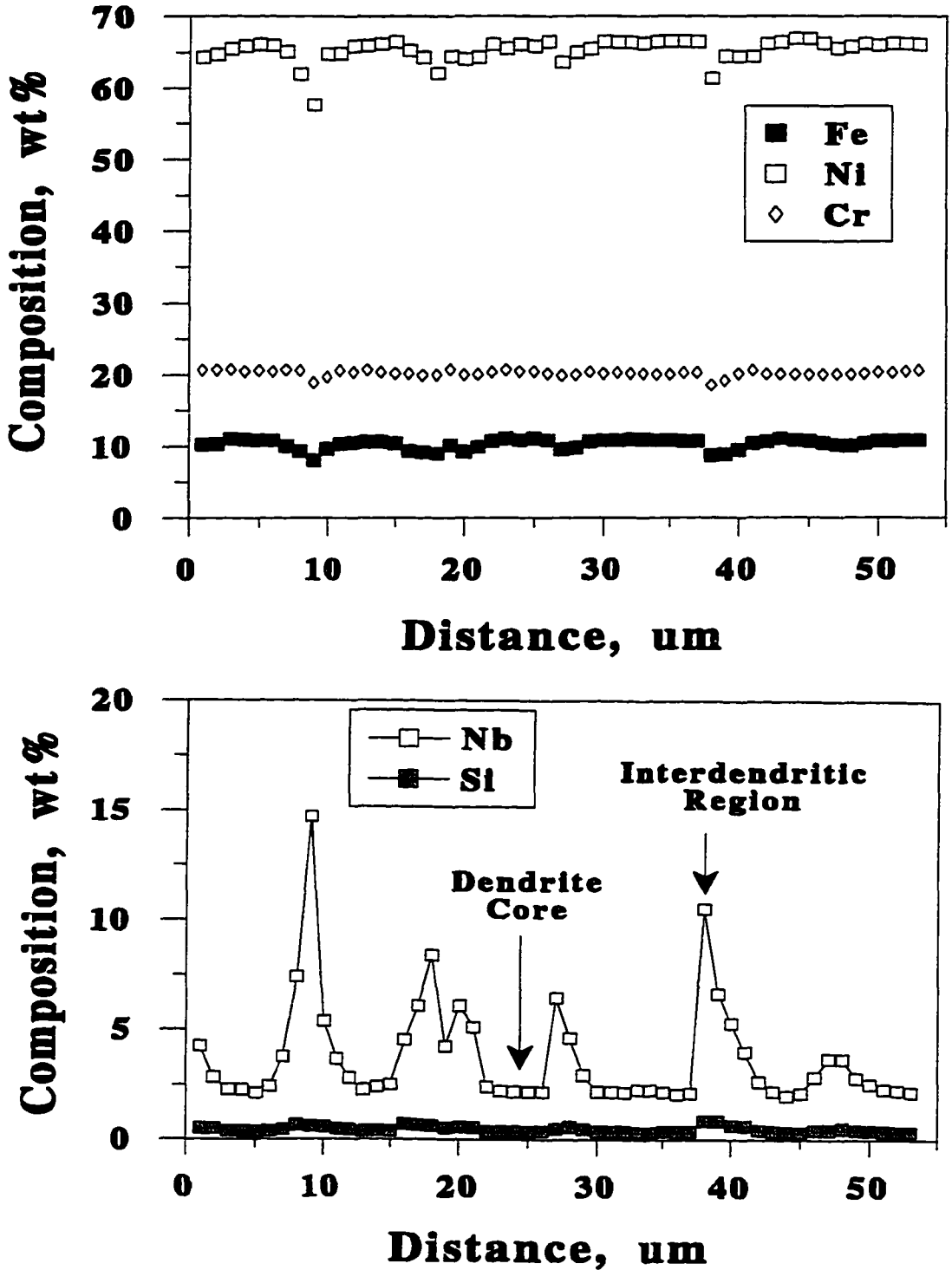

Figure 4.55. EPMA trace acquired across normally cooled dendrites in weld of Alloy 8.

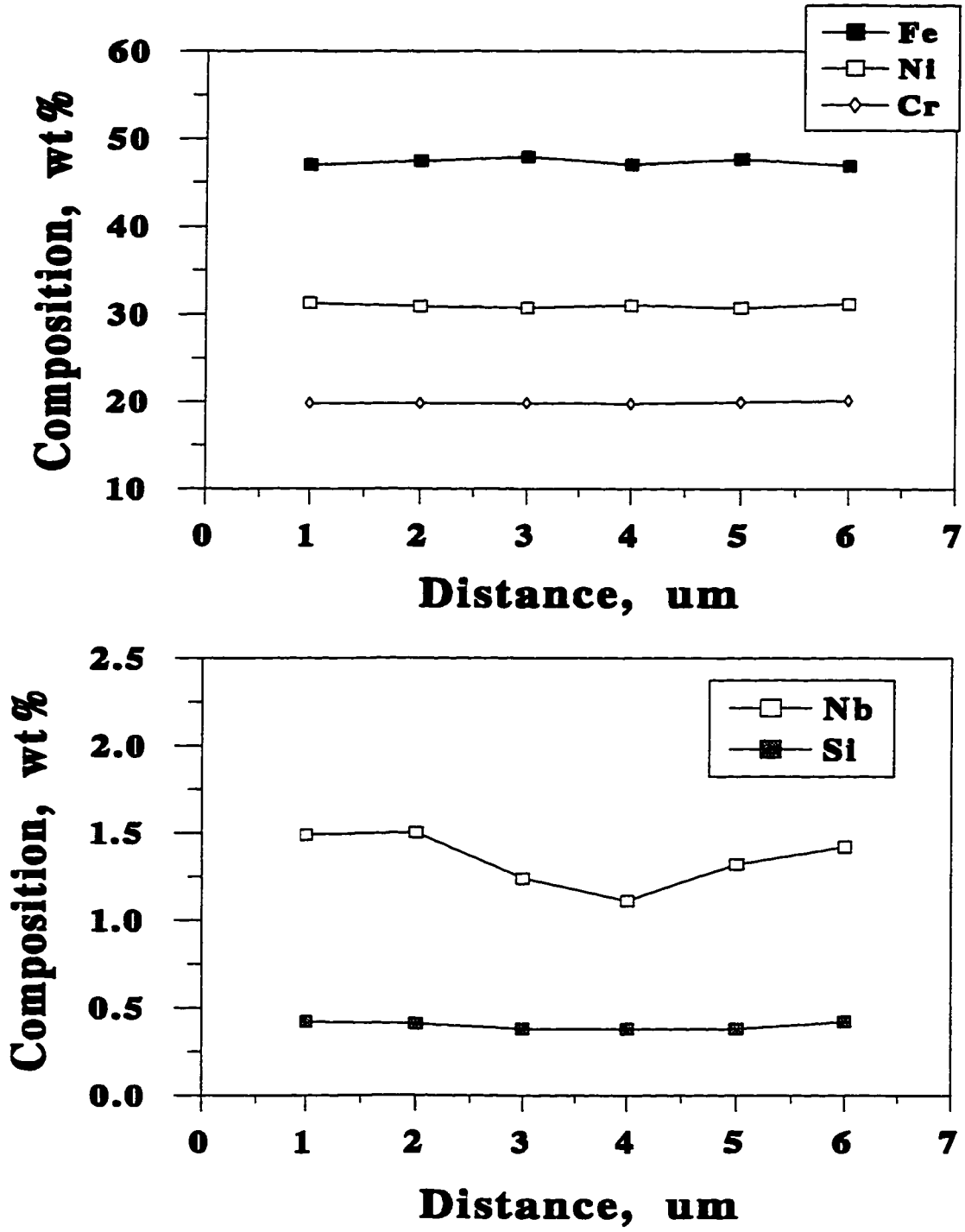

Figure 4.56. EPMA composition trace from a quenched dendrite in Alloy 16.

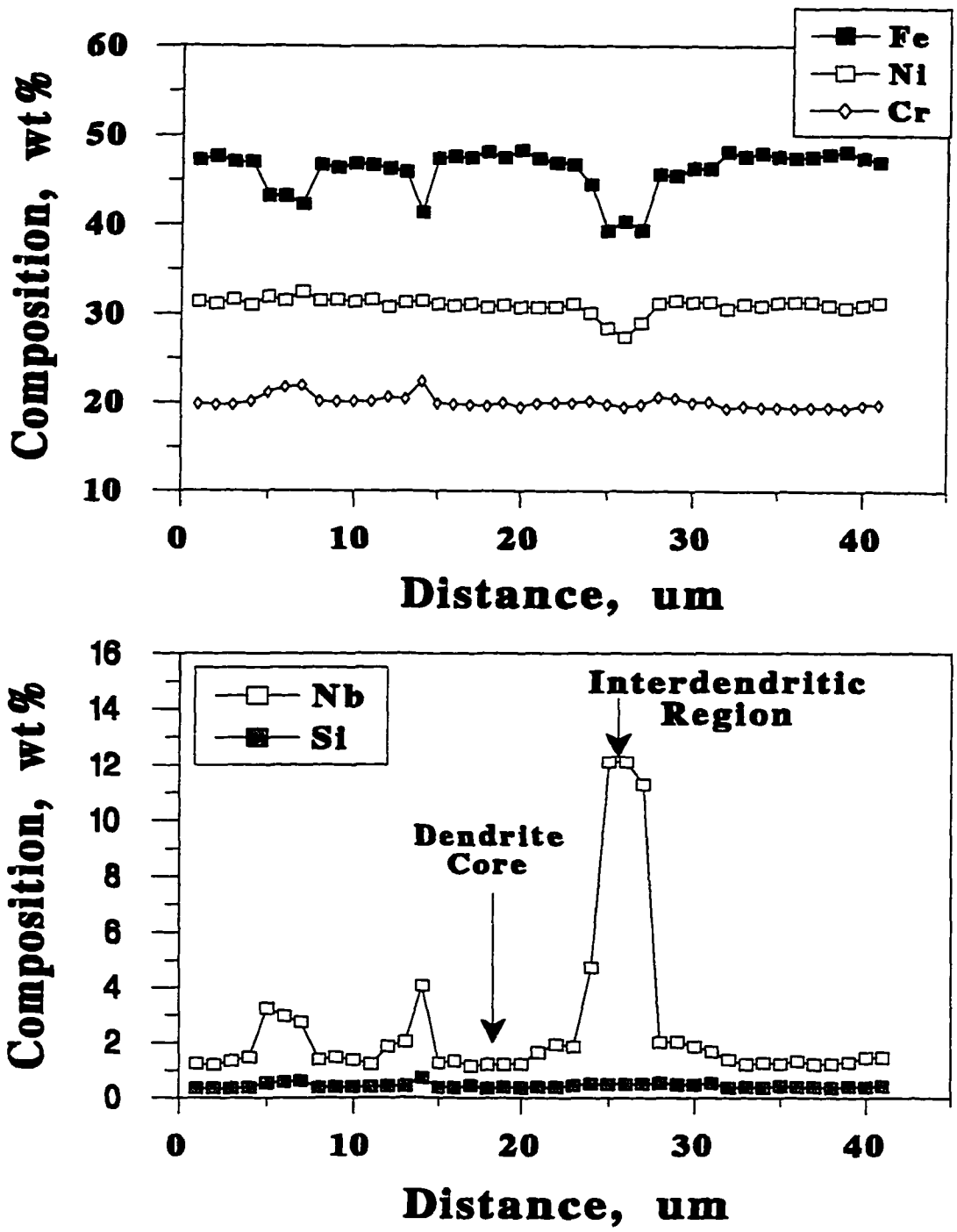

Figure 4.57. EPMA trace acquired across normally cooled dendrites in weld of Alloy 16.

Table 4.12 Comparison of dendrite core compositions in quenched and normally cooled welds.

Alloy/Sample	Fe	Ni	Cr	Nb	Si
Alloy 8 Quenched	10.8	65.8	20.5	2.13	0.42
Alloy 8 Normally Cooled	10.8	66.4	20.4	2.13	0.37
Alloy 16 Quenched	47.0	31.0	19.7	1.11	0.38
Alloy 16 Normally Cooled	47.5	31.1	19.8	1.21	0.39

Having shown that solid state diffusion is insignificant for the elements listed in Table 4.12, it is now possible to combine the Scheil equation and EPMA data to determine equilibrium distribution coefficients for these elements. At the onset of solidification, the following conditions apply: $f_s = 0$, $C_l = C_o$, and $C_s = C_{core}$. Using these initial solidification conditions in eq. (4.21) leads to

$$k = \frac{C_{core}}{C_o} \qquad (4.23)$$

where k is the equilibrium distribution coefficient at the beginning of solidification. Thus, the ratio of dendrite core concentration (determined by EPMA) to nominal concentration provides a value of k at the onset of solidification. In addition to the EPMA traces presented above, composition traces were also conducted across normally cooled weld metals in Alloys 4, 7, and 15. These results are shown in Figures 4.58, 4.59, and 4.60. The dendrite core and nominal compositions for all the alloys analyzed by EPMA are summarized in Table 4.13.

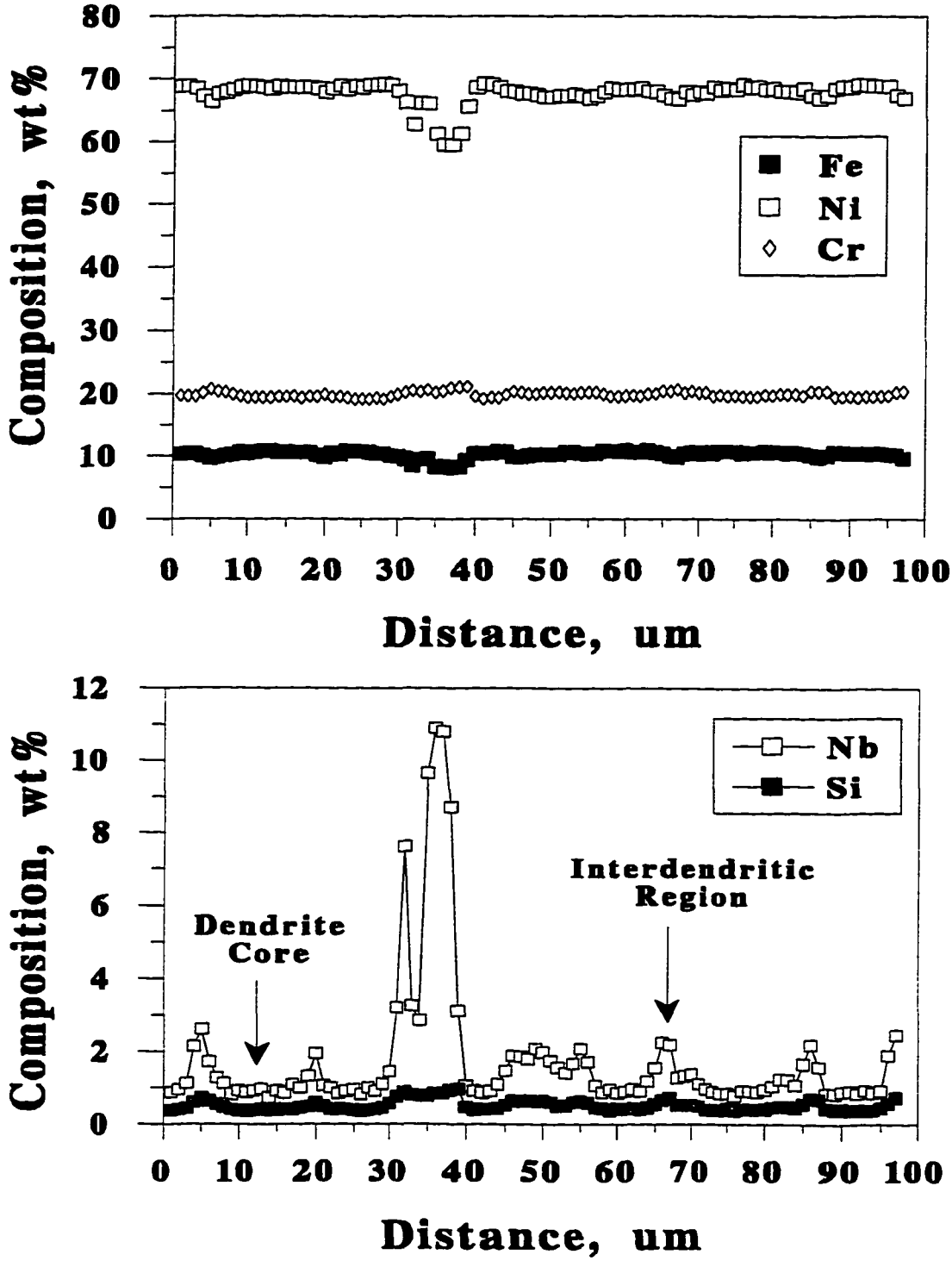

Figure 4.58. EPMA composition trace conducted across parallel dendrites in weld of Alloys 4.

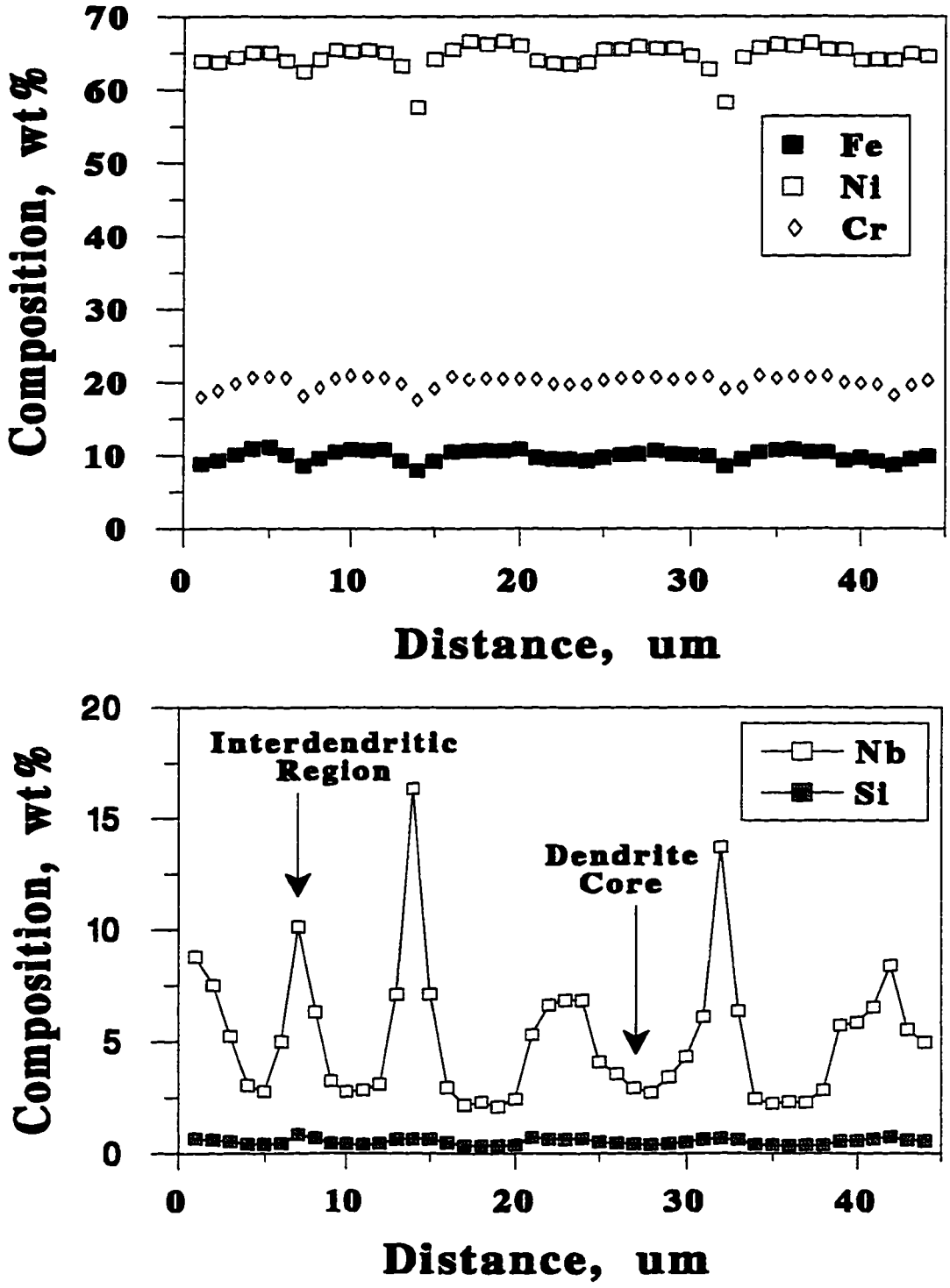

Figure 4.59. EPMA composition trace conducted across parallel dendrites in weld of Alloys 7.

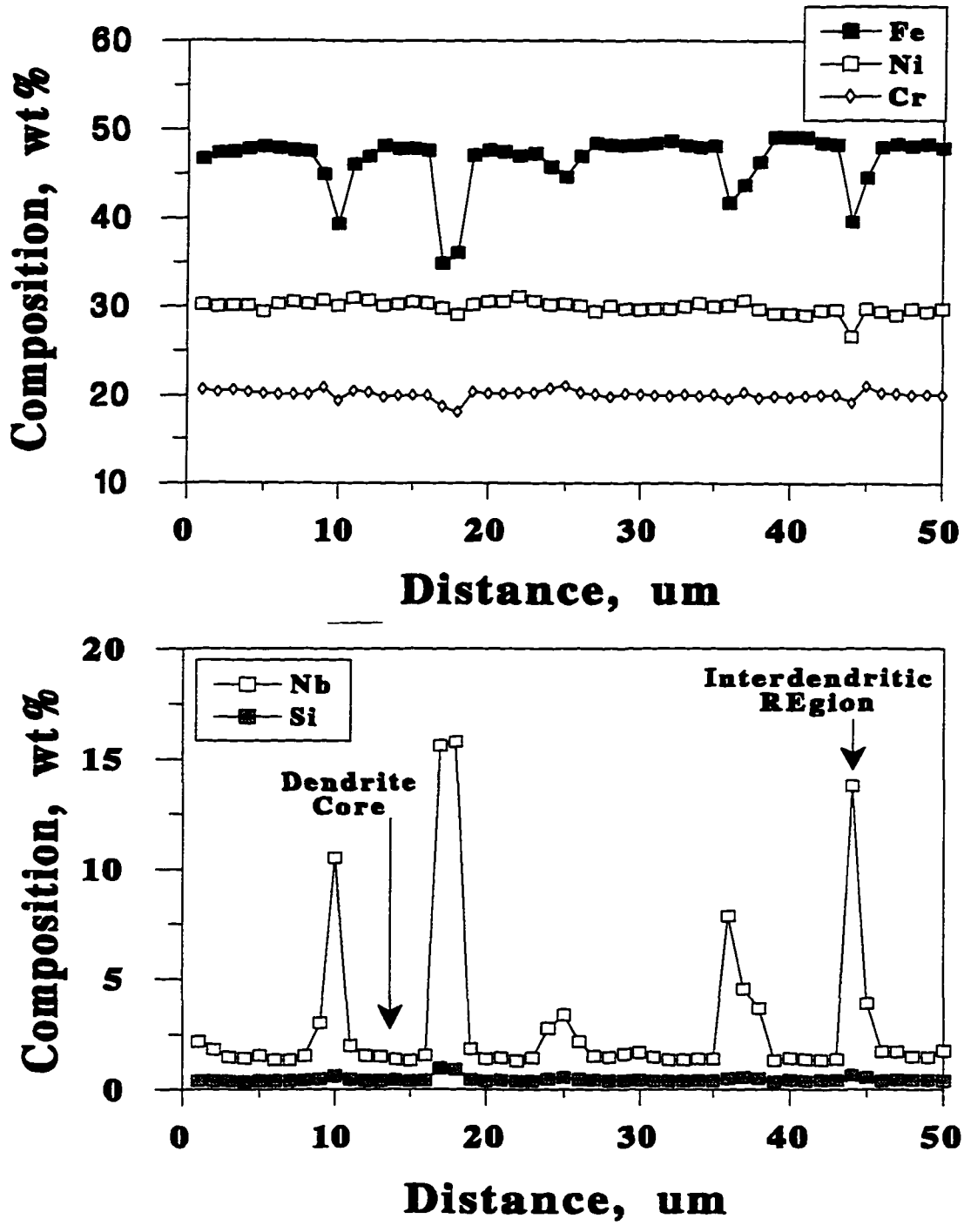

Figure 4.60. EPMA composition trace conducted across parallel dendrites in weld of Alloys 15.

Table 4.13 Dendrite core compositions, nominal compositions, and distribution coefficients. All compositions in wt%.

Alloy/ Sample	Compositions & k values	Iron	Nickel	Chromium	Niobium	Silicon
Alloy 4 Weld	Dendrite Core	10.6 ± 0.2	68.7 ± 0.3	19.5 ± 0.1	0.84 ± 0.03	0.33 ± 0.02
	Nominal	10.72	67.60	19.08	1.91	0.40
	k value	0.99	1.02	1.02	0.44	0.83
Alloy 7 Weld	Dendrite Core	10.6 ± 0.1	66.5 ± 0.2	20.4 ± 0.1	2.16 ± 0.07	0.36 ± 0.01
	Nominal	10.70	65.53	19.30	4.86	0.52
	k value	0.99	1.01	1.06	0.44	0.69
Alloy 8 Weld	Dendrite Core	10.8 ± 0.1	66.4 ± 0.4	20.4 ± 0.3	2.13 ± 0.09	0.37 ± 0.02
	Nominal	10.80	64.96	18.90	4.72	0.52
	k value	1.00	1.02	1.08	0.45	0.71
Alloy 8 Quenched Weld	Dendrite Core	10.8	65.8	20.5	2.13	0.42
	Nominal	10.80	64.96	18.90	4.72	0.52
	k value	1.00	1.01	1.08	0.45	0.81
Average value of k in Nickel-Base Alloys		1.00	1.02	1.06	0.45	0.76
Alloy 15 Weld	Dendrite Core	48.2 ± 0.8	30.1 ± 0.7	20.1 ± 0.2	1.32 ± 0.02	0.38 ± 0.02
	Nominal	45.40	30.03	19.54	4.88	0.66
	k value	1.06	1.00	1.03	0.27	0.58
Alloy 16 Weld	Dendrite Core	47.5 ± 0.5	31.1 ± 0.3	19.8 ± 0.2	1.21 ± 0.02	0.39 ± 0.04
	Nominal	44.47	30.89	19.45	4.77	0.64
	k value	1.07	1.01	1.02	0.25	0.61
Alloy 16 Quenched Weld	Dendrite Core	47.0	31.0	19.7	1.11	0.38
	Nominal	44.47	30.89	19.45	4.77	0.64
	k value	1.06	1.00	1.01	0.23	0.59
Average value of k in Iron-Base Alloys		1.06	1.00	1.02	0.25	0.58

Within the range of alloys examined, the data in Table 4.13 indicate that k for each element is independent of the nominal alloy content. Thus, average values of k are presented in the table. Values of k for Nb and Si in the Ni base alloys were also

determined from DTA data. These values are compared to those obtained by EPMA data in Table 4.14. There is excellent agreement between the k_{Nb} values determined from DTA and EPMA data, particularly when one considers that this data requires input from three different sources: wet chemical analysis for nominal alloy compositions; EPMA data for dendrite core compositions; and DTA data for liquidus and solidus temperatures. The values of k for Si are also in reasonable agreement, considering this is a light element and is present in minor amounts where accurate analysis by EPMA can be difficult. This agreement between k values obtained from relatively high cooling rate weld metals and slow heating rate DTA samples has an important implication. As discussed in Section 2.2.2.4, dendrite tip undercooling due to radius of curvature and solutal build up can have an affect on the dendrite core composition. As displayed in Figure 2.10, the process of undercooling results in an enrichment of the dendrite core composition. Such undercooling considerations are obviously not operable in determinations of distribution coefficients from the slow heating rate DTA data. The fact that k values determined through dendrite core EPMA data and slow heating rate DTA data are essentially equivalent implies that undercooling is insignificant under the solidification conditions studied in this work.

Table 4.14. Comparison of distribution coefficients determined through EPMA and DTA data.

Solute	Measurement Technique	
	Differential Thermal Analysis	Electron Microprobe
Niobium	0.46	0.45
Silicon	0.65	0.76

4.3.2.3 COMPARISON TO COMMERCIAL SUPERALLOY SYSTEMS

Table 4.15 compares the range of k values reported in the literature for commercial alloy systems and determined from experimental alloys in this study. Values of k for the solute elements in the Ni-X binary systems are also listed. It is readily apparent that all the matrix elements (Fe,Ni,Cr) exhibit similar behavior and show little tendency for segregation during solidification (i.e., their k values are all close to unity). The values of k_{Si} in the multi-component alloys are consistently higher than that in the Ni-Si system, indicating that Si exhibits a stronger segregation potential in the simple Ni-Si binary system. This may be attributed to the segregation of other solutes (e.g., Nb and C) in the multi-component alloys which are not present in the pure Ni-Si system. In this case, the pile up of other solutes at the solid/liquid interface may drive the Si back into the austenite matrix [4.32], thus reducing its' tendency to be rejected into the liquid. The fact that Nb and C are present in these alloys, and that their k values are consistently lower than that of Si, tends to support this possibility.

As previously discussed, the segregation potential of Nb and C play a key role in microstructural development during solidification in these alloys. The value of k_C determined here is similar to that in the Ni-C binary and that obtained by Cieslak in IN625. Cieslak [4.7] found that both the liquidus and solidus slopes for C in IN625 are higher than those in the simple Ni-C binary system. Compared to the Ni-C system, the solidus slope in IN625 increases more than the liquidus slope, reducing the value of k_C from 0.28 in the Ni-C binary to 0.21 in IN625. It is interesting to note that the liquidus and solidus slopes of C determined in this work are substantially lower than either of the

values for the Ni-C binary or IN625, but the ratios of these quantities yields a values of k_C which is similar to IN625 and the Ni-C system. The reason for this is presently unclear.

The low value of k determined for Nb in the Fe base alloys is rather surprising, considering that k_{Nb} values reported in the literature for commercial superalloys range from 0.42 to 0.54 [4.2, 4.7]. Such a low value of k implies that Nb segregates more strongly to the liquid in the Fe base alloys than in the Ni base alloys. This increased segregation tendency of Nb is expected to have significant affects in terms of secondary phase formation, since both of the secondary phases which form during solidification (NbC and Laves) are Nb rich. The main difference among commercial alloys used in previous studies and those used here is in Fe content, where Alloys 9 through 16 exhibit nominal Fe contents higher than most commercial superalloys. To serve as a check on the k_{Nb} value determined here for the Fe base alloys, an autogenous weld in a commercial Nb-bearing stainless steel, 20Cb-3, was prepared and analyzed by the same procedure used for the experimental alloys. This alloy has a nominal Fe content of 40.2 wt%. The results of the EPMA analysis are shown in Figure 4.61. The strong segregation potential of Nb is readily apparent in this alloy. The summary of nominal composition (determined by wet chemical analysis), dendrite core compositions, and k values are summarized in Table 4.17. Note that the value of k for Nb in this Fe base alloy is only 0.33.

Reference to the Ni-Nb phase diagram [4.4] indicates that the maximum solid solubility of Nb in γ-Ni is 18.2 wt% Nb (at 1286°C). In contrast, γ-Fe can only dissolve a maximum of 1.5 wt% Nb at a comparable temperature of 1210°C [4.4]. Thus, based on

these significant differences, it might be expected that iron additions to these alloys would decrease the solubility of Nb in the γ-(Fe,Ni-Cr) matrix. Thus, as the Fe-rich γ dendrites begin to form, less Nb is taken into the solid and, as a result, more is rejected to the liquid (in comparison to the Ni base alloys). This effect would induce a concomitant decreases in the value of k_{Nb}. Figure 4.62 plots k_{Nb} against the nominal Fe content of the alloys listed in Table 4.15. The general trend between k_{Nb} and nominal iron content is readily apparent. This effect accounts, at least in part, for the relatively high amounts eutectic-type constituents observed in the Fe base alloys. This can be understood by examination of the Scheil equation (eq. 4.21). The counterpart to eq. (4.21) which describes the relation between fraction liquid and liquid composition is given by

$$C_l = C_o f_l^{(k-1)} \qquad (4.24a)$$

When the liquid composition, C_l, reaches a line of two fold saturation on the liquidus surface (the "eutectic" composition, C_e), $C_l \rightarrow C_e$ and the remaining liquid, f_l, transforms to a eutectic-type constituent(s), f_e. Inserting these conditions into eq. (4.24) and solving for f_e yields

$$f_e = \left(\frac{C_e}{C_o}\right)^{\frac{1}{k-1}} \qquad (4.24b)$$

Thus, for a given value of C_e and C_o, the value of f_e will increase as k decreases. This effect is readily apparent in the quantitative image analysis results displayed in Figure

4.33, where the total amount of eutectic-type constituent(s) is consistently higher in the Fe base alloys. This phenomenon will be considered in quantitative detail in the next chapter.

Table 4.15. Comparison of distribution coefficients determined from commercial alloys and the experimental alloys in this study

Alloy	Fe	Ni	Cr	Nb	Si	C	Ref.
Alloys 1 through 8	1.00	1.02	1.06	0.46	0.71	0.27	--
Alloys 9 through 16	1.06	1.00	1.02	0.25	0.58	ND	--
IN 625	ND	ND	ND	0.54	0.57	0.21	4.7
IN 625/C Steel	1.02	1.04	1.05	0.46	ND	ND	4.11
IN 718	1.04	1.00	1.03	0.48	0.67	ND	4.8
IN 909	1.10	0.97	NP	0.49	0.67	ND	4.3
Thermospan	1.10	0.97	1.10	0.42	0.69	ND	4.2
20 Cb-3	1.08	0.97	0.96	0.33	0.89	ND	--
Ni-Nb Binary	--	--	--	0.75	--	--	4.31
Ni-Si Binary	--	--	--	--	0.50	--	4.30
Ni-C Binary	--	--	--	--	--	0.28	4.29

ND - Not determined
NP - Not present

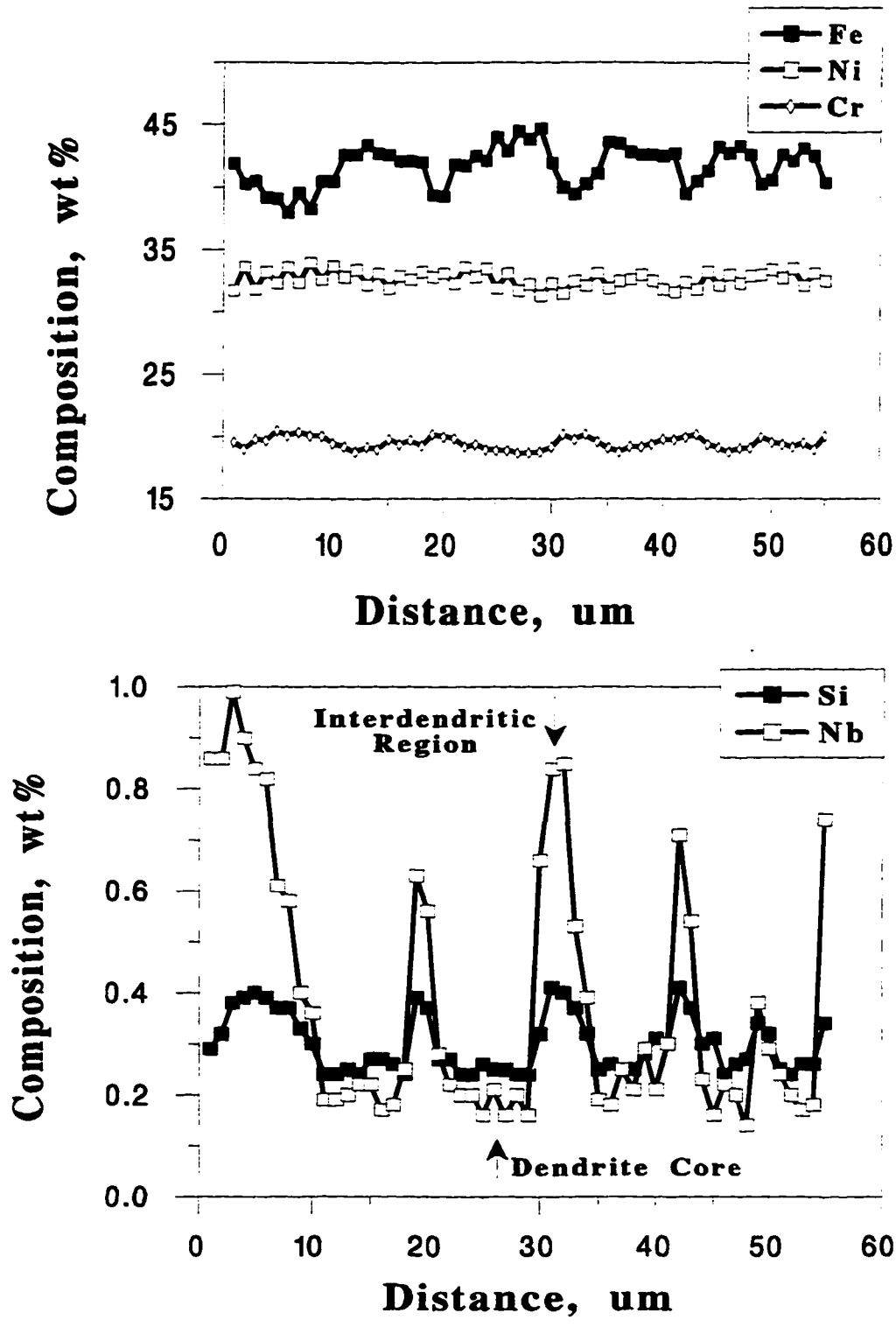

Figure 4.61. EPMA composition trace conducted across parallel dendrites in weld of commercial Alloy 20Cb-3.

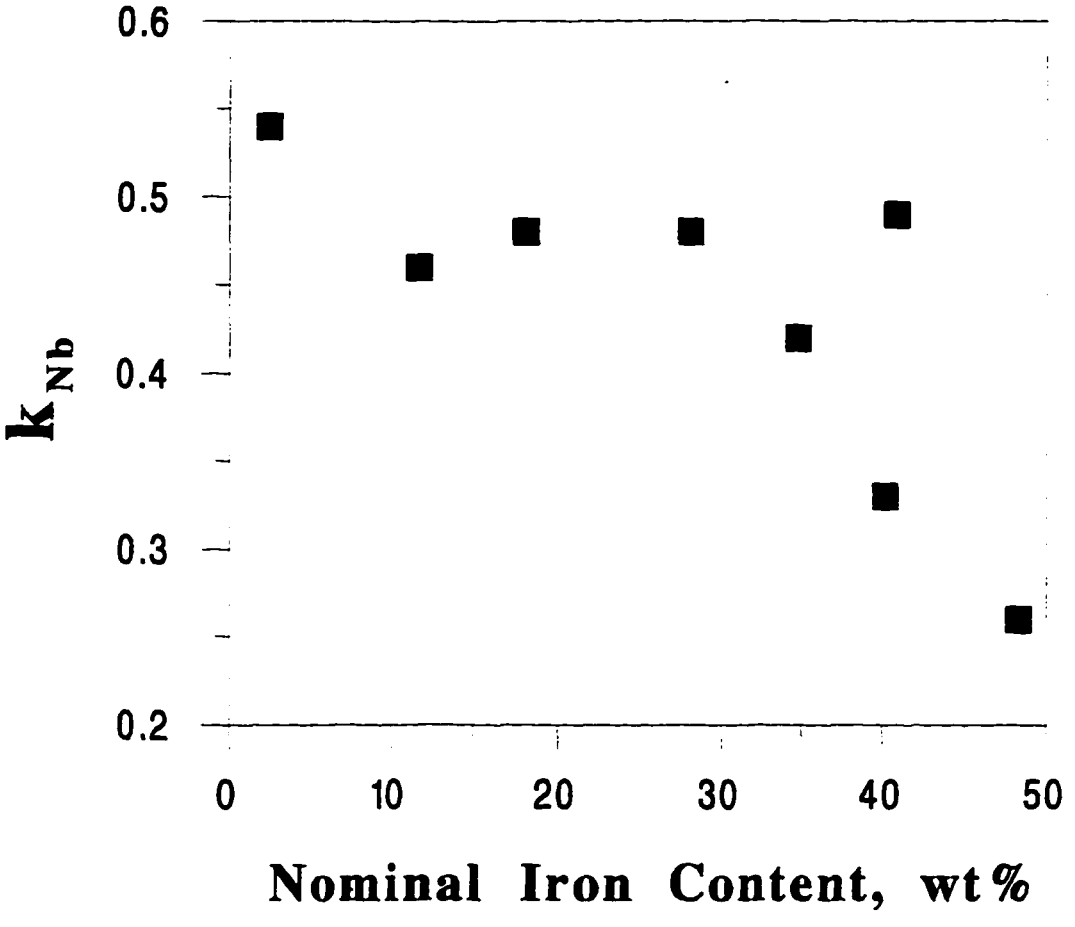

Figure 4.62. Plot of Nb equilibrium distribution coefficient, k_{Nb}, against the nominal Fe content of commercial and experimental superalloys.

Table 4.16. Comparisons of liquidus and solidus slopes determined in Ni-X binary systems (X = Nb, C), IN625, and this study.

Solute	Slope (°C/wt%)	Ni-X Binary	IN 625	Alloys 1-8	Alloys 9-16
Niobium	Liquidus	-8.4	-11.1	-8.3	-10.3
	Solidus	-11.2	-20.6	-17.9	--
Carbon	Liquidus	-70	-109	-34.1	-38.2
	Solidus	-250	-507	-126	--

Table 4.17. Summary of nominal composition, dendrite core compositions, and k values for 20Cb-3.

20Cb-3	Fe	Ni	Cr	Nb	Si
C_o, wt%	40.18	33.24	19.88	0.49	0.28
C_{core}, wt%	43.3 (0.8)	32.3 (0.5)	19.1 (0.3)	0.16 (0.02)	0.25 (0.01)
k	1.08	0.97	0.96	0.33	0.89

4.4 PSEUDO-TERNARY SOLIDIFICATION SURFACES

The ternary Ni-Nb-C liquidus projection shown in Figure 4.45 provides a basis for developing a qualitative understanding of microstructural evolution during solidification. This diagram describes the locus of compositions which separate the lines of two fold saturation between γ, NbC, and Laves (Ni_3Nb). The liquidus projection, combined with solidification parameters and a suitable solute redistribution model, can also be applied for developing a quantitative treatment of solidification. In the previous section,

solidification parameters were determined for the alloys of interest to this study, and the equilibrium lever law and Scheil equation were demonstrated to provide reasonable representations of the solute redistribution behavior of C and Nb, respectively. In this section, ternary liquidus surface-like diagrams are estimated for the alloys of interest to this study. Since the alloys are not true ternary systems and the data for the diagrams are obtained from weld metals and DTA samples solidifying under non-equilibrium conditions, the diagrams are more appropriately referred to as pseudo-ternary solidification surfaces.

The distribution coefficients for the matrix elements (Fe,Ni,Cr) in commercial systems and these experimental alloys are similar and take on a value close to unity, indicating they all behave in a comparable manner and exhibit little tendency for segregation. Thus, the (Fe,Ni,Cr) elements in the γ matrix are all grouped together to form one "component" of the diagram. Based on the similarity between reaction sequences observed in these multi-component alloys and those expected in the Ni-Nb-C system, Nb and C are chosen as the solute elements in this pseudo-ternary solidification model. Lastly, the Ni_3Nb phase is replaced by the Laves phase. The system can now be represented by a γ-Nb-C solidification diagram which exhibits primary phase fields of γ, NbC, and Laves. The objective of this section is to estimate where the lines of two fold saturation separating the γ, NbC, and Laves phases are positioned in this γ-Nb-C solidification diagram.

4.4.1 Nb COMPOSITIONS ALONG THE TWO FOLD SATURATION LINES

The general solidification process for alloys in this study which exhibit both the $L \rightarrow (\gamma + NbC)$ and $L \rightarrow (\gamma + Laves)$ eutectic-type reactions is shown schematically in Figure 4.63. The process is shown for a representative volume element which starts at the dendrite core, where $f_s = 0$, and extends to the mid-point between two neighboring dendrites, where $f_s = 1$. The corresponding solidification path is depicted on the solidification surface in the top right of the figure. Solidification starts with formation of primary γ dendrites (Step 1). The dendrites advance into the liquid and cause an enrichment of Nb and C as the path proceeds from Step 1 to Step 2. At Step 2, the liquid composition reaches the line of two fold saturation separating γ and NbC. Thus, the Nb and C contents in the liquid at Step 2 define one point on the γ/NbC line of two fold saturation. The exact liquid composition at Step 2 depends on the solidification path during primary $L \rightarrow \gamma$ solidification which, in turn, depends on the nominal Nb and C contents and values of k_{Nb} and k_C. For example, alloys with high C contents will exhibit a primary solidification path which intersects the line of two fold saturation relatively far into the C rich side of the solidification surface. After reaching the line of two fold saturation between γ and NbC, solidification continues from Step 2 to Step 3 as γ and NbC form simultaneously from the liquid. At step 3, the liquid composition reaches the class II reaction, at which point the $L \rightarrow (\gamma + NbC)$ reaction is replaced by the $L \rightarrow (\gamma +$ Laves) reaction, and the remaining liquid transforms to the γ/Laves eutectic-type constituent as solidification goes to completion (Step 4). The volume fraction of each eutectic-type constituent is also noted in the figure. This description represents the general

solidification process for the alloys utilized in this study. In Chapter 6, this general process will be divided into four individual classification schemes which account for the various microstructural morphologies that develop in the weld metals during solidification cracking.

The liquid composition at Steps 2 and 3 must be known in order to estimate the data points for the solidification surface. The liquid composition at Step 2 is related to the volume fractions and compositions of the γ/NbC and γ/Laves eutectic-type constituents in the as-solidified microstructure (i.e., that shown in Step 4) by

$$C^*_{\gamma/NbC} = \frac{f_{\gamma/NbC}\, C_{\gamma/NbC} + f_{\gamma/Laves}\, C_{\gamma/Laves}}{f_{\gamma/NbC} + f_{\gamma/Laves}} \qquad (4.25)$$

where $C^*_{\gamma/NbC}$ is the Nb concentration in the liquid at Step 2, $f_{\gamma/NbC}$ and $f_{\gamma/Laves}$ are the volume fractions of the γ/NbC and γ/Laves constituents, and $C_{\gamma/NbC}$ and $C_{\gamma/Laves}$ are the average Nb contents of the γ/NbC and γ/Laves constituents. The liquid composition at Step 3 is simply equivalent to the average composition of the γ/Laves constituent in the as-solidified microstructure. It was possible to obtain all the quantities in eq. (4.25) for Alloys 6, 8, 14, and 16, and this data is summarized in Table 4.18. As previously discussed, there was a trace amount of Laves phase in Alloy 6 which could not be accurately quantified, thus $f_{\gamma/Laves} \approx 0$ for this alloy. Considering that the Laves phase was rarely observed in this alloy, this approximation should not lead to significant error.

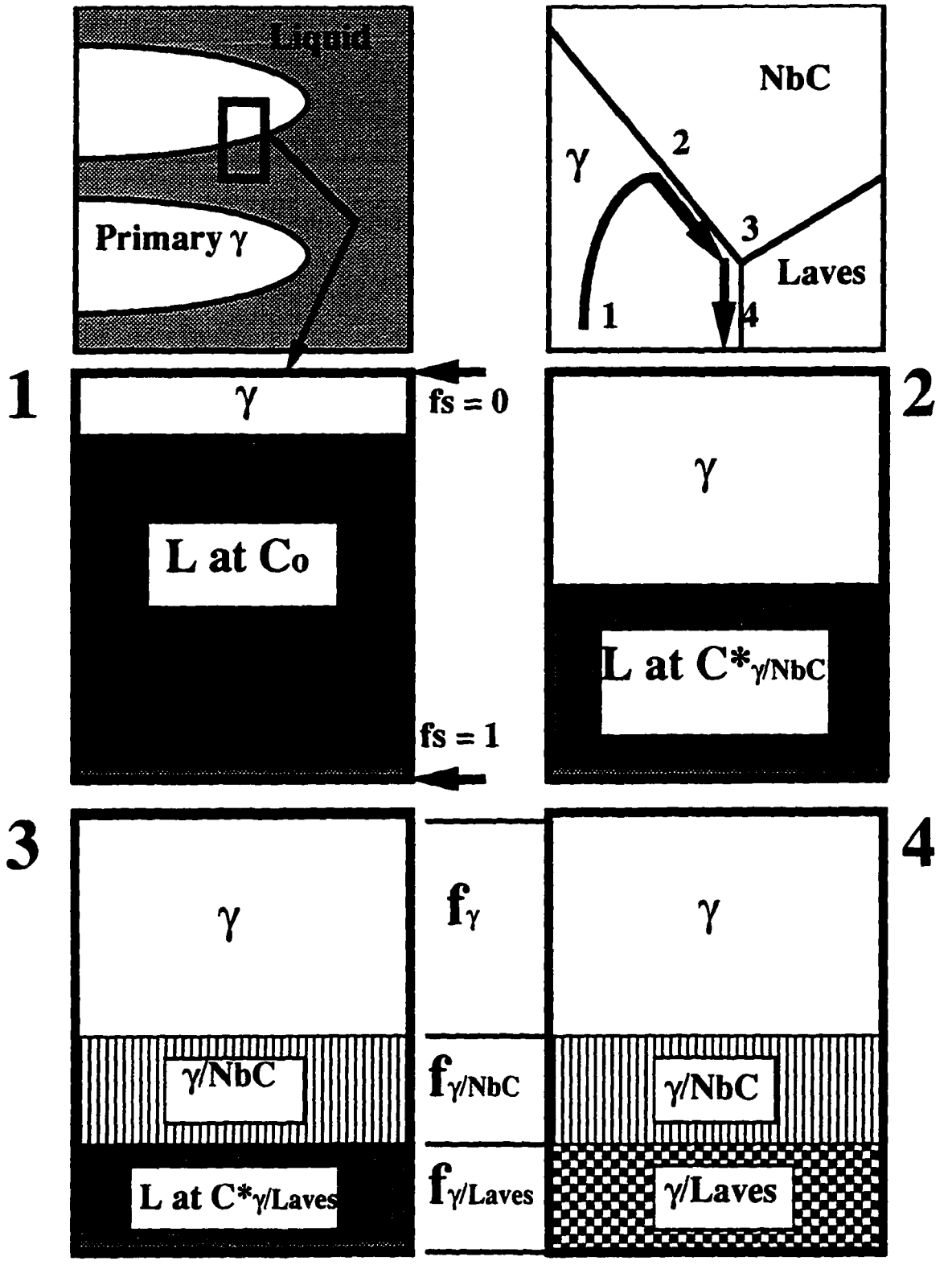

Figure 4.63. General solidification process for alloys in this study.

The accuracy of these values can be checked by comparing the measured amounts of total eutectic versus those predicted via the Scheil equation. According to eq. (4.24b), when the liquid composition reaches a line of two fold saturation on the liquidus surface (i.e., the "eutectic" composition, C_e), $C_l \rightarrow C_e$ and $f_l \rightarrow f_e$, where f_e is the total amount of eutectic type constituent in the as-solidified microstructure. The values of total eutectic constituent calculated via equation (4.24b) are compared to measured values in Table 4.19. For the Ni base alloys, $k_{Nb} = 0.46$ while, for the Fe base alloys, $k_{Nb} = 0.25$. The C_e values used in eq. (4.24b) are those shown in Table 4.18. The agreement between experimentally measured and calculated values is very good, particularly when one considers the comparison requires input data from four different sources: C_o (wet chemical analysis), C_e (EPMA and QIA), k_{Nb} (EPMA and DTA), and $f_{\gamma/NbC}$ and $f_{\gamma/Laves}$ (QIA).

The Nb composition of the γ/Laves constituent was obtained on a number of weld metals and DTA samples (Table 4.7). The Nb contents are summarized in Table 4.20. Reference to Table 4.7 indicates there is an apparent trend between the Fe, Nb, and Si contents of the γ/Laves constituent. In general, the Nb content tends to decrease as the Fe and Si contents increase. Thus, less Nb is apparently needed in the liquid at Step 3 to start forming the γ/Laves constituent as the Fe and Si contents of the liquid increase. Considering that Fe and Si both promote the Laves phase, this trend is not surprising. However, there is insufficient data for any quantitative correlations. The only distinction made is here is to separate the average value of the γ/Laves constituent based on the nominal matrix composition, where the Fe base alloys exhibit a slightly lower Nb content than the Ni base alloys. Alloy Fe-1 was not included in the average Nb value reported for

the Fe base alloys in Table 20, as it exhibited a high Fe and low Nb value compared to the other alloys. In summary, the Nb values listed in Table 4.18 provide several data points for estimating the position of the two fold saturation line separating the γ and NbC phases (Step 2), while the Nb values in Table 4.20 provide an approximation to the point on the diagram where the L → (γ + NbC) reaction is replaced by the L → (γ + Laves) reaction (Step 3). The corresponding values of C content in the liquid which are needed to fully define the solidification diagram are addressed below.

Table 4.18 Liquid Nb concentrations at the line of two fold saturation separating γ and NbC.

Alloy	γ/NbC		γ/Laves		$C^*_{\gamma/NbC}$
	$f_{\gamma/NbC}$ (Vol. %)	Comp. (wt% Nb)	$f_{\gamma/Laves}$ (Vol.%)	Comp. (wt% Nb)	(wt% Nb)
6	13.3	13.3	~0	--	13.3
8	13.7	12.5	1.5	21.5	13.4
14	18.8	10.9	5.0	22.4	13.3
16	17.5	10.8	6.1	18.3	12.8

Table 4.19. Comparison of calculated and measured total volume fractions of eutectic-type constituents.

Alloy	C_o wt% Nb	C_e wt% Nb	k_{Nb}	f_e, Calc. Vol. %	f_e, Meas. Vol. %
6	4.87	13.3	0.46	15.6	13.3 ± 2.5
8	4.72	13.4	0.46	14.5	15.2 ± 1.6
14	4.51	13.3	0.25	23.7	23.8 ± 1.6
16	4.77	12.8	0.25	26.8	23.6 ± 2.1

Table 4.20 Summary γ/Laves compositions used for determining the two fold saturation line between γ and Laves.

Alloy/ Sample	Nb Content (wt%)	Average of Ni base Alloys	Alloy/ Sample	Nb Content (wt%)	Average of Fe Base Alloys
Alloy 7 DTA	24.3	23.1	Alloy 13 Weld	21.1	20.4
Alloy 7.5 DTA	23.5		Alloy 13 DTA	20.9	
Alloy 8 DTA	21.5		Alloy 14 Weld	22.4	
Ni-1 GTA Melt	23.1		Alloy 15 Weld	20.1	
			Alloy 16 Weld	18.3	
			Alloy 16 DTA	19.8	

4.4.2 C COMPOSITIONS ALONG THE TWO FOLD SATURATION LINES

Due to the limitations of the EPMA technique, the C contents of the γ/NbC and γ/Laves constituents can not measured experimentally. However, if the solidification path of the alloys during primary $L \rightarrow \gamma$ solidification is known quantitatively, than the C content in the liquid can be calculated. The solidification path describes the relation between the Nb and C composition in the liquid as solidification progresses. Thus, knowledge of the solidification path relation can be combined with the experimentally determined Nb compositions (Tables 4.18 and 4.20) to calculate the corresponding values of C content in the liquid. The possible range of C in the liquid for each Nb content will be bound in order to assess the potential range for error using this approach.

The maximum carbon content which is possible in the liquid can be determined by assuming that C exhibits negligible diffusion in γ during solidification. Although this behavior is certainly not expected based on the information shown previously in Figure 4.51, the result provides an upper limit of the C content in the liquid at any corresponding value of Nb. Mehrabian and Flemings [4.33] have shown that, when the diffusion of two solutes in a ternary system is negligible, the Scheil equation can be used to describe the solidification path for primary phase solidification. This is obtained by first writing the Scheil expressions describing the relation between f_l and C_l for each solute (Nb and C)

$$f_l = \left(\frac{C_{l,Nb}}{C_{o,Nb}}\right)^{\frac{1}{k_{Nb}-1}} \qquad (4.26a)$$

$$f_l = \left(\frac{C_{l,C}}{C_{o,C}}\right)^{\frac{1}{k_C-1}} \qquad (4.26b)$$

By equating (4.26a) and (4.26b), since the value of f_l is the same in each case, a relation is obtained which describes the solidification path of the alloy

$$C_{l,Nb} = C_{o,Nb}\left(\frac{C_{l,C}}{C_{o,C}}\right)^{\frac{k_{Nb}-1}{k_C-1}} \qquad (4.27)$$

Equation (4.27) describes the relation between $C_{l,Nb}$ and $C_{l,C}$ during solidification. Of all

the possible types of solute redistribution behavior, eq. (4.27) predicts the maximum amount of solute which will exist in the liquid at any time during solidification. (As shown in the previous section, the Scheil equation is expected to provide a good description of mass transport for Nb.)

The minimum amount of C possible in the liquid occurs when the diffusivity of C is high enough to maintain equilibrium. Under this condition the equilibrium lever law holds and the relation between f_l and C_l for carbon is given by

$$f_l = \frac{C_{o,C} - k_C C_{l,C}}{(1-k_C)\, C_{l,C}} \qquad (4.28)$$

Proceeding in the same manner used to derive eq. (4.27), the f_l values given by eq. (4.26a) and eq. (4.28) must be equivalent. Thus, equating (4.26a) and (4.28) and solving for $C_{l,Nb}$, a new solidification path relation is obtained

$$C_{l,Nb} = C_{o,Nb}\left[\frac{C_{o,C} - k_C C_{l,C}}{(1 - k_C)\, C_{l,C}}\right]^{k_{Nb}-1} \qquad (4.29)$$

Equation (4.29) describes the solidification path of the liquid during primary solidification of γ assuming that Nb diffusion in the solid is negligible while C diffuses fast enough to maintain equilibrium. Based on the discussion in the previous section, where diffuusivty effects of Nb and C were considered, this relation should provide a realistic

description of the primary solidification paths in these alloys. Eq. (4.29) is physically consistent at the limits of solidification. At the beginning of solidification, the liquid composition should equal the nominal composition for both solutes. Insertion of $C_{l,C} = C_{o,C}$ into (4.29) yields $C_{l,Nb} = C_{o,Nb}$. Under equilibrium conditions for carbon, the liquid will reach a maximum concentration of $C_{o,C}/k_C$ when solidification is complete while the Nb concentration in the liquid should tend toward infinity as predicted by the Scheil equation. Insertion of $C_l = C_{o,C}/k_C$ into equation (12) yields $C_{l,Nb} = \infty$.

Figures 4.64a and 4.65a show the primary $L \rightarrow \gamma$ solidification paths of several alloys as an example to eqs. (4.27) (blue path) and (4.29) (red path). For Alloys 7 and 8, $k_{Nb} = 0.46$ and $k_C = 0.27$. For Alloys 15 and 16, $k_{Nb} = 0.25$. No value of k_C could be determined for C in the Fe base alloys. Thus, the value determined for the Ni base alloys was used. This should provide a reasonable estimate as the values of k_C summarized in Table 4.15 do not exhibit a large range and the liquidus slopes for C in the Ni base and Fe base alloys are similar. The primary solidification paths of the high C alloys (8 and 16) are terminated at the Nb compositions given in Table 4.18, since this is the point where the $L \rightarrow (\gamma + NbC)$ reaction will begin. Since only minor amounts of the γ/NbC constituent was present in Alloys 7 and 15, the solidification paths of these low C alloys are terminated at the γ/Laves compositions given in Table 4.20. These results show that the possible range of C content in the liquid during solidification is relatively narrow, particularly when the nominal C content in the alloy is low.

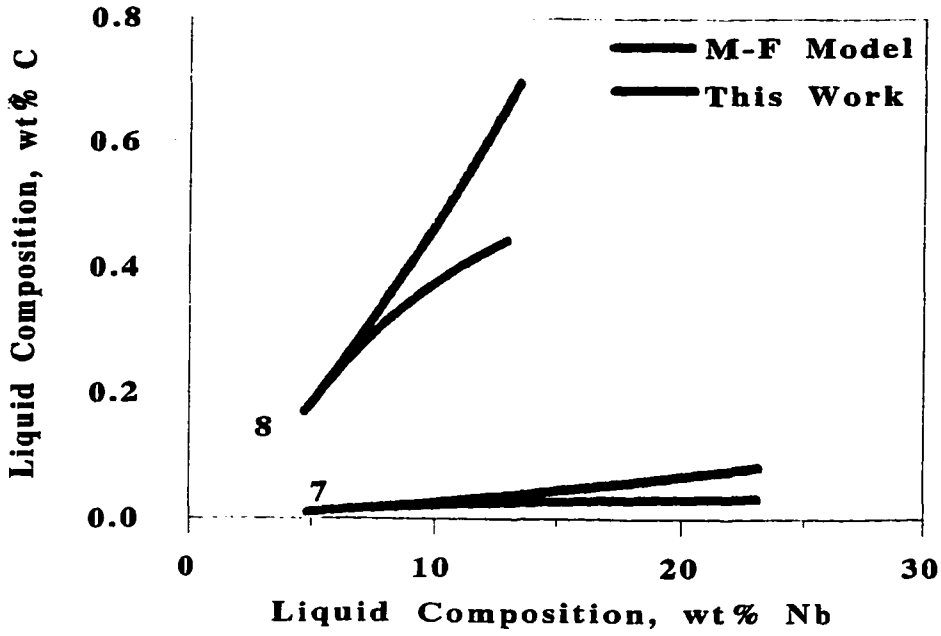

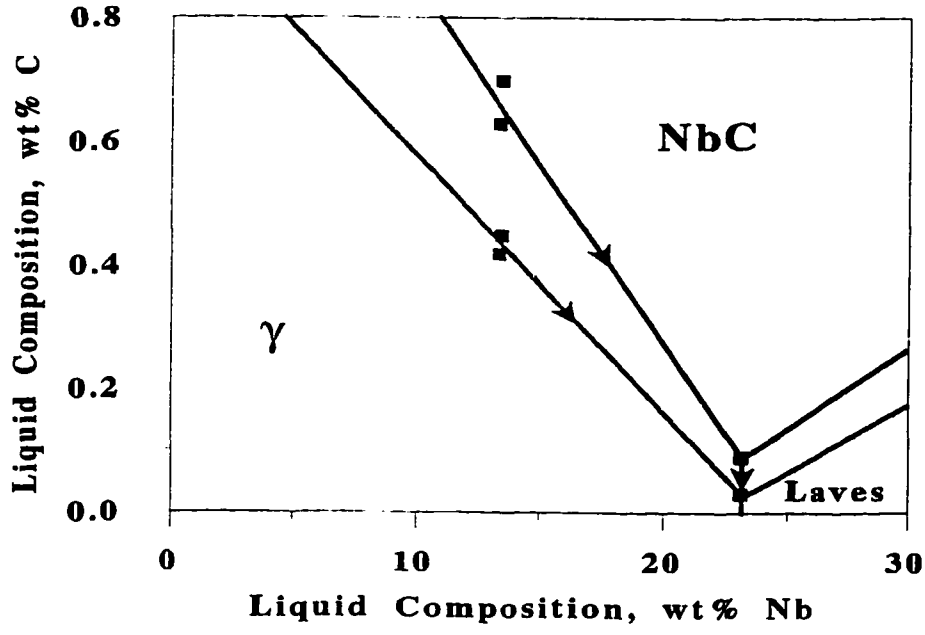

Figures 4.64. a) Primary L → γ solidification paths of Alloys 7 and 8 as predicted by eqs. (4.27) and (4.29). b) Plot of measured Nb contents and corresponding calculated C contents.

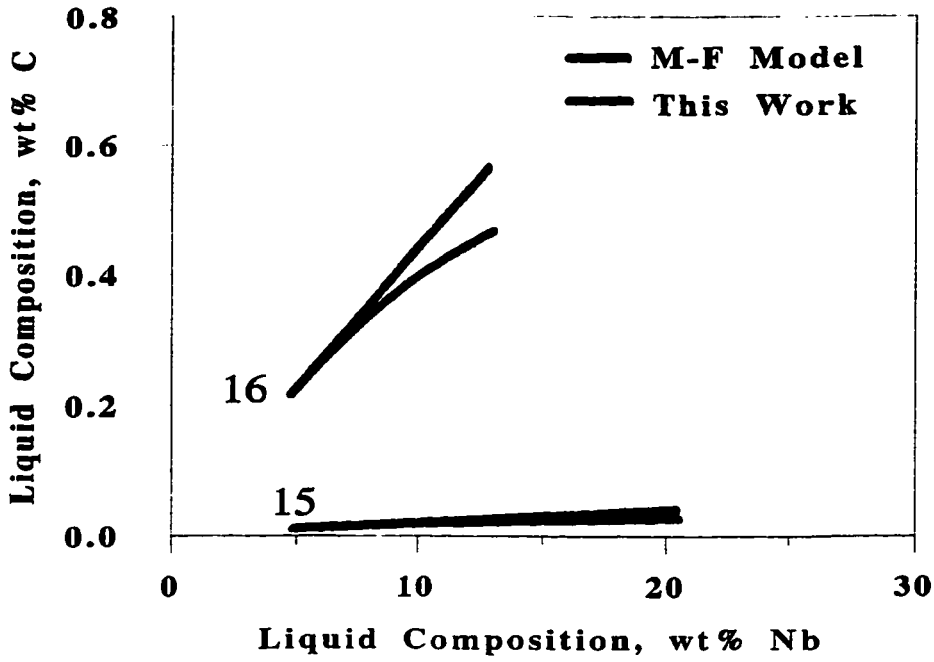

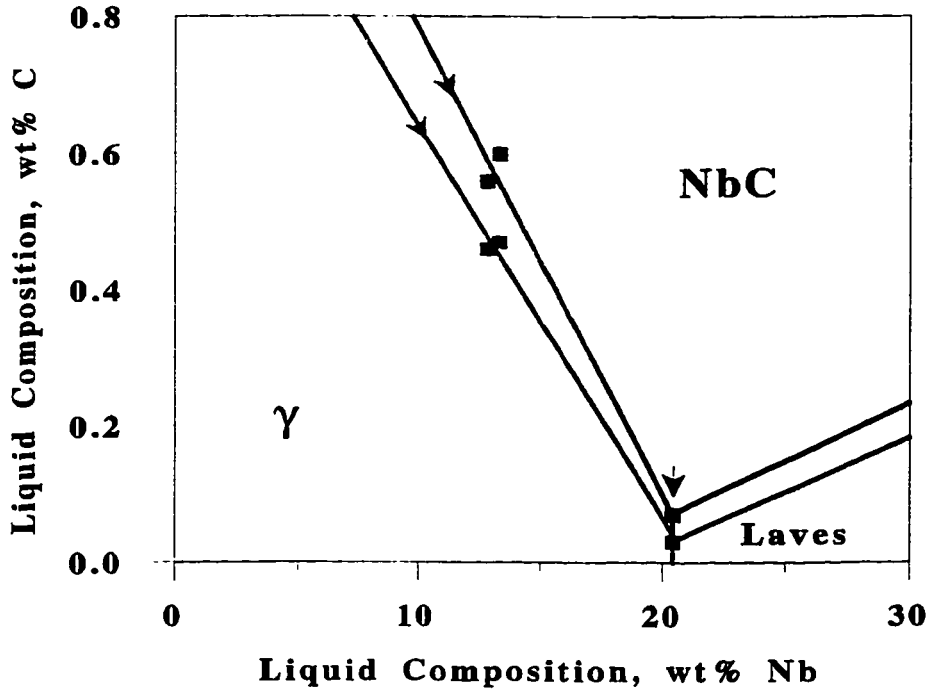

Figure 4.65. a) Primary L → γ solidification paths of Alloys 15 and 16 as predicted by eqs. (4.27) and (4.29). b) Plot of measured Nb contents and corresponding calculated C contents.

Figures 4.64b and 4.65b plot the C contents which are calculated through eqs. (4.27) and (4.29) using the Nb values given in Tables 4.18 and 4.20. Here, points on γ/NbC boundary are given by the experimental Nb contents in Table 4.18 and corresponding calculated C contents. The point where the L → (γ + NbC) reaction is replaced by the L → (γ + Laves) reaction is estimated by the Nb contents given in Table 4.20 and the corresponding calculated C contents. As there is obviously not enough data to reveal any potential curvature in the boundaries, they are approximated as straight lines. Considering that the region of interest on the solidification surfaces exists over a narrow C concentration, this should provide a reasonable estimate. The direction of the solidification path (i.e., decreasing temperature) along the L → (γ + NbC) reaction is determined from the DTA data (Tables 4.4, and 4.5), where the low C alloys exhibit a lower L → (γ + NbC) reaction temperature than the high C alloys. The reasons for this will be discussed in more detail in the next chapter. Since the γ/NbC and γ/Laves constituents are not intermixed in the as-solidified microstructures, the direction of the solidification path along the γ/Laves boundary is directed toward the γ-Nb "binary" side of the diagram. In other words, solidification is not terminated by the ternary-type L → (γ + NbC + Laves) reaction, where all three phases would be intermixed in the as-solidified microstructure. Instead, solidification is terminated by the binary-type L → (γ + Laves) reaction, in which the γ/NbC and γ/Laves constituents are spatially separated. (The position of the NbC/Laves boundary was not determined as it is not needed here. The lines for this boundary are drawn only for clarity.) There is not a large difference among the solidification diagrams determined though the C contents calculated from eqs.

(4.27) and (4.29). Considering this, together with the expected equilibrium behavior of C shown in Figure 4.51, the diagrams which are derived through the C values calculated with eq. (4.29) will be utilized for representing the solidification behavior of these alloys. The accuracy of these diagrams will be assessed in the next chapter through solidification modelling.

4.4.3 COMPARISON TO CALCULATED LIQUIDUS SURFACES AND Ni-Nb-C SYSTEM

As a check to the diagrams presented in Figures 4.64 and 4.65, pseudo-ternary liquidus projections were calculated using the Therm-Calc software program [4.44]. The calculations were performed for austenite matrix compositions containing two different Fe levels: one at Ni-8Fe-18Cr-1Si-Nb-C and one at Ni-30Fe-18Cr-1Si-Nb-C (all values in wt%). The Ni was allowed to vary during the calculations as the Nb and C contents were changed. Cr and Si were held constant at values of 18wt% and 1wt%, respectively. These values were selected based on the EPMA composition data of the γ/NbC and γ/Laves constituents given in Table 4.6 and 4.7. The calculated liquidus projections are compared to the solidification surfaces in Figure 4.66. Comparison of the solidification surfaces to the ternary Ni-Nb-C system is made in Figure 4.67.

The Thermo-Calc results predict that Fe additions will decrease the amount of Nb needed in the liquid to start the L $\rightarrow$ (γ + Laves) reaction. This result is revealed through the experimental data as well, but the effect is not as strong as that predicted by the thermodynamic calculations. More importantly, there is reasonable agreement among the

general positions of the two fold saturation lines between the diagrams calculated from the Thermo-Calc program and determined experimentally. Note that, in the simple Ni-Nb-C system, the L $\rightarrow$ (γ + Laves) reaction is initiated at a C content of $\approx$ 1 wt%. In contrast, the experimental solidification surface predicts that this reaction is much closer to the γ -Nb "binary" side of the diagram. The thermodynamic calculations support this. A similar trend is observed for the L $\rightarrow$ (γ + NbC) reaction. As noted earlier, the ternary Ni-Nb-C system reported in the literature [4.15] is only an estimate, which may account for some of the discrepancy observed here.

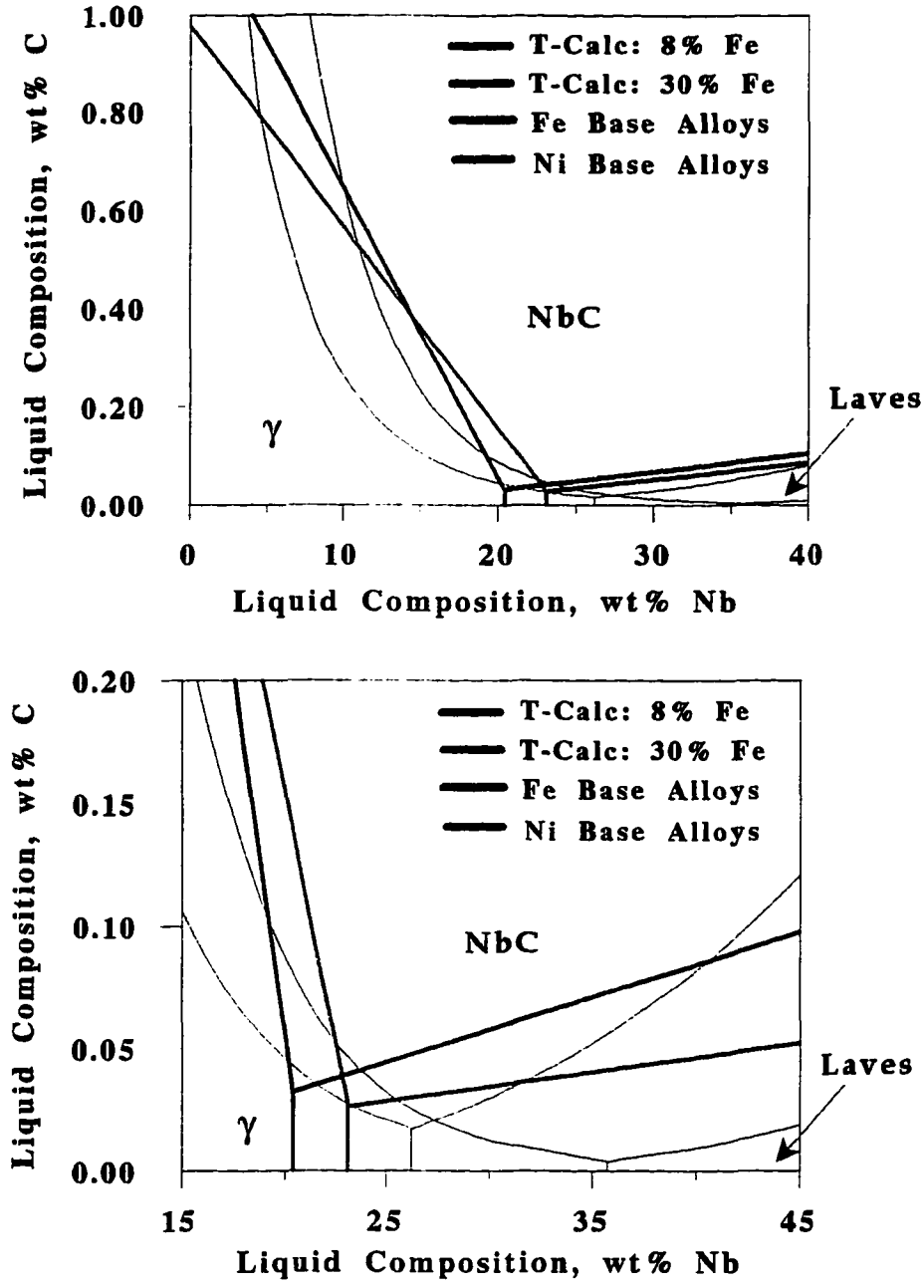

Figure 4.66. Comparison of thermodynamically calculated liquidus projection to the solidification surfaces.

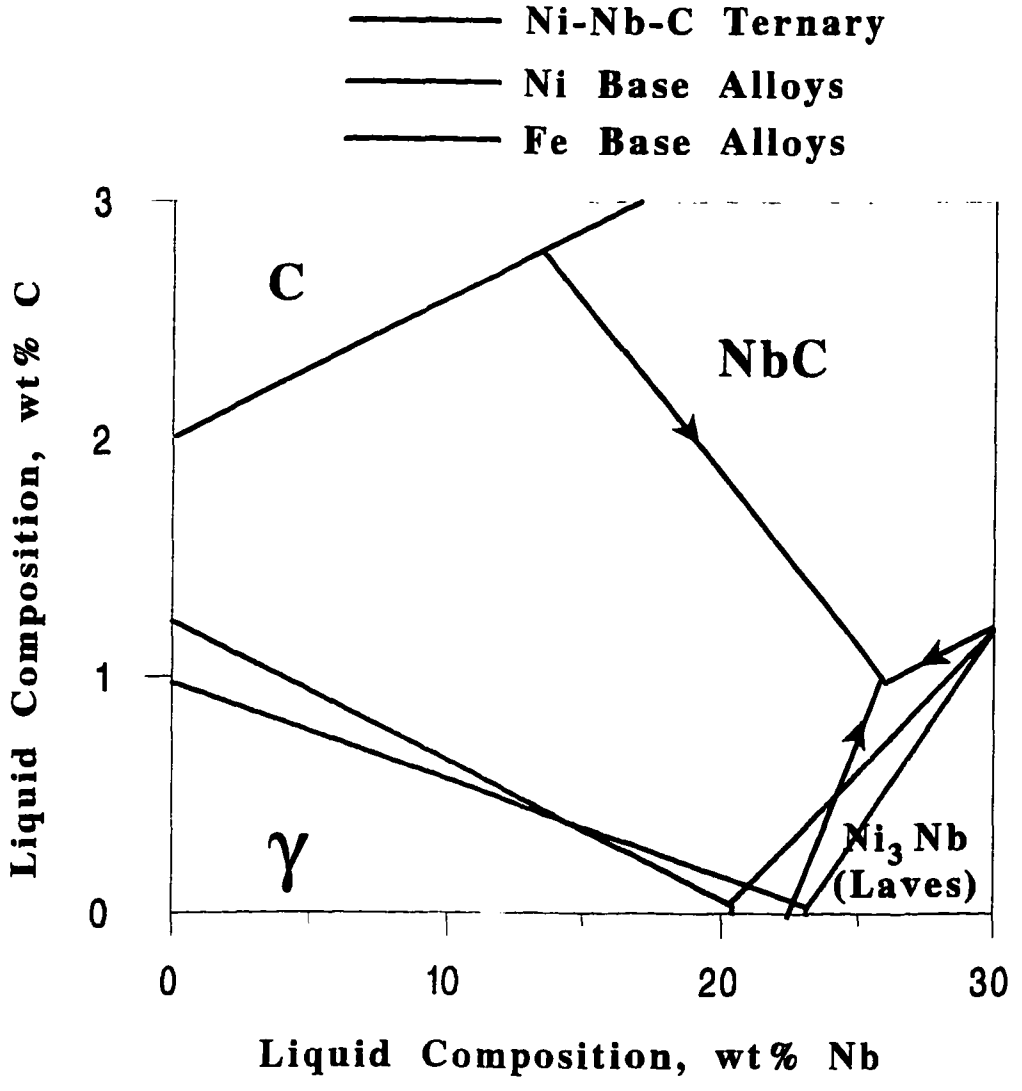

Figure 4.67. Comparison of the solidification surfaces to the ternary Ni-Nb-C system.

4.5 CHAPTER CONCLUSIONS

In this chapter, the general solidification behavior of experimental alloys simulating compositions of commercial Ni base and Fe base superalloys containing Nb, Si, and C was investigated by differential thermal analysis and microstructural characterization techniques. The following conclusions can be drawn from this work.

1. The general solidification sequence of these alloys can be described by a three step process: 1) Primary $L \rightarrow \gamma$ solidification in which the interdendritic liquid becomes enriched in Nb and C, followed by 2) a eutectic-type $L \rightarrow (\gamma + NbC)$ reaction which depletes the interdendritic liquid of C, and 3) termination of solidification by a second eutectic-type reaction $L \rightarrow (\gamma + Laves)$. This solidification reaction sequence is similar to that expected in the ternary Ni-Nb-C system and observed experimentally in many commercial alloy systems.

2. The $L \rightarrow (\gamma + NbC)$ reaction generally occurs over a broad temperature range and is initiated at higher temperatures as the nominal C content of the alloys is increased. The $L \rightarrow (\gamma + Laves)$ reaction occurs over a narrow temperature range.

3. The distribution coefficients (k) for all solute elements (Nb, Si, and C) are less than unity while the "solvent" elements (Fe,Ni,Cr) exhibit little tendency for segregation ($k \approx 1$). This is in agreement with results reported on comparable commercial alloy systems.

4. An interactive effect between the segregation potential of Nb and nominal Fe content has been observed, where the value of k_{Nb} decreases in a linear-type fashion from 0.54 to 0.25 as the Fe content is increased from ≈ 2 wt% to ≈ 47 wt%. This behavior is the major factor contributing to the formation of relatively high amounts of eutectic-type constituents in the Fe base alloys.

5. Carbon additions promote formation of the γ/NbC constituent. The addition of Fe and Si will reduce the amount of Nb needed in the liquid to initiate the L → (γ + Laves) reaction. As a result, the amount of γ/Laves constituent increases with increasing Fe and Si. The effect of Nb depends on the C content. At high C levels, Nb additions will promote formation of γ/NbC. When the C level is low, Nb generally promotes formation of the γ/Laves constituent.

6. Under the current processing conditions in which the cooling rate is ≈ 660 °C/s, the diffusion of Nb in austenite is negligible during solidification and the Scheil equation provides a good description of solute redistribution. Microsegregation calculations for C, via the Klyne-Kurz model and literature data on diffusion rates of C in γ, indicate that C can diffuse fast enough to maintain equilibrium during solidification and the lever law can be used to describe the redistribution behavior for C.

7. An analytical solidification path expression, eq. (4.29), has been proposed to describe the change in liquid composition during solidification in a ternary system in which one solute exhibits negligible diffusion while the other solute diffuses infinitely fast in the solid.

8. A pseudo-ternary γ-Nb-C solidification surface has been proposed which identifies the liquid compositions required to initiate the $L \rightarrow (\gamma + NbC)$ and $L \rightarrow (\gamma + Laves)$ eutectic type reactions. The Nb compositions of the diagram were checked by comparison of calculated volume fractions of eutectic type constituents (via the Scheil equation) and those measured experimentally, and good agreement is found. The general positions of two fold saturation lines on the proposed surface were compared to those predicted by thermodynamic calculations and reasonable agreement is found.

The solidification parameters, pseudo-ternary γ-Nb-C solidification surface, and established solute redistribution behavior of Nb and C will be combined in the next chapter to numerically model microstructural evolution in these experimental superalloys.

5. MODELLING OF SOLUTE REDISTRIBUTION AND MICROSTRUCTURAL EVOLUTION

In the previous chapter, solidification parameters and pseudo-ternary solidification surfaces were developed for the experimental alloys of this study. In addition, the Scheil equation and equilibrium lever law were shown to provide good descriptions of mass transport for Nb and C, respectively. This result as very useful, as it avoids the need for considering any kinetic effects associated with diffusion of solute in the solid. This permits development of a relatively simple analytical treatment of solute redistribution during solidification. In this chapter, the solidification parameters and pseudo-ternary solidification surfaces determined from the previous chapter are applied to develop a solidification model which describes solute redistribution and associated microstructural development. A model previously developed by Mehrabian and Flemings, which assumes negligible diffusion of each solute in a ternary system, is first outlined. This model is then modified to account for the assumption of infinitely fast diffusion for C and applied to the pseudo-ternary approach utilized here. The inputs to the model consist of alloy solidification parameters (nominal alloy composition and distribution coefficient for each solid phase) and positions of the line of two fold saturation on the pseudo-ternary solidification diagrams. As output, the model predicts the amount and composition of all solid phases forming at any point during solidification. Results of the total and individual amounts of eutectic type constituents calculated with the approach are compared to the measured values, and reasonable agreement is found considering the assumptions required in the model.

5.1 MEHRABIAN-FLEMINGS SOLUTE REDISTRIBUTION MODEL

The M-F model [5.1] is based on the same assumptions used in the Scheil equation (dendrite tip undercooling and solid state diffusion are negligible, thermodynamic equilibrium is maintained at the solid/liquid interface, and diffusion is infinitely fast in the liquid). This model essentially contains two sets of solute redistribution relations. The first set describes the variation in liquid composition during solidification of the primary phase, while the second set describes solute redistribution during eutectic-type reactions which occur along the line of two fold saturation. These relations are described below in context to the current pseudo-ternary approach where Nb and C are taken as the solute elements.

5.1.1 PRIMARY L $\rightarrow \gamma$ SOLIDIFICATION

The relation describing the variation in liquid composition during solidification of the primary phase was already introduced in the previous chapter through eq. (4.27):

$$C_{l,Nb} = C_{o,Nb}\left(\frac{C_{l,C}}{C_{o,C}}\right)^{\frac{k_{Nb}-1}{k_C-1}} \qquad (5.1)$$

When the liquid composition given by (5.1) intersects a line of two fold saturation on the liquidus surface, the remaining liquid (f_l) will transform to one or more eutectic-type constituents. Thus, the value of f_l at that point represents the total amount of eutectic-type constituent(s), f_e , in the final solidification microstructure. The number and amount of

eutectic-type constituents which form depends on the details of the particular alloy system. In order to calculate the total volume fraction of eutectic-type constituent, the line of two fold saturation on the liquidus surface is first represented by a linear equation. For the two solutes of interest here:

$$C_{l,c} = a + bC_{l,Nb} \qquad (5.2a)$$

where **a** and **b** are constants. In this case, **a** is the C content at the line of two fold saturation between γ and NbC at 0 wt% Nb and **b** is the slope of the line. In order to find the intersection of the primary solidification path and the line of two fold saturation, eq. (5.2a) is first solved in terms of $C_{l,Nb}$

$$C_{l,Nb} = \frac{C_{l,c} - a}{b} \qquad (5.2b)$$

and eqs. (5.1) and (5.2b) are simply equated

$$\frac{C_{l,c} - a}{b} = C_{o,Nb}\left(\frac{C_{l,c}}{C_{o,c}}\right)^{\frac{k_{Nb} - 1}{k_c - 1}} \qquad (5.3)$$

Eq. (5.3) provides a unique value of liquid composition, $C_{l,C}$, in terms on the nominal alloy composition and distribution coefficients for the two solutes. This value of $C_{l,C}$ defines the C content in the liquid where the solidification path intersects the line of two fold saturation. The corresponding Nb content in the liquid is given by substituting this value of $C_{l,C}$ into either eq. (5.1) or (5.2b). Once these values are known, either one can be used as C_e in the previous relation given as eq. (4.24b) to calculate the remaining fraction of liquid which transforms to eutectic-type constituent(s).

$$f_e = \left(\frac{C_{e,i}}{C_{o,i}}\right)^{\frac{1}{k_i - 1}} \qquad (5.4)$$

where the subscript *i* refers to either solute.

5.1.2 EUTECTIC-TYPE SOLIDIFICATION

When the primary solidification path intersects the line of two fold saturation, the solidification reaction changes from L $\rightarrow \gamma$ to L $\rightarrow (\gamma + NbC)$ as the two solid phases begin forming from the liquid. Thus, an additional term is required in the differential Scheil mass balance which was used to describe primary solidification. In the general case, the two solid phases reject solute to the liquid. For the solute Nb, the amount of Nb rejected to the liquid by forming a small amount of γ (df_γ) and NbC (df_{NbC}) is given by [5.1]

$$df_\gamma (C_{l,Nb} - C_{\gamma,Nb}) + df_{NbC}(C_{l,Nb} - C_{NbC,Nb}) = f_l dC_{l,Nb} \qquad (5.5)$$

where C_{ij} is the concentration of element j in phase i. In this particular case, the value of $C_{NbC,Nb}$ is constant at $\approx$ 90 wt% Nb (Table 4.1) while the value of C_{LNb} along the line of two fold saturation varies from about 10 to 23 wt% Nb (Figures 4.64 and 4.65). Thus, the value of $(C_{l,Nb} - C_{NbC,Nb})$ in eq. (5.5) is negative. In physical terms, this implies that the NbC acts in a manner similar to the liquid in that it absorbs Nb rejected by the γ phase. The objective here is to use eq. (5.5) to obtain a relation between df_l and df_{LNb} in terms of known quantities. In order to do this, it is first noted that

$$f_\gamma + f_{NbC} + f_l = 1 \qquad (5.6)$$

and

$$df_\gamma + df_{NbC} + df_l = 0 \qquad (5.7)$$

or

$$df_\gamma = - df_{NbC} - df_l \qquad (5.8)$$

The solid compositions $C_{\gamma,Nb}$ and $C_{NbC,Nb}$ can be expressed in terms of liquid composition through the distribution coefficient:

$$C_{\gamma,Nb} = k_{\gamma,NbC} C_{l,Nb} \qquad (5.9)$$

$$C_{NbC,Nb} = k_{NbC,Nb} C_{l,Nb} \qquad (5.10)$$

where $k_{i,j}$ is the distribution coefficient for element *j* between phase *i* and the liquid. Inserting (5.8), (5.9), and (5.10) into (5.5) and rearranging yields:

$$\frac{df_l}{dC_{l,Nb}} = -\frac{1}{(1 - k_{\gamma,Nb})} \frac{f_l}{C_{l,Nb}} - \frac{(k_{NbC,Nb} - k_{\gamma,Nb})}{(1 - k_{\gamma,Nb})} \frac{df_{NbC}}{dC_{l,Nb}} \qquad (5.11)$$

In this case, NbC is a stoichiometric compound so the value of $C_{NbC,Nb}$ can be taken as a constant and $k_{NbC,Nb}$ can be determined through (5.10) when $C_{l,Nb}$ is known. Thus, at any particular value of $C_{l,Nb}$ along the line of two fold saturation, all the values except f_l and $df_{NbC}/dC_{l,Nb}$ in (5.11) are known. An expression for $df_{NbC}/dC_{l,Nb}$ can be obtained by following the same mass balance procedure used for Nb. The result is

$$\frac{df_l}{dC_{l,C}} = -\frac{1}{(1 - k_{\gamma,C})} \frac{f_l}{C_{l,C}} - \frac{(k_{NbC,C} - k_{\gamma,C})}{(1 - k_{\gamma,C})} \frac{df_{NbC}}{dC_{l,C}} \qquad (5.12)$$

The carbon and niobium concentrations in the liquid along the line of two fold saturation are related by (5.2a). Taking the derivative of $C_{L,C}$ in (5.2a) with respect to $C_{L,Nb}$ yields

$$\frac{dC_{l,c}}{dC_{l,Nb}} = b \qquad dC_{l,c} = b\, dC_{l,Nb} \qquad (5.13)$$

Inserting (5.13) into (5.12) and solving for $df_{NbC}/dC_{L,Nb}$

$$\frac{df_{NbC}}{dC_{l,Nb}} = - \frac{df_l}{dC_{l,Nb}} \frac{(1 - k_{\gamma,c})}{(k_{NbC,c} - k_{\gamma,c})} - \frac{b}{(k_{NbC,c} - k_{\gamma,c})} \frac{f_l}{C_{l,c}} \qquad (5.14)$$

Inserting (5.14) into (5.11) provides a relation between $df_l/dC_{L,Nb}$, f_l, $C_{L,Nb}$ and $C_{L,C}$.

$$\frac{df_l}{dC_{l,Nb}} = \frac{\frac{f_l}{(1 - k_{\gamma,Nb})} \left[\frac{b}{C_{l,c}} \frac{(k_{NbC,Nb} - k_{\gamma,Nb})}{(k_{NbC,c} - k_{\gamma,c})} - \frac{1}{C_{l,Nb}}\right]}{\left[1 - \frac{(1 - k_{\gamma,c})}{(1 - k_{\gamma,Nb})} \frac{(k_{NbC,Nb} - k_{\gamma,Nb})}{(k_{NbC,c} - k_{\gamma,c})}\right]} \qquad (5.15)$$

The distribution coefficients for Nb and C in γ are assumed to be constant at the values measured in the previous chapter. Since the values of $C_{NbC,Nb}$ and $C_{NbC,C}$ are constant, the distribution coefficients for Nb and C in the NbC phase can be calculated from knowledge of the liquid composition at any point during solidification. The concentration of C in NbC found in Ni-16Cr-8Fe alloys has been reported as 9.5 wt% C [5.2]. Therefore, in this

work, the values of $C_{NbC,Nb}$ and $C_{NbC,C}$ are taken as 90.5 wt% Nb and 9.5 wt% C, respectively. This is in good agreement with the EPMA data shown in Table 4.1. Thus, eq. (5.15) describes the variation in fraction liquid with liquid composition ($C_{l,Nb}$ and $C_{l,C}$) at any value of f_l along the line of two fold saturation between γ and NbC.

This relation can be used to calculate solute redistribution during the eutectic-type $L \rightarrow (\gamma + NbC)$ reaction using a finite difference technique in the following manner: The first values of f_l (= f_e) , $C_{l,Nb}$ and $C_{l,C}$ are calculated from the intersection of the solidification path and line of two fold saturation, as given by eqs. (5.2), (5.3), and (5.4). These values are used to calculate the first value of $(df_l/dC_{l,Nb})_1$. The value of $(C_{l,Nb})_1$ is incremented by a very small amount, $\Delta C_{l,Nb}$, along the line of two fold saturation to a new value of $(C_{l,Nb})_2 = (C_{l,Nb})_1 + \Delta C_{l,Nb}$. The corresponding value of $(C_{l,C})_2$ is determined through eq. (5.2a). The corresponding value of $(f_l)_2$ is calculated by a small extrapolation of the value of $(df_l/dC_{l,Nb})_1$ by

$$(f_l)_2 = (f_l)_1 + \left(\frac{df_l}{dC_{l,Nb}}\right)_1 \Delta C_{l,Nb} \qquad (5.16)$$

The value of $(df_l/dC_{l,Nb})_1$ is also used in eq. (5.14) to calculate $(df_{NbC}/dC_{l,Nb})_1$, and the value of $(f_{NbC})_2$ is calculated via

$$(f_{NbC})_2 = (f_{NbC})_1 + \left(\frac{df_{NbC}}{dC_{l,Nb}}\right)_1 \Delta C_{l,Nb} \qquad (5.17)$$

The value of $(f_\gamma)_1$ is given by $(f_\gamma)_1 = 1 - (f_l)_1 - (f_{NbC})_1$. The values of $(C_{l,Nb})_2$, $(C_{l,C})_2$, and $(f_l)_2$ are then put back into eq. (5.15) and the calculations are repeated. The values of $k_{NbC,Nb}$ and $k_{NbC,C}$ are calculated at each step by knowledge of the NbC and liquid compositions. When the values of $C_{l,Nb}$ and $C_{l,C}$ reach the transition point where the L $\rightarrow$ (γ + NbC) reaction is replaced by the L $\rightarrow$ (γ + Laves) reaction, the remaining fraction liquid at that point transforms to the γ/Laves eutectic-type constituent and solidification is complete. The composition of γ at any point during solidification is calculated by knowledge of the liquid composition and distribution coefficients.

The procedure above provides the relation between the fraction liquid and liquid composition at any point along the line of two fold saturation which, in turn, permits calculation of the volume fractions of each eutectic-type constituent present in the as solidified microstructure. These relations are derived assuming that Nb and C each exhibit negligible diffusion in the austenite matrix. While this is a good assumption for Nb, the opposite extreme of infinitely fast diffusion is more appropriate for C. The M-F model is now modified to allow for such behavior.

5.2 MODIFICATION TO MEHRABIAN-FLEMINGS MODEL

5.2.1 PRIMARY L → γ SOLIDIFICATION

The relation describing the variation in Nb and C contents in the liquid during primary γ solidification under conditions of negligible Nb diffusion and infinitely fast C diffusion was already introduced in the previous chapter through eq. (4.29):

$$C_{l,Nb} = C_{o,Nb}\left[\frac{C_{o,C} - k_C C_{l,C}}{(1 - k_C)\, C_{l,C}}\right]^{k_{Nb}-1} \qquad (5.18)$$

This relation is analogous to eq. 5.1 of the M-F model. The procedure for calculating the total volume fraction of eutectic-type constituents which form after primary solidification is similar to that described above for the M-F model. Eq. (5.18) is set equal to eq. (5.2b) to find the C content of the liquid, $C_{l,C}$, at the point where the primary solidification path intersects the line of two fold saturation.

$$\frac{C_{l,C} - a}{b} = C_{o,Nb}\left[\frac{C_{o,C} - k_C C_{l,C}}{(1 - k_C)\, C_{l,C}}\right]^{k_{Nb}-1} \qquad (5.19)$$

The corresponding Nb content, $C_{l,Nb}$, is calculated by back substitution of this value of $C_{l,C}$ into eq. (5.2a). Lastly, this value of $C_{l,Nb}$ is used to calculate the total amount of eutectic-type constituent through eq. (5.4).

5.2.2 EUTECTIC-TYPE SOLIDIFICATION

Since Nb diffusion is still assumed negligible, the differential mass balance for Nb given by eq. (5.11) in the M-F model remains valid. For C, the equilibrium lever law is used, with the addition of a new term to account for formation of NbC from the liquid. This is similar to the additional term which was needed in the differential mass balance for Nb given by eq. (5.5). The equilibrium mass balance for C along the line of two fold saturation is given by

$$C_{o,C} = f_l C_{l,C} + f_\gamma C_{\gamma,C} + f_{NbC} C_{NbC,C} \qquad (5.20)$$

As with the M-F model, it is now necessary to use eq. (5.20) for obtaining an expression for $df_{NbC}/dC_{l,Nb}$ which can be inserted into eq. (5.11) to arrive at the final relation for $df_l/dC_{l,Nb}$. Eq. (5.20) can be used to define a relation between f_{NbC} and $C_{l,Nb}$ by first noting that

$$f_\gamma = 1 - f_{NbC} - f_l \qquad (5.21)$$

$$C_{\gamma,C} = k_{\gamma,C} C_{l,C} \qquad (5.22)$$

Eqs. (5.21) and (5.22) are inserted into (5.20) to arrive at a relation between f_{NbC} and $C_{l,Nb}$

$$f_{NbC} = \frac{C_{o,c} - C_{l,c}\,[\,f_l + k_{\gamma,c}(1 - f_l)\,]}{(C_{NbC,c} - k_{\gamma,c}C_{l,c})} \qquad (5.23)$$

Under the general case of a second phase forming (which, in this particular case, is the NbC phase), the composition of the secondary solid phase would have to be expressed in terms of the liquid composition through the distribution coefficient in order to arrive at a general expression for f_{NbC} in terms of the liquid composition. However, in this particular case, the NbC is a stoichiometric compound which forms at constant composition. Thus, $C_{NbC,C}$ is a constant in eq. (5.23) and such an approach is not needed.

The derivative of f_{NbC} with respect to $C_{L,C}$ can be found be applying the quotient rule of derivatives and is given by

$$\frac{df_{NbC}}{dC_{l,c}} = \frac{k_{\gamma,c}C_{o,c} - C_{NbC,c}\,[\,f_l + k_{\gamma,c}(1 - f_l)\,]}{(C_{NbC,c} - k_{\gamma,c}C_{l,c})^2} \qquad (5.24)$$

Eq. (5.13) is now inserted into eq. (5.24) to arrive at the desired relationship between df_{NbC} and $dC_{l,Nb}$

$$\frac{df_{NbC}}{dC_{l,Nb}} = \frac{b\,k_{\gamma,C}C_{o,C} - b\,C_{NbC,C}\,[f_l + k_{\gamma,C}(1 - f_l)]}{(C_{NbC,C} - k_{\gamma,C}C_{l,C})^2} \qquad (5.25)$$

Eq. (5.25) is analogous to eq. (5.14) of the M-F model, except that eq. (5.25) describes the condition of C equilibrium. Lastly, eq. (5.25) is inserted into eq. (5.11) to obtain the final relation between df_l and $dC_{l,Nb}$

$$\frac{df_l}{dC_{l,Nb}} = -\frac{1}{(1 - k_{\gamma,Nb})}\frac{f_l}{C_{l,Nb}} - \left[\frac{(k_{NbC,Nb} - k_{\gamma,Nb})}{(1 - k_{\gamma,Nb})}\right]\left[\frac{b\,k_{\gamma,C}C_{o,C} - b\,C_{NbC,C}\,[f_l + k_{\gamma,C}(1 - f_l)]}{(C_{NbC,C} - k_{\gamma,C}C_{l,C})^2}\right] \qquad (5.26)$$

Eq. (5.26) is analogous to eq. (5.15) in the M-F model, and the finite difference calculation procedure is conducted in the same manner described previously. These relations are utilized in the next section to calculate the total and individual amounts of eutectic type constituents which form in the experimental alloys.

5.3 MODELLING RESULTS

The parameters used to calculate the compositions and fractions of each phase forming during solidification are summarized in Table 5.1. The values of $k_{\gamma,Nb}$ and $k_{\gamma,C}$ are those derived from EPMA and DTA data in the previous chapter. The value of $k_{\gamma,C}$ in the Fe base alloys was assumed equivalent to that in the Ni base alloys. As previously discussed, this should be a reasonable estimate. All these values are assumed constant during solidification. The C content of the NbC phase (9.5 wt% C) is based on the value

reported for NbC in Ni-16Cr-8Fe [5.2]. This is in good agreement with the NbC composition in the simple Nb-C system which exhibits a rather narrow range of 9 to 12 wt% C [5.3]. Nb is assumed to fill the remaining composition, so that $C_{NbC,Nb}$ = 90.5 wt% Nb. The values of $C_{Nb,L\rightarrow(\gamma+Laves)}$ and $C_{C,L\rightarrow(\gamma+Laves)}$ listed in Table 5.1 represent the point on the solidification surfaces where the L $\rightarrow$ (γ + NbC) reaction is replaced by the L $\rightarrow$ (γ + Laves) reaction. When the Nb and C contents in the liquid reach these points, the remaining liquid (f_l) transforms to the γ/Laves constituent ($f_{\gamma/Laves}$) and the calculations are terminated. The amount of the γ/NbC constituent is then given by $f_{\gamma/NbC} = f_e - f_{\gamma/Laves}$, where f_e is the total amount of eutectic. The value of f_e is calculated by determining the fraction of liquid remaining at the point where the primary solidification path intersects the line of two fold saturation. The constants **a** and **b** were determined by linear regression analysis from the point of ($C_{Nb,\ L\rightarrow(\gamma+Laves)}$, $C_{C,L\rightarrow(\gamma+Laves)}$) to the data points on the line of two fold saturation determined in Section 4.4.

Table 5.1. Summary of solidification parameters used in finite difference calculations.

QUANTITY	Ni Base Alloys	Fe Base Alloys	UNITS
$k_{\gamma Nb}$	0.46	0.25	unitless
$k_{\gamma C}$	0.27	0.27	unitless
$C_{NbC,Nb}$	90.5	90.5	wt% Nb
$C_{NbC,C}$	9.5	9.5	wt% C
a	0.98	1.24	wt% C
b	-0.04	-0.06	wt% C/wt% Nb
$C_{Nb,\ L\rightarrow(\gamma + Laves)}$	23.1	20.4	wt% Nb
$C_{C,\ L\rightarrow(\gamma + Laves)}$	0.03	0.03	wt% C

5.3.1 PRIMARY L → γ SOLIDIFICATION

The solidification path of each alloy was calculated via eq. (5.18) (Nb diffusion negligible and C diffusion infinitely fast) and plotted on the respective solidification surface. The results of the calculations are presented in Figures 5.1, 5.2, and 5.3. Figures 5.1 and 5.2 plot the results for the Ni base and Fe base alloys, respectively. The results are grouped according to alloys with similar Nb contents. Figure 5.3a compares the solidification paths of Ni base alloys with similar C contents and variations in Nb, and Figure 5.3b compares the solidification paths of a Ni base and Fe base alloy with similar levels of solute elements (Nb, Si, and C). The solidification path for each alloy initiates at the nominal composition and generally progresses towards the line of two fold saturation between γ and NbC as the liquid becomes enriched in Nb and C. When the primary L → γ path strikes the line of two fold saturation, solidification then proceeds along the line of two fold saturation in the direction of decreasing temperature (i.e., toward the γ - NbC "binary"). The amount of solid formed during primary solidification is proportional to the total distance of the primary solidification path. This relation is useful, as it allows for fast, qualitative interpretations of alloying effects by simple visual inspection of the results.

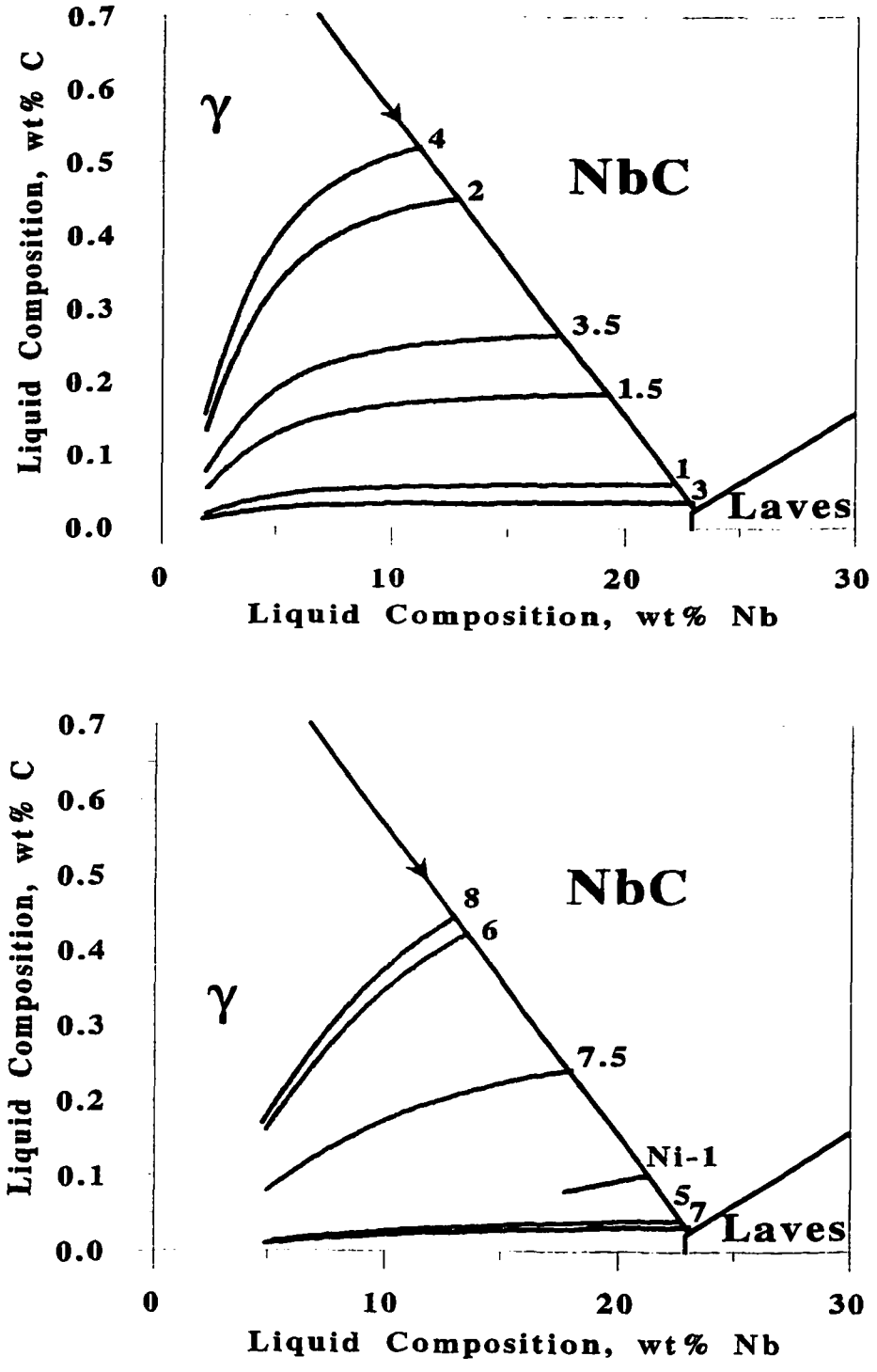

Figure 5.1 Calculated solidification paths for the Ni base alloys.

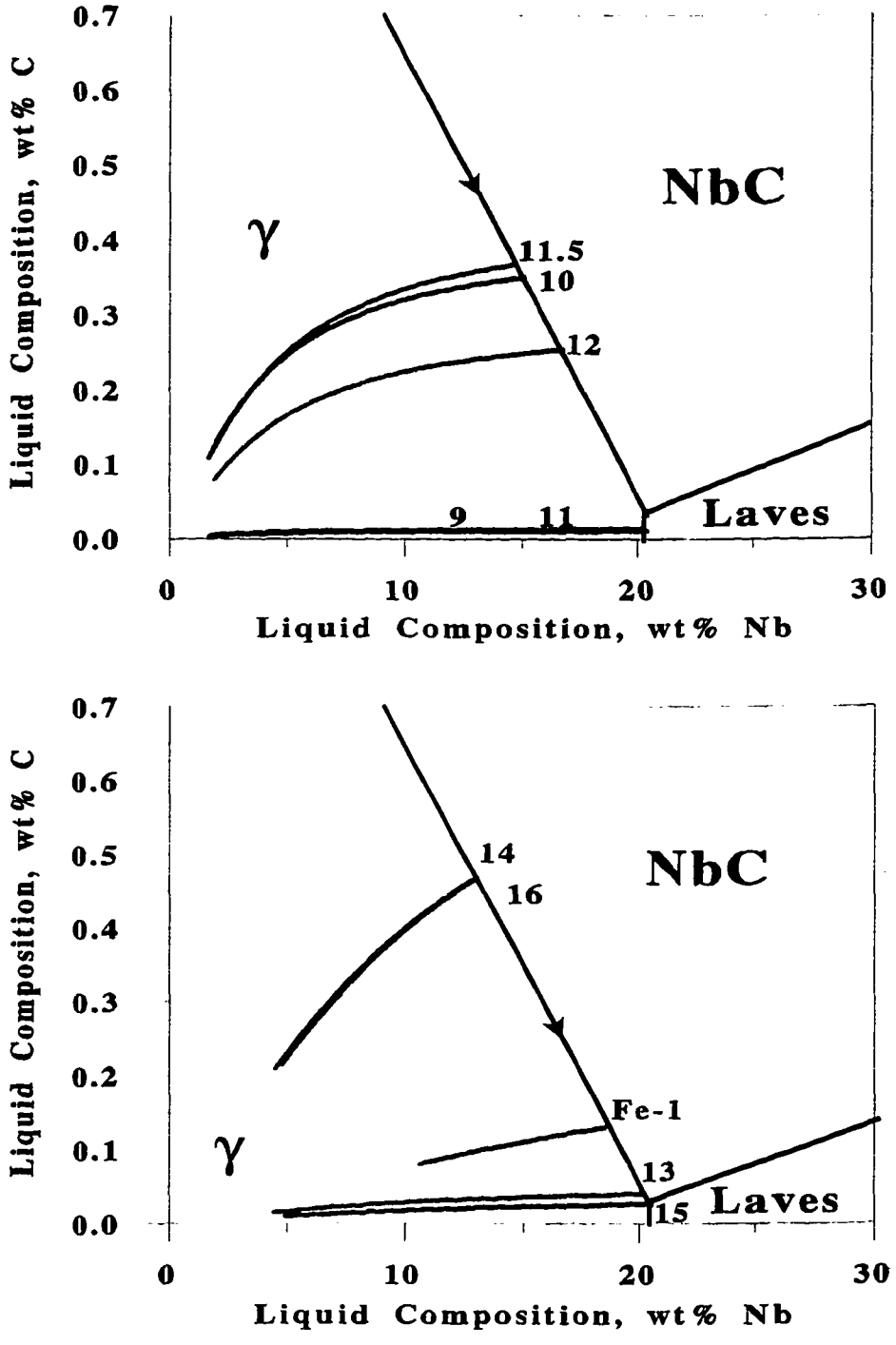

Figure 5.2 . Calculated solidification paths for the Fe base alloys.

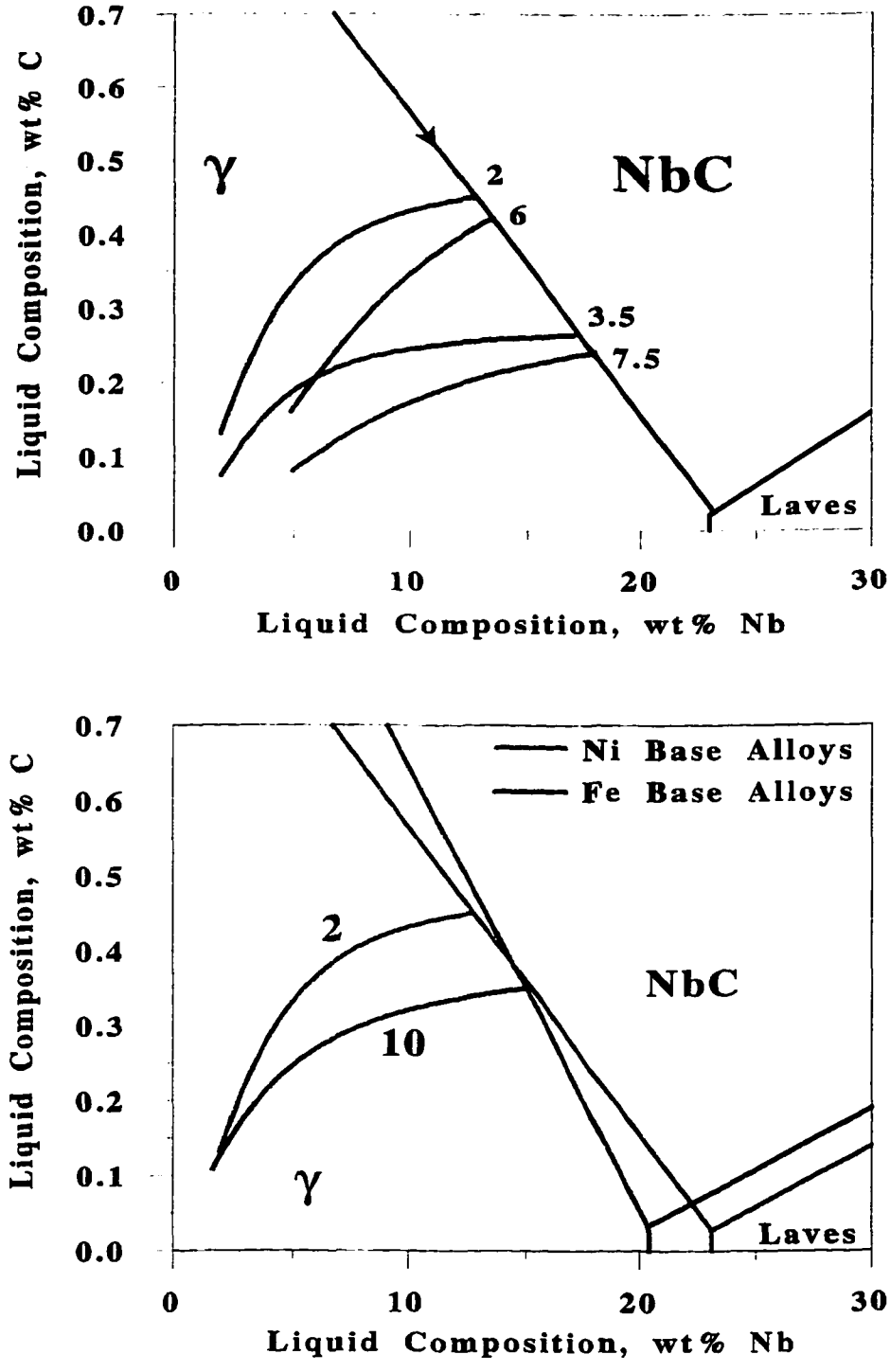

Figure 5.3. a) Calculated solidification paths of Alloys 2, 3.5, 6, and 7.5. b) Calculated solidification paths of Alloys 2 and 10.

These diagrams provide several key points concerning the solidification behavior of these alloys. First, it is readily apparent that the point of intersection between the primary solidification path and line of two fold saturation is a strong function of C content. Although C additions are intuitively expected to promote the γ/NbC eutectic type constituent, this analysis provides a quantitative rationale for the observed behavior. As the C content is increased, the intersection point occurs at higher C contents. As a result, the liquid composition must "travel" a long distance down the $L \rightarrow (\gamma + NbC)$ line of two fold saturation, forming γ/NbC as it travels, before the γ/Laves constituent can possibly form. The relative temperature at which the $L \rightarrow (\gamma + NbC)$ reaction starts is also readily assessed, where high nominal C contents drive the initiation of the reaction to higher temperatures. The experimental DTA data generally show this trend (e.g., compare Alloy 3.5 to 4 and Alloy 7.5 to 8 in Tables 4.4). The only exception to this behavior occurs between alloys with variations in Si content. For example, Figure 5.1b suggests that Alloy 8 should have a higher reaction start temperature than Alloy 6, but the experimental DTA data reveals the opposite case. This difference is caused by the higher Si content of Alloy 8. Since the liquidus slope for Si is negative (-23.4 °C/wt% in the Ni base alloys), the entire liquidus surface for Alloy 8 is shifted to a lower temperature relative to the surface of Alloy 6. The higher Si content of the γ/NbC constituent measured by EPMA in Alloy 8 (Table 4.6) supports this. This pseudo-ternary approach can not account for such effects from a third solute element. However, the general influence of Si will become apparent in the modelling results and will be discussed in qualitative terms where appropriate.

The increase in reaction temperature with increasing C content is not initially intuitive, particularly when one considers that the liquidus slope for C is negative. This, at first, suggests that any increase in carbon in the liquid should drive the reaction to lower temperatures. The true effect can be understood by considering the relation between Nb and C along the line of two fold saturation. The slope of this line, **b**, is -0.04 wt%C/wt%Nb for the Ni base alloys. Thus, for every 0.04 wt% increase in C content, there is a corresponding decrease of 1 wt% Nb in the liquid. Assuming the liquidus slope for each element is constant and equal to the values given in Table 4.10: $m_{l,C}$ = -34.1 °C/wt%C and $m_{l,Nb}$ = -8.3 °C/wt%Nb, then there is a drop in the reaction temperature of ≈ 1.4 °C for every increase of 0.04 wt%C. However, there is a simultaneous increase in the reaction temperature of 8.3 °C for the corresponding decrease in 1 wt% Nb content. Thus, a net increase of ≈ 6.9° C in reaction temperature is expected with every 0.04 wt% increase in C content (1 wt% decrease in Nb content). A similar trend is expected for the Fe base alloys as well, where a rise of ≈ 8°C in reaction temperature would be expected for every 1 wt% decrease in Nb content. Figure 5.4 plots the temperatures for the L → (γ + NbC) and L → (γ + Laves) reactions as a function of Nb composition. This plot, in effect, provides a cross-sectional view of the three-dimensional solidification surface. In Figure 5.4a, for example, at any liquid composition less than 23.1 wt% the L → (γ + NbC) reaction is occurring at the indicated temperature. Once the liquid composition reaches 23.1 wt% Nb, the L → (γ + Laves) reaction is initiated. The reaction temperatures were obtained from the DTA measurements. The Nb compositions are determined from a combination of QIA/EPMA data (Table 4.18) and values calculated by the intersection

of the primary solidification path with the line of two fold saturation. There appears to be a rather sharp drop in temperature as the $L \rightarrow (\gamma + \text{Laves})$ reaction is approached. This has important implications with regards to weldability as discussed in the next chapter. The slope of the lines for the $L \rightarrow (\gamma + \text{NbC})$ reaction in the Ni base and Fe base alloys show an increase in reaction temperature of ≈ 3.5 °C and ≈ 5.1 °C for every decrease in 1 wt% Nb, respectively. Although these are not in perfect agreement with the values of 6.9 and 8°C calculated above, they are reasonably close.

At a given C content, the Nb concentration also has a significant effect on the primary solidification path. This is revealed by comparing Alloy 2 to 6 and Alloy 3.5 to 7.5 in Figure 5.3a. When Nb is low, the C content in the liquid increases relatively quickly during the early stage of solidification. The rate of C build-up then decreases as the solute becomes depleted in the liquid. Overall, the reaction start temperature will increase with decreasing Nb (i.e., increasing C/Nb ratio). Again, this trend is consistent with the experimental DTA data. Since the length of the primary solidification paths for the high Nb alloys are shorter, these alloys will exhibit more liquid at the intersection point (i.e., more total eutectic-type constituent). The primary solidification paths of the two GTA melt alloys (Ni-1 and Fe-1) are also plotted. These alloys have very high Nb and relatively low C. Thus, the primary solidification path intersects the γ/NbC two fold saturation line just above the class II reaction point. At this point, there is a large fraction of liquid which is high in Nb. As a result, each alloy forms a large amount of the γ/Laves constituent after traveling a relatively short distance down the $L \rightarrow (\gamma + \text{NbC})$ reaction line (see Figures 4.31 and 4.32). The nominal composition of Alloy Ni-1 is particularly

close to the L → (γ + NbC) reaction line. This may account for the difficulty encountered in revealing two distinct reaction peaks in the DTA scan (Figure 4.39).

The effect of matrix composition is presented in Figure 5.3b. Alloys 2 and 10 have very similar levels of solute content, but different matrix compositions. Thus, the main difference here is in the value of k_{Nb} (k_{Nb} in Ni base Alloys = 0.46 while k_{Nb} in the Fe base Alloys = 0.25). As k is reduced, Nb segregates more aggressively to the liquid. Thus, at any given level of C in the liquid, the Fe base alloys will always possess more Nb. As a result, the Fe base alloys will have more liquid remaining after primary solidification, and the Nb content in that remaining liquid will be higher. These two effects from the reduced k_{Nb} value, combined with the slightly lower L → (γ + Laves) "eutectic" composition of 20.4 wt% Nb, are the reasons for the higher amounts of total and γ/Laves eutectic-type constituents observed in the Fe base alloys.

Lastly, the order of eutectic-type reactions predicted by this approach is readily read from the diagrams. Any alloy which exhibits a primary L → γ path that terminates above the class II reaction is expected to undergo the L → (γ + NbC) reaction prior to terminating solidification with the L → (γ + Laves) reaction. This behavior is predicted for all the alloys except 9, 11, and 15. This is in reasonable agreement with experimental observations, where all the alloys exhibited the NbC phase. For the Fe base alloys, the value of k_C determined in the Ni base alloys had to be used. This may account for at least some of the discrepancy observed in Alloys 9, 11, and 15, and suggests that the actual value of k_C in the Fe base alloys is lower than that in the Ni base alloys. With a lower value of k, carbon would segregate more strongly to the liquid and extend the primary L

$\rightarrow \gamma$ path farther into the C rich side of the solidification surface so that it would tend to terminate above the class II reaction. In addition, the point of the class II reaction is taken from an average of all the Nb values determined in the γ/Laves constituent. However, as displayed by the EPMA data in Table 4.7, this point is actually dependent on the amount of Fe, Cr, and Si in the liquid. The Nb content in the liquid required to satisfy the condition for the $L \rightarrow (\gamma + \text{Laves})$ reaction generally decreases with increasing Fe, Cr, and Si. Thus, representing the class II reaction as a single point will also lead to some error. However, the variation in Nb content is rather small and the potential variation in C content in the liquid, as bounded by eqs. (4.27) and (4.29), is also very small. Thus, this estimate should not lead to significant error.

The accuracy of this pseudo-ternary approach for the primary $L \rightarrow \gamma$ reaction portion of solidification can be evaluated by comparing the values of calculated and measured amounts of total eutectic-type constituent. These values are summarized in Table 5.2, where the alloys are grouped to make comparisons among the two matrix compositions which contain similar levels of solute elements. The results are plotted in Figure 5.5. The general trends discussed qualitatively above can now be viewed in quantitative fashion. The total amount of eutectic increases with increasing C and Nb contents and a change in matrix composition from low to high Fe. The results between calculated and measured total eutectic constituent is good, especially considering that the input data for this model comes from a number of different experimental techniques (EPMA, DTA, QIA, wet chemical analysis). This also provides some confidence that the position of the line of two fold saturation separating γ and NbC is reasonably accurate.

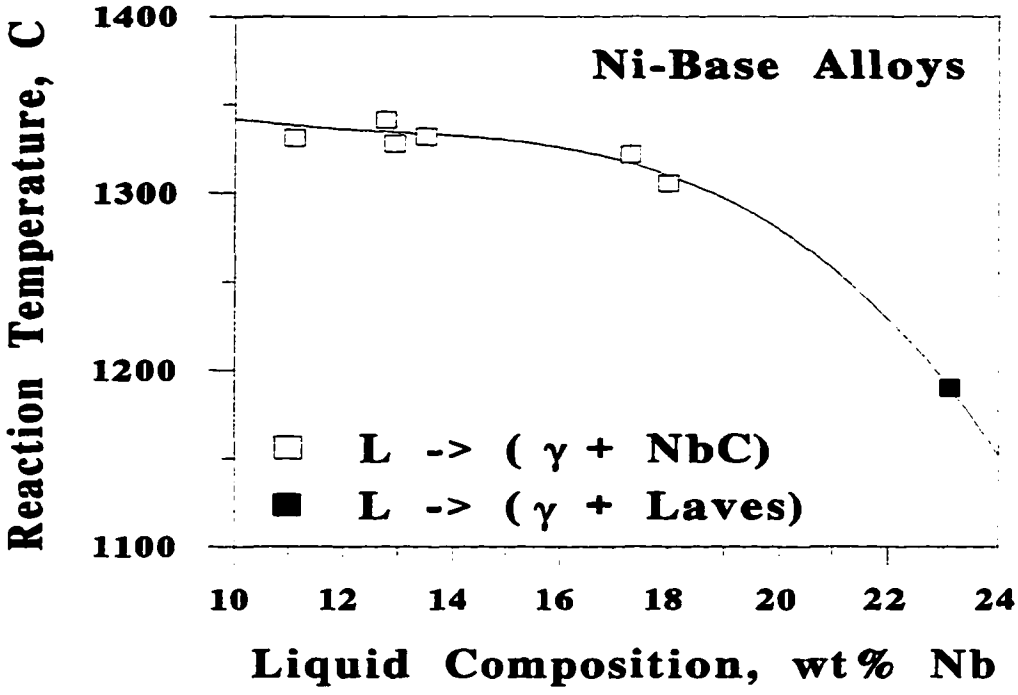

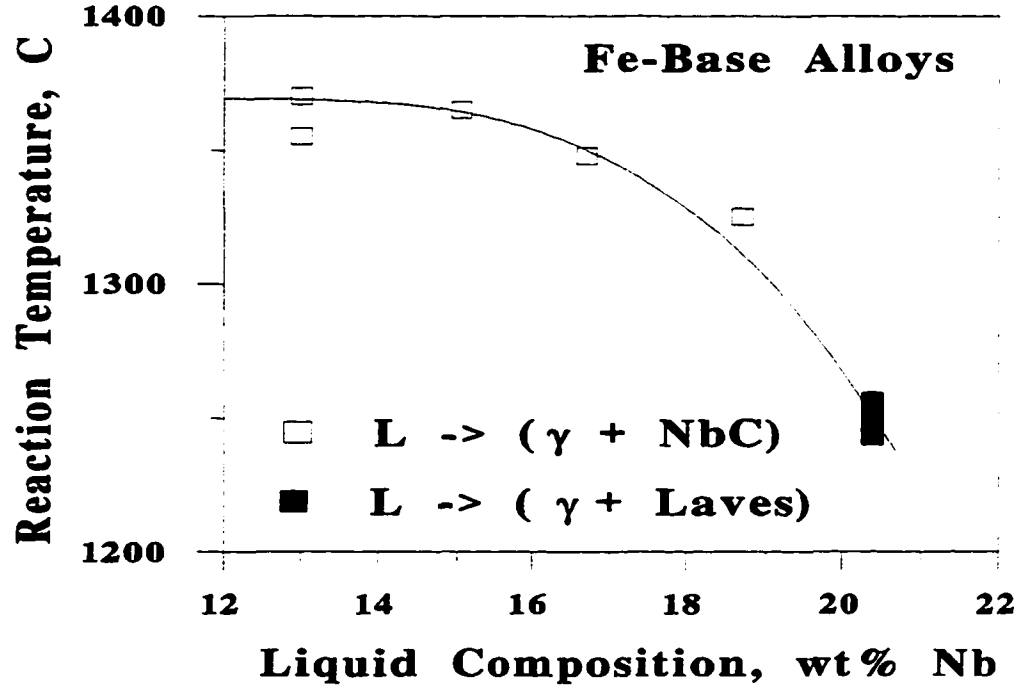

Figure 5.4. Variation in reaction temperature with Nb content in the liquid. a) Ni base alloys. b) Fe base alloys.

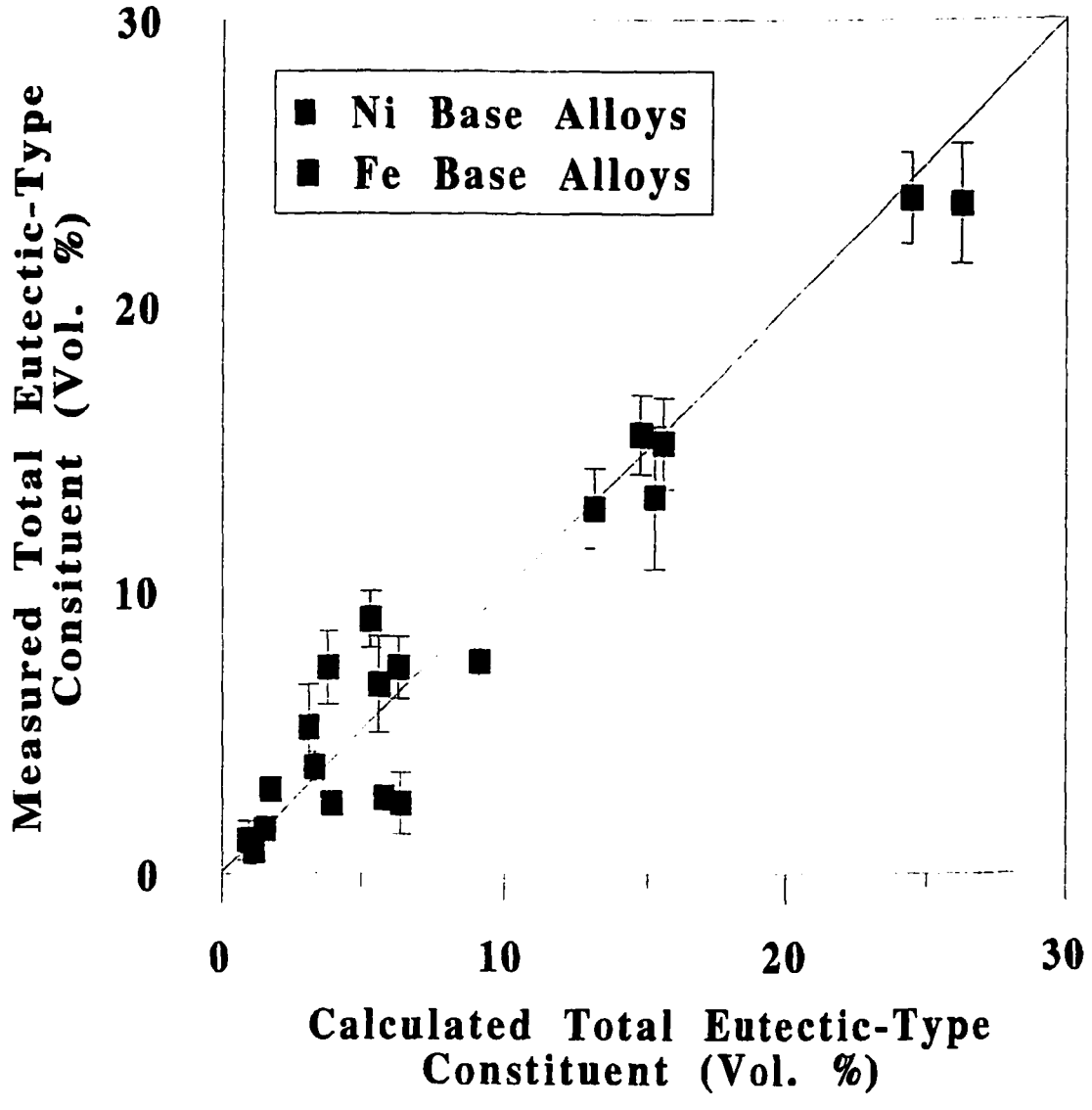

Figure 5.5. Comparison between calculated and measured total volume percentages of eutectic-type constituents.

Table 5.2 Comparison of measured and calculated total eutectic type constituents.

Alloy	Measured (Vol. %)	Calculated (Vol. %)	Alloy	Measured (Vol. %)	Calculated (Vol. %)
1	0.8 ± 0.2	1.1	9	3.8 ± 0.5	3.3
1.5	1.6 ± 0.4	1.5	--	--	--
2	5.2 ± 1.5	3.1	10	9.0 ± 1.0	5.3
3	1.2 ± 0.7	0.9	11	2.5 ± 0.4	3.9
3.5	3.0 ± 0.4	1.7	12	7.3 ± 1.1	5.6
4	7.3 ± 1.3	3.8	11.5	6.7 ± 1.7	6.3
5	2.5 ± 1.1	6.4	13	12.9 ± 1.4	13.1
6	13.3 ± 2.5	15.2	14	23.8 ± 1.6	24.4
7	2.7 ± 0.4	5.8	15	15.5 ± 1.4	14.8
7.5	7.5 ± 0.5	9.1	--	--	--
8	15.2 ± 1.6	15.5	16	23.6 ± 2.1	26.2

5.3.2 EUTECTIC-TYPE SOLIDIFICATION

Solute redistribution during the eutectic-type solidification stage was calculated for each alloy with a finite difference technique using eq. (5.26). Calculations were also conducted using the M-F Model, eq. (5.15), in order to reveal the effect of C diffusion. The results of calculations for several alloys, which represent the range of behavior, are shown in Figures 5.6 through 5.9. The top figures show results for the entire solidification process, where solute redistribution during primary solidification is calculated through eq. (5.18) and the final stages of eutectic-type solidification is calculated with both the standard and modified M-F model. The final stages of solidification are shown in more detail in the bottom figure. Each figure shows the variation in γ and liquid composition

during solidification. Solute redistribution during the L → (γ + NbC) reaction was calculated until the liquid composition became enriched in Nb and depleted in C to the point where the L → (γ + Laves) reaction is initiated. At this point, the remaining liquid transforms to the γ/Laves constituent and the calculations were terminated. The measured and calculated values of the individual eutectic-type constituents are summarized in Table 5.3 and compared in the Figures 5.10 and 5.11.

At any value of liquid composition during solidification, the condition of negligible C diffusion (M-F Model) will always produce a higher fraction of liquid (i.e., less solid) than that predicted under conditions of infinitely fast C diffusion. The M-F model was developed under the same assumptions used to derive the Scheil equation and represents the most severe case of microsegregation. Thus, just as in the analogous two component Scheil equation, this model predicts that some finite amount of liquid will persists during solidification until it becomes sufficiently rich in solute to reach a local minimum on the liquidus surface. At this point, solidification will terminate via the appropriate reaction which exists at the local minimum. For the particular alloys studied here, this implies that some finite amount of the γ/Laves constituent will always be predicted. This is readily evident in the data of Table 5.3 and Figure 5.11, where the M-F model always predicts that some γ/Laves will exist after solidification. Any departure of this "Scheil-type" condition towards equilibrium behavior, which occurs when C is allowed to diffuse infinitely fast, will always predict a higher amount of solid for a given liquid composition. As a result of this effect, the modified form of the M-F model always predicts a higher amount of γ/NbC constituent, and it is possible for solidification to be

completed along the L $\rightarrow$ (γ + NbC) reaction line before the liquid composition has a chance to satisfy conditions for the L $\rightarrow$ (γ + Laves) reaction. This solidification sequence is predicted for Alloys 1.5, 2, 3.5, 4, 6, 8, 10, and 11.5. Experimentally, this solidification sequence is observed in Alloys 2, 3.5, and 4.

It should be noted, however, that the differences in the model results are generally small. This can be understood by considering the exchange of C between liquid and the two solid phases, γ and NbC. The C rejected by the liquid during solidification must be dissolved by γ and NbC. The liquid reaches a maximum C content of $\approx$0.5 wt% during solidification. Considering that $k_{\gamma,C} = 0.27$, the γ will only dissolve a maximum of $\approx$ 0.14 wt% C. In contrast, NbC requires 9.5 wt% C to form. Thus, nearly all the C rejected by the liquid is absorbed by the NbC. This is, in fact, why the C content in the liquid begins to decrease when NbC starts forming. Thus, any modification concerning C transport within the γ phase is not expected to have any significant effect on the overall solute redistribution behavior.

Based on the diffusion behavior of C, the modified form of the M-F model is expected to yield results which are more representative of these alloys. However, the small difference in the results for these particular alloys, together with the simplifying assumptions made in the pseudo-ternary approach, do not permit any detailed comparisons. The modified form does accurately predict the completion of solidification during the L $\rightarrow$ (γ + NbC) reaction for Alloys 2, 3.5, and 4, as no γ/Laves constituent was observed in these alloys. However, the same model also predicts that no γ/Laves should be present in Alloys 6, 8, 10, and 11.5, while this constituent is observed

experimentally in small amounts. Considering the assumptions invoked with this approach, the resolution of such fine detail is not expected. The presence of γ/Laves in Alloys 8 and 11.5 can be attributed to their high Si content. In effect, less Nb is needed in the liquid to satisfy conditions for the L $\rightarrow$ (γ + Laves) reaction as the Si content is raised. For a given alloy, the Si content in the γ/NbC constituent is always lower than that in the γ/Laves (compare EPMA data for Alloys 8, 14, and 16 in Tables 4.6 and 4.7). This indicates that the distribution coefficient for Si remains below unity during the L $\rightarrow$ (γ + NbC) reaction. Thus, the line of two fold saturation for the L $\rightarrow$ (γ + NbC) reaction is actually shifting to lower Nb values as solidification progresses. Alloys with higher nominal Si contents will induce more of a shift in the position and are therefore more likely to reach the composition conditions for the L $\rightarrow$ (γ + Laves) reaction. All other factors being equal, the higher Si alloys always show the larger amount of γ/Laves (e.g., compare Alloy 6 to 8 and Alloy 10 to 11.5). Such effects can not be accounted for with this approach. Nevertheless, there is reasonable agreement between measured and calculated total and individual eutectic-type constituents using this approach. This confirms that the model developed here correctly captures the major factors controlling the solidification behavior of this important class of alloys. In addition, the modified form of the M-F model developed here is general enough to apply to other alloy systems in which variations in the diffusion behavior of one of the solutes may lead to more pronounced effects.

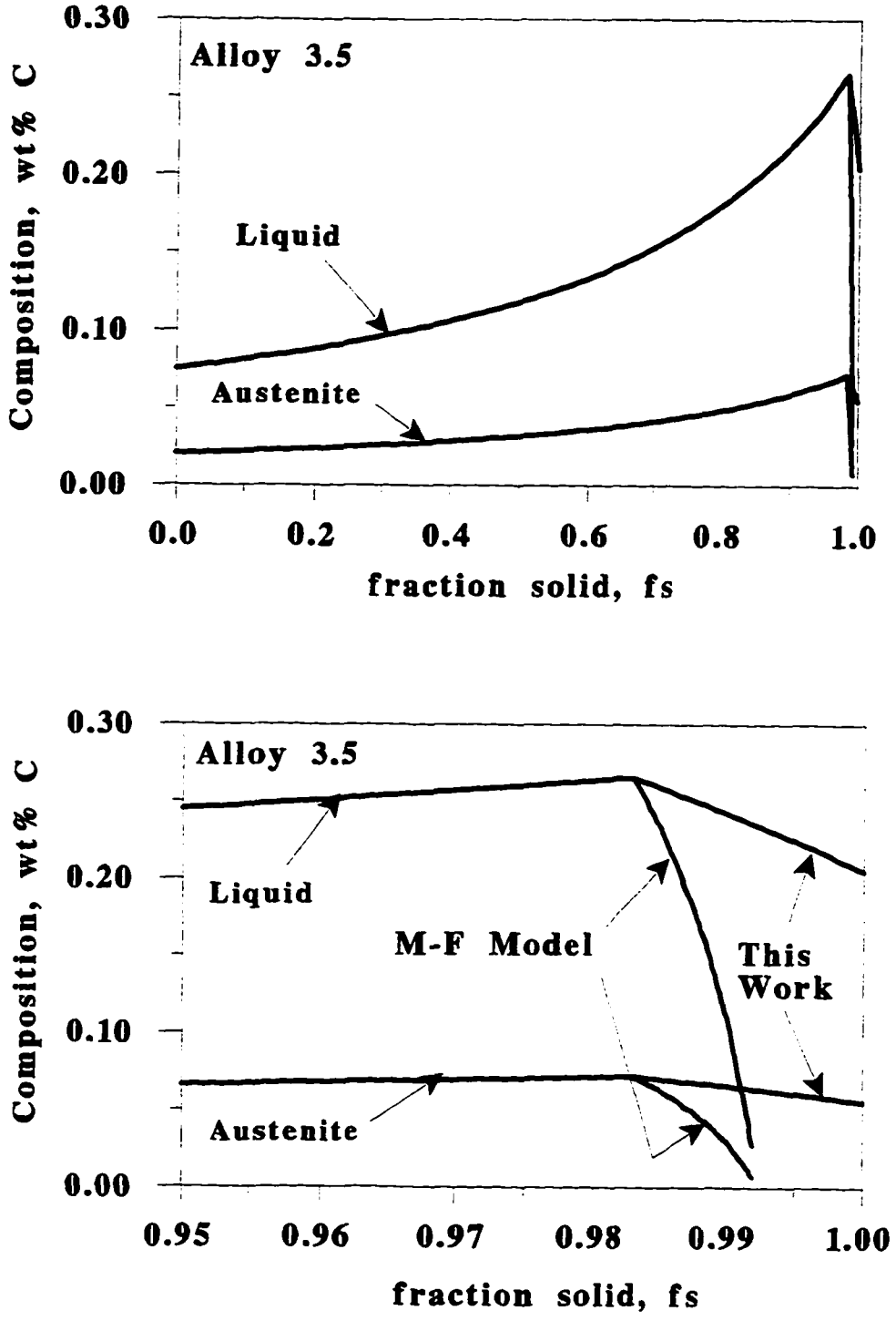

Figure 5.6a. Calculated variation in C content in liquid and γ phases as a function of fraction solid for Alloy 3.5.

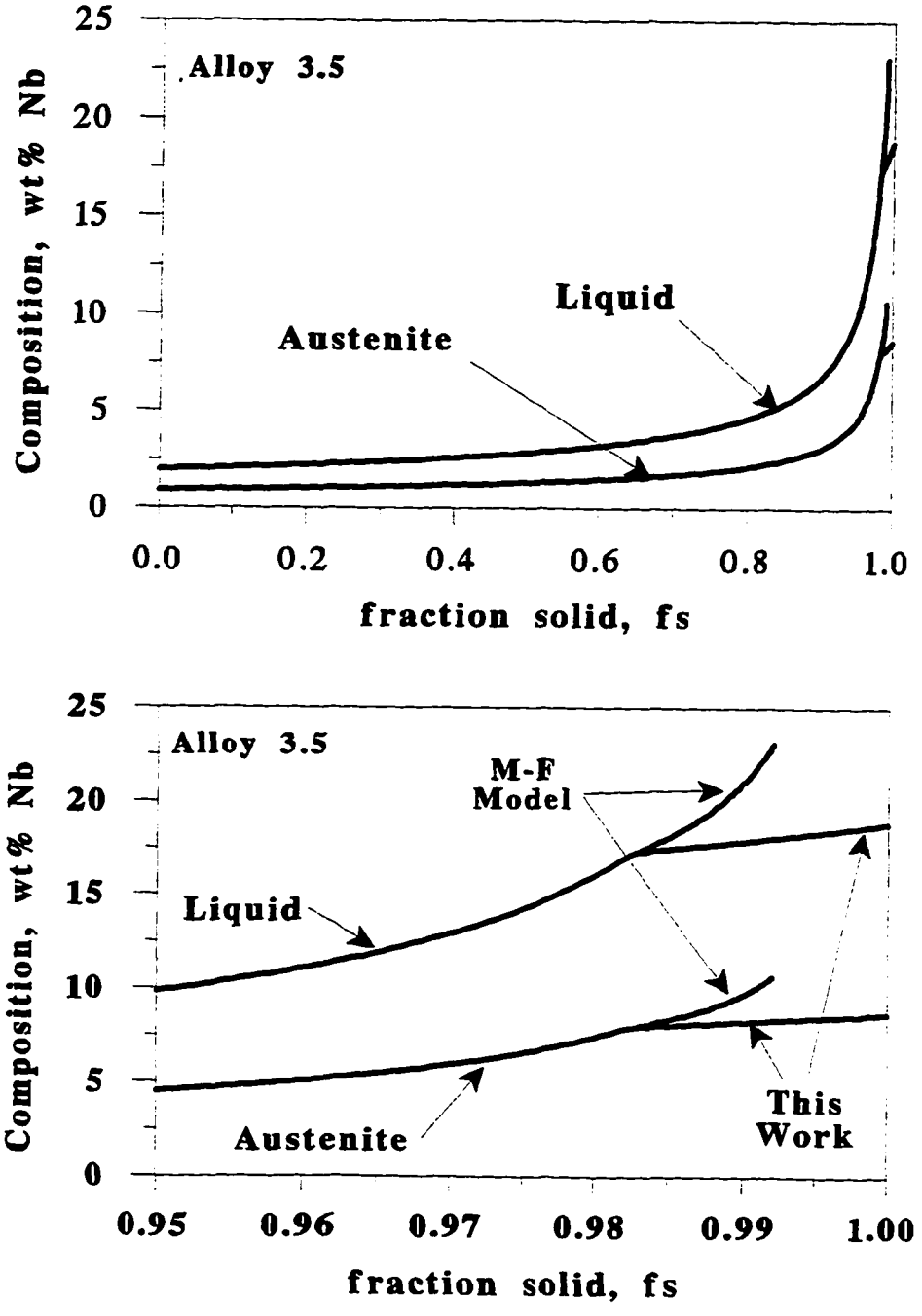

Figure 5.6b. Calculated variation in Nb content in liquid and γ phases as a function of fraction solid for Alloy 3.5.

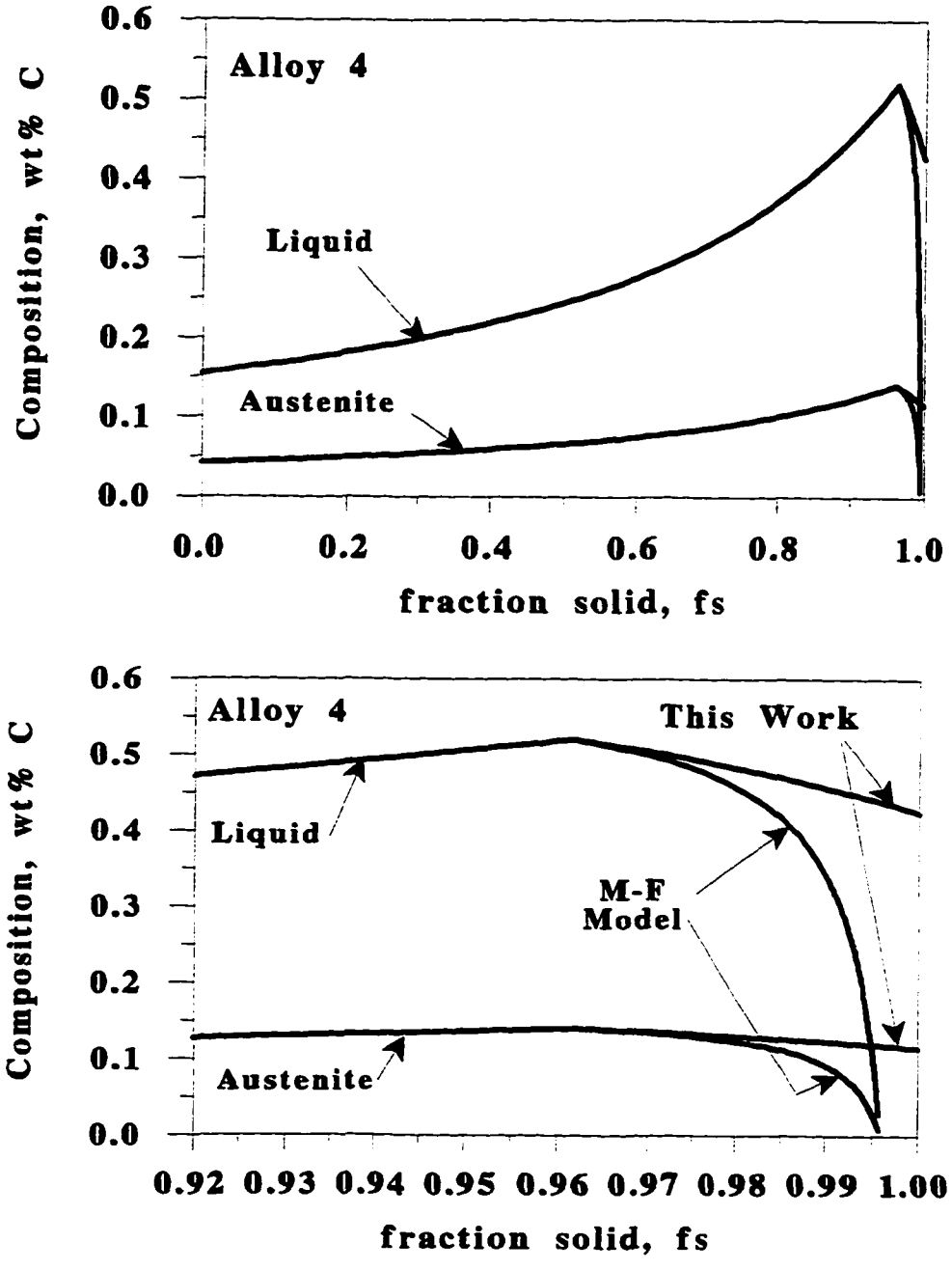

Figure 5.7a. Calculated variation in C content in liquid and γ phases as a function of fraction solid for Alloy 4.

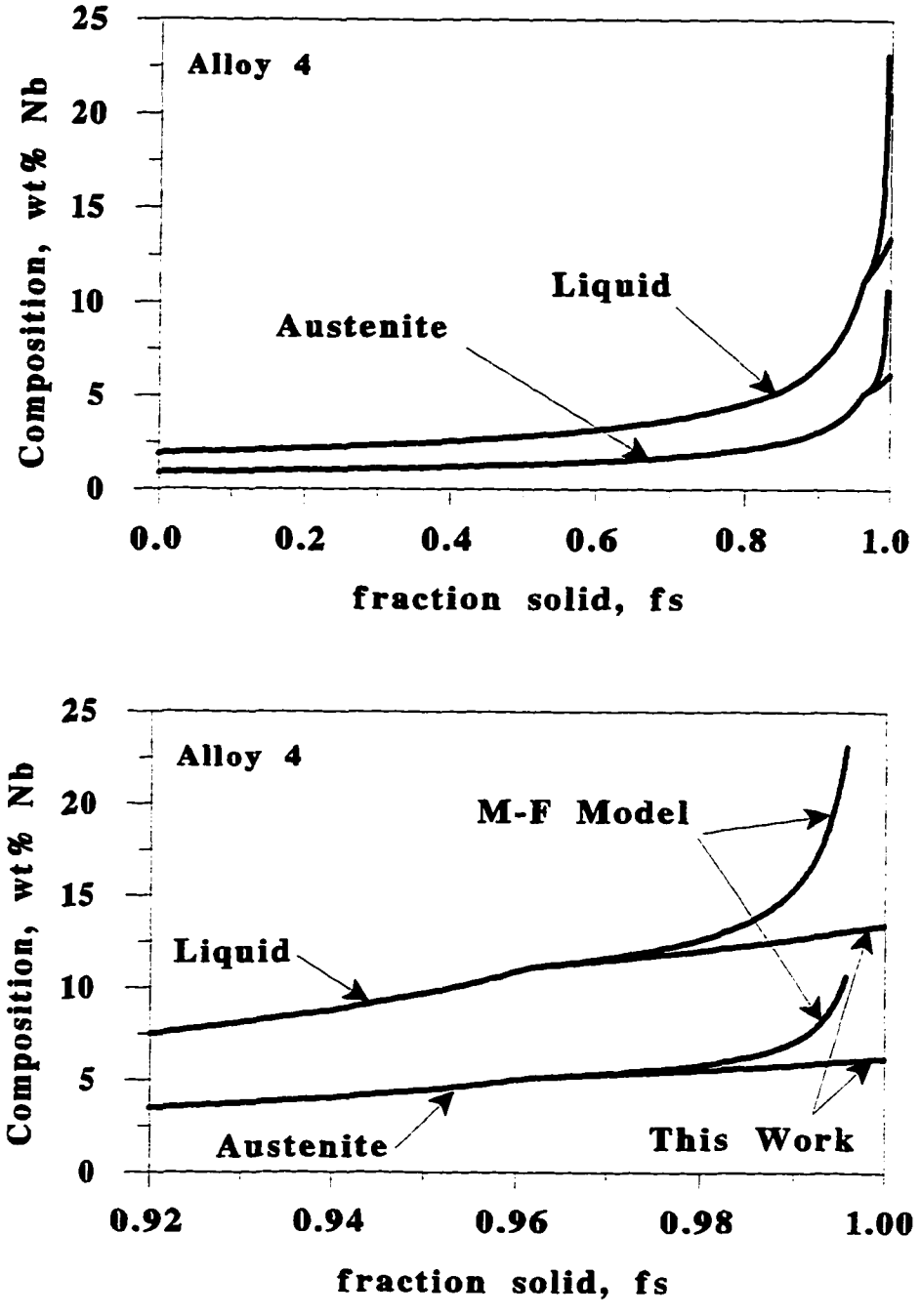

Figure 5.7b. Calculated variation in Nb content in liquid and γ phases as a function of fraction solid for Alloy 4.

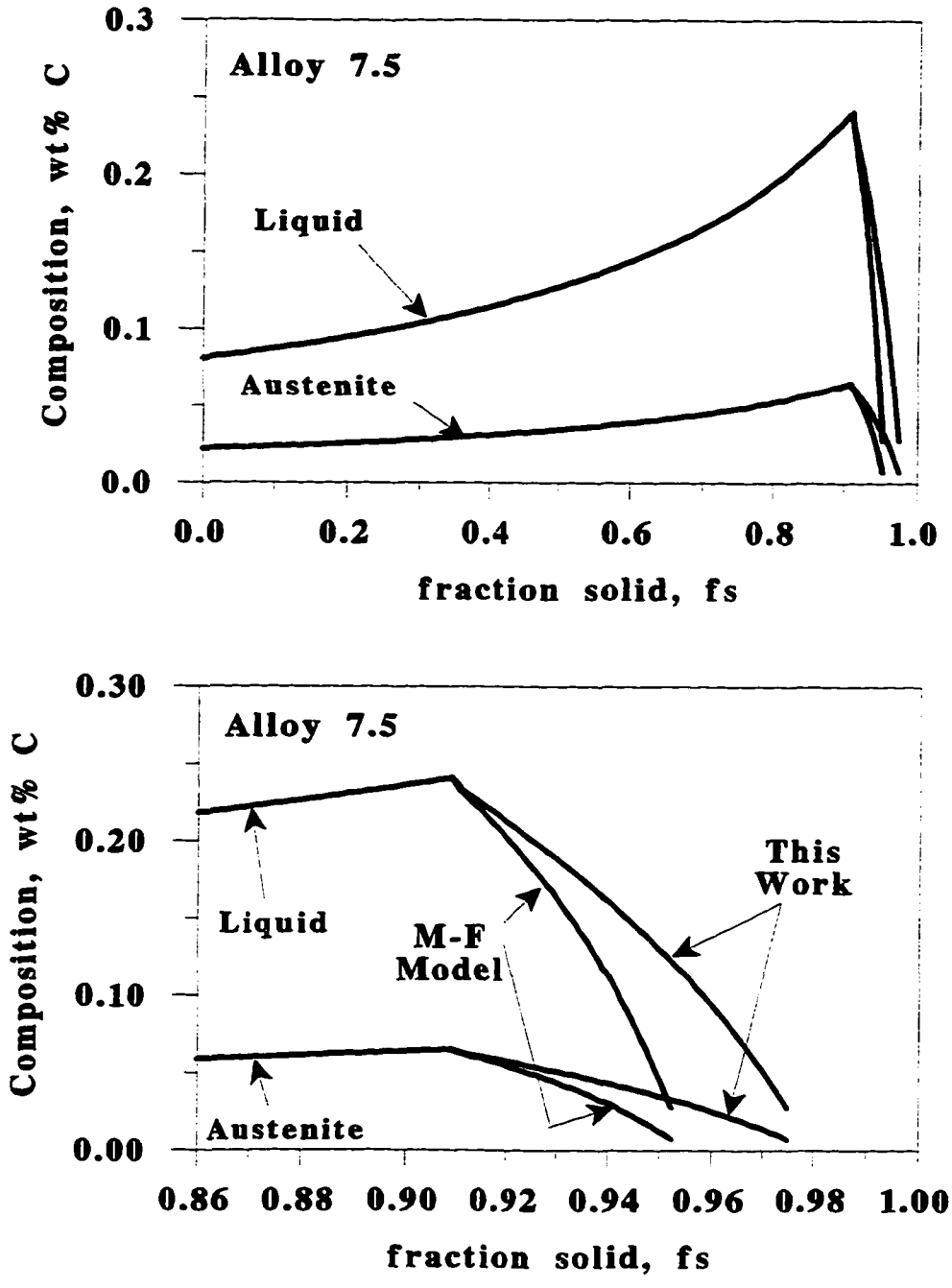

Figure 5.8a. Calculated variation in C content in liquid and γ phases as a function of fraction solid for Alloy 7.5.

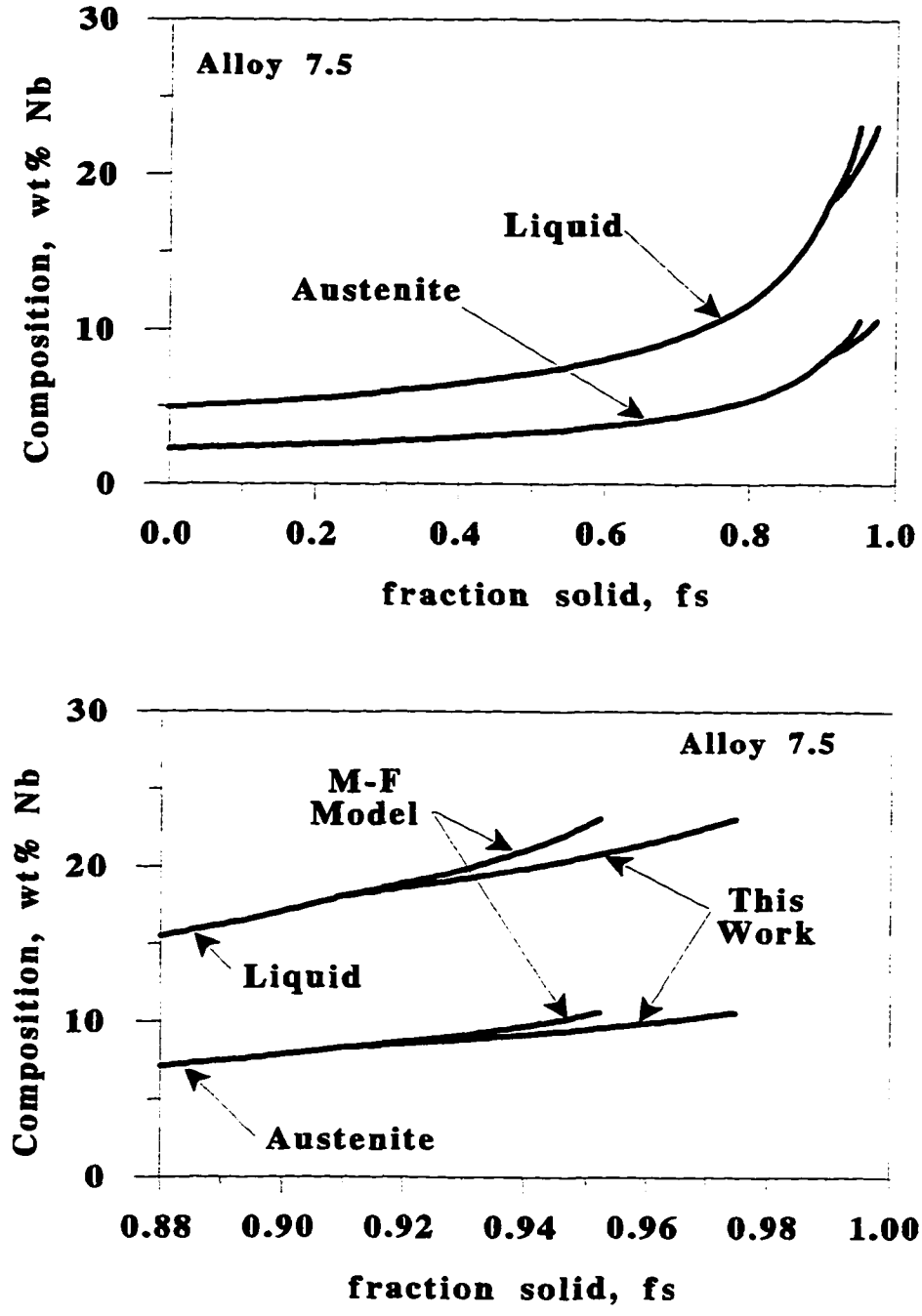

Figure 5.8b. Calculated variation in Nb content in liquid and γ phases as a function of fraction solid for Alloy 7.5.

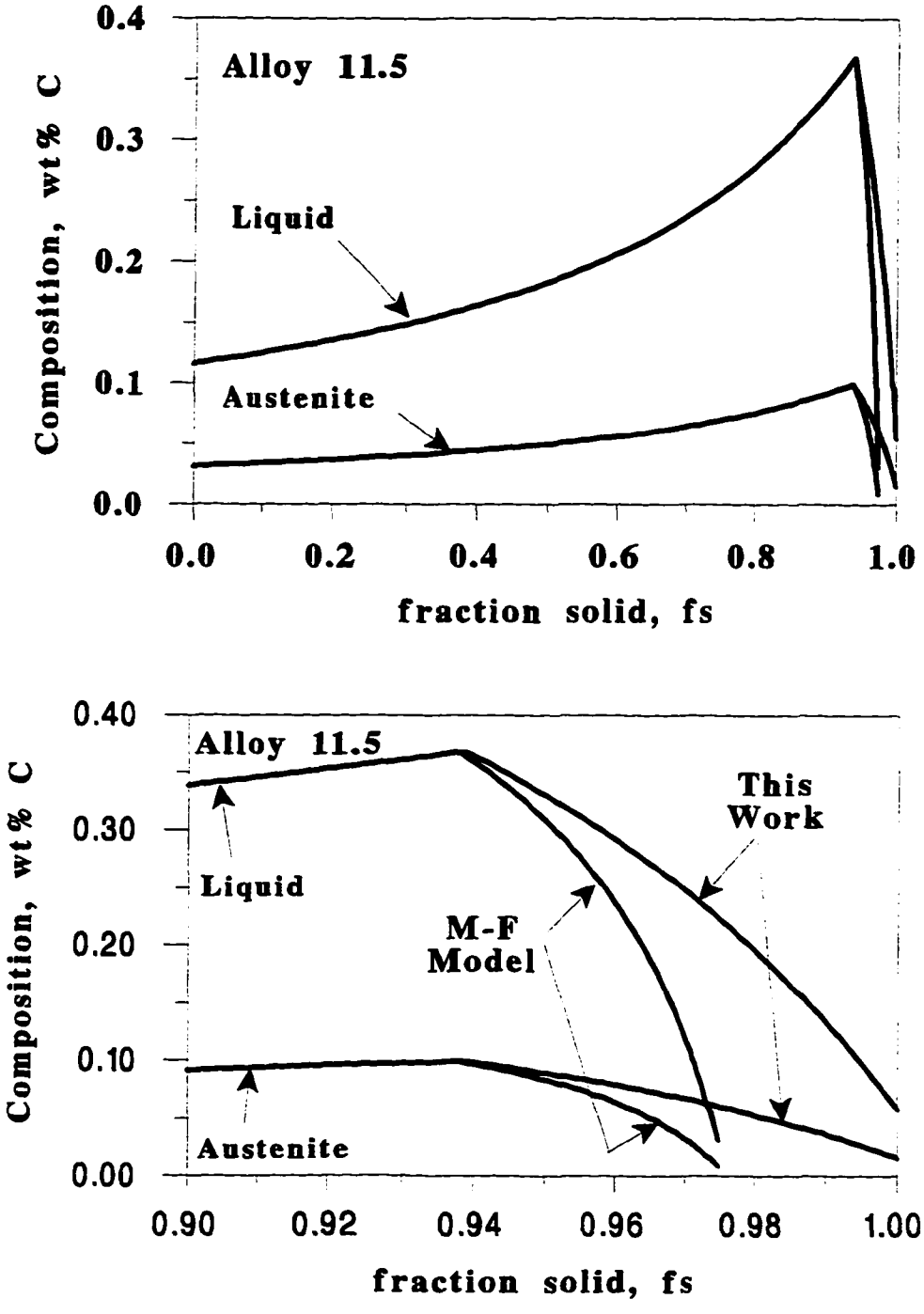

Figure 5.9a. Calculated variation in C content in liquid and γ phases as a function of fraction solid for Alloy 11.5.

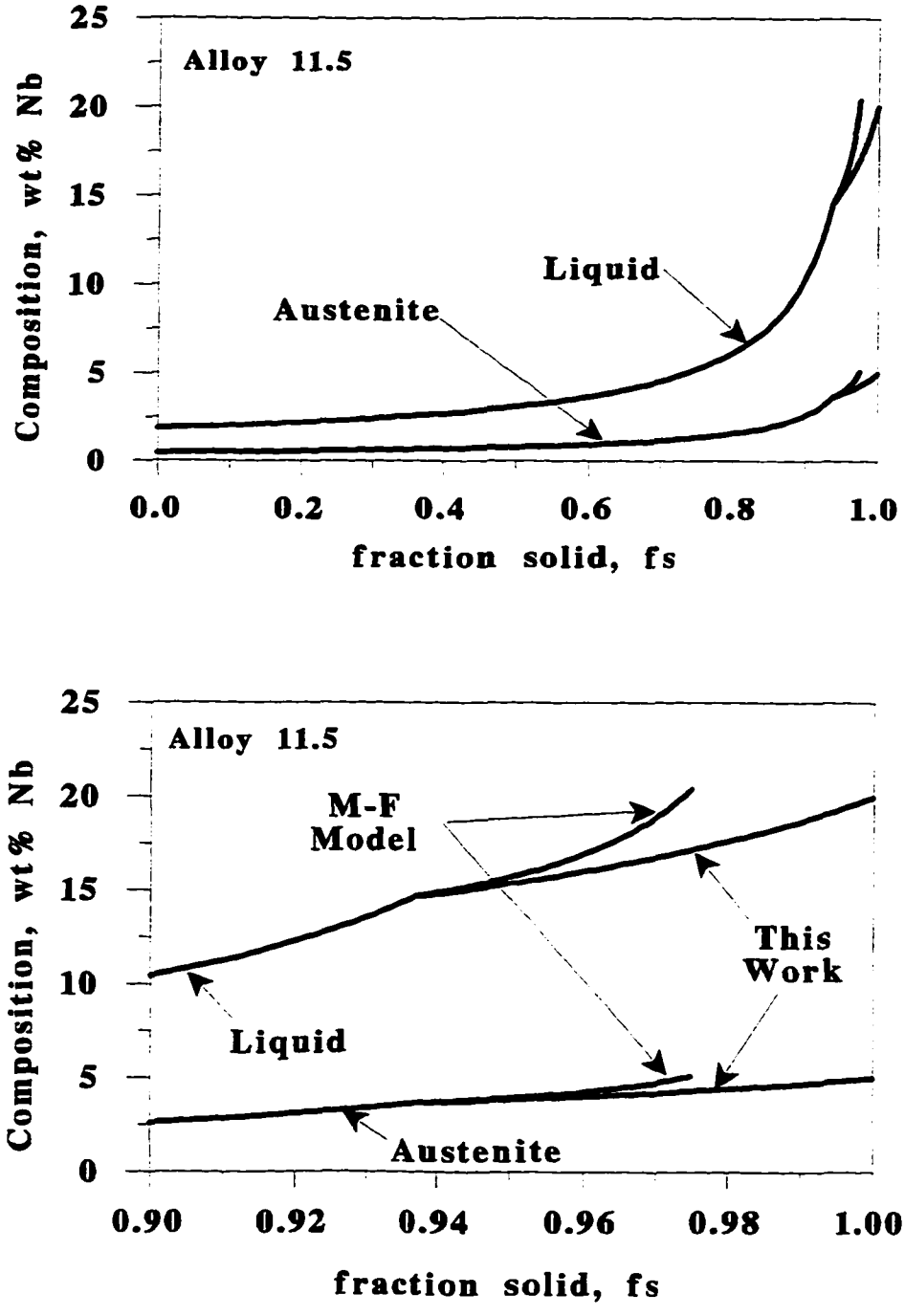

Figure 5.9b. Calculated variation in Nb content in liquid and γ phases as a function of fraction solid for Alloy 11.5.

Table 5.3. Comparison of individual γ/NbC and γ/Laves eutectic constituent volume percentages.

Alloy	γ/NbC - Volume Percent			γ/Laves - Volume Percent		
	Measured	Calculated		Measured	Calculated	
		This Work	M-F Model		This Work	M-F Model
1	---	0.7	0.1	---	0.4	1.0
1.5	---	1.5	0.6	---	0	0.9
2	5.2 ± 1.5	3.1	2.7	0	0	0.4
3	---	0.2	0.1	---	0.7	0.8
3.5	3.0 ± 0.4	1.7	0.9	0	0	0.8
4	7.3 ± 1.3	3.8	3.5	0	0	0.3
5	~0[1]	0.2	0.2	~2.5 ± 1.1	6.2	6.2
6	~13.3 ± 2.5	15.2	12.4	~0[2]	0	2.8
7	~0[1]	0.7	0.3	~2.7 ± 0.4	5.1	5.5
7.5	5.2 ± 0.5	7.4	4.5	2.3 ± 0.5	1.7	4.6
8	13.7 ± 1.6	15.5	13.1	1.5 ± 0.7	0	2.4
9	~0[1]	0	0	~3.8 ± 0.5	3.3	3.3
10	~9.0 ± 1.0	5.3	3.2	~0[2]	0	2.1
11	~0[1]	0	0	~2.5 ± 0.4	3.9	3.9
11.5	6.6 ± 1.1	6.3	4.0	0.7 ± 0.1	0	2.3
12	4.4 ± 1.7	4.9	2.4	2.3 ± 0.8	0.7	3.2
13	~0[1]	0.3	0.2	~12.9 ± 1.4	12.8	12.9
14	18.8 ± 1.6	19.8	18.9	5.0 ± 0.6	4.6	5.5
15	~0[1]	0	0	15.5 ± 1.4	14.8	14.8
16	17.5 ± 2.1	20.8	20.3	6.1 ± 0.7	5.4	5.9

1 - NbC or γ/NbC present in too low an amount to accurately quantify.
2 - Laves or γ/Laves present in too low an amount to accurately quantify.

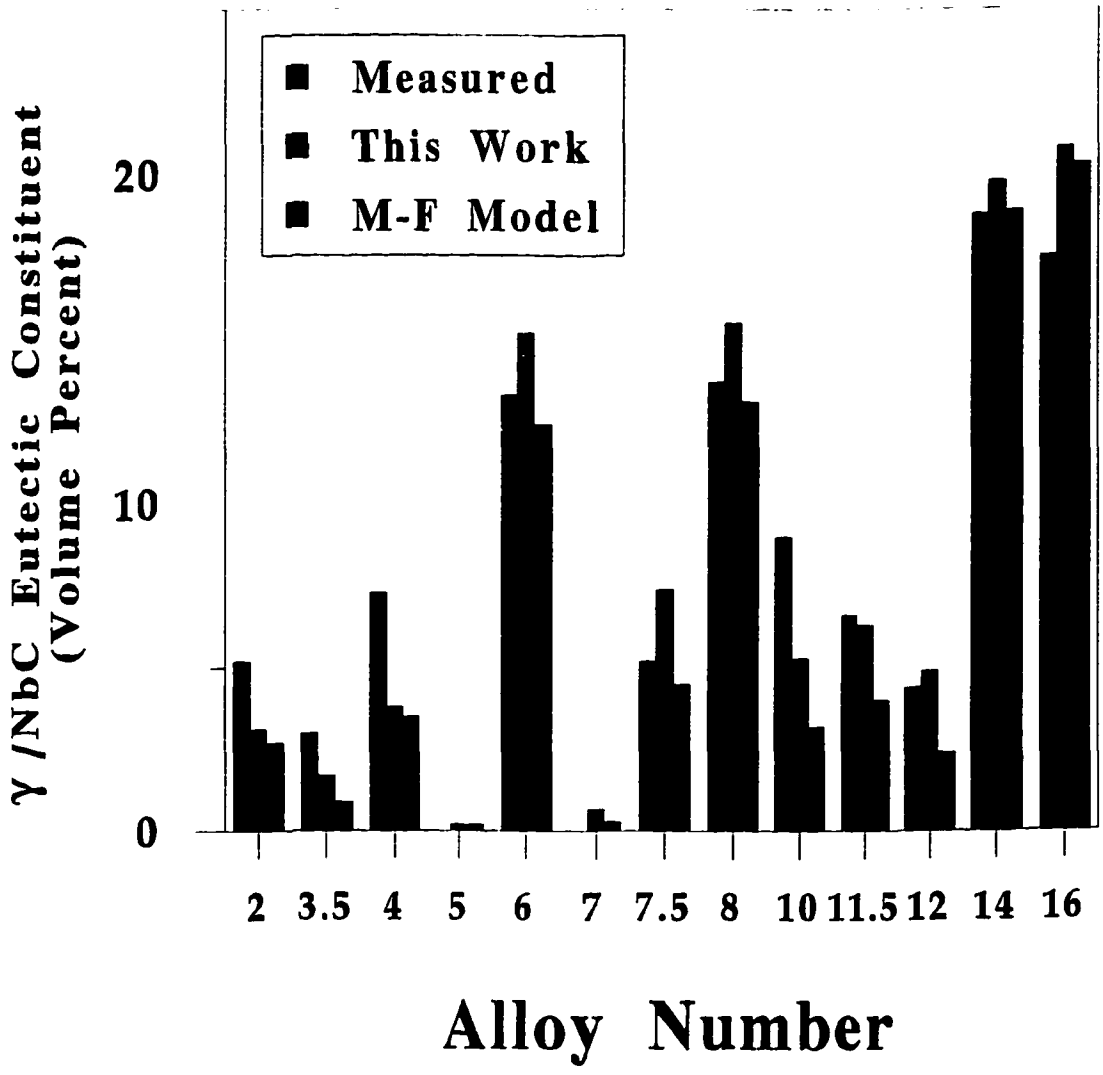

Figure 5.10. Comparison between measured and calculated volume percentages of γ/NbC eutectic-type constituent.

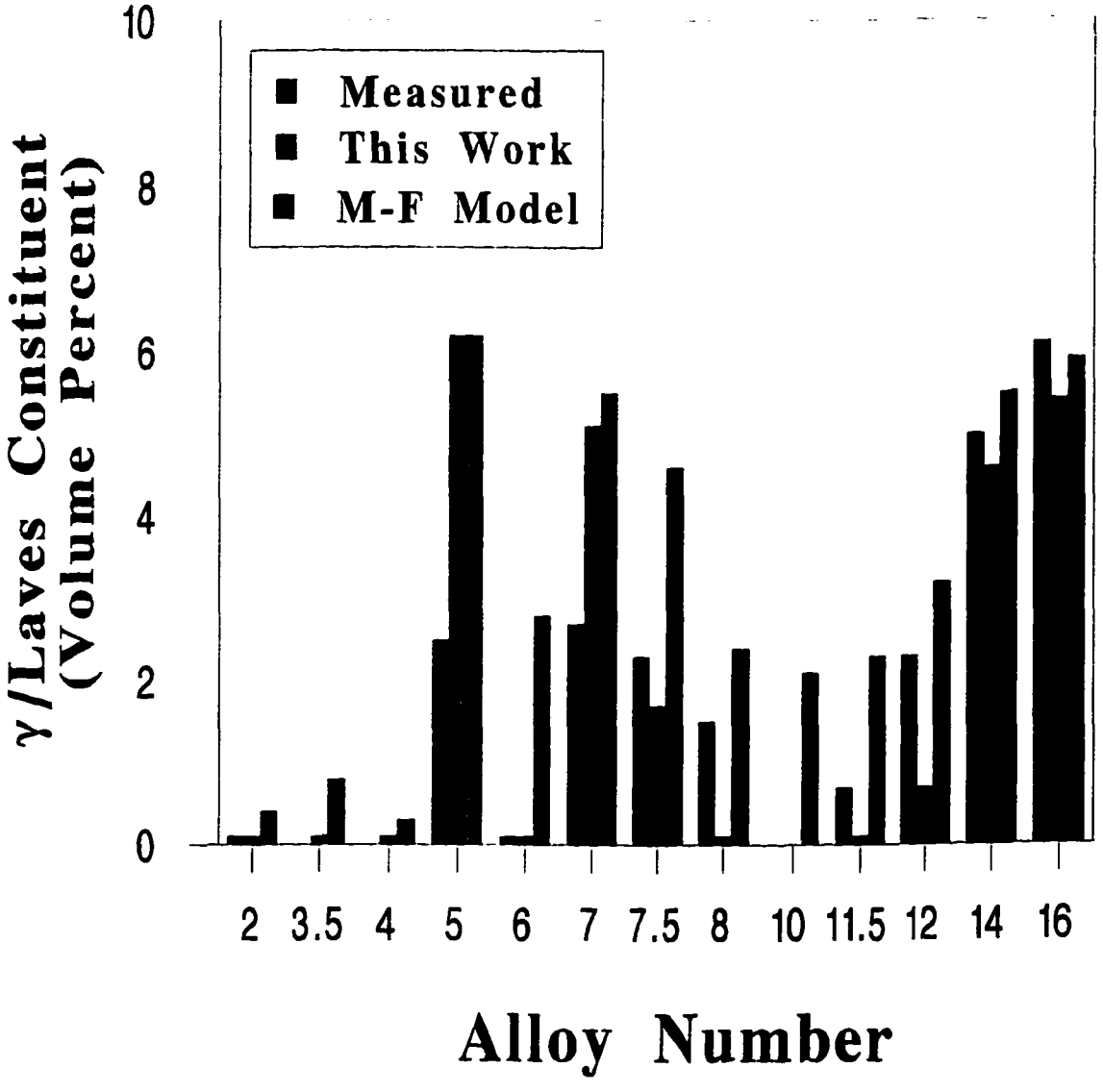

Figure 5.11. Comparison between measured and calculated volume percentages of γ/Laves eutectic-type constituent.

5.4 CHAPTER CONCLUSIONS

Solute redistribution and microstructural evolution have been modelled for experimental alloys which simulate compositions of Ni base and Fe base superalloys containing Nb, Si, and C. The multi-component alloys were modelled as a ternary system by grouping the matrix (Fe,Ni,Cr) elements together as the "solvent" to form the γ component of the γ-Nb-C "ternary system". The variation in fraction liquid and liquid composition during the primary $L \rightarrow \gamma$ and eutectic type $L \rightarrow (\gamma + NbC)$ stages of solidification were calculated for conditions of negligible Nb diffusion and infinitely fast C diffusion in the solid phase. The proposed model is based on the solute redistribution equations for eutectic-type solidification originally developed by Mehrabian and Flemings. Results of the calculations were superimposed on the pseudo ternary γ-Nb-C solidification surface to predict the solidification reaction sequences along with the total and individual amounts of γ/NbC and γ/Laves eutectic-type constituents which form during solidification. Comparison is made to experimentally measured values, and reasonable agreement is found. The model results permit quantitative interpretations of composition-microstructure relations in these Nb bearing experimental alloys and should provide useful insight into comparable commercial alloy systems as well. These results will be used in the next chapter to determine the relation between composition, microstructure, and fusion zone cracking susceptibility.

6. FUSION ZONE SOLIDIFICATION CRACKING

As discussed in Section 2.1, the propensity for solidification cracking depends primarily on the solidification temperature range (ΔT_s) and amount/morphology of solid and liquid phases in the mushy zone that exists behind the weld pool. The value of ΔT_s dictates the size of the mushy zone, where larger solidification temperature ranges translate into longer mushy zones. As the crack susceptible mushy zone increases, the distance available for crack propagation also increases. The exact length that a solidification crack propagates through the mushy zone depends on the amount and morphology of the solid and liquid phases. If the last residual liquid to solidify is present as a continuous film which separates neighboring grain boundaries and dendrites, solid/solid bridging is difficult. Under this condition, the support of forces (from thermal and solidification contraction stresses) across grain boundaries and interdendritic regions is difficult and cracks can typically propagate through all or most of the mushy zone. In contrast, if the last liquid exists as isolated globules, then solid/solid bridging can occur and the resistance to crack propagation increases. In this case, the advancing solidification crack may only traverse through a portion of the mushy zone. In addition, if a relatively large amount of liquid exists just above the terminal solidus temperature, any cracks which form may be healed by the free-flowing liquid. These concepts will become apparent in the analysis which follows.

6.1 EFFECT OF SOLIDIFICATION TEMPERATURE RANGE

Figure 6.1 shows the MCL of each alloy. The alloy compositions are summarized in Table 3.2. Within the Ni base alloys, there is a clear separation in weldability among the low C (≤ 0.017 wt%) and high C (≥0.052 wt%) alloys. Within the Fe base alloys, the addition of C is only beneficial when the Nb content is at a low value (≤ 1.93 wt%), and the C level must be above 0.108 wt% to provide the advantageous effect. For example, Alloys 11.5 and 12 have essentially identical levels of all other elements except C (Alloy 12 has 0.079 wt%C and Alloy 11.5 has 0.116 wt%C). This small variation in C content leads to a substantial difference in the MCL values. Within the Fe base alloys with high Nb (Alloys 13-16), C has no beneficial effect even at the 0.21 wt% level.

MCL values for commercial alloys, tested under identical conditions, are also plotted in the figure. Alloys IN718 and IN625 are Nb bearing superalloys that have been shown to be fairly susceptible to solidification cracking [6.1, 6.2, 6.3]. Other Nb bearing alloys have shown this relatively high susceptibility as well [6.4, 6.5]. These alloys have C levels of ≈ 0.04 wt%, which is intermediate to the experimental alloys utilized here. It is interesting to note that their MCL values fall within the range of the experimental alloys. This indicates that the experimental alloys accurately simulate the weldability behavior of comparable commercial superalloys. The low MCL value of 304 stainless steel is typical, as this is alloy is known to exhibit excellent weldability. The high C alloys show cracking resistance which is comparable to 304 stainless steel. This is a significant improvement over the experimental and commercial alloys with low to moderate C contents.

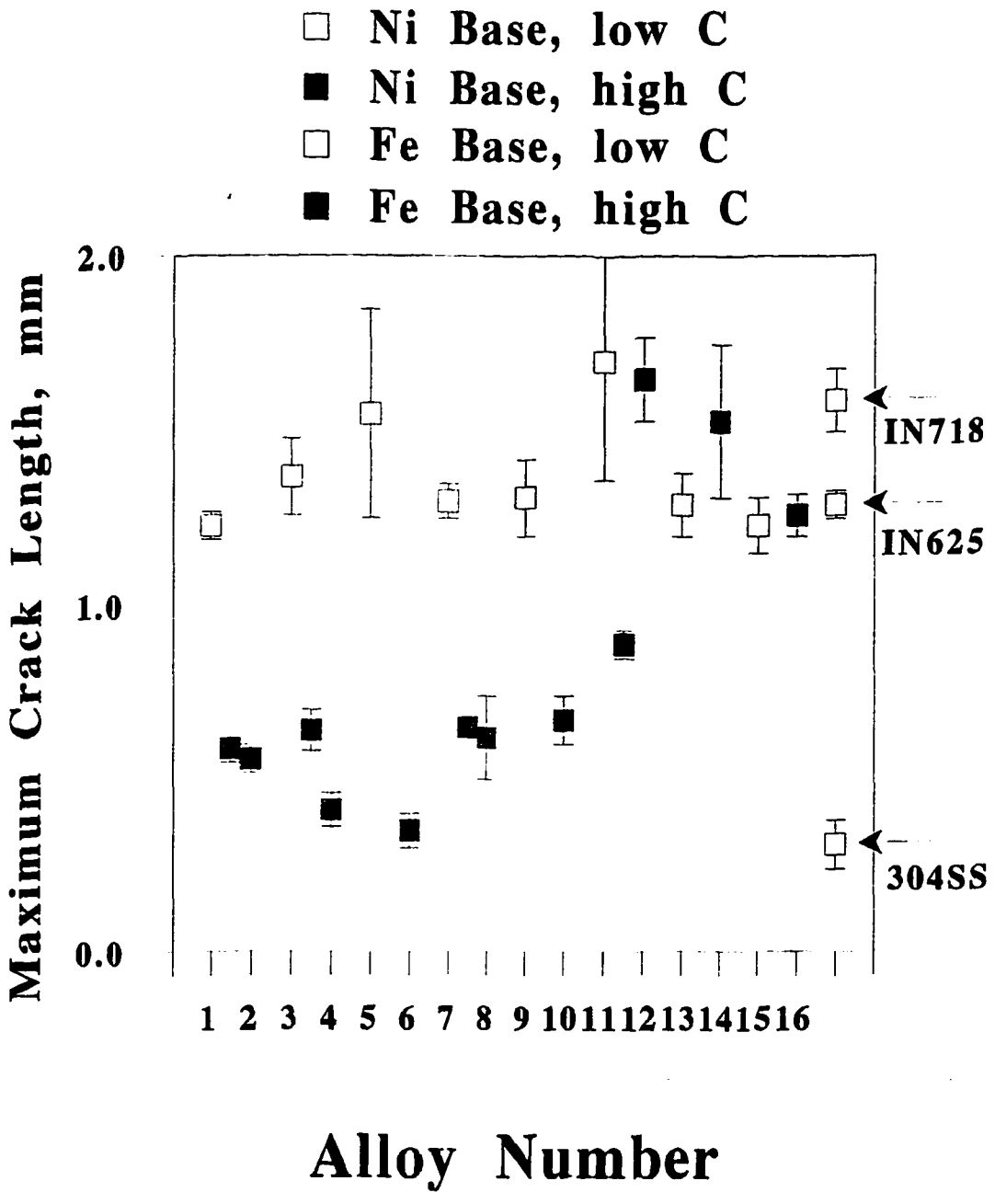

Figure 6.1 Summary of maximum crack length values for all alloys.

As discussed in the previous chapter, C content has a significant effect on the primary solidification paths of these alloys. As the C content is increased, the primary solidification path is driven far into the C-rich side of the solidification surface and intersects the γ/NbC line of two fold saturation at a relatively high temperature near the end of solidification. Thus, C additions are generally expected to decrease the solidification temperature range. Considering this effect, together with the general relation between cracking tendency and the solidification temperature range, a correlation between MCL and ΔT_s might be expected. The ΔT_s and MCL data are summarized in Table 6.1. The solidification temperature range is most appropriately given by the difference between the liquidus, determined through DTA heating scans, and the terminal solidus temperature measured during cooling. The on-heating liquidus temperature is utilized since the weld metal solidifies epitaxially from the base metal and requires little undercooling [6.6]. The terminal solidus temperature corresponds to the temperature of the last eutectic-type reaction.

As discussed in Section 4.2, all samples except Alloys 2, 3.5, and 4 exhibited the γ/Laves eutectic-type constituent. Thus, the temperature of the $L \rightarrow (\gamma + \text{Laves})$ reaction should be utilized as the value for the terminal solidus temperature for all alloys except 2, 3.5, and 4. Although this reaction temperature could not be directly measured for all the alloys, it can be estimated reasonably well. For the Ni base alloys, the $L \rightarrow (\gamma +$ Laves) reaction temperature could be measured in Alloy Ni-1 (1190°C). The γ/Laves constituent in this sample exhibited a composition very similar to that observed in Alloys 7, 7.5, and 8. Thus, the reaction temperature measured for Alloy Ni-1 should serve as a

good estimate for the terminal solidus temperatures of the Ni base alloys which complete solidification by the L → (γ + Laves) reaction. The L → (γ + Laves) reaction temperature could not be directly measured in the Fe base alloys with low Nb. The values measured in the high Nb iron base alloys exhibit a fairly narrow range of 13 °C. Thus, the average of these values should provide a good estimate for the low Nb alloys. For Alloys 2, 3.5, and 4, the terminal solidus is taken as the value measured for the L → (γ + NbC) reaction as no γ/Laves constituent was observed. Positive identification of secondary phases could not be made in Alloy 1 or 1.5, so no solidification temperature range is reported for these alloys.

Figure 6.2 plots the MCL as a function of the solidification temperature range, and no correlation is readily apparent. Many alloys exhibit a rather wide solidification temperature range, but show good weldability (low MCL). This suggests that crack propagation is being affected by the amount and distribution of solid and liquid phases within the mushy zone. Such potential effects can be assessed by conducting detailed examinations of the eutectic-type constituents in the vicinity of solidification cracks. These constituents transform from the terminal liquid which existed in the grain boundary and interdendritic regions just before solidification is complete. Thus, the amount and morphology of these constituents provides a basis for developing an understanding of the distribution of solid and liquid phases within the mushy zone. This was the primary impetus for conducting detailed SEM examinations of solidification cracks in each alloy, the results of which were presented in Section 4.1 for phase identification purposes. These figures are now utilized again to develop an understanding of the relation between microstructural evolution and solidification cracking in the mushy zone.

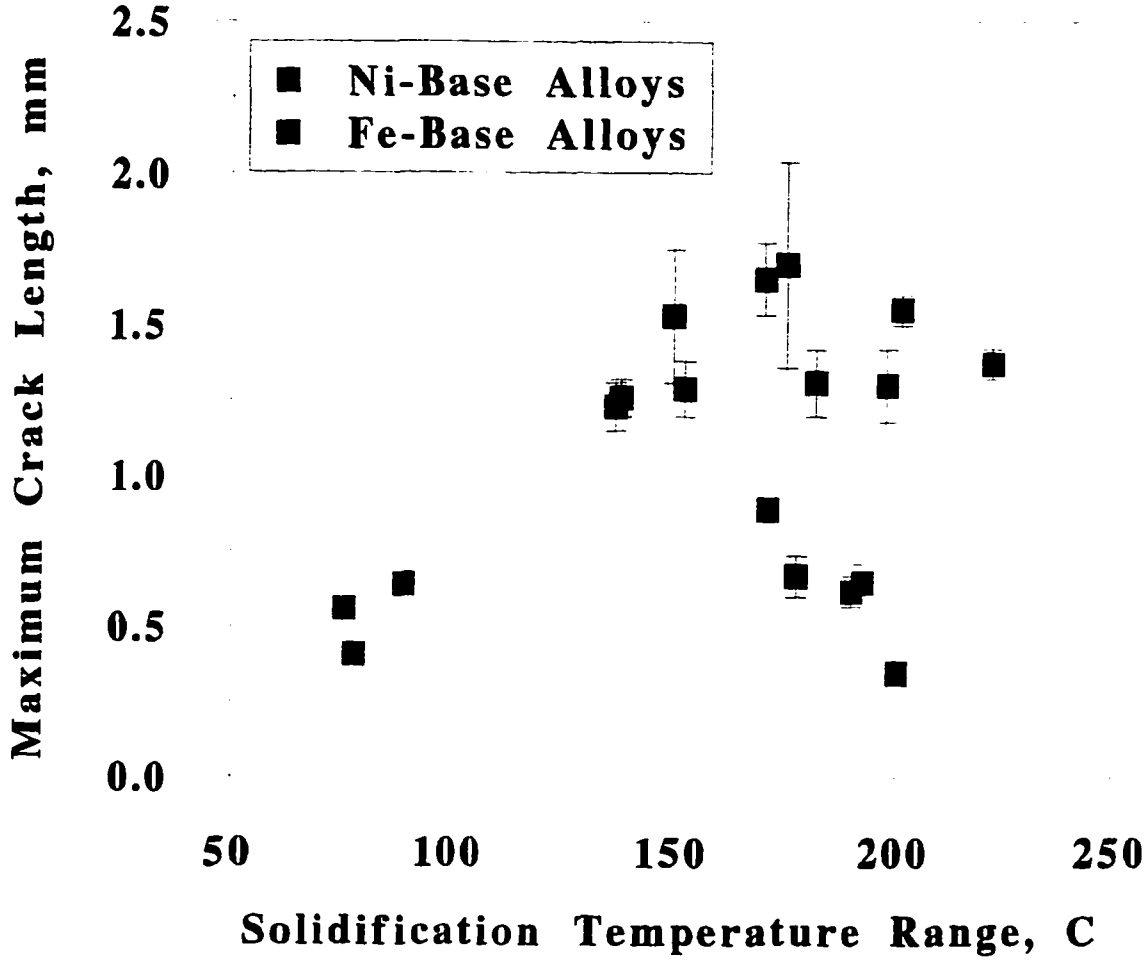

Figure 6.2. Maximum crack length as a function of the actual solidification temperature range.

Table 6.1. Summary of solidification temperature ranges and maximum crack lengths.

Alloy	Liquidus Temperature (°C)	Terminal Solidus Temperature (°C)	Solidification Temperature Range (°C)	Maximum Crack Length (mm)
1	1420 (1.7)	1190*	---	1.23 (0.04)
1.5	1418.0 (0.3)	1190*	---	0.59 (0.04)
2	1416.7 (1.2)	1341.5 (0.7)	75.2	0.56 (0.04)
3	1412.3 (0.6)	1190*	222.3	1.37 (0.11)
3.5	1410.5 (0.7)	1322.0 (1.4)	88.5	0.64 (0.06)
4	1407.3 (0.6)	1330.0 (1.3)	77.3	0.41 (0.05)
5	1391.0 (1.0)	1190.0*	201.0	1.55 (0.30)
6	1390.0 (1.0)	1190.0*	200.0	0.35 (0.05)
7	1387.7 (1.5)	1190.0*	197.7	1.30 (0.05)
7.5	1382.0 (1.4)	1190.0*	192.0	0.65 (0.01)
8	1379.3 (0.6)	1190.0*	189.3	0.62 (0.12)
9	1430.4 (0.9)	1249.3**	181.1	1.31 (0.11)
10	1426.1(0.8)	1249.3**	176.8	0.67 (0.07)
11	1423.9 (1.1)	1249.3**	174.6	1.70 (0.34)
11.5	1419.6 (0.2)	1249.3**	170.3	0.89 (0.04)
12	1418.8 (0.2)	1249.3**	169.5	1.65 (0.12)
13	1401.1 (0.7)	1249.5 (3.5)	151.6	1.29 (0.09)
14	1392.0 (0.3)	1243.0 (2.1)	149.0	1.53 (0.22)
15	1392.6 (0.6)	1256.3 (1.2)	136.3	1.23 (0.08)
16	1385.6 (0.3)	1248.2 (4.8)	137.4	1.26 (0.06)

* Estimated from sample Ni-1

** Estimated from average of Fe base high Nb alloys

6.2 MICROSTRUCTURAL EVOLUTION DURING SOLIDIFICATION CRACKING

The general solidification process of these alloys was described in Section 4.4 with the aid of Figure 4.63 . By combining the SEM photomicrographs of varestraint samples with the solidification path calculations discussed in Chapter 5, it is possible to extend this general model to identify four individual types of microstructural morphologies which develop as solidification cracking occurs in the mushy zone. These microstructural classifications provide a phenomenalogical explanation of the observed variations in morphology and concomitant solidification cracking propensity. They also shed light upon a more appropriate relation between MCL and ΔT_s which could not be resolved by the initial plot in Figure 6.2. All of the alloys can be grouped into one of these four morphological classification schemes. Table 6.2 lists the classification scheme which applies to each alloy.

Table 6.2 Morphological classification schemes

Microstructure Type	Alloys within Classification
Type I	2, 3.5, 4
Type II	6, 7.5, 8, 10, 11.5
Type III	12, 14, 16
Type IV	1, 3, 5, 7, 9, 11, 13, 15

The development of each microstructural morphology is described schematically in Figures 6.3 through 6.6. At the bottom of each figure, the formation of two

neighboring dendrites within a grain are depicted growing into the leading edge of the weld pool. The relation between temperature and phase stability in the mushy zone is shown by the temperature gradient diagram in the middle of the figure, where the dendrite tips are at the liquidus temperature. This point, given by zero distance, represents the boundary between the liquid weld pool and solid+liquid mushy zone. The point at which the actual temperature in the mushy zone reaches the terminal solidus temperature defines the boundary between the mushy zone and solidified weld metal. The relation between temperature, distance, phase stability, and the solidification path is given by combining the γ-Nb-C solidification surface with the other two figures.

The Type I microstructure which develops during solidification cracking (Figure 6.3) is found in the Ni base alloys with low Nb and high C that exhibit only the $L \rightarrow (\gamma + NbC)$ reaction (i.e. Alloys 2, 3.5, and 4). The SEM photomicrographs of these alloys are presented in Figures 4.3, 4.5, and 4.6. At Step 1, the dendrite tips form from liquid of nominal composition as the actual temperature intersects the liquidus temperature. Due to the high C/Nb ratio of these alloys, the interdendritic liquid then becomes highly enriched in C as the solidification path progresses towards the line of two fold saturation between γ and NbC. At Step 2, the primary solidification path intersects the line of two fold saturation at a relatively high temperature. As a result, the γ/NbC starts forming at a short distance from the dendrite tips. In other words, the primary $L \rightarrow \gamma$ solidification process is complete within a small distance behind the advancing weld pool. There is a moderate amount of liquid present at Step 2. This is directly evident from the measured amount of the γ/NbC constituent, which is in the range of 3.0 to 7.3 volume percent. The

remaining liquid is completely consumed along the line of two fold saturation, so the γ/Laves constituent does not form. From this description, it is apparent that the mushy zone in these alloys is expected to be relatively small. Thus, the distance available for crack propagation is also relatively small, and this provides a major contribution to the excellent weldability observed in these alloys.

In addition to the small mushy zone, the microstructures of Alloy 2 and 4 exhibit significant amounts of γ/NbC which often back-fills a substantial length of the crack. A smaller amount of γ/NbC is observed in the cracks in Alloy 1.5. Direct evidence of this back filling process was often observed on the varestraint samples, and an example of this in Alloy 2 is shown in Figure 6.7a. The step on the surface of the weld (outlined by arrowheads) forms as the liquid pool is disturbed when the strain is applied. Thus, this step represents the boundary between the liquid weld pool and mushy zone at the instant the sample was strained. A similar boundary is observed in the SEM photomicrograph of this alloy (Figure 4.3a-arrowheads). Note that, in both of these figures, the solidification cracks do not extend up to the boundary because liquid near the γ/NbC composition has flowed in to heal the cracks as they form. The level of liquid needed for back-filling has been reported to be in the range of 6-10 volume percent [6.7, 6.8], which is very close to the amount of terminal liquid present in Alloys 2 and 4 (5.2 ± 1.5 to 7.3 ± 1.3). Thus, when strain is imposed on the mushy zone of these alloys, a crack can only propagate a small distance and the leading edge of the crack is healed by back-filling. This description accounts for the small MCL values, large amounts of γ/NbC observed within the solidification crack, and lack of the γ/Laves constituent.

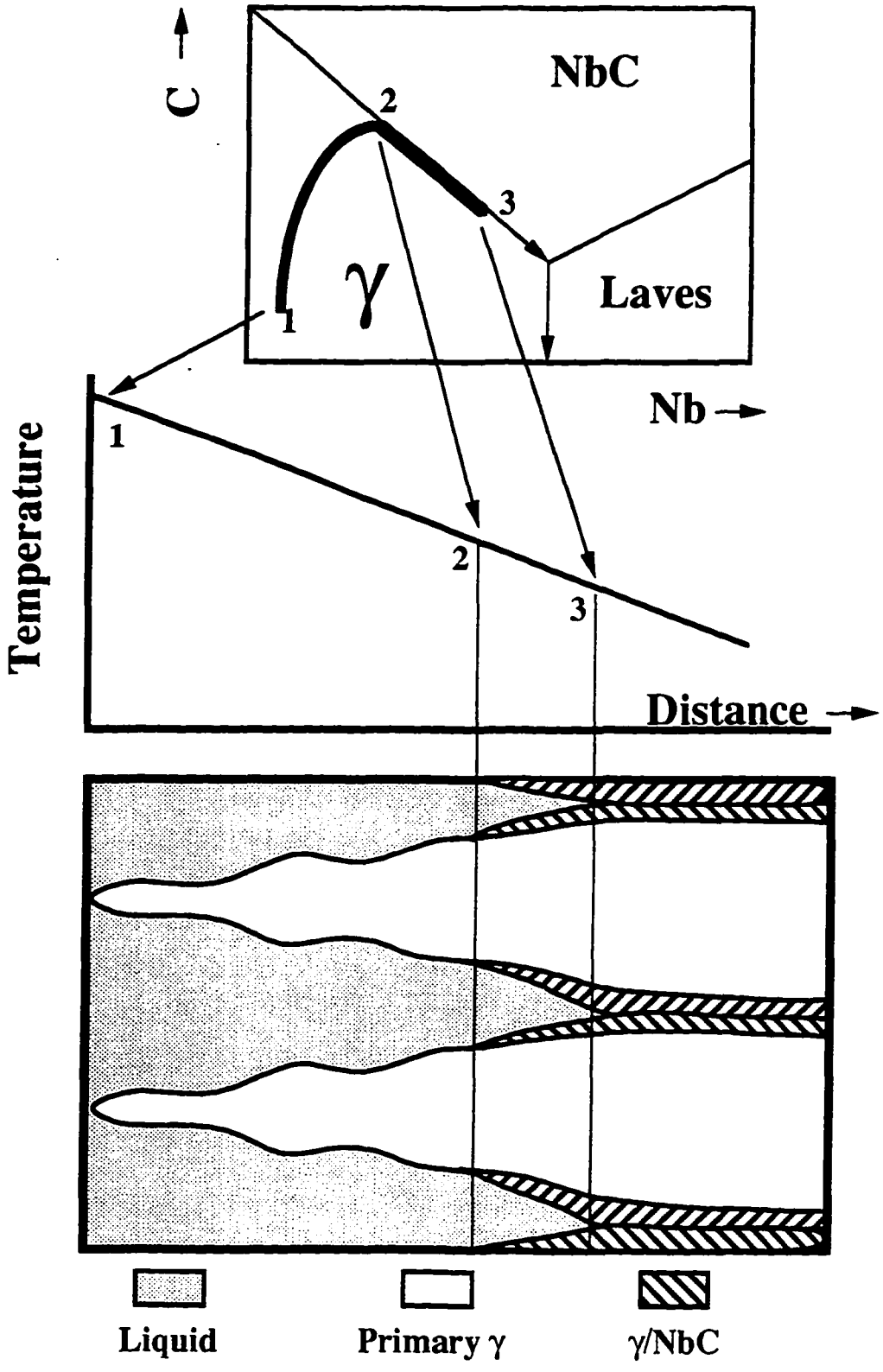

Figure 6.3. Schematic illustration showing formation of the Type I microstructure.

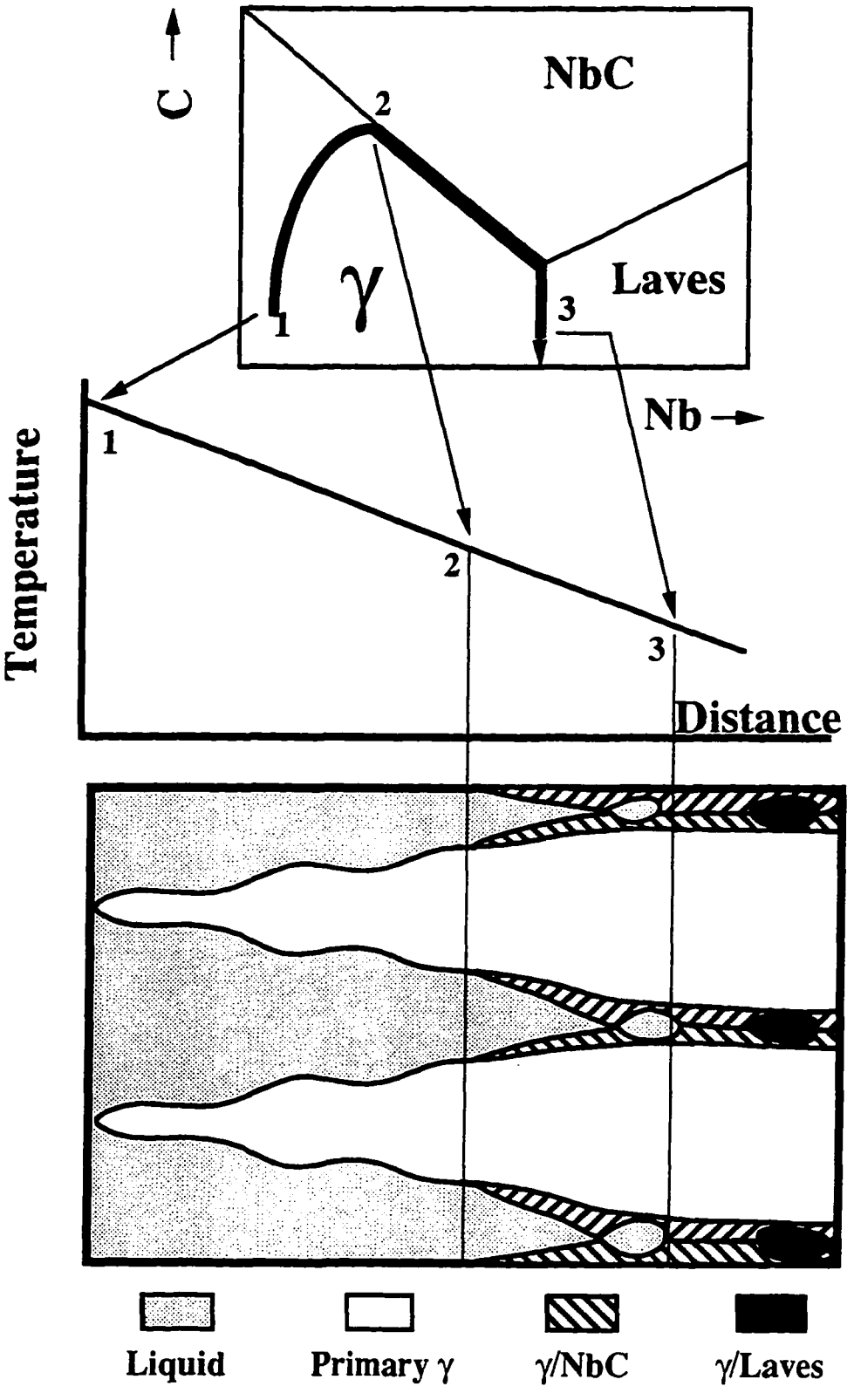

Figure 6.4. Schematic illustration showing formation of the Type II microstructure.

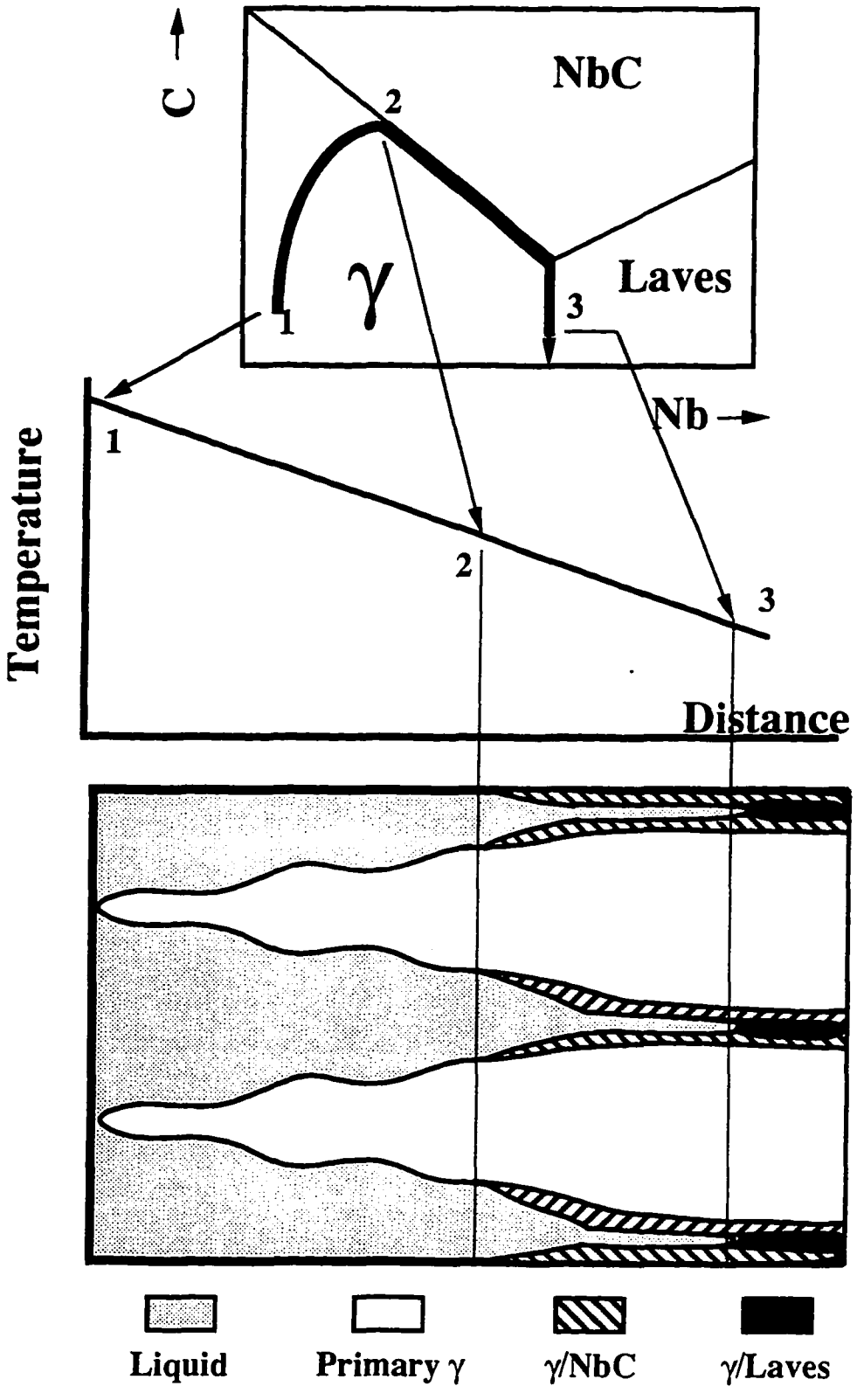

Figure 6.5. Schematic illustration showing formation of the Type III microstructure.

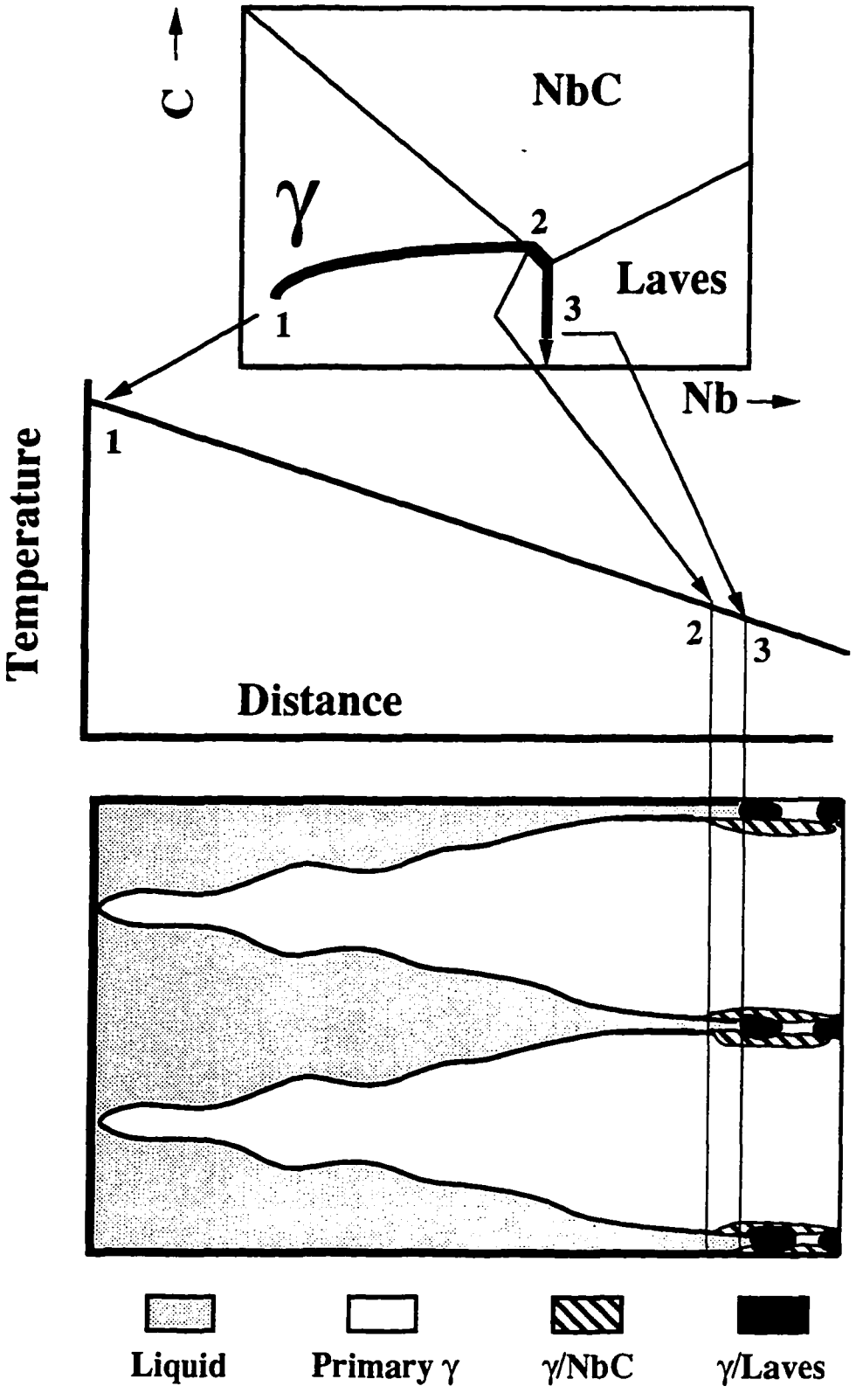

Figure 6.6. Schematic illustration showing formation of the Type IV microstructure.

Development of the Type II microstructure is shown in Figure 6.4. This morphology is observed in the high Nb/high C nickel base alloys and low Nb/high C iron base alloys. The solidification process is similar to Type I, except that a larger amount of liquid is generally present at Step 2 which is not completely consumed during the L $\rightarrow$ (γ + NbC) reaction. As a result, the class II reaction point is reached and the γ/Laves constituent forms. Reference to Figure 5.4 shows that the L $\rightarrow$ (γ + Laves) reaction occurs at very low temperatures. Thus, the presence of liquid at the γ/Laves composition will extend the mushy zone out to larger distances. This has the potential of increasing the maximum crack length. However, the amount of γ/Laves constituent which forms in any of these alloys never exceeds 2.3 volume percent. At this level, the γ/NbC always envelops the γ/Laves and keeps it isolated. This is readily apparent in the SEM photomicrographs of these alloys (Figures 4.8, 4.10, 4.11, 4.13, and 4.15). This suggests that the last residual liquid, from which the γ/Laves forms, is also isolated within the mushy zone during crack advancement. With this type of morphology, the isolated liquid pockets should have little or no deleterious effect and crack propagation through the entire mushy zone is therefore unlikely. The varestraint data tend to support this. The MCL values for these alloys is in the range of 0.35 to 0.89 mm, which is similar to the range of 0.41 to 0.64 mm observed in the Type I alloys which form no γ/Laves and have excellent weldability. This may account for the lack of correlation between ΔT_s and MCL in Figure 6.2 and will be discussed in more detail later. Evidence of back-filling is clearly evident in these alloys as well. This is not surprising, considering that these alloys contain 7.3 to 15.2 volume percent of liquid at Step 2. A typical example of back-filling in Alloy

6 is shown in the LOM photomicrograph of Figure 4.8. The accompanying SEM photomicrograph in that figure is taken from the same crack. Evidence of back-filling on the varestraint sample of Alloy 8 is shown in Figure 6.7b.

The amount of total eutectic-type constituent in the Type II alloys, which corresponds to the amount of liquid at Step 2, is always above 7.3 volume percent. It is interesting to note that two alloys which fit into this microstructure type (Alloys 7.5 and 11.5) have almost identical amounts of liquid at Step 2 as Alloy 4, yet Alloy 4 does not form the γ/Laves constituent. The ability for liquid to remain after the $L \rightarrow (\gamma + NbC)$ reaction, and subsequently transfer to γ/Laves, depends not only on the amount of liquid at Step 2 but also on the relative position of Step 2 and the segregation potential of Nb during the $L \rightarrow (\gamma + NbC)$ reaction. For example, Alloy 7.5 and Alloy 4 have essentially identical amounts of liquid at Step 2 (7.5 volume percent). However, due to its lower C/Nb ratio, the primary solidification path of Alloy 7.5 intersects the γ/NbC two fold saturation line closer to the class II reaction point. Thus, the remaining liquid in Alloy 7.5 does not have to "travel" as far as that in Alloy 4 to satisfy the composition conditions for the $L \rightarrow (\gamma + Laves)$ reaction. Alloy 11.5 also has about 7.5 volume percent liquid at Step 2. In this case, the lower value of k_{Nb} causes Nb to segregate more aggressively to the liquid so that the γ/Laves composition can be reached in the liquid.

Formation of the Type III microstructure is shown in Figure 6.5. This morphology is observed in the iron base Alloys 12, 14, and 16. The main difference between this morphology and that of Type II lies within the amount and distribution of the γ/Laves constituent, where the Type III alloys form γ/Laves in larger quantities. As a result, the

γ/Laves is observed in a continuous network (see Figures 4.16, 4.18, and 4.20). As discussed in detail in Section 5.3, the large amounts of γ/Laves which form in the Fe base alloys is attributed mostly to the low value of k_{Nb}. As a result of this behavior, the advantageous effect of C, observed in the Ni base alloys with high Nb and high C, is lost in the iron base alloys with comparable composition. The actual size of the mushy zone in these alloys is expected to be similar to that for the iron base Alloys 10 and 11.5, since each type terminates solidification with the L → (γ + Laves) reaction. However, with the residual liquid existing in a continuous network all the way down to the terminal L → (γ + Laves) reaction, crack propagation through the entire mushy zone is more favorable for the Type III microstructure. Thus, the solidification temperature range governing crack propagation in these alloys should be appropriately given by the entire solidification range measured through DTA. Note that the MCL values observed for these alloys (1.26 to 1.65 mm) are consistently higher than the those observed in the Type II alloys (0.35 to 0.89 mm) where the terminal liquid is isolated.

Lastly, the evolution of Type IV microstructures are shown in Figure 6.6. All of the low C alloys fit into this classification scheme. These alloys exhibit a primary solidification path which travels very close to the γ - Nb "binary" side of the solidification surface. The primary path just barely intersects the line of two fold saturation between γ and NbC before solidification terminates with the L → (γ + Laves) reaction. Referring again to Figure 5.4, the eutectic type reactions in this region of the solidification surface occur at low temperatures. Thus, with this solidification path, the mushy zone is relatively large and consists mainly of liquid and primary γ with small

amounts of γ/NbC and γ/Laves. The total amount of terminal liquid in these alloys is generally low, between 0.8 and 3.8 volume percent. The only exception to this is Alloys 13 and 15, which form relatively large amounts of γ/Laves (12.9 - 15.5 volume percent) in a continuous network. The MCL values of all these alloys are high (1.23 to 1.70 mm), suggesting that crack propagation though all or most of the mushy zone is likely.

Based on these considerations, the terminal solidus temperatures affecting solidification cracking for Type III and Type IV microstructures should be appropriately given by the temperature of the terminal L → (γ + Laves) reaction. However, assuming crack propagation is difficult through the isolated regions of residual liquid in the Type II microstructures, the temperature range affecting solidification cracking for these alloys would be more realistically represented by using the temperature of the L → (γ + NbC) reaction as the terminal solidus point. The MCL and ΔT_s data are re-plotted in Figure 6.8 with this adjustment, and the trend between cracking susceptibility and the solidification temperature range is now more apparent. The data are grouped into two distinct regions of the plot, which separate the low and high C alloys. This improved correlation, although only qualitative, serves to support the proposed mechanisms of crack propagation through the various types of microstructures.

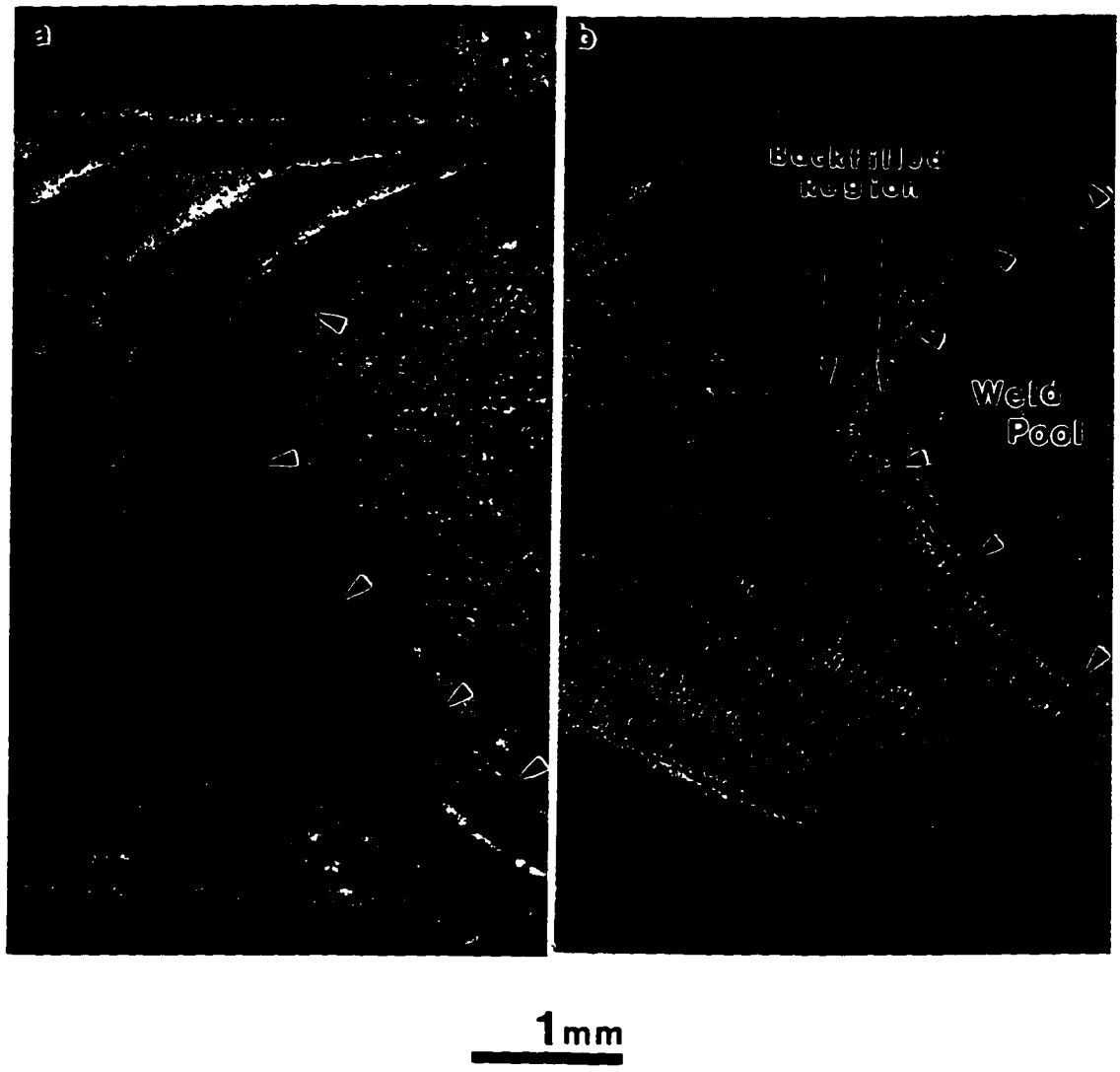

Figure 6.7 Stereomicroscope photographs showing evidence of back-filling in varestraint samples of Alloy 4 (a) and Alloy 8 (b).

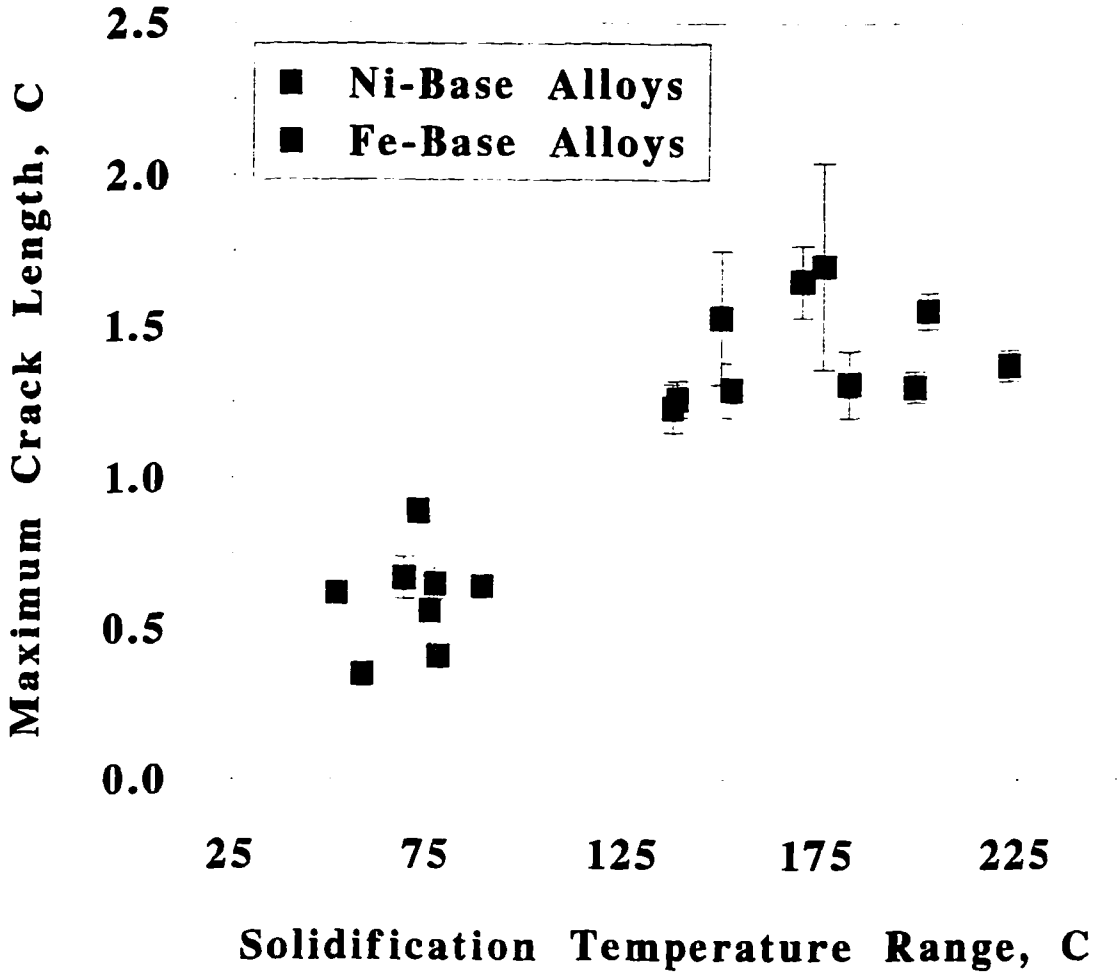

Figure 6.8. Re-plot of maximum crack length as a function of adjusted solidification temperature range.

6.3 DISTRIBUTION OF LIQUID IN THE MUSHY ZONE

The conventional solidification cracking concepts discussed above essentially attempt to relate the cracking propensity to the liquid distribution and size of the mushy zone. This can be assessed in more detail by combining knowledge of the temperature gradient with the liquidus equation and solute redistribution relations. The objective of combining such equations is to develop plots which reveal the variation in the fraction of liquid with distance in the mushy zone. This approach is developed here and some preliminary results are presented.

Ignoring possible interactive effects among the solutes, which have been proven to be insignificant here, the liquidus equation for any multi-component system is given by

$$T_l = T_o + \Sigma\, m_{l,i}\, C_{l,i} \qquad (6.1)$$

where $m_{l,i}$ is the liquidus slope for the *ith* solute in the system, $C_{l,i}$ is the concentration of the *ith* solute in the liquid, and T_o is the melting temperature of the pure solvent. The solutes in this case refer to Nb, Si, and C. The liquidus slopes for all these elements were measured through DTA techniques in Section 4.3 . Here, T_o is given by the constant in the linear regression equations (eqs. 4.10 and 4.11). Solute redistribution of Nb and Si can be described with the Scheil equation. Thus, the relation between $C_{l,i}$ and fraction liquid, f_l, for these two elements during primary $L \rightarrow \gamma$ solidification is given by

$$C_{l,Nb} = C_{o,Nb}\, f_l^{(k_{Nb}-1)} \qquad (6.2a)$$

$$C_{l,Si} = C_{o,Si}\, f_l^{(k_{Si}-1)} \qquad (6.2b)$$

For C, the lever law is appropriate and the C_{Li} - f_l relation is given by

$$C_{l,C} = \frac{C_{o,C}}{f_l + k_C(1 - f_l)} \qquad (6.2c)$$

Inserting eqs. (6.2) into (6.1) yields a relation between temperature and the fraction liquid:

$$T_l = T_o + m_{l,Nb}C_{o,Nb}f_l^{(k_{Nb}-1)} + m_{l,Si}C_{o,Si}f_l^{(k_{Si}-1)} + m_{l,C}\left[\frac{C_o}{f_l+k_C(1-f_l)}\right] \qquad (6.3$$

Thus, when the liquidus slopes and distributions coefficients are known, the variation in fraction liquid with temperature during primary solidification can be calculated with eq. (6.3). The variation in fraction liquid with distance in the mushy zone can be determined by combining eq. (6.3) with the temperature gradient. The temperature gradient is given by the ratio of cooling rate to growth rate, where the growth rate at the weld centerline

(where the MCL typically develops) is equivalent to the travel speed. The travel speed utilized here is 3.3 mm/s and the cooling rate was estimated as 660 °C/s through dendrite arm spacing measurements. Thus, the temperature gradient, G, is ≈ 200 °C/mm. At the trailing edge of the weld pool, the liquid is at the liquidus temperature, T_l. Assuming G is constant and taking x = 0 at T = T_l, the relation between temperature and distance in the mushy zone is given by

$$x = \frac{T_l - T}{G} \qquad (6.4)$$

Thus, eqs. (6.3) and (6.4) can be used to determine the variation in f_l with distance in the mushy zone during the primary solidification stage. When the $L \rightarrow (\gamma + NbC)$ reaction begins, the relation between f_l and C_l is now given by eqs. (5.15) or (5.26). At this point, the effect of Si is ignored and only the relation between f_l, $C_{l,Nb}$ and $C_{l,C}$ is considered. Equations (5.15) and (5.26) were used in Chapter 5 to establish the relations between f_l and $C_{l,Nb}$ during the $L \rightarrow (\gamma + NbC)$ reaction. Having established these relations for all the alloys, a relation between temperature and liquid composition during the eutectic-type transformations is now needed. Such a relation is provided in empirical form in Figure 5.4, where the temperature of the lines of two fold saturation are described empirically in terms of $C_{l,Nb}$. The lines in the plots are the best fit using a third order polynomial. Thus, the relations between f_l and $C_{l,Nb}$ established in Chapter 5 can be joined with the empirical relation between T and $C_{l,Nb}$ given in Figure 5.4 to establish the relation

between f_l and T. This is then combined with eq (6.4) to describe the relation between f_l and x in the mushy zone during the $L \rightarrow (\gamma + NbC)$ reaction. The $L \rightarrow (\gamma + Laves)$ reaction occurs over a relatively narrow temperature range and is therefore estimated to occur isothermally. Thus, the point at which the liquid composition satisfies conditions for the $L \rightarrow (\gamma + Laves)$ reaction denotes the end of the mushy zone and the value of f_l at that point corresponds to the amount of the γ/Laves constituent which forms isothermally at that location. Lastly, the f_l-x relation developed for the eutectic-type transformations is joined to the f_l-x relation for primary solidification in order to construct the entire f_l-x curve in the mushy zone.

This method is obviously only an approximation as a number of simplifying assumptions are invoked. (i.e., constant liquidus slopes and distribution coefficients, no significant effect from Si during solute redistribution during the eutectic-type reactions, isothermal solidification of γ/Laves). It was also necessary to reduce the liquidus slopes by 20 to 30 % in order to bring the results of f_l-x calculations from the primary solidification stage into agreement with the calculations for the $L \rightarrow (\gamma + NbC)$ stage. Considering the assumptions, this adjustment is not unreasonable. These results can only be viewed as semi-quantitative. Nevertheless, the calculated sizes of the mushy zones are realistic and the information provides useful comparisons among alloys with variations in compositions.

Figure 6.9 shows a typical f_l-x curve for Alloy 3.5. Experimentally, this alloy terminates solidification with the $L \rightarrow (\gamma + NbC)$ reaction. The modified form of the M-F model (eq. 5.26) accurately predicts this behavior and was therefore used for the f_l-x

calculations during the $L \rightarrow (\gamma + NbC)$ reaction. With this plot, it is possible to determine the amount of solid and liquid phases as a function of position, and such labels are provided on the curve. The entire mushy zone size is calculated to be ≈ 0.6 mm. This is comparable to the MCL of 0.64 mm measured on the varestraint sample. Of course, the similarity between these two values does not imply perfect agreement between the calculated mushy zone size and that expected experimentally since the exact length of crack propagation through the mushy zone is unknown. Considering the assumptions made in the calculations, the similarities in these two values is probably fortuitous.

Figure 6.10 compares the variations in fraction liquid in the mushy zone for three alloys with essentially identical levels of Nb and Si, but variations in C. Alloys 3.5 and 4 exhibit the Type I microstructures while Alloy 3 has the Type IV microstructure. The kinks in the curves for Alloys 3.5 and 4 mark the position where the $L \rightarrow (\gamma + NbC)$ reaction starts. For Alloy 3, primary solidification occurs over a broad temperature range and very little eutectic-type constituent is formed at the end of the mushy zone. Since the primary solidification path for Alloy 3 covers a broad temperature range, the mushy zone is relatively large. The effect of C content on the distribution of liquid and size of the mushy zone is readily evident in this figure. As the C content is increased, the $L \rightarrow (\gamma + NbC)$ reaction occurs at higher temperatures and the reaction is therefore initiated at shorter distances behind the liquid weld pool. Once the reaction starts, the remaining liquid is consumed over a short distance (small temperature range) and, in effect, "closes up" the mushy zone. This is analogous to the behavior expected in a simple binary system, except that the eutectic type transformation occurs over a temperature range rather

than isothermally. The calculated mushy zones sizes of 0.41 mm, 0.58 mm, and 1.12 mm scale well with the MCL values of 0.41, 0.64, and 1.37 mm, respectively.

Figure 6.11 shows similar results for Alloys 7 (Type IV microstructure) and 8 (Type II microstructure). Experimentally, a small amount of liquid persists after the L $\rightarrow$ (γ + NbC) reaction in Alloy 8, and solidification terminates when this liquid transforms to the γ/Laves constituent. The original M-F model (eq. 5.15) predicts this behavior and was therefore used for the f_l-x calculations during the L $\rightarrow$ (γ + NbC) reaction. The effect of C is again readily apparent. When the L $\rightarrow$ (γ + NbC) starts, a relatively large amount of liquid is consumed over a short distance and the mushy zone tends to close up. In this particular case, the actual sizes of the mushy zones between the low and high C alloys are equivalent since the actual solidification temperature range for each is the same. However, the high C alloy exhibits a smaller fraction of solute rich liquid over $\approx$ 70% of the mushy zone. This accounts for the formation of the γ/Laves constituent as isolated pockets in the Type II microstructures. Thus, these f_l-x diagrams are generally consistent with experimental observations and provide valuable relations between composition-solidification-fusion zone cracking relations in these alloys. The approach should be applicable to other alloy systems and can be applied when the appropriate phase diagram quantities are known. Calculations of these curves for all the alloys used in this research are planned for more detailed analysis in future work.

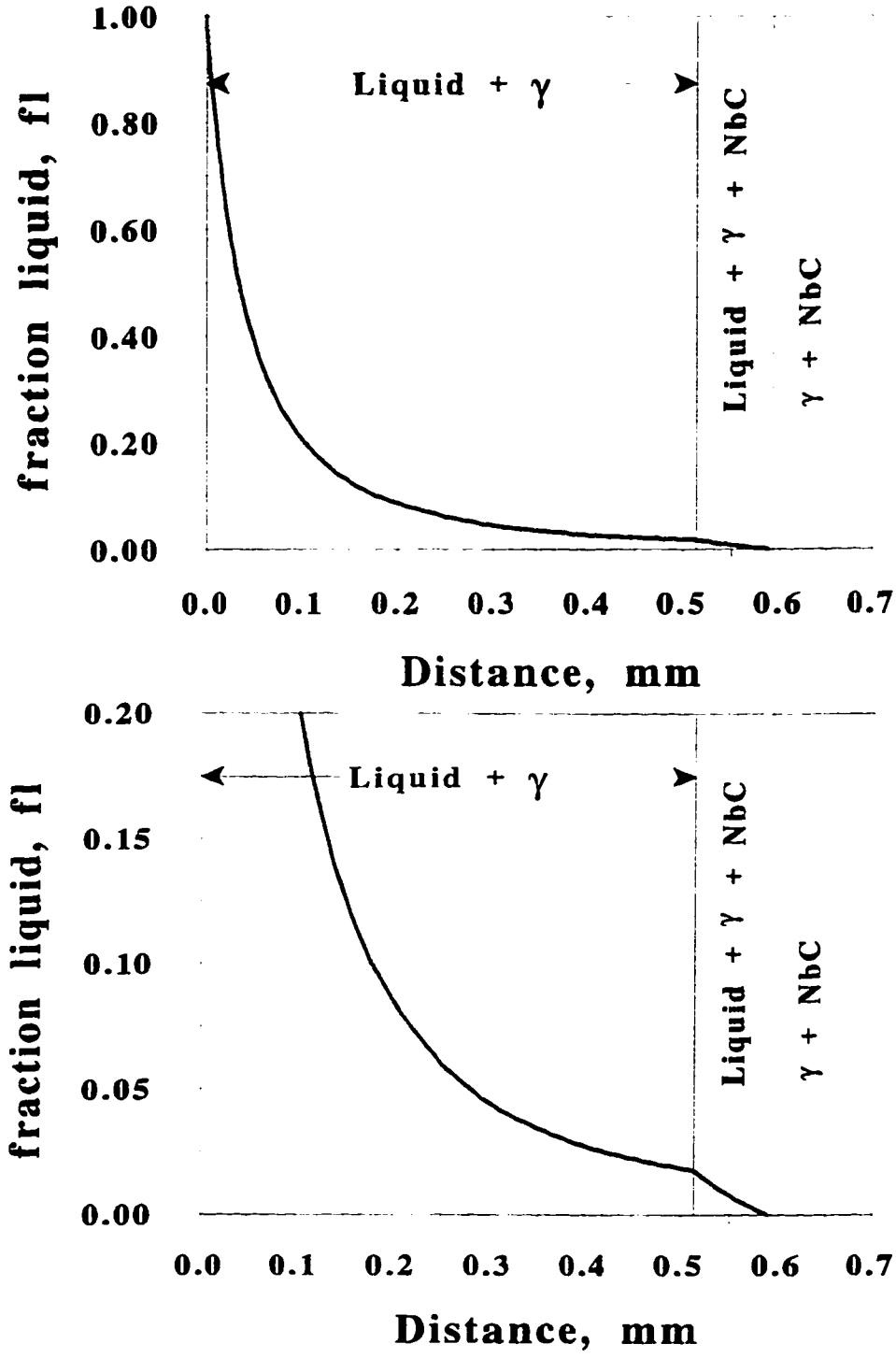

Figure 6.9. Variation in fraction liquid with distance in the mushy zone of Alloy 3.5.

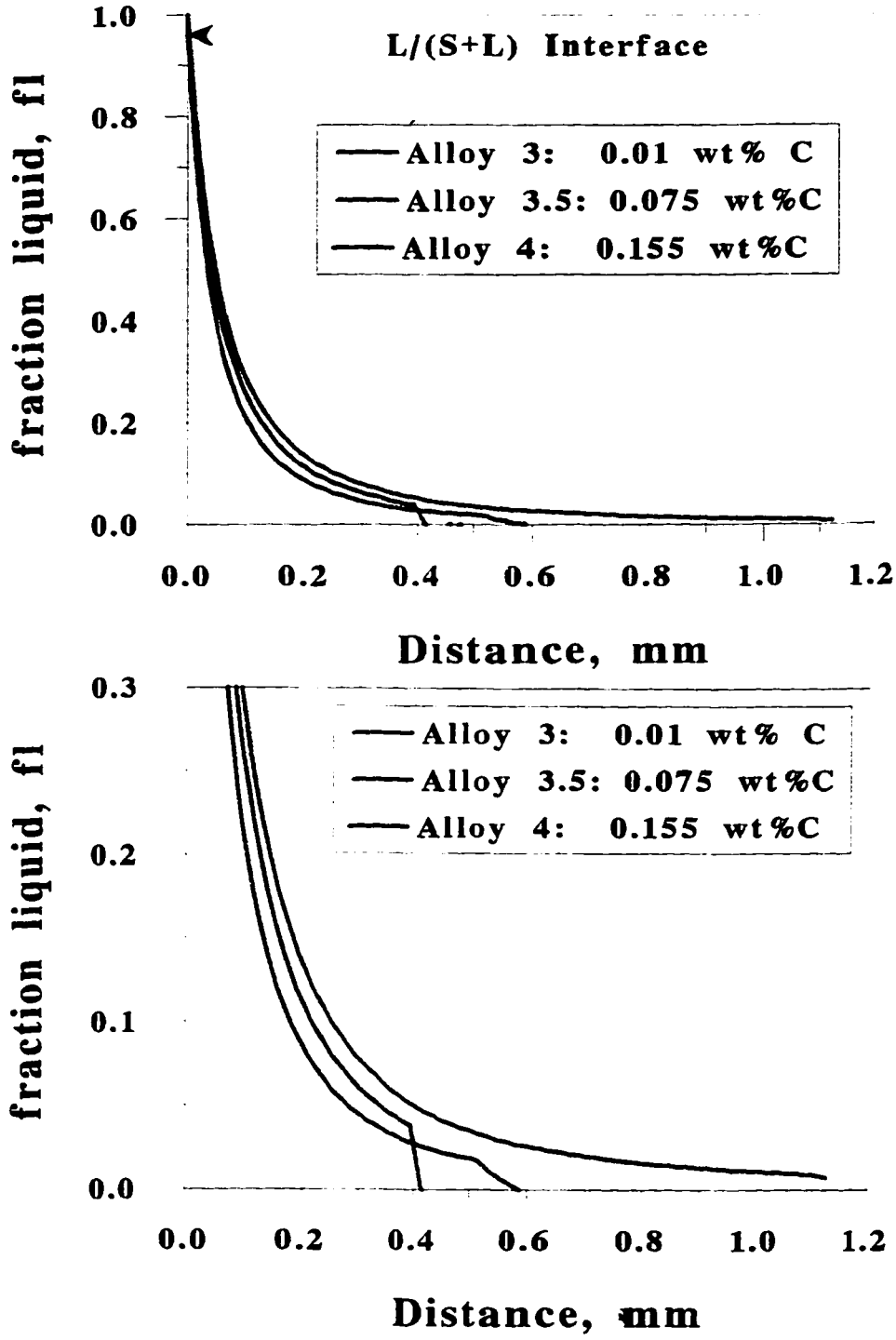

Figure 6.10. Variation in fraction liquid with distance in the mushy zone of Alloys 3, 3.5, and 4.

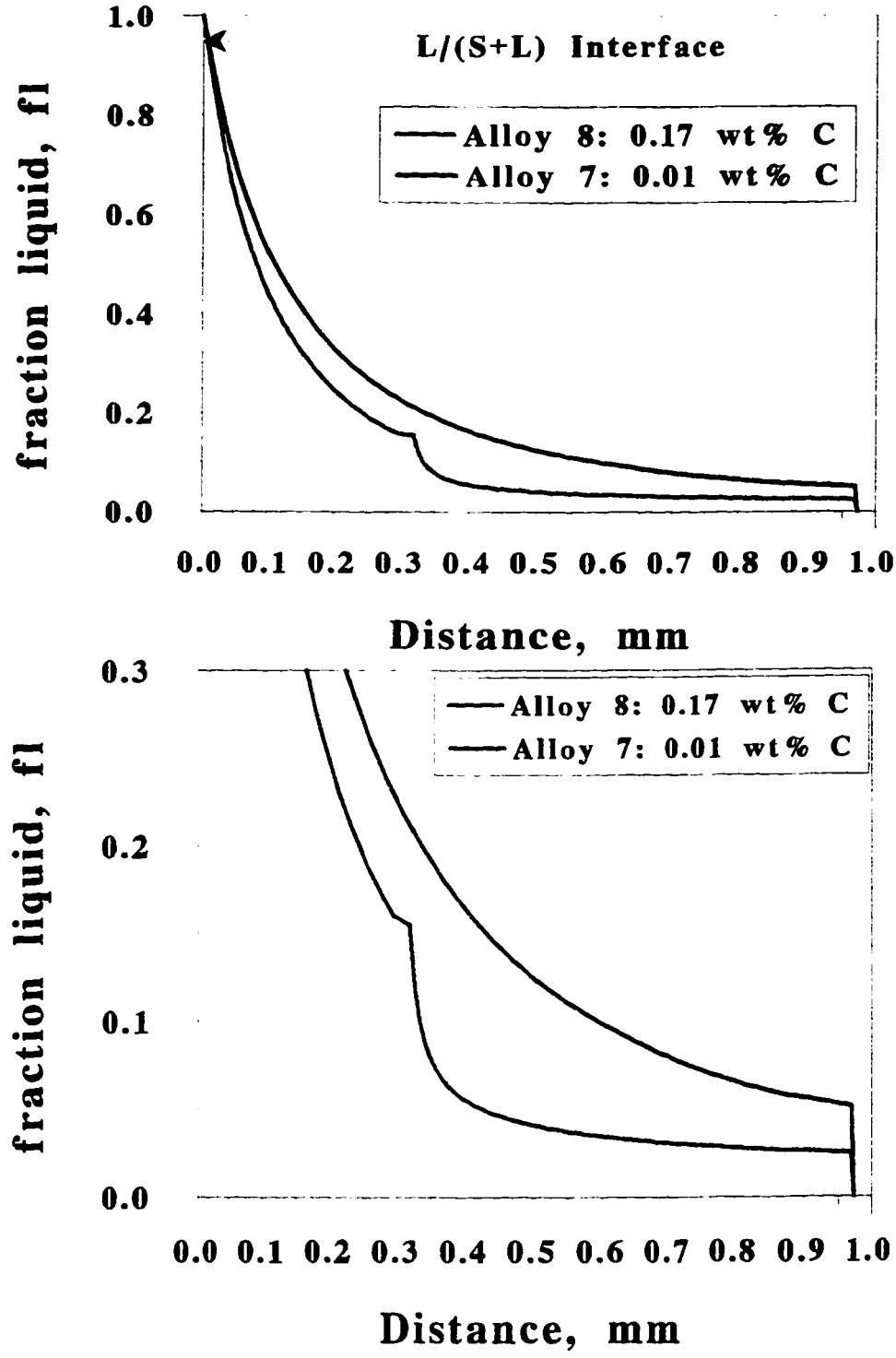

Figure 6.11. Variation in fraction liquid with distance in the mushy zone of Alloys 7 and 8.

6.4 CHAPTER CONCLUSIONS

The fusion zone solidification cracking susceptibility of experimental Ni base and Fe base superalloys containing Nb, Si, and C has been investigated through varestraint testing, microstructural characterization, and solidification modelling. The following conclusions can be drawn from this work:

1. In the Ni base alloys, C additions above 0.052 wt% significantly improve the solidification cracking resistance. As C content is increased, the primary L $\rightarrow \gamma$ solidification stage occurs over a relatively narrow temperature range and decreases the crack susceptible mushy zone. At high Nb levels, Si additions to the Ni base alloys have a slightly adverse effect on cracking resistance by promoting the L $\rightarrow (\gamma$ + Laves) reaction and extending the solidification temperature range.

2. Carbon additions to the Fe base alloys are only advantageous when the Nb level is below $\approx$ 2 wt%, and the C level must be above $\approx$0.12 wt% for the beneficial effect to be observed. When the Nb level is high in the Fe base alloys, a large amount of terminal liquid at the γ/Laves composition will exists as a continuous film and thus override any beneficial effect of C. The high amounts of γ/Laves observed in the Fe base alloys is attributed mainly to the increased segregation potential of Nb and, to a lesser extent, on the reduced amount of Nb needed in the liquid to satisfy the L $\rightarrow (\gamma$ + Laves) reaction.

3. There is generally no direct relation between the actual solidification temperature range and fusion zone cracking susceptibility of these experimental alloys, suggesting that crack propagation through the mushy zone is affected by the amount and morphology of solid and liquid phases in the mushy zone.

4. A classification scheme is proposed to provide a phenomenalogical explanation of the relation between the solidification temperature range, microstructural morphology, and cracking propensity. This morphological description leads to an improved correlation between the (adjusted) solidification temperature range and fusion zone cracking tendency.

5. A method is proposed for calculating the distribution of liquid in the mushy zone as an aid to determining the effect of alloy additions on solidification cracking susceptibility. The model combines the general liquidus equation of a multi-component system, solute redistribution relations, and temperature gradient information. Preliminary calculations are presented for several alloys, and the results are found to reveal some important relations between alloy composition, the distribution of liquid in the mushy zone, and cracking susceptibility. In particular, the results directly show that C additions reduce the size of the crack susceptible mushy zone. The model should be readily applicable to any binary or multi-component alloy system when the proper phase diagram quantities and solute redistribution behavior are known or can be estimated.

7. RESEARCH SUMMARY AND CONCLUSIONS

The solidification behavior and weldability of experimental alloys simulating compositions of commercial Ni base and Fe base superalloys containing Nb, Si, and C was investigated by differential thermal analysis, weld-quench experiments, microstructural characterization (LOM, SEM, EPMA BEKP) Varestraint testing, and solidification modelling. The following conclusions can be drawn from this work.

7.1 SOLIDIFICATION

1. The general solidification sequence of these alloys can be described by a three step process: 1) Primary $L \rightarrow \gamma$ solidification in which the interdendritic liquid becomes enriched in Nb and C, followed by 2) a eutectic-type $L \rightarrow (\gamma + NbC)$ reaction which depletes the interdendritic liquid of C, and 3) termination of solidification by a second eutectic-type reaction $L \rightarrow (\gamma + Laves)$. This solidification reaction sequence is similar to that expected in the ternary Ni-Nb-C system and observed experimentally in many commercial alloy systems.

2. The $L \rightarrow (\gamma + NbC)$ reaction generally occurs over a broad temperature range and is initiated at higher temperatures as the nominal C content of the alloys is increased. The $L \rightarrow (\gamma + Laves)$ reaction occurs over a narrow temperature range.

3. The distribution coefficients (k) for all solute elements (Nb, Si, and C) are less than unity while the "solvent" elements (Fe,Ni,Cr) exhibit little tendency for segregation ($k \approx$

1). This is in agreement with results reported on comparable commercial alloy systems.

4. An interactive effect between the segregation potential of Nb and nominal Fe content has been observed, where the value of k_{Nb} decreases in a linear-type fashion from 0.54 to 0.25 as the Fe content is increased from ≈ 2 wt% to ≈ 47 wt%. This behavior is the major factor contributing to the formation of relatively high amounts of eutectic-type constituents in the Fe base alloys.

5. Carbon additions promote formation of the γ/NbC constituent. The addition of Fe and Si will reduce the amount of Nb needed in the liquid to initiate the L → (γ + Laves) reaction. As a result, the amount of γ/Laves constituent increases with increasing Fe and Si. The effect of Nb depends on the C content. At high C levels, Nb additions will promote formation of γ/NbC. When the C level is low, Nb generally promotes formation of the γ/Laves constituent.

6. Under the current processing conditions in which the cooling rate is ≈ 660 °C/s, the diffusion of Nb in austenite is negligible during solidification and the Scheil equation provides a good description of solute redistribution. Microsegregation calculations for C, via the Klyne-Kurz model and literature data on diffusion rates of C in γ, indicate that C can diffuse fast enough to maintain equilibrium during solidification and the lever law can be used to describe the redistribution behavior for C.

7. An analytical solidification path expression, eq. (4.29), has been proposed to describe the change in liquid composition during solidification in a ternary system in which one solute exhibits negligible diffusion while the other solute diffuses infinitely fast in the solid.

8. A pseudo-ternary γ-Nb-C solidification surface has been proposed which identifies the liquid compositions required to initiate the $L \rightarrow (\gamma + NbC)$ and $L \rightarrow (\gamma + Laves)$ eutectic type reactions. The Nb compositions of the diagram were checked by comparison of calculated volume fractions of eutectic type constituents (via the Scheil equation) and those measured experimentally, and good agreement is found. The general positions of two fold saturation lines on the proposed surface were compared to those predicted by thermodynamic calculations and reasonable agreement is found.

9. The multi-component alloys were modelled as a ternary system by grouping the matrix (Fe,Ni,Cr) elements together as the "solvent" to form the γ component of the γ-Nb-C "ternary system". The variation in fraction liquid and liquid composition during the primary $L \rightarrow \gamma$ and eutectic type $L \rightarrow (\gamma + NbC)$ stages of solidification were calculated for conditions of negligible Nb diffusion and infinitely fast C diffusion in the solid phase. The proposed model is based on the solute redistribution equations for eutectic-type solidification originally developed by Mehrabian and Flemings. Results of the calculations were superimposed on the pseudo ternary γ-Nb-C solidification surface to predict the solidification reaction sequences along with the total and individual amounts of γ/NbC

and γ/Laves eutectic-type constituents which form during solidification. Comparison is made to experimentally measured values, and reasonable agreement is found. The model results permit quantitative interpretations of composition-microstructure relations in these Nb bearing experimental alloys and should provide useful insight into comparable commercial alloy systems as well. These results will be used in the next chapter to determine the relation between composition, microstructure, and fusion zone cracking susceptibility.

7.2 WELDABILITY

1. In the Ni base alloys, C additions above 0.052 wt% significantly improve the solidification cracking resistance. As C content is increased, the primary L $\rightarrow$ γ solidification stage occurs over a relatively narrow temperature range and decreases the crack susceptible mushy zone. At high Nb levels, Si additions to the Ni base alloys have a slightly adverse effect on cracking resistance by promoting the L $\rightarrow$ (γ + Laves) reaction and extending the solidification temperature range.

2. Carbon additions to the Fe base alloys are only advantageous when the Nb level is below $\approx$ 2 wt%, and the C level must be above $\approx$0.12 wt% for the beneficial effect to be observed. When the Nb level is high in the Fe base alloys, a large amount of terminal liquid at the γ/Laves composition will exists as a continuous film and thus override any beneficial effect of C. The high amounts of γ/Laves observed in the Fe base alloys is attributed mainly to the increased segregation potential of Nb and, to a lesser extent, on

the reduced amount of Nb needed in the liquid to satisfy the $L \rightarrow (\gamma + \text{Laves})$ reaction.

3. There is generally no direct relation between the actual solidification temperature range and fusion zone cracking susceptibility of these experimental alloys, suggesting that crack propagation through the mushy zone is affected by the amount and morphology of solid and liquid phases in the mushy zone.

4. A classification scheme is proposed to provide a phenomenalogical explanation of the relation between the solidification temperature range, microstructural morphology, and cracking propensity. This morphological description leads to an improved correlation between the (adjusted) solidification temperature range and fusion zone cracking tendency.

5. A method is proposed for calculating the distribution of liquid in the mushy zone as an aid to determining the effect of alloy additions on solidification cracking susceptibility. The model combines the general liquidus equation of a multi-component system, solute redistribution relations, and temperature gradient information. Preliminary calculations are presented for several alloys, and the results are found to reveal some important relations between alloy composition, the distribution of liquid in the mushy zone, and cracking susceptibility. In particular, the results directly show that C additions reduce the size of the crack susceptible mushy zone. The model should be readily applicable to any binary or multi-component alloy system when the proper phase diagram quantities and solute redistribution behavior are known or can be estimated.

8. FUTURE RESEARCH

The results and analyses established in this research provide a frame work for future studies which can be undertaken in order to improve the understanding of solidification concepts and fusion zone solidification cracking susceptibility. Several areas of suggested future work are described below.

1. Multi-Component Solidification Modelling

A pseudo-ternary approach to solute redistribution and microstructural modelling was taken in this work by choosing Nb and C as the "solutes", since they had the most pronounced effect on microstructural evolution. This approach could not quantitatively account for effects from the third element (Si) or variations in the matrix composition (Fe,Ni,Cr). As discussed, these quaternary additions have the effect of shifting the two fold saturation lines during solidification. It is interesting to note that the thermodynamic calculations of the liquidus surfaces (Figure 4.66) are in reasonable agreement with the experimentally determined solidification surfaces. Thus, it should be possible to use the Thermo-Calc software program to describe the position of the two fold saturation lines at any particular point during solidification in a multi-component alloy. In addition, there is no limit to the number of solutes which can be included in the mass balance equations utilized to describe solute redistribution. Thus, it should be possible to extend the mass balance equations to include additional solute elements and to combine this information with the Thermo-calc calculations to account for shifts which occur in the two fold saturation lines during solidification. Such an approach would permit a more

comprehensive model which accounts for effects from all elements in the system.

2. Microstructural Modification by Rapid Solidification Processing

The segregation behavior of Niobium has a pronounced effect on microstructural development and associated solidification cracking susceptibility of these experimental alloys as well as commercial alloy systems. The strong segregation potential of Nb is also deleterious from a mechanical property standpoint. Niobium is added as either a solid solution strengthener or precipitation hardening element. However, its effectiveness is lost in as-cast microstructures where the dendrite cores become significantly depleted of solute, particularly in high Fe alloys which exhibit low k_{Nb} values. The high cooling rates associated with laser and electron beam processes provide an opportunity to induce significant dendrite tip undercooling and concomitant solute trapping. Under such conditions, it should be possible to increase the amount of Nb retained in the solid, thereby improving mechanical properties and possibly improving resistance to solidification cracking. Such details can be modeled using rapid solidification theory and the alloy solidification parameters which have been determined in this research. Thus, the results provided in this work set the basis for this possible future research.

3. Modelling of Mushy Zones

The method outlined in Chapter 6 for calculating the variation in fraction liquid in the mushy zone should be used for detailed calculations of all the alloys investigated in this program. It may also be possible to improve the accuracy of the calculations by

using liquidus temperature-composition relations established over the entire liquidus surface through the Thermo-Calc software program. This would avoid the need for the empirical relations and permit inclusion of quaternary and higher order elements.

9. REFERENCES

CHAPTER 2

2.1 T. Zacharia, *Welding Journal*, 1994, Vol. 73, pp. 164s-172s.

2.2 J.A. Brooks, *Proceedings of Internal Conference on Modeling and Control of Joining Processes*, December 8-10, 1993, Orlando, Fl.

2.3 J.C. Boreland, *British Welding Journal*, 1960, Vol. 7, pp. 508-512.

2.4 D.C.G. Lees, *Journal of Institute of Metals*, 1946, Vol. 72, p. 343.

2.5 F. Matsuda, H. Nakagawa, S. Katayama, and Y. Arata, *Transactions of the Japan Welding Society*, 1982, Vol. 13, pp. 41-58.

2.6 C.D. Lundin, C.H. Lee, and C.Y.P. Qiao, *Welding Journal*, 1993, Vol. 72, pp. 321s-328s.

2.7 M. J. Cieslak, *Welding Journal*, 1991, Vol. 70, pp. 49s-56s.

2.8 Y. Nakao, H. Ohshige, S. Koga, H. Nishihara, and J. Sugitani, *Journal of the Japan Welding Society*, 1982, Vol. 51, pp. 989-995.

2.9 J.C. Boreland and R.N. Younger, *British Welding Journal*, 1960, Vol. 7, pp. 22-59.

2.10 G.R. Rundell, in *Effects of Minor Elements on the Weldability of High-Nickel Alloys*, Welding Research Council, New York, NY, 1969, pp. 36-46.

2.11 D.A. Porter and K.E. Easterling, *Phase Transformations in Metals and Alloys*, VNR International, England, 1981, p. 211.

2.12 T.W Clyne and G.J. Davies, *TMA Proceedings of the International Conference on Solidification*, Sheffield, 1979, pp. 275-278.

2.13 Y. Arata, F. Matsuda, and S. Katayama, *Transactions of the Japanese Welding*

Research Institute, 1977, pp. 105-116.

2.14 J.A. Brooks, *Proceedings of Weldability of Materials*, October 8-12, 1990, ASM, pp. 41-48.

2.15 J.A. Brooks and M.I. Baskes, *Proceedings of Advances in Welding Science and Technology*, May 18-22, 1986, ASM, pp. 93-100.

2.16 G.A. Knorovsky, M.J. Cieslak, T.J. Headley, A.D. Romig, Jr., and W.F. Hammetter, *Metallurgical Transactions A*, 1989, Vol. 20A, pp. 2149-2158.

2.17 M.J. Cieslak, G.A. Knorovsky, T.J. Headley, and A.D. Romig, Jr., *Metallurgical Transactions A*, 1986, Vol. 17A, pp. 2107-2116.

2.18 M.J. Cieslak, J.J. Stephens, and M.J. Carr, *Metallurgical Transactions A.*, 1988, Vol. 19A, pp. 657-667.

2.19 G. Jolley and J.E. Geraghty, *Solidification and Casting of Metals*, 1979, The Metals Society, pp. 411-415.

2.20 E. Scheil: *Z. Metallk.*, 1942, Vol. 34, p. 70.

2.21 M.C. Flemmings, *Solidification Processing*, McGraw-Hill, New York, 1974.

2.22 J.W. Rutter and B. Chalmers, *Canadian Journal of Physics*, 1953, Vol. 31, p. 15.

2.23 H.D. Brody and M.C. Flemings, *Transactions of AIME*, 1966, Vol. 236, pp. 615-623.

2.24 T.W. Clyne and W. Kurz, *Metallurgical Transactions A*, 1981, Vol. 12A, pp. 965-971.

2.25 T.F. Bower, H.D. Brody and M.C. Flemings, *Transactions of AIME*, 1966, Vol. 236, pp. 624-634.

2.26 S.A. David and J.M. Vitek, *International Materials Review.*, 1989, Vol. 34, pp. 213-

245.

2.27 T.P. Battle, *International Materials Review*, 1992, Vol. 37, pp. 249-270.

2.28 D.H. Kirkwood, *Materials Science and Engineering*, 1984, Vol. 65, pp. 101-109.

2.29 M.H. Burden and J.D. Hunt, *Journal of Crystal Growth*, 1974, Vol. 22, pp. 109-116.

2.30 M. Solari and H. Biloni, *Journal of Crystal Growth*, 1980, Vol. 49, pp. 451-457.

2.31 W.W. Mullins and R.F. Sekerka, *Journal of Applied Physics*, 1964, Vol. 35, p. 444.

2.32 W.F. Savage, *Welding in the World*, 1980, Vol. 18, pp. 89-111.

2.33 J.C. Lippold and W.F. Savage, *TMS-AIME Proceedings of Casting and Welding Process Modelling*, 1980, Rindye, NH.

2.34 J.W. Elmer, Sc.D. Thesis, Massachusetts Institute of Technology, Cambridge, MA, 1988.

2.35 R. Trivedi, *Journal of Crystal Growth*, 1980, Vol. 49, p. 219.

2.36 J.A. Sarreal, *Journal of Crystal Growth*, 1984, Vol. 69, p. 362.

2.37 J.A. Sarreal, *Journal of Crystal Growth*, 1985, Vol. 72, p. 578.

2.38 J.A. Sarreal, *Metallurgical Transactions A*, 1986, Vol. 17A, pp. 2063-2073.

2.39 P.W. Fuerschbach and G.A. Knorovsky, *Welding Journal*, 1991, Vol. 70, pp. 287s-297s.

2.40 J.N. DuPont and A.R. Marder, Thermal Efficiency of Arc Welding Processes, submitted to *Welding Journal*.

2.41 V.G. Rivlin and G.V. Raynor, *International Materials Review*, 1980, Vol. 25, pp. 21-38.

2.42 M.J. Cieslak, T.J. Headley, T. Kollie, and A.D. Romig, Jr., *Metallurgical*

Transactions A, 1988, Vol. 19A, pp. 2319-2331.

2.43 M. Hansen and K. Anderko, eds., *Constitution of Binary Alloys*, 2nd Ed., McGraw-Hill Book Co., New York, NY, 1958, pp. 374-375, 1010-1012, 1039-1042.

2.44 V.K. Ruttewit and G. Masing, *Z. Metallk.*, 1940, Vol. 32, pp. 52-61.

2.45 I.J. Duerden and W. Hume-Rothery, *J. Less-Common Metals*, 1966, Vol. 11, pp. 381-387.

2.46 M.J. Cieslak, T.J. Headley, G.A. Knorovsky, A.D. Romig, Jr., and T. Kollie, *Metallurgical Transactions A*, 1990, Vol. 21A, pp. 479-488.

2.47 K.E. Easterling, *Introduction to the Physical Metallurgy of Welding*, Butterworths, Boston, 1983, pp 56-59.

2.48 H.L. Eiselstein: *Advances in the Technology of Stainless Steels 369,* 1965, pp. 62-79.

2.49 M.J. Cieslak, T.J. Headley, A.D. Romig, Jr., *Metallurgical Transactions A*, 1986, Vol. 17A, pp. 2035-2047.

2.50 T. Ogawa and E. Tsunetomi, *Welding Journal*, 1982, Vol. 61, pp. 82s-93s.

2.51 J.N. DuPont and A.R. Marder, Dilution in Single Pass Arc Welds, *Metallurgical and Material Transactions B,* Vol. 27B, 1996, pp. 481-489.

2.52 M.J. Cieslak, *Welding Journal*, 1987, Vol. 66, pp. 57s-60s.

2.53 M.J. Cieslak, C.R. Hills, and T.J. Headley, *Microbeam Analysis*, 1986, A.D. Romig and W.F. Chalmers, eds., pp. 69-73.

2.54 R.A. Patterson and J.O. Milewski, *Welding Journal*, 1985, Vol. 64, pp. 227s-231s.

2.55 E.S. Robitz, Jr., and D.P. Edmonds, *Abstracts of Papers of 67th American Welding*

Society Meeting, pp. 136-138.

2.56. J.N. DuPont, Solidification of an Alloy 625 Weld Overlay, *Metallurgical and Material Transactions A*, Vol. 27A, 1996, pp. 3612-3620.

CHAPTER 3

3.1 Metals Handbook, Vol. 3, *Alloy Phase Diagrams*, ASM International, Materials Park, OH, 1992, p. 2-312.

3.2 W.F. Savage and C.D. Lundin, *Welding Journal*, 1965, vol. 44, pp 433s - 442s.

3.3 W.F. Savage and C.D. Lundin, *Welding Journal*, 1966, vol. 45, pp 497s - 503s.

3.4 M. Kajihara, T. Yoshikawa, M. Kikucki, and K. Yamauchi, *Iron and Steel Institute of Japan*, Vol. 32, No. 6, 1992, pp. 755-763.

3.5 S.R. Keown and F.B. Pickering, in *Niobium: Proceedings of the International Symposium*, H. Stuart (ed.). The Metallurgical Society of AIME, 1984, pp. 1113-1141.

3.6 K.F.J. Heinrich, *Microbeam Analysis*, Proc. of 21st Int. Conf., A.D. Romig, Jr. and W.F. Chambers (eds.), Albuquerque, New Mexico, 1986, pp. 279-280.

3.7 R.P. Goehner and J.R. Michael, *Journal of Research of the National Institute of Standards and Technology*, Vol. 101, No. 3, 1996, pp 301-308.

CHAPTER 4:

4.1 *Binary Alloy Phase Diagrams*, Vol. 1, T. B. Massalski (Ed.), American Society for Materials, Materials Park, Ohio, 1990, p. 863,

4.2 C.V. Robino, J.R. Michael, and M.J. Cieslak, The Solidification and Welding

Metallurgy of Thermo-Span Alloy, accepted for publication in Science and Technology of Welding and Joining.

4.3 M.J. Cieslak, T.J. Headley, G.A. Knorovsky, A.D. Romig, Jr., and T. Kollie, *Metallurgical Transactions A*, 1990, Vol. 21A, pp. 479-488.

4.4 *Metals Handbook*, 8th ed., American Society for Metals, 1973, vol. 8.

4.5 Z. Blazina and R. Trojko, *J. Less Common Metals*, 1986, vol. 119, pp. 297-305.

4.6 S.T. Wlodek, *Trans. Am. Soc. Met.*, 1963, vol. 56, pp. 287-303.

4.7 M.J. Cieslak, T.J. Headley, T. Kollie, and A.D. Romig, Jr., *Metallurgical Transactions A*, 1988, Vol. 19A, pp. 2319-2331.

4.8 G.A. Knorovsky, M.J. Cieslak, T.J. Headley, A.D. Romig, Jr., and W.F. Hammetter, *Metallurgical Transactions A*, 1989, Vol. 20A, pp. 2149-2158.

4.9 R. Nakkalil, N.L. Richards, and M.C. Chaturvedi, *Metallurgical Transactions A*, 1993, Vol. 24A, pp. 1169-1179.

4.10 Y. Nakao, H. Ohshige, S. Koga, H. Nishihara, and J. Sugitani, *Journal of the Japan Welding Society*, 1982, Vol. 51, pp. 989-995.

4.11 J.N. DuPont, Solidification of an Alloy 625 Weld Overlay, *Metallurgical and Material Transactions A*, Vol. 27A, 1996, pp. 3612-3620.

4.12 Q.H. Zhao, Y.P. Gao, J.H. Devletian, J.M. McCarthy, and W.E. Wood, *International Trends in Welding Science and Technology*, Proc. of 3rd Int. Conf., S.A. David and J.M. Vitek (eds.) ASM, Materials Park, OH, 1992, pp. 339-43.

4.13 M.J. Cieslak, C.R. Hills, and T.J. Headley, *Microbeam Analysis*, 1986, A.D. Romig and W.F. Chalmers, eds., pp. 69-73.

4.14 R. F. Speyer, *Thermal Analysis of Materials*, Marcel Dekker, New York, NY, 1994.

4.15. H.H. Stadelmaier and M.L. Fiedler, *Z. Metallkd.*, 1975, vol. 66 (4), pp. 224-225.

4.16 M.C. Flemings, *Solidification Processing*, McGraw-Hill, New York, NY, 1974.

4.17 F.N. Rhines, Phase Diagrams in Metallurgy, R.F. Mehl and M.B. Beaver (Eds.), McGraw Hill, New York, NY, 1956, pp. 175-185.

4.18 J. W. Elmer, Ph.D. Thesis, Massachusetts Institute of Technology, September, 1988.

4.19 H. Nakaqawa, Journal of Japan Welding Society, vol. 39 (94), 1970.

4.20 S. Katayama and A. Matsunawa, *Proc. ICALEO*, 1984, pp. 60-67.

4.21 A. Goldsmith, T.E. Waterman, and Harry J. Hirschborn, *Handbook of Thermophysical Properties of Solid Materials*, Vol. 2, The Macmillan Co., New York, NY, 1961. pp 160. 161.

4.22 C.F. Lucks and H.W. Deem, *Thermal Properties of Thirteen Metals*, STP No. 227, ASTM, Philadelphia, PA 1958.

4.23 P.W. Fuerschbach and G.A. Knorovsky: *Welding Journal,* 1991, vol. 70 (11), pp. 287s - 297s.

4.24 D.G. MacIssac, Y. Shiohara, M.G., Chu, and M.C. Flemings, *Grain Refinement in Castings and Welds*, AIME Publication, G.J. Abbaschian and S.A. David (Eds.), 1983, pp. 87-96.

4.25 H.D. Brody and M.C. Flemings, *Transactions of AIME*, 1966, Vol. 236, pp. 615-623.

4.26 S. Kurokawa, J.E. Ruzzante, A.M. Hey, and F. Dyment, *Metal Science*, Sept. 1983, vol. 17, pp. 433-38.

4.27 S.K. Bose and H.J. Grabke, *Z. Metallk*, 1978, 69 (1), pp. 8-15.

4.28 T.W. Clyne and W. Kurz, *Metallurgical Transactions A*, 1981, Vol. 12A, pp. 965-971.

4.29 M. Hansen and K. Anderko, eds., *Constitution of Binary Alloys*, 2nd Ed., McGraw-Hill Book Co., New York, NY, 1958, pp. 374-375, 1010-1012, 1039-1042.

4.30 V.K. Ruttewit and G. Masing, *Z. Metallk.*, 1940, Vol. 32, pp. 52-61.

4.31 I.J. Duerden and W. Hume-Rothery, *J. Less-Common Metals*, 1966, Vol. 11, pp. 381-387.

4.32 T.P. Battle, *International Materials Review*, 1992, Vol. 37, pp. 249-270.

4.33 R. Mehrabian and M.C. Flemings, *Metallurgical Transactions A*, 1970, Vol. 1, pp. 455-464.

4.44 B. Sundman, B. Jansson, and J.O. Anderson, *CALPHAD*, 1985, vol. 9, pp. 153-190.

CHAPTER 5:

5.1 R. Mehrabian and M.C. Flemings, *Metallurgical Transactions A*, 1970, Vol. 1, pp. 455-464.

5.2 *Binary Alloy Phase Diagrams*, Vol. 1, T. B. Massalski (Ed.), American Society for Materials, Materials Park, Ohio, 1990, p. 863.

5.3 M. Kajihara, T. Yoshikawa, M. Kikucki, and K. Yamauchi, *Iron and Steel Institute of Japan*, Vol. 32, No. 6, 1992, pp. 755-763.

5.4 Z. Blazina and R. Trojko, *J. Less Common Metals*, 1986, vol. 119, pp. 297-305.

CHAPTER 6:

6.1 G.A. Knorovsky, M.J. Cieslak, T.J. Headley, A.D. Romig, Jr., and W.F. Hammetter, Metallurgical Transactions A, 1989, Vol. 20A, pp. 2149-2158.

6.2 M. J. Cieslak, *Welding Journal*, 1991, Vol. 70, pp. 49s-56s.

6.3 J.N. DuPont, Solidification of an Alloy 625 Weld Overlay, *Metallurgical and Material Transactions A*, Vol. 27A, 1996, pp. 3612-3620.

6.4 C.V. Robino, J.R. Michael, and M.J. Cieslak, The Solidification and Welding Metallurgy of Thermo-Span Alloy, accepted for publication in Science and Technology of Welding and Joining.

6.5 Y. Nakao, H. Ohshige, S. Koga, H. Nishihara, and J. Sugitani, *Journal of the Japan Welding Society*, 1982, Vol. 51, pp. 989-995.

6.6 S.A. David and J.M. Vitek, *International Materials Review.*, 1989, Vol. 34, pp. 213-245.

6.7 Y. Arata, F. Matsuda, and S. Katayama, *Transactions of the Japanese Welding Research Institute*, 1977, pp. 105-116.

6.8 J.A. Brooks, *Proceedings of Weldability of Materials*, October 8-12, 1990, ASM, pp. 41-48.

VITA

John Neuman DuPont was born in Collingswood, N.J. to the parents of Alden and Pauline DuPont on February 27, 1964. He graduated from Pennridge High School in Perkasie, PA in June of 1982. He earned a B.S. degree in Metallurgical Engineering in 1990 (cum laude) from Ohio State University and an M.S. Degree Materials Science and Engineering from Lehigh University in 1994. John has worked in the Energy Research Center at Lehigh University as a Research Scientist since 1990 while pursuing his Ph.D. degree in Materials Science and Engineering. While at Lehigh, he has overseen development of the welding research laboratory and conducted government and industrial-sponsored research in the areas of process modelling and optimization, welding and solidification modelling of superalloys, and erosion properties of weld overlays and has authored or co-authored 15 publications in these areas. He was an ASM scholarship recipient in 1989-1990, received the Mars G. Fontana and Presidents Academic Excellence Awards at Ohio State in 1990, the AWS National Fellowship Award in 1995, and the American Welding Society Charles H. Jennings Memorial Best Paper Award in 1996. He is presently a Ph.D. candidate at Lehigh University in Materials Science and Engineering. He is a member of the American Welding Society and the Welding Research Council committees on Hardfacing and High Alloys. When finished his Ph.D. degree, he plans on consuming large amounts of beer and re-learning the art of fun and fishing.